THE UNIVERSITY OF CHICAGO

FIRST-PRINCIPLES STUDY OF EXCITED STATES AND OPTICAL PROPERTIES OF QUANTUM MATERIALS

A DISSERTATION SUBMITTED TO
THE FACULTY OF THE DIVISION OF THE PHYSICAL SCIENCES
IN CANDIDACY FOR THE DEGREE OF
DOCTOR OF PHILOSOPHY

DEPARTMENT OF CHEMISTRY

BY

YU JIN

CHICAGO, ILLINOIS

MARCH 2024

To my family

TABLE OF CONTENTS

LIST OF FIGURES

LIST OF TABLES

ACKNOWLEDGMENTS

I am profoundly grateful to my PhD advisor, Prof. Giulia Galli, whose invaluable guidance and expertise have been crucial to my academic journey. During my times of struggle, particularly when I faced depression, her unwavering support was a beacon of hope. Prof. Galli consistently encouraged me to broaden my horizons and embrace every opportunity that came my way. It is with sincere appreciation that I acknowledge her role in my achievements; without her steadfast support, completing my PhD would not have been possible.

I would like to thank my thesis committee members, Prof. Laura Gagliardi and Prof Alex High, for their invaluable advice and guidance.

I extend my heartfelt thanks to two mentors who were instrumental in my PhD journey: Prof. Marco Govoni and Dr. He Ma. Prof. Govoni guided me through all my method development projects, providing crucial advice on the design and implementation of theories and algorithms. His assistance in scientific writing has been invaluable. Dr. He Ma introduced me to the theoretical study of light-matter interaction, imparting extensive knowledge in both the theoretical underpinnings and practical applications of first-principles calculations.

I am grateful to my collaborators in the Galli group for their invaluable contributions. I extend my thanks to Dr. Victor Wen-zhe Yu, Dr. He Ma, Dr. Han Yang, Dr. Christian Vorwerk, Dr. Nan Sheng, and Andrew Xu for their assistance with the WEST code and their insightful input on various method development projects. My gratitude also goes to Dr. Mykyta Onizhuk, Dr. Vrindaa Somjit, Yizhi Zhu, Benchen Huang, Shreya Verma, and Anil Bilgin for their enriching discussions on spin-defect projects, and to Dr. Mariami Rusishvili for our enlightening collaboration on the perovskite project. Additionally, I would like to acknowledge my many friends in the Galli group. Their friendship has been immensely appreciated. I am truly thankful for the warm and supportive environment they have created, making my time in the group both enjoyable and rewarding.

In addition to my time with the Galli group, my PhD journey was greatly enriched by the

opportunity to collaborate with several distinguished research groups in diverse areas. I am grateful for the experiences gained while working with Prof. Alex High's group, Prof. Laura Gagliardi's group, and Prof. David Awschalom's group. These collaborations allowed me to engage with many brilliant individuals who imparted various perspectives and methodologies, significantly broadening the scope and depth of my PhD studies. Their collective wisdom and diverse approaches have been invaluable in shaping my academic growth.

Lastly, my deepest gratitude goes to my family, particularly my parents, whose unwavering support has been the cornerstone of my achievements. I also wish to express my heartfelt thanks to my girlfriend, Jane, for her companionship and steadfast support throughout my entire PhD journey. Her presence and encouragement have been sources of strength and inspiration during this significant phase of my life.

ABSTRACT

First-principles studies, grounded in quantum mechanics, offer a profound understanding of materials and chemical systems at the most fundamental level without relying on empirical data. By providing detailed insights into electronic structures, atomic interactions, and potential energy surfaces, first-principles calculations have become indispensable in the exploration and design of new materials and molecules. These studies not only enhance our comprehension of existing systems but also pave the way for innovative applications in fields ranging from energy storage and catalysis to pharmaceuticals and nanotechnology. In this dissertation, I will present several advancements in the development and application of quantum mechanical methods for first-principles simulations of solid-state systems, focusing on their excited states and optical properties.

First, I will present the development and implementation of the linear-response time-dependent density functional theory and its analytical nuclear forces. A multilevel parallelization scheme, numerical approximations, and GPU accelerations enable the study of excited state energy and atomic geometry relaxation of solid-state systems containing thousands of electrons at the level of hybrid functional. We demonstrated its capability by studying the excited states of several point defects in semiconductors and insulators.

Next, I will present our effort in developing and implementing the generating function approach to compute the vibrationally resolved optical spectra for point defects in solids. We assessed the validity of theoretical and numerical approximations used in first-principles calculations by computing the photoluminescence spectra for prototypical point defects, the divacancy centers in SiC, and the nitrogen vacancy in diamond and compared them with experimental results. We also addressed the importance of correcting for finite-size effects.

Following the development, implementation, and validation of several theoretical approaches, I then present an application study on the vibrationally resolved optical spectra for the nitrogen vacancy center in diamond, focusing on the optical transitions between

the highly correlated singlet states. Our development and implementation of the spin-flip time-dependent density functional theory and analytical nuclear forces enable us to compute the energy and vibrations in the highly correlated singlet states, and our development and implementation of the generating function approach enable us to compute the vibrationally resolved absorption spectrum between the highly correlated singlet states, resulting in good agreement with the experiments.

I will then present several applications of first-principles methods for the study of spin defects in semiconductors, including the study of the photoionization process of the neutral divacancy center in silicon carbide and the neutral substitutional nitrogen in diamond. These studies are instrumental in the interpretation of experimental results and the design of new spin defects for quantum technology applications.

Finally, I will present a theoretical study of several inorganic metal-halide perovskite systems, focusing on the formation of the self-trapped exciton and the associated broadband emission. We investigated the exciton-phonon coupling and multiphonon optical processes. This study provides insights for designing metal-halide perovskites with tailored emission properties.

CHAPTER 1

INTRODUCTION

Over the past several decades, the role of first-principles calculations has been increasingly recognized in advancing our understanding of complex scientific phenomena. These calculations, rooted in the fundamental principles of quantum mechanics, offer critical insights into the behavior of atomic, molecular, and solid-state systems. Their applications are broad, encompassing areas such as molecular engineering, renewable energy, and semiconductor design [1–6]. These approaches mark a transformative shift in scientific research, enabling precise predictions and a deeper understanding of material properties and interactions at the atomic level, which are crucial for innovation in technology and science.

A pivotal area of study within first-principles calculations is the interaction between light and matter. This interaction is crucial for advancements in light harvesting technologies and for the interpretation and prediction of optical spectroscopy [7–11]. A comprehensive first-principles study of light-matter interaction necessitates the examination of both the ground state and the excited states, each contributing uniquely to our understanding of these processes. This dissertation concentrates on the processes of optical absorption and emission involving transitions between electronic states, typically ranging from ultraviolet to visible wavelengths. Centering on the study of light-matter interaction, there are two major themes in the dissertation. The first theme of the dissertation revolves around the development and implementation of theoretical methods for investigating electronic excited states and optical processes.

Density Functional Theory (DFT) stands as a highly successful method in the realm of first-principles calculations, with a striking balance between computational efficiency and accuracy. Central to DFT is the Kohn-Sham formulation, where the many-electron Schrodinger equation is transformed into the Schrodinger equation of non-interacting electrons [12], namely the Kohn-Sham equations. This transformation makes DFT a robust and

reliable framework for investigating ground-state properties, including electronic structure, transport, and thermodynamics, of a variety of systems spanning from simple molecules to complex materials.

Complementing DFT, time-dependent density functional theory (TDDFT) has been formulated to investigate electronic excited states [13, 14]. In linear-response TDDFT, a small external perturbation, such as the electric field accompanying photons, is applied to the system, and the response function of the system is studied. Electronic excitations can be obtained from the poles of the response function by solving the Casida equation [15, 16]. TDDFT stands out due to its relatively low computational cost and its capability to provide analytical forces for optimizing atomic geometries [17], which makes it an invaluable tool for studying the physical processes of excited states in complex systems. The power of TDDFT has been leveraged in the past two decades in the quantum chemistry community for the study of excited states and the potential energy surfaces of molecular systems and the related optical processes [18–23]. However, its applications to solid-state systems have been mostly limited to the study of optical absorption spectra [24–26], mainly due to the lack of efficient implementations for the analytical forces on nuclei. In Chapter 3, we present an efficient implementation of linear-response TDDFT and its analytical forces acting on nuclei with the plane-wave pseudo-potential approach, allowing for the study of excited-state energy and atomic forces of solid-state systems with thousands of electrons.

The advancement toward computational spectroscopy marks a significant step forward. However, this progression involves several approximations that, while essential for computational feasibility, pose challenges in the precise prediction and interpretation of spectroscopic observables. Particularly, optical transitions between electronic states often engage nuclear vibrations, leading to vibrationally resolved optical spectra. This phenomenon has been extensively examined in molecular systems within the quantum chemistry field. For solid-state systems, though, research is not as advanced. This is due to the complexities in handling

vibrational degrees of freedom in electronically excited states and the inherently infinite number of vibrations involved in these processes. In Chapter 4, we introduce an approach using the generating function method for calculating vibrationally resolved optical spectra. This method effectively accounts for a vast number of vibrations. We also explore strategies to compensate for finite-size effects and incorporate the impact of extensive, delocalized vibrational modes. Additionally, we evaluate the accuracy of the approximations used in determining vibrationally resolved optical spectra.

The second theme of the dissertation revolves around the practical application of the methods described above. Their utility in studying the excited states and optical properties of various material systems is explored. The first area of study is point defects in semiconductors and insulators, which hold great potential in the application of quantum information science by acting as quantum bits (qubits) [27]. The initialization and reading of these point defect qubits are commonly conducted through optical methods, making a first-principles analysis of light-defect interactions crucial for interpreting spectroscopic data, designing experiments, and identifying new defect candidates. In Chapter 5, we present a theoretical study of the vibrationally resolved optical spectra between highly correlated electronic excited states for a point defect, employing spin-flip TDDFT and analytical nuclear forces to study the coupling between the electronic and nuclear degrees of freedom in optical processes. Chapter 6 delves into theoretical studies that aid in understanding experiments related to photo-ionization, stimulated emission, and other processes in point defects within diamond and silicon carbide. These studies provide critical insights into the optical processes of point defects, supporting the broader field of quantum technology research.

Additionally, the methodologies we developed were applied to investigate the excited states and optical properties of metal-halide perovskites, a class of materials with considerable potential in photovoltaic applications. In Chapter 7, we conduct a theoretical exploration of the formation of self-trapped excitons. This involves utilizing our efficient

implementation of the TDDFT approach to analyze the atomic geometry distortions that occur due to the creation of self-trapped excitons. We calculated the associated broadband emission spectra using a similar method as for other optical spectra. A significant finding of our study is the importance of direct atomic geometry optimization. We demonstrate that relying solely on exciton-phonon coupling calculations at the ground state atomic geometry is inadequate for accurate predictions.

We conclude the dissertation with a brief summary of the methods we developed to compute the excited states and optical processes and their applications on various material systems. We also discuss possible directions for further research that this dissertation points toward.

CHAPTER 2

THEORETICAL BACKGROUND

2.1 Born-Oppenheimer approximation

The behavior of molecules and materials at the microscopic level is determined by the interactions between electrons and atomic nuclei. For a microscopic system consisting of N_{el} electrons and N_{nuc} nuclei, its eigenstate, $|\Phi_{\mathcal{I}}\rangle$, satisfies the many-body Schrodinger equation

$$\hat{H}|\Phi_{\mathcal{I}}\rangle = E_{\mathcal{I}}|\Phi_{\mathcal{I}}\rangle, \tag{2.1}$$

where $E_{\mathcal{I}}$ is the eigenenergy, and $\hat{H}$ is the many-body Schrodinger equation under the nonrelativistic approximation

$$\hat{H} = \hat{T}_{\mathrm{N}} + \hat{T}_{\mathrm{e}} + \hat{U}_{\mathrm{e-e}} + \hat{U}_{\mathrm{e-N}} + \hat{U}_{\mathrm{N-N}}. \tag{2.2}$$

Here $\hat{U}_{\mathrm{e-e}}$, $\hat{U}_{\mathrm{e-N}}$, and $\hat{U}_{\mathrm{N-N}}$ represent the electron-electron, electron-nuclei, nuclei-nuclei interaction, which are defined as

$$U_{\mathrm{e-e}}(\{\mathbf{r}\}) = \sum_{i<j}^{N_{\mathrm{el}}} \frac{1}{|\mathbf{r}_i - \mathbf{r}_j|}, \tag{2.3}$$

$$U_{\mathrm{e-N}}(\{\mathbf{r}\},\{\mathbf{R}\}) = -\sum_{i=1}^{N_{\mathrm{el}}}\sum_{I=1}^{N_{\mathrm{nuc}}} \frac{Z_I}{|\mathbf{r}_i - \mathbf{R}_I|}, \tag{2.4}$$

$$U_{\mathrm{N-N}}(\{\mathbf{R}\}) = \sum_{I<J}^{N_{\mathrm{nuc}}} \frac{Z_I Z_J}{|\mathbf{R}_I - \mathbf{R}_J|}. \tag{2.5}$$

Here, $\{\mathbf{r}\}$ and $\{\mathbf{R}\}$ represent coordinates of all electrons and nuclei, respectively. $\hat{T}_{\mathrm{N}}$ and $\hat{T}_{\mathrm{e}}$ are the kinetic operators of nucleus and electron,

$$T_{\mathrm{e}} = -\sum_{i=1}^{N_{\mathrm{el}}} \frac{1}{2}\nabla_i^2, \tag{2.6}$$

$$T_{\mathrm{N}} = -\sum_{I=1}^{N_{\mathrm{nuc}}} \frac{1}{2M_I}\nabla_I^2, \tag{2.7}$$

where Z_I is the nuclear charge, and M_I represents the mass of the electron (I-th nucleus). Since the mass of the nucleus is usually much larger than the electron, resulting in much faster motion of the latter, we can treat $\hat{T}_{\mathrm{N}}$ as a perturbation. Under the zeroth order approximation, the Schrodinger equation for electrons reads

$$\hat{H}_{\mathrm{el}}(\{\mathbf{R}\})|\Psi_i(\{\mathbf{R}\})\rangle = V_i(\{\mathbf{R}\})|\Psi_i(\{\mathbf{R}\})\rangle, \tag{2.8}$$

where

$$\hat{H}_{\mathrm{el}}(\{\mathbf{R}\}) = \hat{T}_{\mathrm{e}} + \hat{U}_{\mathrm{e-e}} + \hat{U}_{\mathrm{e-N}} + \hat{U}_{\mathrm{N-N}} \tag{2.9}$$

is the Hamiltonian of electrons which depends on the nuclear coordinates $\{\mathbf{R}\}$, and $V_i(\{\mathbf{R}\})$ is the energy of the many-electron state $|\Psi_i(\{\mathbf{R}\})\rangle$.

In the coordinate representation, for given nuclear coordinates $\{\mathbf{R}\}$, the total wavefunction $\Phi_{\mathcal{I}}(\{\mathbf{r}\},\{\mathbf{R}\})$ can be expanded using $\{\Psi_i(\{\mathbf{r}\},\{\mathbf{R}\})\}$ as basis functions

$$\Phi_{\mathcal{I}}(\{\mathbf{r}\},\{\mathbf{R}\}) = \sum_i \Theta_{\mathcal{I},i}(\{\mathbf{R}\})\ \Psi_i(\{\mathbf{r}\},\{\mathbf{R}\}), \tag{2.10}$$

or equivalently

$$|\Phi_{\mathcal{I}}\rangle = \sum_i |\Theta_{\mathcal{I},i}\rangle|\Psi_i\rangle, \tag{2.11}$$

which is the Born-Oppenheimer expansion [28]. $|\Theta_{\mathcal{I},i}\rangle$ can be computed by solving the

eigenvalue equation

$$\left[\hat{T}_{\mathrm{N}} + \hat{V}_i\right] |\Theta_{\mathcal{I},i}\rangle - \sum_j \hat{\Lambda}_{ij} |\Theta_{\mathcal{I},j}\rangle = E_{\mathcal{I}} |\Theta_{\mathcal{I}}, i\rangle, \tag{2.12}$$

where $\hat{\Lambda}_{ij}$ is the nonadiabatic coupling operator. By assuming that the coupling terms $\hat{\Lambda}_{ij}$ is approximately zero, we arrive at the Born-Oppenheimer adiabatic approximation

$$\left[\hat{T}_{\mathrm{N}} + \hat{V}_i\right] |\Theta_{\mathcal{I},i}\rangle = E_{\mathcal{I}} |\Theta_{\mathcal{I},i}\rangle. \tag{2.13}$$

Here, $V_i(\{\mathbf{R}\})$ is the i-th adiabatic potential energy surface (PES), which can be obtained by solving Eq 2.8, the Schrodinger equation for the electrons, at fixed nuclear coordinates $\{\mathbf{R}\}$. Within the Born-Oppenheimer approximation, nuclei move on adiabatic PES.

2.2 Density functional theory

Under the Born-Oppenheimer adiabatic approximation, the electronic and nuclear degrees can be separated, and the many-body Schrodinger equation for electrons, Eq. (2.8), can be solved at fixed nuclear coordinates. However, the exact solution of the many-body Schrodinger equation for electrons grows exponentially as the system size increases, and approximations are required for practical calculations. Density functional theory (DFT) is one of the most successful electronic structure theories to study the ground state of a many-electron system.

In the DFT framework, the many-electron Hamiltonian is separated into the following two terms:

$$\hat{H}_{\mathrm{el}} = \hat{H}_{\mathrm{int}} + \hat{V}_{\mathrm{ext}}, \tag{2.14}$$

where $\hat{H}_{\mathrm{int}} = \hat{T} + \hat{V}_{\mathrm{e-e}}$, and $\hat{V}_{\mathrm{ext}} = \sum_{i=1}^{N_{\mathrm{el}}} \int V_{\mathrm{ext}}(\mathbf{r}) \delta(\mathbf{r} - \mathbf{r}_i) \mathrm{d}\mathbf{r}$ is the external field felt by the many-electron system, including the interaction between the electrons and nuclei and other

external fields.

In 1964, Hohenberg and Kohn proved the following two theorems [29]:

1. *The external potential and hence the total energy is a unique functional of the electron density.*

2. *The functional that delivers the ground-state energy of the system gives the lowest energy if and only if the input density is the true ground-state density.* In other words, the energy content of the Hamiltonian reaches its absolute minimum, i.e., the ground state, when the charge density is that of the ground state. For any positive integer N and potential $V_{\text{ext}}(\mathbf{r})$, a density functional $F[\rho]$ exists such that

$$E_{(v,N)}[\rho] = F[\rho] + \int V_{\text{ext}}(\mathbf{r})\rho(\mathbf{r})\mathrm{d}\mathbf{r} \tag{2.15}$$

   reaches its minimal value at the ground-state density of N electrons in the potential $V_{\text{ext}}(\mathbf{r})$. The minimal value of $E_{(v,N)}[\rho]$ is then the ground-state energy of this system, and the charge density $\rho(\mathbf{r})$ that minimizes the functional $E_{(v,N)}[\rho]$ is the exact ground-state charge density of the interacting system.

In 1965, Kohn and Sham introduced a non-interacting system that has the same charge density as the interacting system, and the total energy functional of the non-interacting system is written as [12],

$$E[\rho] = T_S[\rho] + E_{\text{H}}[\rho] + E_{\text{xc}}[\rho] + \int \mathrm{d}\mathbf{r} V_{\text{ext}}(\mathbf{r})\rho(\mathbf{r}), \tag{2.16}$$

where $E_{\text{H}}[\rho]$ is the Hartree energy for the Coulomb interactions between electrons in the non-interacting system

$$E_{\text{H}}[\rho] = \frac{1}{2}\iint \frac{\rho(\mathbf{r})\rho\left(\mathbf{r}'\right)}{|\mathbf{r}-\mathbf{r}'|}\mathrm{d}\mathbf{r}\mathrm{d}\mathbf{r}'. \tag{2.17}$$

$T_S[\rho]$ is the kinetic energy of the non-interacting system,

$$T_s[\rho] = \sum_{i=1}^{N_{\rm el}} \int d\mathbf{r} \varphi_i^*(\mathbf{r}) \left(-\frac{1}{2}\nabla^2 \right) \varphi_i(\mathbf{r}), \tag{2.18}$$

where φ_i are Kohn-Sham orbitals that define the electron density as $\rho(\mathbf{r}) = \sum_{i=1}^{N_{\rm el}} |\varphi_i(\mathbf{r})|^2$. $E_{\rm xc}[\rho]$ is the exchange-correlation energy defined as $E_{\rm xc}[\rho] = F[\rho] - T_S[\rho] - E_{\rm H}[\rho]$.

The Kohn-Sham orbital $\varphi_i(\mathbf{r})$ and its energy ε_i can be obtained by solving the Kohn-Sham equation

$$\left[-\frac{\hbar^2}{2m}\nabla^2 + V_{\rm eff}(\mathbf{r}) \right] \varphi_i(\mathbf{r}) = \varepsilon_i \varphi_i(\mathbf{r}), \tag{2.19}$$

which is found by minimizing the total energy Eq. (2.16). The effective Kohn-Sham potential is defined as $V_{\rm eff}(\mathbf{r}) = V_{\rm ext}(\mathbf{r}) + V_{\rm H}(\mathbf{r}) + V_{\rm xc}(\mathbf{r})$, where $V_{\rm H}(\mathbf{r})$ and $V_{\rm xc}(\mathbf{r})$ are the Hartree and the exchange-correlation potentials

$$V_{\rm H}(\mathbf{r}) = \int \frac{\rho\left(\mathbf{r}'\right)}{|\mathbf{r} - \mathbf{r}'|} \mathrm{d}\mathbf{r}' \tag{2.20}$$

and

$$V_{\rm xc}(\mathbf{r}) = \frac{\delta E_{\rm xc}[\rho]}{\delta \rho(\mathbf{r})}. \tag{2.21}$$

The exact expression of the exchange-correlation energy is unknown; thus, proper approximations must be made to do practical calculations. One of the most famous approximate exchange-correlation energies is the local density approximation (LDA), where the functional depends only on the density at the coordinate where the functional is evaluated [30]

$$E_{\rm xc}^{\rm LDA}[\rho] = \int \varepsilon_{\rm xc}(\rho)\rho(\mathbf{r}) \mathrm{d}\mathbf{r}. \tag{2.22}$$

The LDA assumes that the density is the same everywhere. The generalized gradient approximation (GGA) was proposed to account for the non-homogeneity of the true electron

density by expanding in terms of the gradient of the density [31]

$$E_{\mathrm{xc}}^{\mathrm{GGA}}[\rho] = \int \varepsilon_{\mathrm{xc}}(\rho, \nabla\rho)\rho(\mathbf{r})\mathrm{d}\mathbf{r}. \tag{2.23}$$

The Perdew–Burke-Ernzerhof (PBE) exchange-correlation functional [31] is an example of the GGA functional.

In addition to LDA and GGA, hybrid functionals are proposed for improved accuracy for exchange-correlation energy and better treatment of non-local interactions by mixing a portion of the Hartree-Fock exchange in the exchange-correlation functional. As an example, The PBE0 functional mixes the PBE exchange energy and Hartree–Fock exchange energy in a set 3:1 ratio, along with the full PBE correlation energy: [32]

$$E_{\mathrm{xc}}^{\mathrm{PBE0}} = \frac{1}{4}E_{\mathrm{x}}^{\mathrm{HF}} + \frac{3}{4}E_{\mathrm{x}}^{\mathrm{PBE}} + E_{\mathrm{c}}^{\mathrm{PBE}} \tag{2.24}$$

The dielectric-dependent hybrid (DDH) functional is another example, where the fraction of the Hartee-Fock exchange is tuned for each system using the dielectric constant [33–36].

2.3 Time-dependent density functional theory within density matrix perturbation theory

DFT is a theory for the electronic ground state, which can formally yield the exact energy and the electron density of the ground state. In DFT, the electron density and the external potential have a one-to-one correspondence. However, the time evolution of the external potential is not considered. In 1984, Runge and Gross extended the Hohenberg-Kohn theory to the case where the electron density and the external potential have a time dependence and strictly proved the time-dependent density functional theory (TDDFT) [13, 14]. In this dissertation, we focus on the linear-response TDDFT, where a small time-dependent external

perturbation, such as an electric field, is applied to the system. Electronic excitations of the system can be obtained from the poles of the corresponding response function by solving the Casida equation [15, 16]. Linear-response TDDFT can be derived based on the density matrix perturbation theory (DMPT) [24, 25, 37–41], which has also been used for the Bethe-Salpeter equation (BSE) [42–44]. DMPT does not require the summation over empty bands, which makes it suitable for the calculations of large systems.

The time-evolution of the density matrix, $\rho(\mathbf{r}, \mathbf{r}', t) = \sum_{v=1}^{N_{\mathrm{occ}}} \varphi_v(\mathbf{r}, t)\varphi_v(\mathbf{r}', t)^*$, is governed by the Liouville-von Neumann equation

$$i\frac{\mathrm{d}\hat{\rho}}{\mathrm{d}t} = \left[\hat{H}, \hat{\rho}\right]. \tag{2.25}$$

In this dissertation we consider the Kohn-Sham Hamiltonian for a PBE0-type hybrid functional, $\hat{H} = -\frac{1}{2}\nabla^2 + \hat{V}_{\mathrm{ext}} + \hat{V}_{\mathrm{H}} + \hat{V}_{\mathrm{xc}}^{\mathrm{loc}} - \alpha_{\mathrm{EXX}}\hat{V}_{\mathrm{EXX}}$, where α_{EXX} is the fraction of the Hartree-Fock exact exchange. When a small time-dependent perturbation field, $\hat{\phi}$, is applied to the system, the change of the density matrix is governed by the linearized Liouville equation within the linear-response regime

$$i\frac{\mathrm{d}\Delta\hat{\rho}}{\mathrm{d}t} = \mathcal{L}\Delta\hat{\rho} + \left[\hat{\phi}, \hat{\rho}^o\right]. \tag{2.26}$$

Here $\Delta\hat{\rho}$ is the linear variation of the density matrix. $\mathcal{L}$ is the Liouville super-operator defined as

$$\mathcal{L}\Delta\hat{\rho} = \left[\hat{H}^o, \Delta\hat{\rho}\right] + \left[\Delta\hat{V}_{\mathrm{Hxc}}^{\mathrm{loc}}, \hat{\rho}^o\right] + \left[\Delta\hat{V}_{\mathrm{EXX}}, \hat{\rho}^o\right], \tag{2.27}$$

where $\Delta\hat{V}_{\mathrm{Hxc}}^{\mathrm{loc}} = \Delta\hat{V}_{\mathrm{H}} + \Delta\hat{V}_{\mathrm{xc}}^{\mathrm{loc}}$ is the linear variation of the Hartree potential and the local part of the exchange and the correlation potential, and $\Delta\hat{V}_{\mathrm{EXX}}$ is the linear variation of the exact exchange potential, and both of them arise from the linear variation of the density

matrix. By performing a Fourier transform to the reciprocal space, one obtains

$$(\omega - \mathcal{L})\,\Delta\hat{\rho} = \left[\hat{\phi}, \hat{\rho}^o\right]. \tag{2.28}$$

Within DMPT, the first-order variation of the density matrix is expressed as:

$$\begin{aligned}\Delta\hat{\rho} &= \left(\hat{P}^v + \hat{P}^c\right)\Delta\hat{\rho}\left(\hat{P}^v + \hat{P}^c\right) \\ &= \hat{P}^c\Delta\hat{\rho}\hat{P}^v + \hat{P}^v\Delta\hat{\rho}\hat{P}^c,\end{aligned} \tag{2.29}$$

where $\hat{P}^v = \sum_{v=1}^{N_{\text{occ}}} |\varphi_v\rangle\langle\varphi_v|$ and $\hat{P}^c = 1 - \hat{P}^v$ are the projectors onto the occupied and unoccupied subspace, respectively. N_{occ} is the number of occupied states, and $|\varphi_v\rangle$ is the v-th occupied orbital of the unperturbed Kohn-Sham Hamiltonian with energy ε_v. In Eq. (2.29) we have used the completeness of the eigenvectors of the Kohn-Sham Hamiltonian, i.e. $\hat{P}^v + \hat{P}^c = 1$, and the property $\hat{P}^v\Delta\rho\hat{P}^v = \hat{P}^c\Delta\hat{\rho}\hat{P}^c = 0$. Introducing the following functions in Eq. (2.29):

$$|a_v\rangle = \hat{P}^c\Delta\hat{\rho}|\varphi_v\rangle \tag{2.30}$$

$$|b_v\rangle = \hat{P}^c\Delta\hat{\rho}^\dagger|\varphi_v\rangle, \tag{2.31}$$

we obtain an expression for $\Delta\hat{\rho}$ that does not contain any explicit summation over empty states:

$$\Delta\hat{\rho} = \sum_{v=1}^{N_{\text{occ}}} \left(|a_v\rangle\langle\varphi_v| + |\varphi_v\rangle\langle b_v|\right). \tag{2.32}$$

The functions $|a_v\rangle$ and $|b_v\rangle$ are obtained by solving the linearized Liouville equation (2.28). By multiplying Eq. (2.28) and its Hermitian conjugate by $\hat{P}^c$ to the left, and by $|\varphi_v\rangle$ to the right, we obtain:

$$\left(\omega - \hat{H}^o + \varepsilon_v\right)|a_v\rangle - \hat{P}^c\left[\Delta\hat{V}^{\text{loc}}_{\text{Hxc}} + \Delta\hat{V}_{\text{EXX}}, \hat{\rho}^o\right]|\varphi_v\rangle = \hat{P}^c\hat{\phi}|\varphi_v\rangle \tag{2.33}$$

$$\left(-\omega - \hat{H}^o + \varepsilon_v\right)|b_v\rangle - \hat{P}^c\left[\Delta\hat{V}^{\mathrm{loc}\dagger}_{\mathrm{Hxc}} + \Delta\hat{V}^{\dagger}_{\mathrm{EXX}}, \hat{\rho}^o\right]|\varphi_v\rangle = \hat{P}^c\hat{\phi}|\varphi_v\rangle. \tag{2.34}$$

Because the two commutators in Eq. (2.33) and in Eq. (2.34) couple the set of $|a_v\rangle$ and $|b_v\rangle$, we introduce the following matrix notation:

$$\omega\begin{pmatrix}\mathcal{I} & 0\\ 0 & -\mathcal{I}\end{pmatrix}\begin{pmatrix}\mathcal{A}\\ \mathcal{B}\end{pmatrix} - \begin{pmatrix}\mathcal{D}+\mathcal{K}^{1e}-\mathcal{K}^{1d} & \mathcal{K}^{2e}-\mathcal{K}^{2d}\\ \mathcal{K}^{2e}-\mathcal{K}^{2d} & \mathcal{D}+\mathcal{K}^{1e}-\mathcal{K}^{1d}\end{pmatrix}\begin{pmatrix}\mathcal{A}\\ \mathcal{B}\end{pmatrix} = \begin{pmatrix}\left\{\hat{P}^c\hat{\phi}|\varphi_v\rangle\right\}\\ \left\{\hat{P}^c\hat{\phi}|\varphi_v\rangle\right\}\end{pmatrix}, \tag{2.35}$$

where $\mathcal{A} = \{|a_v\rangle\}$ and $\mathcal{B} = \{|b_v\rangle\}$, $v \in [1, N_{\mathrm{occ}}]$. $\mathcal{I}$ is the identity operator, and

$$\mathcal{D}\mathcal{A} = \left\{\hat{P}^c\left(\hat{H}^o - \epsilon_v\right)|a_v\rangle : v \in [1\ldots N_{\mathrm{occ}}]\right\}, \tag{2.36}$$

$$\mathcal{K}^{1e}\mathcal{A} = \left\{2\int \mathrm{d}\mathbf{r}' P_c\left(\mathbf{r},\mathbf{r}'\right)\varphi_v\left(\mathbf{r}'\right)\sum_{v'}^{N_{\mathrm{occ}}}\int \mathrm{d}\mathbf{r}'' f^{\mathrm{loc}}_{\mathrm{Hxc}}\left(\mathbf{r}',\mathbf{r}''\right)\varphi^*_{v'}\left(\mathbf{r}''\right)a_{v'}\left(\mathbf{r}''\right) : v \in [1\ldots N_{\mathrm{occ}}]\right\}, \tag{2.37}$$

$$\mathcal{K}^{2e}\mathcal{A} = \left\{2\int \mathrm{d}\mathbf{r}' P_c\left(\mathbf{r},\mathbf{r}'\right)\varphi_v\left(\mathbf{r}'\right)\sum_{v'}^{N_{\mathrm{occ}}}\int \mathrm{d}\mathbf{r}'' f^{\mathrm{loc}}_{\mathrm{Hxc}}\left(\mathbf{r}',\mathbf{r}''\right)a^*_{v'}\left(\mathbf{r}''\right)\varphi_{v'}\left(\mathbf{r}''\right) : v \in [1\ldots N_{\mathrm{occ}}]\right\}, \tag{2.38}$$

$$\mathcal{K}^{1d}\mathcal{A} = \left\{\alpha_{\mathrm{EXX}}\int \mathrm{d}\mathbf{r}' P_c\left(\mathbf{r},\mathbf{r}'\right)\sum_{v'}^{N_{\mathrm{occ}}}a_{v'}\left(\mathbf{r}'\right)\int \mathrm{d}\mathbf{r}'' v_c\left(\mathbf{r}',\mathbf{r}''\right)\varphi^*_{v'}\left(\mathbf{r}''\right)\varphi_v\left(\mathbf{r}''\right) : v \in [1\ldots N_{\mathrm{occ}}]\right\}, \tag{2.39}$$

$$\mathcal{K}^{2d}\mathcal{A} = \left\{\alpha_{\mathrm{EXX}}\int \mathrm{d}\mathbf{r}' P_c\left(\mathbf{r},\mathbf{r}'\right)\sum_{v'}^{N_{\mathrm{occ}}}\varphi_{v'}\left(\mathbf{r}'\right)\int \mathrm{d}\mathbf{r}'' v_c\left(\mathbf{r}',\mathbf{r}''\right)a^*_{v'}\left(\mathbf{r}''\right)\varphi_v\left(\mathbf{r}''\right) : v \in [1\ldots N_{\mathrm{occ}}]\right\}. \tag{2.40}$$

Equations for the application of $\mathcal{D}$, $\mathcal{K}^{1e}$, $\mathcal{K}^{2e}$, $\mathcal{K}^{1d}$, and $\mathcal{K}^{2d}$ on $\mathcal{B}$ can be obtained substituting

$|a_v\rangle$ with $|b_v\rangle$ in Eqs. (2.36)–(2.40). Here v_c is the bare Coulomb interactions. $f^{\rm loc}_{\rm Hxc}(\mathbf{r},\mathbf{r}') = v_c(\mathbf{r},\mathbf{r}') + f^{\rm loc}_{\rm xc}(\mathbf{r},\mathbf{r}')$, with

$$f^{\rm loc}_{\rm xc}(\mathbf{r},\mathbf{r}') = \left.\frac{\delta V^{\rm loc}_{\rm xc}(\mathbf{r})}{\delta\rho(\mathbf{r}')}\right|_{(\rho^o,\nabla\rho^o)} \tag{2.41}$$

representing the local part of the exchange-correlation kernel within the adiabatic approximation, i.e., the kernel is frequency-independent.

Instead of solving Eq. (2.35) directly for different ω, one could solve the following generalized eigenvalue problem to directly compute the excited states

$$\begin{pmatrix} \mathcal{D}+\mathcal{K}^{1e}-\mathcal{K}^{1d} & \mathcal{K}^{2e}-\mathcal{K}^{2d} \\ \mathcal{K}^{2e}-\mathcal{K}^{2d} & \mathcal{D}+\mathcal{K}^{1e}-\mathcal{K}^{1d} \end{pmatrix} \begin{pmatrix} \mathcal{A}_s \\ \mathcal{B}_s \end{pmatrix} = \omega_s \begin{pmatrix} \mathcal{I} & 0 \\ 0 & -\mathcal{I} \end{pmatrix} \begin{pmatrix} \mathcal{A}_s \\ \mathcal{B}_s \end{pmatrix}. \tag{2.42}$$

Here, $(\mathcal{A}_s, \mathcal{B}_s)$ is the eigenvector of the s-th excited state, and ω_s is the corresponding vertical excitation energy. Eq. (2.42) is equivalent to the Casida equations for singlet excited states, starting with a closed-shell singlet ground state. The eigenvalue equation generalized to the spin-polarized case for both the spin-conserving and spin-flip excitations are given in Chapter 3.2.

The derivative of the excitation energy with respect to nuclear coordinates can be efficiently calculated using the extended Lagrangian approach by Hutter [17], enabling the study of atomic geometry relaxation in electronic excited states, which is discussed in detail in Chapter 3.2.

2.4 Harmonic approximation to the adiabatic potential energy

Under the Born-Oppenheimer adiabatic approximation, the many-body Schrodinger equation for nuclei,

$$\left[\hat{T}_{\rm N} + V(\mathbf{R})\right]\Theta_{\mathcal{I}}(\mathbf{R}) = E_{\mathcal{I}}\Theta_{\mathcal{I}}(\mathbf{R}), \tag{2.43}$$

can be solved once the potential energy $V(\mathbf{R})$ for any nuclear coordinate $\mathbf{R}$ is known by solving the many-electron problem. Here, we use $\mathbf{R}$ to replace $\{\mathbf{R}\}$ and omit the index of $V(\mathbf{R})$ for simplicity. However, in the study of the optical processes that occur around the equilibrium coordinates $\mathbf{R}_0$, the potential energy $V(\mathbf{R})$ can be expanded near $\mathbf{R}_0$

$$\begin{aligned} V_{\text{vib}}(\mathbf{R}) &= V(\mathbf{R}) - V(\mathbf{R}_0) \\ &= \frac{1}{2} \sum_{I,J=1}^{N_{\text{nuc}}} \sum_{\alpha,\beta=x,y,z} \left(\Delta R_{I,\alpha} \sqrt{M_I}\right) D_{I\alpha,J\beta} \left(\sqrt{M_J} \Delta R_{J,\beta}\right) + \mathcal{O}(\Delta R^3), \end{aligned} \tag{2.44}$$

where $V(\mathbf{R}_0)$ is the potential energy of the system at the equilibrium atomic geometry, and $\Delta R_{I\alpha}$ represents the displacement of the I-th nucleus from the equilibrium coordinate in the α-th direction. $\mathbf{D}$ is called the mass-weighted force-constant matrix or the dynamic matrix, defined as the second-order derivative of the potential energy at the equilibrium coordinate

$$D_{I\alpha,J\beta} = \frac{1}{\sqrt{M_I M_J}} \left(\frac{\partial^2 V(\mathbf{R})}{\partial R_{I\alpha} \partial R_{J\beta}} \right) \Big|_{\mathbf{R}=\mathbf{R}_0}. \tag{2.45}$$

With the harmonic approximation, Eq. (2.43) can be rewritten as

$$\frac{1}{2} \left(\nabla_{\mathbf{q}}^2 + \mathbf{q}^\top \mathbf{D} \mathbf{q} \right) \Theta_{\mathcal{I}}(\mathbf{q}) = E_{\text{vib},\mathcal{I}} \Theta_{\mathcal{I}}(\mathbf{q}), \tag{2.46}$$

where $E_{\text{vib},\mathcal{I}} = E_{\mathcal{I}} - V(\mathbf{R}_0)$, $q_{I\alpha} = \sqrt{M_I} \Delta R_{I\alpha}$, and $\nabla_{q_{I\alpha}}^2 = \frac{\nabla_{R_{I\alpha}}^2}{M_I}$. By performing linear transformation to $\mathbf{q}$ using the unitary matrix $\mathbf{U}$ obtained from the eigenvalue decomposition of the dynamical matrix $\mathbf{D} = \mathbf{U} \mathbf{\Lambda} \mathbf{U}^\top$, Eq. (2.46) can be decoupled and becomes

$$\frac{1}{2} \left[\nabla_{\mathbf{Q}}^2 + \mathbf{Q}^\top \mathbf{\Lambda} \mathbf{Q} \right] \Theta_{\mathcal{I}}(\mathbf{Q}) = E_{\text{vib},\mathcal{I}} \Theta_{\mathcal{I}}(\mathbf{Q}) \tag{2.47}$$

where we define $\mathbf{Q} = \mathbf{U}^\top \mathbf{q}$. Eq. (2.47) can be decomposed into $3N_{\text{nuc}}$ independent equations

$$\frac{1}{2}\left(\nabla^2_{Q_k} + \Lambda_k Q_k^2\right) \chi_{k,n_k^{\mathcal{I}}}(Q_k) = E_{\text{vib},k,n_k^{\mathcal{I}}} \chi_{k,n_k^{\mathcal{I}}}(Q_k), \tag{2.48}$$

and the total nuclear wavefunction can be represented as $\Theta_{\mathcal{I}}(\mathbf{Q}) = \prod_{k=1}^{3N_{\text{nuc}}} \chi_{k,n_k^{\mathcal{I}}}(Q_k)$, and the total energy is $E_{\text{vib},\mathcal{I}} = \sum_{k=1}^{3N_{\text{nuc}}} E_{\text{vib},k,n_k^{\mathcal{I}}}$.

$\mathbf{Q}$ defines a set of normal modes. For the system at the equilibrium geometry, the normal modes with zero eigenvalues correspond to the transitional and rotational motions. The rest of the normal modes correspond to vibrations with frequency $\omega_k = \sqrt{\Lambda_k}$. The solution of Eq. (2.48) gives wavefunctions and energies of the one-dimensional quantum harmonic oscillator:

$$\chi_{k,n_k^{\mathcal{I}}}(Q_k) = \frac{1}{\sqrt{2^{n_k^{\mathcal{I}}} n_k^{\mathcal{I}}!}} \left(\frac{\omega_k}{\pi}\right)^{\frac{1}{4}} \exp\left[\frac{-\omega_k Q_k^2}{2}\right] H_{n_k^{\mathcal{I}}}\left(\sqrt{\omega_k} Q_k\right), \tag{2.49}$$

$$E_{\text{vib},k,n_k^{\mathcal{I}}} = \left(n_k^{\mathcal{I}} + \frac{1}{2}\right)\hbar\omega_k, \tag{2.50}$$

where $n_k^{\mathcal{I}}$ is the vibrational quantum number, and $H_{n_k^{\mathcal{I}}}$ is the $n_k^{\mathcal{I}}$-th order Hermite polynomial.

There are multiple approaches to computing the dynamic matrix Eq. (2.45). The dynamic matrix can be computed numerically using the finite difference approach, providing the gradient of the adiabatic PES with respect to nuclear coordinates can be efficiently computed [45]. Alternative ways of computing dynamic matrices also exist. For a ground state studied using DFT, the dynamic matrix can be computed either using the density functional perturbation theory (DFPT) [46–49], the DMPT approach [50], and by the solution of the coupled-perturbed Kohn–Sham equations [51–54]. In a TDDFT excited state study, the dynamic matrix can be computed by solving the Z-vector equations, the coupled-perturbed Kohn-Sham equations, and the coupled-perturbed TDDFT equations [55–57].

2.5 Theoretical treatment of photoluminescence

Photoluminescence intensity between the initial state $\Phi_{\mathcal{I}}$ and the final state $\Phi_{\mathcal{F}}$ can be computed as the rate of the spontaneous emission using Fermi's golden rule [58, 59]

$$I(\hbar\omega, T) = \frac{n_D(\hbar\omega)^3}{3\pi\epsilon_0 c^3\hbar^4} \sum_{\mathcal{I}} \sum_{\mathcal{F}} P_{\mathcal{I}}(T) \left|\langle \Phi_{\mathcal{I}} \left|\hat{\boldsymbol{\mu}}_{\text{total}}\right| \Phi_{\mathcal{F}}\rangle\right|^2 \times \delta\left(E_{\mathcal{I}} - E_{\mathcal{F}} - \hbar\omega\right), \tag{2.51}$$

where $\hbar\omega$ is the photon energy, T denotes the temperature, n_D is the refractive index of the system, ϵ_0 in the vacuum permittivity, c is the speed of light in vacuum, and $\hbar$ is the Planck constants. Here we are considering transitions from all possible initial states $\Phi_{\mathcal{I}}$ to all possible final states $\Phi_{\mathcal{F}}$, with $E_{\mathcal{I}}$ and $E_{\mathcal{F}}$ corresponding to their energies. $P_m(T)$ is the thermal population of the m-th initial state. $\hat{\boldsymbol{\mu}}$ is the total dipole moment operator for both electrons and nuclei

$$\boldsymbol{\mu} = -e\sum_{i=1}^{N_{\text{el}}} \mathbf{r}_i + e\sum_{I}^{N_{\text{nuc}}} Z_I \mathbf{R}_I. \tag{2.52}$$

Here, we adopt the electric dipole approximation, assuming that the wavelength of the photon is much larger than the size of the microscopic system being studied.

In this dissertation, we constrain ourselves to the spontaneous emission from a given electronic excited state to the ground state. Adopting the Born-Oppenheimer approximation, we can express the total wavefunction of the initial excited state and the final ground state as a product of the electronic wavefunction and the nuclear wavefunction

$$|\Phi_{\mathcal{I}}\rangle = |\Psi_{\text{ES}}\rangle|\Theta_{\text{ES},\mathcal{I}}\rangle, \quad |\Phi_{\mathcal{F}}\rangle = |\Psi_{\text{GS}}\rangle|\Theta_{\text{GS},\mathcal{F}}\rangle, \tag{2.53}$$

where $\mathcal{I}$ ($\mathcal{F}$) is the index of the nuclear wavefunction for the excited state (ground state). Their total energy can be expressed as $E_{\mathcal{I}} = V_{\text{ES}} + E_{\text{ES,vib},\mathcal{I}}$ and $E_n = V_{\text{GS}} + E_{\text{GS,vib},\mathcal{F}}$, where V_{ES} (V_{GS}) stands for the energy of the electronic wavefunction of the ground state (excited state), while $E_{\text{ES},\mathcal{I}}$ ($E_{\text{GS},\mathcal{F}}$) stands for the energy of the $\mathcal{I}$-th ($\mathcal{F}$-th) nuclear wave-

function of the ground state (excited state). The thermal population of the initial excited state becomes the thermal population of all nuclear wavefunctions

$$P_{\mathcal{I}}(T) = P_{\mathrm{ES},\mathcal{I}}(T) = \frac{1}{Z}\exp\left(-\frac{E_{\mathrm{ES,vib},\mathcal{I}}}{k_B T}\right), \tag{2.54}$$

where k_B is the Boltzmann constant, and $Z = \sum_{\mathcal{I}} \exp\left(-\frac{E_{\mathrm{ES,vib},\mathcal{I}}}{k_B T}\right)$.

Under these constraints, the total dipole moment can be reduced to the electronic dipole moment, $\hat{\boldsymbol{\mu}}_{\mathrm{total}} = \hat{\boldsymbol{\mu}}_{\mathrm{el}}$, since the terms containing the nuclear dipole moment vanish due to the orthonormality of electronic wavefunctions. Therefore, the photoluminescence intensity can be expressed as

$$\begin{aligned} I(\hbar\omega, T) = \frac{n_D(\hbar\omega)^3}{3\pi\epsilon_0 c^3\hbar^4} \sum_{\mathcal{I}}\sum_{\mathcal{F}} P_{\mathrm{ES},\mathcal{I}}(T) \left|\left\langle \Theta_{\mathrm{ES},\mathcal{I}} \left| \boldsymbol{\mu}_{\mathrm{el,ES}\to\mathrm{GS}} \right| \Theta_{\mathrm{GS},\mathcal{F}} \right\rangle\right|^2 \\ \times \delta\left[\left(V_{\mathrm{ES}} + E_{\mathrm{ES,vib},\mathcal{I}}\right) - \left(V_{\mathrm{GS}} + E_{\mathrm{GS,vib},\mathcal{F}}\right) - \hbar\omega\right]. \end{aligned} \tag{2.55}$$

Here, $\boldsymbol{\mu}_{\mathrm{el,ES}\to\mathrm{GS}} = \langle\Psi_{\mathrm{ES}}|\hat{\boldsymbol{\mu}}_{\mathrm{el}}|\Psi_{\mathrm{GS}}\rangle = \boldsymbol{\mu}_{\mathrm{e}}$ is the electric transition dipole moment, which can be expanded as a function of the nuclear coordinates

$$\boldsymbol{\mu}_{\mathrm{el,ES}\to\mathrm{GS}}(\mathbf{R}) = \boldsymbol{\mu}_{\mathrm{el,ES}\to\mathrm{GS}}(\mathbf{R_0}) + \nabla_{\mathbf{R}}\boldsymbol{\mu}_{\mathrm{el,ES}\to\mathrm{GS}}\Big|_{\mathbf{R_0}} (\mathbf{R}-\mathbf{R}_0)^{\top} + \mathcal{O}\left((\mathbf{R}-\mathbf{R}_0)^2\right). \tag{2.56}$$

For systems with intrinsic large transition dipole moment, we can adapt the Franck-Condon principle and only keep the zeroth order term. In the TDDFT framework, the transition dipole moment can be computed using the transition density

$$\boldsymbol{\mu}_{\mathrm{el,ES}\to\mathrm{GS}} = \int \Delta\rho(\mathbf{r})\mathbf{r}\mathrm{d}\mathbf{r} = \sum_{v=1}^{N_{\mathrm{occ}}} \int \left(\varphi_v^*(\mathbf{r})a_v(\mathbf{r}) + b_v^*(\mathbf{r})\varphi_v(\mathbf{r})\right)\mathbf{r}\mathrm{d}\mathbf{r}. \tag{2.57}$$

at fixed nuclear coordinates.

The calculation of the overlap of nuclear wavefunctions can be simplified by employing the

displaced harmonic approximation, assuming that the nuclear wavefunctions of the ground and the excited state can be approximated as the product of the same set of one-dimensional harmonic oscillator wavefunctions expect a rigid displacement

$$\left|\Theta_{\mathrm{ES},\mathcal{I}}\right\rangle = \prod_{k=1}^{3N_{\mathrm{nuc}}} \left|\chi_{kn_k^{\mathcal{I}}}\left(Q_k - \Delta Q_k\right)\right\rangle, \quad \left|\Theta_{\mathrm{GS},\mathcal{F}}\right\rangle = \prod_{k=1}^{3N_{\mathrm{nuc}}} \left|\chi_{kn_k^{\mathcal{F}}}\left(Q_k\right)\right\rangle. \tag{2.58}$$

Here $\left|\chi_{kn_k^{\mathcal{I}}}\left(Q_k\right)\right\rangle$ is the $n_k^{\mathcal{I}}$-th vibrational level of the k-th one-dimensional harmonic oscillator. Q_k is the normal mode of the k-th harmonic oscillator, and ΔQ_k is the projection of the displacement between the equilibrium nuclear coordinates of the electronic excited state and the ground state on Q_k,

$$\Delta Q_k = \sum_{I=1}^{N_{\mathrm{nuc}}} \sum_{\alpha=x,y,z} \sqrt{M_I}\left(R_{0,\mathrm{ES},I\alpha} - R_{0,\mathrm{GS},I\alpha}\right) U_{k,I\alpha}, \tag{2.59}$$

where $\mathbf{U}_k$ is the k-th eigenvector of the dynamic matrix $\mathbf{D}$. The energy of the nuclear wavefunction can be expressed as

$$E_{\mathrm{ES,vib},\mathcal{I}} = \sum_k \left(n_k^{\mathcal{I}} + \frac{1}{2}\right)\hbar\omega_k, \quad E_{\mathrm{GS,vib},\mathcal{F}} = \sum_k \left(n_k^{\mathcal{F}} + \frac{1}{2}\right)\hbar\omega_k \tag{2.60}$$

using the vibrational energy $\hbar\omega_k$. The thermal population can hence be written as

$$P_{\mathrm{ES,vib},\mathcal{I}}(T) = \prod_{k=1}^{3N_{\mathrm{nuc}}} P_{\mathrm{vib},n_k^{\mathcal{I}}}(T), \tag{2.61}$$

where $P_{\mathrm{vib},n_k^{\mathcal{I}}}(T) = \frac{1}{Z_k}\exp\left(-\frac{n_k^{\mathcal{I}}\hbar\omega_k}{k_B T}\right)$ with $Z_k = \sum_{n_k^{\mathcal{I}}}\exp\left(-\frac{n_k^{\mathcal{I}}\hbar\omega_k}{k_B T}\right)$.

Therefore, the photoluminescence intensity becomes

$$
\begin{aligned}
&I(\hbar\omega, T) \\
&= \frac{n_D(\hbar\omega)^3 |\boldsymbol{\mu}_{\mathrm{el,ES}\to\mathrm{GS}}|^2}{3\pi\epsilon_0 c^3 \hbar^4} \sum_{\mathcal{I}} \sum_{\mathcal{F}} \left(\prod_k P_{\mathrm{vib},n_k^{\mathcal{I}}}(T) \left| \left\langle \chi_{k n_k^{\mathcal{I}}}(Q_k - \Delta Q_k) \middle| \chi_{k n_k^{\mathcal{F}}}(Q_k) \right\rangle \right|^2 \right) \\
&\times \delta \left(E_{\mathrm{ZPL}} + \sum_k n_k^{\mathcal{I}} \hbar\omega_k - \sum_k n_k^{\mathcal{F}} \hbar\omega_k - \hbar\omega \right).
\end{aligned}
\tag{2.62}
$$

Here $E_{\mathrm{ZPL}} = V_{\mathrm{ES}}(\mathbf{R}_{0,\mathrm{ES}}) - V_{\mathrm{GS}}(\mathbf{R}_{0,\mathrm{GS}})$ is the energy of the zero-phonon line (ZPL), which is also equivalent to the adiabatic excitation energy between the PESs of the electronic excited and ground states under the displaced harmonic oscillator approximation. The overlap between the wavefunctions of displaced one-dimensional harmonic oscillators can be computed analytically as

$$
\left| \left\langle \chi_{k n_k^{\mathcal{I}}}(Q_k - \Delta Q_k) \middle| \chi_{k n_k^{\mathcal{F}}}(Q_k) \right\rangle \right|^2 = e^{-S_k} S_k^{n_k^{\mathcal{F}} - n_k^{\mathcal{I}}} \left(\frac{n_k^{\mathcal{I}}!}{n_k^{\mathcal{F}}!} \right) \left[L_{n_k^{\mathcal{I}}}^{n_k^{\mathcal{F}} - n_k^{\mathcal{I}}}(S_k) \right]^2, \tag{2.63}
$$

where $S_k = \frac{\omega_k \Delta Q_k^2}{2\hbar}$ is the partial Huang-Rhys factor [60]. L_m^{n-m} are the associated Laguerre polynomials [61]. In practical calculations, the summation in Eq. (2.62) can be avoided using the generating function approach, as discussed in detail in Chapter 4.2.

CHAPTER 3

EXCITED STATE PROPERTIES OF POINT DEFECTS IN SEMICONDUCTORS AND INSULATORS INVESTIGATED WITH TIME-DEPENDENT DENSITY FUNCTIONAL THEORY

This chapter is adapted with permission from Y. Jin, V. Yu, M. Govoni, A. Xu, and G. Galli. Journal of Chemical Theory and Computations. 19 (23), 8689-8705 (2023). https://doi.org/10.1021/acs.jctc.3c00986.

In this Chapter, we present a formulation of spin-conserving and spin-flip, hybrid time-dependent density functional theory (TDDFT), including the calculation of analytical forces, which allows for efficient calculations of excited state properties of solid-state systems with hundreds to thousands of atoms. We discuss an implementation on both GPU and CPU based architectures, along with several acceleration techniques. We then apply our formulation to the study of several point defects in semiconductors and insulators, specifically the negatively charged nitrogen-vacancy and neutral silicon-vacancy centers in diamond, the neutral divacancy center in 4H silicon carbide, and the neutral oxygen-vacancy center in magnesium oxide. Our results highlight the importance of taking into account structural relaxations in excited states, in order to interpret and predict optical absorption and emission mechanisms in spin-defects.

3.1 Introduction

Optically active point defects in semiconductors and insulators present a promising avenue for the development of quantum technologies [27]. Specific examples include the negatively charged nitrogen-vacancy center (NV^-) in diamond and the neutral divacancy center (VV^0) in 4H silicon carbide (SiC), both of which have been extensively studied [62–64], for applications ranging from quantum sensing [65, 66] and quantum communication [67–70], to

potentially quantum computation [71, 72]. These point defects may function as quantum bits (qubits), with an optical spin-polarization cycle for initialization and readout that involves both radiative and non-radiative transitions between many-body ground and excited states [73]. A comprehensive understanding of the physics underlying these transitions is essential to interpret experiments and to formulate general guidelines for the use of point defects in quantum technologies [74–76].

First-principles methods have significantly contributed to the understanding of the electronic structure of the ground and excited states of point defects in a variety of semiconductors and insulators [77–80]. Many first-principles studies on the electronic excited states of point defects have used the constrained occupation density functional theory (CDFT) method, often called ΔSCF, where the occupations of localized defect orbitals are adjusted to represent a specific excited state [81]. Similar to ground state DFT calculations, the ΔSCF approach has the advantage of a relatively low computational cost; in addition, it allows for the straightforward calculation of analytical nuclear forces and thus for geometry optimizations, vibrational mode calculations in excited states, and for the investigation of vibrationally resolved optical spectra [59, 82, 83]. However, the ΔSCF approach is only applicable to excited states that are well approximated by a single Slater determinant, and it is prone to numerical convergence issues in the case of (near-)degenerate excited states. Other, potentially more accurate approaches are based on quantum embedding theories [84, 85], e.g. the quantum defect embedding theory (QDET) [86–88], and the density matrix embedding theory (DMET) [89–91], where an active space representing the manifold of defect states is identified, and such states are treated at a higher level of theory than the electronic structure of the rest of the host crystal. For example, one may use Full-Configuration Interaction (FCI) for an accurate description of multi-configuration excited states of point defects in semiconductor and oxides [92–98], with the rest of the crystal treated at the DFT or many-body perturbation theory (GW) level of theory. However, embedding methods have so far

been limited to single-point calculations at fixed atomic geometries, and a formalism to carry out geometry optimizations in electronic excited states is not yet available.

Linear-response time-dependent density functional theory (LR-TDDFT) is a computational method frequently used to study excited state and optical properties of molecules and solids [15, 16]. In particular, spin-conserving and spin-flip TDDFT allows for the description of excited states as linear combinations of single excitations with different spin-multiplicities [99–105]. In several cases, it has been shown that the accuracy of the TDDFT method using hybrid functionals is comparable to that of higher-level electronic structure methods, such as the solution of the Green's function based GW plus Bethe–Salpeter Equation (GW/BSE) and equation-of-motion coupled cluster (EOM-CC) methods [106–109]. The computational workload of TDDFT calculations scales as $\mathcal{O}(N_{\mathrm{occ}}^2 N_g \log(N_g))$ when using hybrid functionals and a plane-wave basis set, where N_{occ} is the number of occupied Kohn-Sham orbitals of the system, and N_g is the number of plane-waves; such scaling is comparable to that of ground state DFT calculations. Further, analytical nuclear forces on nuclei can be computed within TDDFT, allowing for geometry optimizations and the calculation of nuclear vibrations in electronic excited states [17].

TDDFT has been used to study excited states of point defects in diamond using cluster models and atomic-centered basis sets [110–116]. However, depending on the size and the system, cluster models may exhibit quantum confinement and their electronic structure may also be impacted by the chosen surface termination. In addition, the optimized geometries in the ground and excited states may differ from the corresponding ones in the solid state. Although TDDFT and analytical nuclear forces have been implemented with a plane-wave pseudopotential method for calculations of solid-state systems with periodic boundary conditions [17, 117–120], the direct use of TDDFT for modeling point defects in calculations with periodic boundary conditions is still rare.

In this work, we present an efficient numerical implementation of spin-conserving and

spin-flip TDDFT, including the evaluation of analytical nuclear forces, in the open-source code WEST [121, 122], which is based on the plane-wave pseudopotential method. Hereafter, we refer to our implementation of TDDFT as WEST-TDDFT. We adopt several numerical approximations to accelerate TDDFT calculations with hybrid functionals in WEST-TDDFT, including the adaptively compressed exchange (ACE) operator [123], the use of the near-sightedness principle [44], and of the inexact Krylov subspace approach [124, 125]. We show that the errors introduced by these approximations can be systematically controlled and that high-accuracy results may be obtained. We show that all together, these approximations lead to about an order of magnitude speed-up in the computation of excited state energies and analytical nuclear forces for the defective systems benchmarked in this work. We also show that with a multilevel parallelization scheme [122], WEST-TDDFT shows strong scaling up to hundreds of CPU and GPU nodes, enabling the study of point defects for systems containing hundreds to thousands of atoms.

To demonstrate the capabilities of WEST-TDDFT, we investigated the excited states and optical properties of several point defects in solids, including the NV^- and the neutrally charged silicon-vacancy center (SiV^0) in diamond, the VV^0 in 4H-SiC, and the neutrally charged oxygen vacancy center (V_O^0) in magnesium oxide (MgO). We used the dielectric-dependent hybrid (DDH) functional in TDDFT calculations, where the coefficient of the Hartree-Fock exact exchange was set to the inverse of the high-frequency dielectric constant of the host material. DDH has been shown to improve the description of the electronic structure of a broad range of systems [33, 34], including systems with impurities [83, 126–130]. Hence, using the DDH functional in TDDFT calculations is expected to lead to a more accurate description of excitonic effects than using semi-local functionals, due to the inclusion of screening effects in the Coulomb interaction between the electron and the hole in the excited state [107, 131, 132]. Our results obtained with TDDFT using the DDH functional offer insights into the mechanisms underlying the optical absorption and emission

processes in these defects.

The rest of the Chapter is organized as follows. Chapter 3.2 introduces the methodology. Chapter 3.3 discusses the numerical approximations adopted in WEST-TDDFT to accelerate the calculations for hybrid functionals. In Chapter 3.6, we present the parallelization and scaling tests of WEST-TDDFT. In Chapter 3.7, we give examples of applying WEST-TDDFT to study the excited state properties of prototypical point defects in solids. We close the Chapter with a summary of all the results and an outlook on future work.

3.2 Method

We describe below the formalism adopted to compute vertical excitation energies (Chapter 3.2.1) and nuclear forces (Chapter 3.2.2) with TDDFT and with spin-flip TDDFT (Chapter 3.2.3). Since our goal is to study excited states of large systems, such as point defects in solids in the dilute limit, we performed TDDFT calculations using only the Γ point to sample the Brillouin zone.

3.2.1 Vertical excitation energies

Within LR-TDDFT, the vertical excitation energy (VEE) ω_s from the ground to the s-th excited state, can be obtained by solving the following eigenvalue problem [15, 16, 133]:

$$\begin{pmatrix} \mathcal{D} + \mathcal{K}^{1e} - \mathcal{K}^{1d} & \mathcal{K}^{2e} - \mathcal{K}^{2d} \\ \mathcal{K}^{2e} - \mathcal{K}^{2d} & \mathcal{D} + \mathcal{K}^{1e} - \mathcal{K}^{1d} \end{pmatrix} \begin{pmatrix} \mathcal{A}_s \\ \mathcal{B}_s \end{pmatrix} = \omega_s \begin{pmatrix} \mathcal{I} & 0 \\ 0 & -\mathcal{I} \end{pmatrix} \begin{pmatrix} \mathcal{A}_s \\ \mathcal{B}_s \end{pmatrix}, \tag{3.1}$$

where $\mathcal{A}_s = \left\{ |a_{s,v\sigma}\rangle : v = 1, \ldots, N_{\mathrm{occ},\sigma}; \sigma = \uparrow, \downarrow \right\}$ and
$\mathcal{B}_s = \left\{ |b_{s,v\sigma}\rangle : v = 1, \ldots, N_{\mathrm{occ},\sigma}; \sigma = \uparrow, \downarrow \right\}$ are two sets of orbitals that enter the definition of the linear change of the density matrix in the σ spin channel with respect to the ground

state density matrix, due to the s-th neutral excitation:

$$\Delta\rho_{s,\sigma} = \sum_{v=1}^{N_{\mathrm{occ},\sigma}} \left(|a_{s,v\sigma}\rangle\langle\varphi_{v\sigma}| + |\varphi_{v\sigma}\rangle\langle b_{s,v\sigma}| \right), \tag{3.2}$$

Here $N_{\mathrm{occ},\sigma}$ is the number of occupied states in the σ spin channel, and $|\varphi_{v\sigma}\rangle$ are the Kohn-Sham (KS) wavefunctions of the ground state.

In this section, we consider neutral excitations, i.e., excitations that do not change the total number of electrons, and $N_{\mathrm{occ},\sigma}$ is individually conserved for each spin channel. Neutral excitations that flip the spin will be discussed in section 3.2.3.

The operators on the left-hand side (LHS) of Eq. (3.1) are defined as:

$$\mathcal{D}\mathcal{A}_s = \left\{ \mathcal{P}^c_\sigma \left(H^{\mathrm{KS}}_\sigma - \varepsilon_{v\sigma} \right) |a_{s,v\sigma}\rangle : v = 1, \ldots, N_{\mathrm{occ},\sigma}; \sigma = \uparrow, \downarrow \right\}, \tag{3.3}$$

$$\mathcal{K}^{1e}\mathcal{A}_s = \Bigg\{ \int \mathrm{d}\mathbf{r}' \mathcal{P}^c_\sigma(\mathbf{r},\mathbf{r}') \varphi_{v\sigma}(\mathbf{r}') \sum_{\sigma'} \int \mathrm{d}\mathbf{r}'' f^{\mathrm{loc}}_{\mathrm{Hxc},\sigma\sigma'}(\mathbf{r}',\mathbf{r}'') \sum_{v'=1}^{N_{\mathrm{occ},\sigma'}} \varphi^*_{v'\sigma'}(\mathbf{r}'') a_{s,v'\sigma'}(\mathbf{r}'') : v = 1, \ldots, N_{\mathrm{occ},\sigma}; \sigma = \uparrow, \downarrow \Bigg\}, \tag{3.4}$$

$$\mathcal{K}^{2e}\mathcal{A}_s = \Bigg\{ \int \mathrm{d}\mathbf{r}' \mathcal{P}^c_\sigma(\mathbf{r},\mathbf{r}') \varphi_{v\sigma}(\mathbf{r}') \sum_{\sigma'} \int \mathrm{d}\mathbf{r}'' f^{\mathrm{loc}}_{\mathrm{Hxc},\sigma\sigma'}(\mathbf{r}',\mathbf{r}'') \sum_{v'=1}^{N_{\mathrm{occ},\sigma'}} a^*_{s,v'\sigma'}(\mathbf{r}'') \varphi_{v'\sigma'}(\mathbf{r}'') : v = 1, \ldots, N_{\mathrm{occ},\sigma}; \sigma = \uparrow, \downarrow \Bigg\}, \tag{3.5}$$

$$\mathcal{K}^{1d}\mathcal{A}_s = \Bigg\{ \alpha_{\mathrm{EXX}} \int \mathrm{d}\mathbf{r}' \mathcal{P}^c_\sigma(\mathbf{r},\mathbf{r}') \sum_{v'=1}^{N_{\mathrm{occ},\sigma}} a_{s,v'\sigma}(\mathbf{r}') \int \mathrm{d}\mathbf{r}'' v_c(\mathbf{r}',\mathbf{r}'') \varphi^*_{v'\sigma}(\mathbf{r}'') \varphi_{v\sigma}(\mathbf{r}'') : v = 1, \ldots, N_{\mathrm{occ},\sigma}; \sigma = \uparrow, \downarrow \Bigg\}, \tag{3.6}$$

$$\mathcal{K}^{2d}\mathcal{A}_s = \Bigg\{ \alpha_{\mathrm{EXX}} \int \mathrm{d}\mathbf{r}' \mathcal{P}^c_\sigma(\mathbf{r},\mathbf{r}') \sum_{v'=1}^{N_{\mathrm{occ},\sigma}} \varphi_{v'\sigma}(\mathbf{r}') \int \mathrm{d}\mathbf{r}'' v_c(\mathbf{r}',\mathbf{r}'') a^*_{s,v'\sigma}(\mathbf{r}'') \varphi_{v\sigma}(\mathbf{r}'') : \\ v = 1,\ldots,N_{\mathrm{occ},\sigma}; \sigma = \uparrow,\downarrow \Bigg\}, \tag{3.7}$$

where H^{KS}_σ is the ground state KS Hamiltonian written for the σ spin channel, and $f^{\mathrm{loc}}_{\mathrm{Hxc},\sigma\sigma'}(\mathbf{r},\mathbf{r}') = v_c(\mathbf{r},\mathbf{r}') + f^{\mathrm{loc}}_{\mathrm{xc},\sigma\sigma'}(\mathbf{r},\mathbf{r}')$ is the sum of the bare Coulomb potential, v_c, and the local part of the time-independent exchange-correlation kernel

$$f^{\mathrm{loc}}_{\mathrm{xc},\sigma\sigma'}(\mathbf{r},\mathbf{r}') = \left. \frac{\delta V^{\mathrm{loc}}_{\mathrm{xc},\sigma}(\mathbf{r})}{\delta \rho_{\sigma'}(\mathbf{r}')} \right|_{(\rho^0,\nabla\rho^0)} . \tag{3.8}$$

$\rho_\sigma(\mathbf{r})$ is the electron density of the spin channel σ, $\mathcal{P}^c_\sigma$ is the projection operator onto the unoccupied Kohn-Sham orbitals with σ spin, i.e., $\mathcal{P}^c_\sigma = 1 - \sum_{v=1}^{N_{\mathrm{occ},\sigma}} |\varphi_{v\sigma}\rangle\langle\varphi_{v\sigma}|$. The parameter α_{EXX} is the fraction of the Hartree-Fock exchange included in the definition of the hybrid functional. For semilocal functionals $\alpha_{\mathrm{EXX}} = 0$ and hence the $\mathcal{K}^{1d}$ and $\mathcal{K}^{2d}$ operators are zero by definition.

Under the Tamm–Dancoff approximation (TDA) [134], which is equivalent to the Configuration Interaction Singles (CIS) method [135] used in quantum chemistry to compute VEEs, the $\mathcal{K}^{2e}$ and $\mathcal{K}^{2d}$ terms in Eq. (3.1) are neglected, yielding $\mathcal{B}_s = 0$, and one solves the following eigenvalue problem:

$$\left(\mathcal{D} + \mathcal{K}^{1e} - \mathcal{K}^{1d}\right) \mathcal{A}_s = \omega_s \mathcal{A}_s \, . \tag{3.9}$$

3.2.2 Excited state nuclear forces

To derive excited states nuclear forces, we use the extended Lagrangian formalism and the Z-vector method of Handy–Schaefer to compute gradients [136]. Such formulation allows us to compute gradients of the excited potential energy surfaces described by Eq. (3.9), while

satisfying all orthonormality constraints of the KS and $|a_{s,v\sigma}\rangle$ orbitals. The implementation of nuclear forces carried out in our work is similar to that of Hutter [17], although we generalize it in section 3.2.3 to spin-flip TDDFT.

To obtain the nuclear force for the I-th atom along the α-th Cartesian direction of a system in the s-th excited state, we need to evaluate the following total derivatives:

$$F_{s,I\alpha} = -\left(\frac{dV^{nn}}{dR_{I\alpha}} + \frac{dE^{\mathrm{KS}}}{dR_{I\alpha}} + \frac{d\omega_s}{dR_{I\alpha}}\right), \tag{3.10}$$

where V^{nn} is the nuclear-nuclear electrostatic potential energy, E^{KS} is the KS ground state total energy, and $\omega_s = \mathcal{A}_s^\dagger \left(\mathcal{D} + \mathcal{K}^{1e} - \mathcal{K}^{1d}\right) \mathcal{A}_s$ is the VEE of the s-th excited state obtained by solving the eigenvalue problem of Eq. (3.14) within the TDA. Without any loss of generality, we simplify the notation in Eq. (3.10) and write all terms as total derivatives with respect to an external parameter τ, and we define an extended Lagrangian, $\mathcal{L}_{\mathrm{ex}}$ (the dependence on the excited state index s is dropped for clarity)

$$F_\tau = -\left(\frac{dV^{nn}}{d\tau} + \frac{d\mathcal{L}_{\mathrm{ex}}}{d\tau}\right), \tag{3.11}$$

where

$$\mathcal{L}_{\mathrm{ex}} = \mathcal{L}_{\mathrm{KS}} + \mathcal{L}_{\mathrm{TDA}} + \mathcal{L}_Z \tag{3.12}$$

and we have defined

$$\mathcal{L}_{\mathrm{KS}} = E^{\mathrm{KS}} - \sum_{v \geq v', \sigma} \Gamma_{vv'\sigma} \left(\langle \varphi_{v\sigma} | \varphi_{v'\sigma} \rangle - \delta_{vv'}\right), \tag{3.13}$$

$$\mathcal{L}_{\mathrm{TDA}} = \sum_{vv'\sigma\sigma'} \langle a_{v\sigma} | (\mathcal{D} + \mathcal{K}^{1e} - \mathcal{K}^{1d})_{vv'\sigma\sigma'} | a_{v'\sigma'} \rangle - \omega \left(\sum_{v\sigma} \langle a_{v\sigma} | a_{v\sigma} \rangle - 1\right), \tag{3.14}$$

$$\mathcal{L}_Z = \sum_{v\sigma} \langle Z_{v\sigma}| \left(H_\sigma^{\mathrm{KS}} |\varphi_{v\sigma}\rangle - \sum_{v'} \Lambda_{vv'\sigma} |\varphi_{v'\sigma}\rangle \right) + c.c. \tag{3.15}$$

By requiring that $\mathcal{L}_{\mathrm{ex}}$ is stationary with respect to $\langle\varphi_{v\sigma}|$, $\langle a_{v\sigma}|$, $\langle Z_{v\sigma}|$, ω, $\Gamma_{vv'\sigma}$ and $\Lambda_{vv'\sigma}$ we obtain the following result:

$$\frac{d\mathcal{L}_{\mathrm{ex}}}{d\tau} = \frac{\partial E^{\mathrm{KS}}}{\partial \tau} + \int \mathrm{d}\mathbf{r} \frac{\partial V_{\mathrm{ext}}(\mathbf{r})}{\partial \tau} \sum_\sigma \left[\Delta\rho_\sigma^{(x)}(\mathbf{r}) + \Delta\rho_\sigma^{(Z)}(\mathbf{r}) \right]. \tag{3.16}$$

In Eq. (3.16), $\frac{\partial E^{\mathrm{KS}}}{\partial \tau}$ is the partial derivative of the KS-DFT total energy with respect to nuclear coordinates obtained from the Hellmann-Feynman theorem, $\frac{\partial V_{\mathrm{ext}}(\mathbf{r})}{\partial \tau}$ is the derivative of the external potential (described using pseudopotentials in our formulation), and we have defined

$$\Delta\rho_\sigma^{(x)}(\mathbf{r}) = \sum_{v=1}^{N_{\mathrm{occ},\sigma}} |a_{v\sigma}(\mathbf{r})|^2 - \sum_{v=1}^{N_{\mathrm{occ},\sigma}} \sum_{v'=1}^{N_{\mathrm{occ},\sigma}} \varphi_{v\sigma}^*(\mathbf{r}) \varphi_{v'\sigma}(\mathbf{r}) \int \mathrm{d}\mathbf{r}' a_{v\sigma}^*(\mathbf{r}') a_{v'\sigma}(\mathbf{r}'), \tag{3.17}$$

and

$$\Delta\rho_\sigma^{(Z)}(\mathbf{r}) = \sum_{v=1}^{N_{\mathrm{occ},\sigma}} \left[Z_{v\sigma}^*(\mathbf{r}) \varphi_{v\sigma}(\mathbf{r}) + \varphi_{v\sigma}^*(\mathbf{r}) Z_{v\sigma}(\mathbf{r}) \right]. \tag{3.18}$$

Here $\mathcal{Z} = \left\{ |Z_{v\sigma}\rangle : v = 1, \ldots, N_{\mathrm{occ},\sigma}; \sigma = \uparrow, \downarrow \right\}$ are vectors obtained by solving the so-called Handy-Schaefer Z-vector equation (obtained by imposing that $\mathcal{L}_{\mathrm{ex}}$ is stationary with respect to $\langle\varphi_{v\sigma}|$); the equation reads:

$$\left(\mathcal{D} + \mathcal{K}^{1e} - \mathcal{K}^{1d} + \mathcal{K}^{2e} - \mathcal{K}^{2d} \right) \mathcal{Z} = \mathcal{U}. \tag{3.19}$$

We have defined $\mathcal{U} = \left\{ -\mathcal{P}_\sigma^c |u_{v\sigma}\rangle : v = 1, \cdots, N_{\mathrm{occ},\sigma}; \sigma = \uparrow, \downarrow \right\}$, with

$$u_{v\sigma}(\mathbf{r}) = \frac{\delta \left[\mathcal{A}^\dagger \left(\mathcal{D} + \mathcal{K}^{1e} - \mathcal{K}^{1d} \right) \mathcal{A} \right]}{\delta \varphi_{v\sigma}^*(\mathbf{r})}. \tag{3.20}$$

A formal expression for $u_{v\sigma}(\mathbf{r})$ is reported in Chapter 3.9.1.

3.2.3 Vertical excitation energies and excited state nuclear forces within spin-flip TDDFT

Here we extend the LR-TDDFT formalism derived in section 3.2.1 and 3.2.2 to include neutral excitations involving a flip of the spin state, i.e., excitations that bring an electron from the spin channel σ to the opposite spin channel $\tilde{\sigma}$, without changing the total number of electrons [99–105]. In the presence of spin-flip (SF) excitations, the LR-TDDFT eigenvalue equation within the TDA, Eq. (3.9), reads

$$\left(\mathcal{D}^{\mathrm{SF}} + \mathcal{K}^{1e,\mathrm{SF}} - \mathcal{K}^{1d,\mathrm{SF}}\right) \mathcal{A}_s^{\mathrm{SF}} = \omega_s \mathcal{A}_s^{\mathrm{SF}} \,. \tag{3.21}$$

The eigenvalue equation without the TDA can be found in Chapter 3.9.1. The variation of the electron density can be written as

$$\Delta\rho_{s,\sigma}^{\mathrm{SF}}(\mathbf{r}) = \sum_{v=1}^{N_{\mathrm{occ},\tilde{\sigma}}} \varphi_{v\tilde{\sigma}}^{*}(\mathbf{r}) a_{s,v\sigma}^{\mathrm{SF}}(\mathbf{r}). \tag{3.22}$$

The operators on the LHS of Eq. (3.21) are defined as

$$\mathcal{D}^{\mathrm{SF}}\mathcal{A}_s^{\mathrm{SF}} = \left\{ \mathcal{P}_\sigma^c \left(H_\sigma^{\mathrm{KS}} - \varepsilon_{v\tilde{\sigma}} \right) |a_{s,v\sigma}^{\mathrm{SF}}\rangle : v = 1, \ldots, N_{\mathrm{occ},\tilde{\sigma}}; \sigma = \uparrow, \downarrow \right\}, \tag{3.23}$$

$$\begin{aligned} \mathcal{K}^{1e,\mathrm{SF}}\mathcal{A}_s^{\mathrm{SF}} = \Bigg\{ & \int \mathrm{d}\mathbf{r}' \mathcal{P}_\sigma^c(\mathbf{r},\mathbf{r}') \varphi_{v\tilde{\sigma}}(\mathbf{r}') \int \mathrm{d}\mathbf{r}'' f_{\mathrm{xc}}^{\mathrm{loc,SF}}(\mathbf{r}',\mathbf{r}'') \sum_{v'=1}^{N_{\mathrm{occ},\tilde{\sigma}}} \varphi_{v'\tilde{\sigma}}^{*}(\mathbf{r}'') a_{s,v'\sigma}^{\mathrm{SF}}(\mathbf{r}'') : \\ & v = 1, \ldots, N_{\mathrm{occ},\tilde{\sigma}}; \sigma = \uparrow, \downarrow \Bigg\}, \end{aligned} \tag{3.24}$$

$$\mathcal{K}^{1d,\mathrm{SF}}\mathcal{A}_s^{\mathrm{SF}} = \Bigg\{ \alpha_{\mathrm{EXX}} \int \mathrm{d}\mathbf{r}' \mathcal{P}_\sigma^c(\mathbf{r},\mathbf{r}') \sum_{v'=1}^{N_{\mathrm{occ},\widetilde{\sigma}}} a_{s,v'\sigma}^{\mathrm{SF}}(\mathbf{r}') \int \mathrm{d}\mathbf{r}'' v_c(\mathbf{r}',\mathbf{r}'') \varphi_{v'\widetilde{\sigma}}^*(\mathbf{r}'') \varphi_{v\widetilde{\sigma}}(\mathbf{r}'') : \\ v = 1,\ldots,N_{\mathrm{occ},\widetilde{\sigma}}; \sigma = \uparrow,\downarrow \Bigg\}. \tag{3.25}$$

The spin-flip exchange-correlation kernel is defined as

$$f_{\mathrm{xc}}^{\mathrm{loc,SF}}(\mathbf{r},\mathbf{r}') = \left. \frac{V_{\mathrm{xc},\sigma}^{\mathrm{loc}}(\mathbf{r}) - V_{\mathrm{xc},\widetilde{\sigma}}^{\mathrm{loc}}(\mathbf{r})}{\rho_\sigma(\mathbf{r}) - \rho_{\widetilde{\sigma}}(\mathbf{r})} \right|_{(\rho^0,\nabla\rho^0)} \delta(\mathbf{r},\mathbf{r}'), \quad \sigma \neq \widetilde{\sigma}. \tag{3.26}$$

Nuclear forces are evaluated using Eq. (3.10), but using the following expression for $\Delta\rho_\sigma^{(x)}$

$$\Delta\rho_\sigma^{(x)}(\mathbf{r}) = \sum_{v=1}^{N_{\mathrm{occ},\widetilde{\sigma}}} |a_{v\sigma}^{\mathrm{SF}}(\mathbf{r})|^2 - \sum_{v=1}^{N_{\mathrm{occ},\sigma}} \sum_{v'=1}^{N_{\mathrm{occ},\sigma}} \varphi_{v\sigma}^*(\mathbf{r}) \varphi_{v'\sigma}(\mathbf{r}) \int \mathrm{d}\mathbf{r}' a_{v\widetilde{\sigma}}^{\mathrm{SF}*}(\mathbf{r}') a_{v'\widetilde{\sigma}}^{\mathrm{SF}}(\mathbf{r}'). \tag{3.27}$$

The Z-vectors are obtained by solving Eq. (3.19), and using the definition for $u_{v\sigma}$ derived in the presence of spin-flip transitions (see Chapter 3.9.1).

3.3 Numerical approximations to compute vertical excitation energies and excited state nuclear forces

In this section, we discuss numerical approximations adopted in WEST-TDDFT for the calculation of VEEs with Eq. (3.9) or Eq. (3.21) for spin-conserving or spin-flip excitations, respectively, and excited state nuclear forces with Eq. (3.10). In particular, we focus on the most computationally expensive terms in the case of hybrid functionals, i.e., the $\mathcal{D}$, the $\mathcal{K}^{1d}$, and the $\mathcal{K}^{2d}$ terms, as defined in Eqs. (3.3), (3.6), and (3.7), respectively. In the following, we present the impact of the approximations and our verification tests performed for the first triplet excited state of the NV^- in diamond, using a conventional $(3 \times 3 \times 3)$ supercell containing 215 atoms, and the dielectric dependent hybrid (DDH) functional [33, 34], with a

plane-wave energy cutoff set to 60 Ry. TDDFT calculations were performed under the TDA.

3.4 Approximating the $\mathcal{D}$ term

When a hybrid functional is used, the Kohn-Sham Hamiltonian H_σ^{KS} that appears in the $\mathcal{D}$ term of Eq. (3.3) contains the exact exchange operator, $V_{\mathrm{X},\sigma}$, whose application to an arbitrary function, $\psi_\sigma(\mathbf{r}')$, is defined as

$$\int V_{\mathrm{X},\sigma}(\mathbf{r},\mathbf{r}')\psi_\sigma(\mathbf{r}')\mathrm{d}\mathbf{r}' = -\sum_{v}^{N_{\mathrm{occ},\sigma}} \varphi_{v\sigma}(\mathbf{r}) \int \frac{\varphi_{v\sigma}^*(\mathbf{r}')\psi_\sigma(\mathbf{r}')}{|\mathbf{r}-\mathbf{r}'|}\mathrm{d}\mathbf{r}' \,. \tag{3.28}$$

To reduce the computational cost associated with the $\mathcal{D}$ term, we approximated $V_{\mathrm{X},\sigma}$ using the ACE operator [123], defined as

$$V_{\mathrm{X},\sigma}^{\mathrm{ACE}}(\mathbf{r},\mathbf{r}') = -\sum_{k=1}^{N_{\mathrm{ACE},\sigma}} \xi_{k\sigma}(\mathbf{r})\xi_{k\sigma}^*(\mathbf{r}'), \tag{3.29}$$

where $N_{\mathrm{ACE},\sigma}$ is the total number of KS orbitals included in the summation that defines the operator. The ACE orbitals $\xi_{k\sigma}$ are obtained as:

$$\xi_{k\sigma}(\mathbf{r}) = \sum_{i=1}^{N_{\mathrm{ACE},\sigma}} W_{i\sigma}(\mathbf{r}) \left(L_\sigma^{-T}\right)_{ik}, \tag{3.30}$$

where $W_{i\sigma}(\mathbf{r}) = \int V_{\mathrm{X},\sigma}(\mathbf{r},\mathbf{r}')\varphi_{i\sigma}(\mathbf{r}')\mathrm{d}\mathbf{r}'$ results from the application of $V_{\mathrm{X},\sigma}$ to KS orbitals in the range of $[1, N_{\mathrm{ACE},\sigma}]$, and $\mathbf{L}_\sigma$ is the lower triangular matrix obtained from the Cholesky factorization $\mathbf{M}_\sigma = -\mathbf{L}_\sigma\mathbf{L}_\sigma^T$, where $\mathbf{M}_\sigma$ is a $N_{\mathrm{ACE},\sigma} \times N_{\mathrm{ACE},\sigma}$ matrix with $M_{ij\sigma} = \int \varphi_{i\sigma}^*(\mathbf{r})W_{j\sigma}(\mathbf{r})\mathrm{d}\mathbf{r}$.

In this work we use the ACE operator, $V_{\mathrm{X},\sigma}^{\mathrm{ACE}}$, to approximate the exact exchange operator, $V_{\mathrm{X},\sigma}$, in the $\mathcal{D}$ term of Eq. (3.3). Since $V_{\mathrm{X},\sigma}$ is to be applied to functions $a_{v\sigma}(\mathbf{r}')$ that are orthogonal to the occupied KS orbitals, unoccupied KS orbitals in the range of

$[N_{\mathrm{occ},\sigma}+1, N_{\mathrm{ACE},\sigma}]$ are included in the construction of the ACE operator, in addition to the occupied KS orbitals in the range of $[1, N_{\mathrm{occ},\sigma}]$.

Figure 3.1 shows a benchmark of the accuracy and time savings associated with the use of the ACE operator in TDDFT calculations of the VEE and forces for the first excited state of the NV^- in diamond. As expected, errors can be made arbitrarily small by increasing the N_{ACE} parameter. We also note that we need a smaller N_{ACE} to converge the calculation of the VEE than that of forces. Setting $N_{\mathrm{ACE},\sigma} = N_{\mathrm{occ},\sigma} + 20$ leads to an error of 27 meV for the VEE, while $N_{\mathrm{ACE},\sigma} = 4N_{\mathrm{occ},\sigma}$ is required to yield a maximum absolute error (mean absolute error) of 4 meV Å^{-1} (0.1 meV Å^{-1}) for the forces. The more stringent requirement on forces stems from high-energy unoccupied KS states more likely contributing to the solution of the Z-vector equation, Eq. (3.19), than to the calculation of the VEE. The use of the ACE operator allows us to evaluate the $\mathcal{D}$ term at a fraction ($\sim$0.05%) of the cost of directly applying the exchange operator, yielding a two-fold reduction of the total wall time for the calculation of the VEE and the forces, as shown in Figure 3.1(c) and (d). In summary, using the ACE operator to approximate the exact exchange operator can significantly reduce the computational cost of the TDDFT calculations for both VEE and nuclear forces, and, as expected, the error caused by the use of the ACE operator can be arbitrarily reduced by increasing the number of KS orbitals used in its construction.

3.5 Approximating the $\mathcal{K}^{1d}$ term

To compute VEEs and analytical forces within TDDFT, the application of the $\mathcal{K}^{1d}$ term (see Eq. (3.6)) to an arbitrary set of functions, $\mathcal{A} = \{a_{v\sigma} : v = 1, \cdots, N_{\mathrm{occ},\sigma}; \sigma = \uparrow, \downarrow\}$ is required. This amounts to carrying out $N^2_{\mathrm{occ},\sigma}$ integration operations entering the definition of $\tau_{vv'\sigma}$, i.e., $\tau_{vv'\sigma}(\mathbf{r}) = \int d\mathbf{r'} v_c(\mathbf{r}, \mathbf{r'}) \varphi^*_{v'\sigma}(\mathbf{r}) \varphi_{v\sigma}(\mathbf{r})$. With the aim of exploiting the near-sightedness principle to reduce the number of integrations, we introduce a unitary transformation of the KS orbitals, i.e., $\varphi_{v\sigma} = \sum_{n=1}^{N_{\mathrm{occ},\sigma}} U_{vn\sigma} \tilde{\varphi}_{n\sigma}$. Because the $\mathcal{K}^{1d}$ is invariant under a unitary

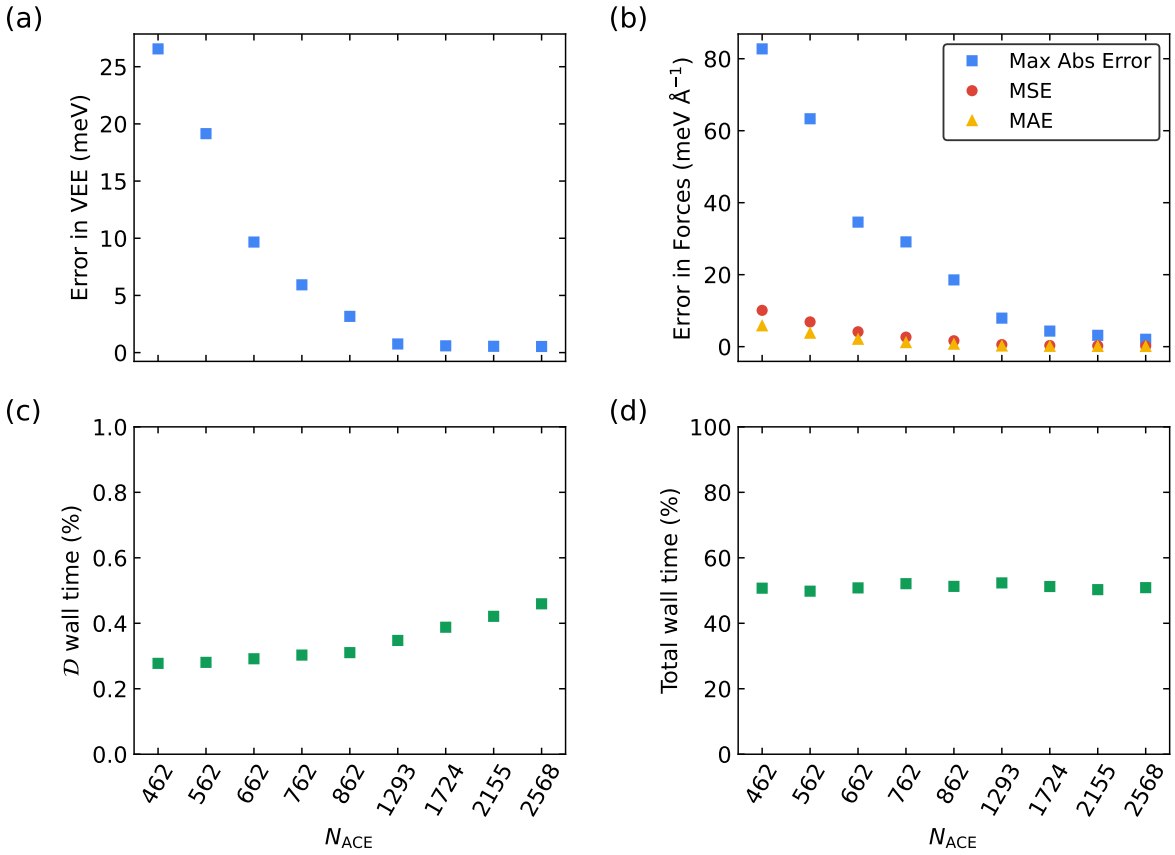

Figure 3.1: Benchmarks of the use of the adaptively compressed exchange (ACE) operator in TDDFT to speed up the calculation of the $\mathcal{D}$ term of Eq. (3.3) as a function of the number of Kohn-Sham orbitals (N_{ACE}) used to build the ACE operator (Eq. (3.29)). Calculations of the first vertical excitation energy (VEE) and forces of the NV^- in diamond are carried using the DDH hybrid functional, and a conventional ($3 \times 3 \times 3$) cell with 215 atoms and 432 (430) electrons in the spin-up (spin-down) channel. We report in panels (a) and (b) the error associated with the use of the ACE approximation for the evaluation of the VEE and the forces, respectively. The error is measured considering as a reference the result obtained by directly implementing the exact exchange operator without any approximation. In panels (c) and (d), we report the time savings observed for the calculation of the $\mathcal{D}$ term and the total wall time, respectively. The total wall time is obtained by summing the timings for the calculation of the VEE and the forces. The time savings are reported as the ratio of wall time measured while using the ACE approximation to that measured with no approximation.

transformation of the KS orbitals, we have

$$
\begin{aligned}
(\mathcal{K}^{1d}\mathcal{A})_{v\sigma} &= \alpha_{\mathrm{EXX}} \int d\mathbf{r}' \mathcal{P}^{c}_{\sigma}(\mathbf{r},\mathbf{r}') \sum_{v'=1}^{N_{\mathrm{occ},\sigma}} a_{v'\sigma}(\mathbf{r}')\tau_{vv'\sigma}(\mathbf{r}') \\
&= \alpha_{\mathrm{EXX}} \int d\mathbf{r}' \mathcal{P}^{c}_{\sigma}(\mathbf{r},\mathbf{r}') \sum_{m=1}^{N_{\mathrm{occ},\sigma}} U_{vm\sigma} \left\{ \sum_{n=1}^{N_{\mathrm{occ},\sigma}} \tilde{a}_{n\sigma}(\mathbf{r}')\tilde{\tau}_{mn\sigma}(\mathbf{r}') \right\},
\end{aligned}
\tag{3.31}
$$

where we have labeled $\tilde{a}_{n\sigma}(\mathbf{r}') = \sum_{v'=1}^{N_{\mathrm{occ},\sigma}} U^{*}_{v'n\sigma} a_{v'\sigma}(\mathbf{r}')$ and $\tilde{\tau}_{mn\sigma}(\mathbf{r}') = \int \mathrm{d}\mathbf{r}'' v_c(\mathbf{r}',\mathbf{r}'')\tilde{\varphi}^{*}_{n\sigma}(\mathbf{r}'')\tilde{\varphi}_{m\sigma}(\mathbf{r}'')$ the transformed orbitals and integrals, respectively. Here we consider the unitary transformation from occupied KS orbitals into maximally localized Wannier functions [137]. We define the overlap function, $S_{mn\sigma}$, between Wannier orbitals:

$$
S_{mn\sigma} = \frac{\int |\tilde{\varphi}_{m\sigma}(\mathbf{r})|^2 |\tilde{\varphi}_{n\sigma}(\mathbf{r})|^2 \mathrm{d}\mathbf{r}}{\sqrt{\int |\tilde{\varphi}_{m\sigma}(\mathbf{r})|^4 \mathrm{d}\mathbf{r} \int |\tilde{\varphi}_{n\sigma}(\mathbf{r}')|^4 \mathrm{d}\mathbf{r}'}}
\tag{3.32}
$$

We proceed by truncating pairs of non-overlapping localized orbitals in Eq. (3.31), i.e., we approximate $\tilde{\tau}_{mn\sigma}(\mathbf{r}) = 0$, if the corresponding overlap function is smaller than a preset threshold ($S_{mn\sigma} < S_{\mathrm{thr}}$). In this way, the number of $\tilde{\tau}_{mn\sigma}(\mathbf{r})$ integrals to be evaluated can be greatly reduced, achieving a linear scaling of the computational workload with respect to the number of orbitals [44].

Figure 3.2 shows the accuracy and time savings associated with the use of localized orbitals in TDDFT calculations. Our benchmarks were conducted for the first excited state of the NV^{-} in diamond. As expected, we can arbitrarily reduce the error by lowering the overlap threshold S_{thr}. For $S_{\mathrm{thr}} = 10^{-3}$, the error in the VEE is only -10 meV, and the maximum absolute error and the mean absolute error in nuclear forces is 9 meV $\mathrm{Å}^{-1}$ and 0.6 meV $\mathrm{Å}^{-1}$, respectively. For $S_{\mathrm{thr}} = 10^{-3}$, the number of $\tilde{\tau}_{mn\sigma}$ integrals, and consequently the computational cost of the $\mathcal{K}^{1d}$ term, is reduced by 92%, and the total wall time for computing the VEE and the forces is reduced by 23%, as shown by Figure 3.2(c) and (d). In

summary, by leveraging near-sightedness, we can significantly reduce the computational cost of the TDDFT calculations for the VEE and the nuclear forces, and the error introduced by the approximation can be systematically decreased as a function of the overlap threshold.

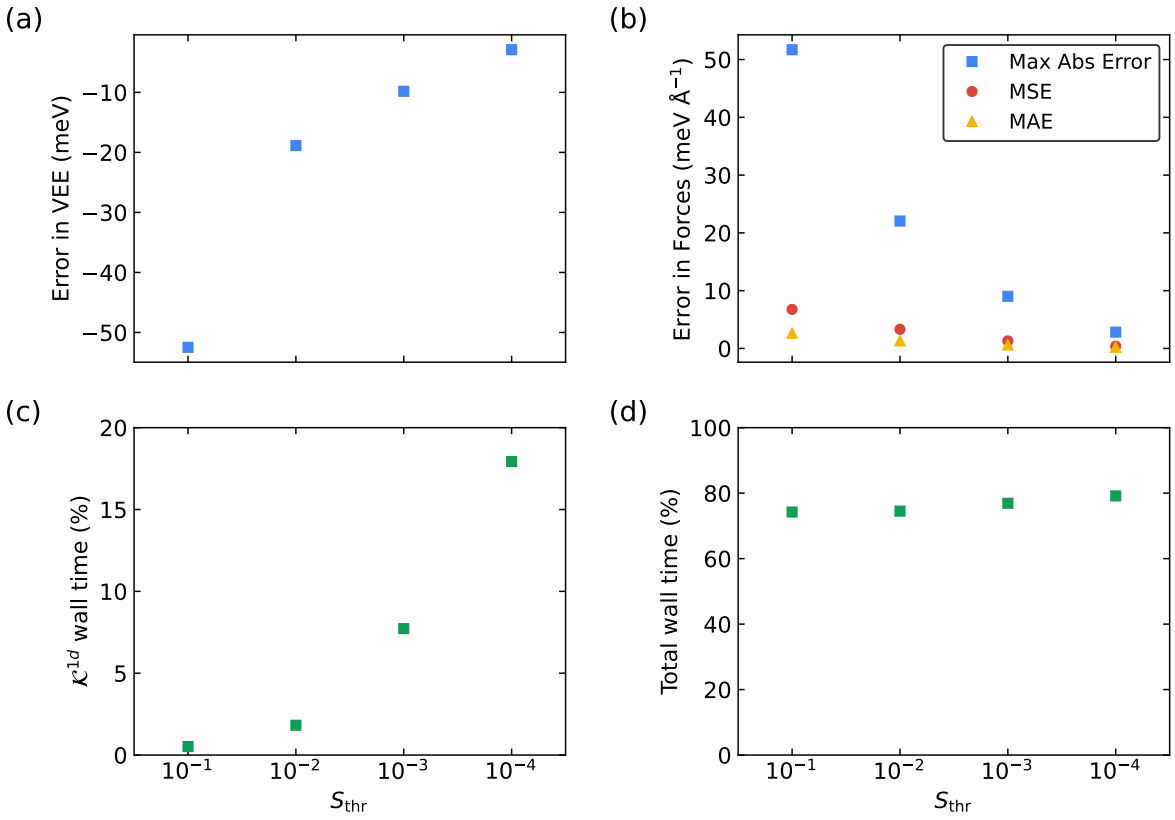

Figure 3.2: Benchmark of the use of the near-sightedness principle (see text) to approximate the $\mathcal{K}^{1d}$ term of Eq. (3.6) in TDDFT calculations, as a function of the overlap threshold S_{thr}. Calculations of the first vertical excitation energy (VEE) and the forces of the NV^- in diamond are carried using the DDH hybrid functional and a conventional $(3 \times 3 \times 3)$ cell with 215 atoms. We report in panels (a) and (b) the error associated with the truncation of pairs of non-overlapping localized orbitals for the evaluation of the VEE and the forces, respectively. In panels (c) and (d), we report the time savings observed for the calculation of the $\mathcal{K}^{1d}$ term and the total wall time, respectively. The total wall time is obtained by summing the timings for the calculation of the energy and the forces. The time savings are reported as the ratio of wall time measured while using truncation to that with no truncation.

3.5.1 Approximating the $\mathcal{K}^{2d}$ term

When computing analytical nuclear forces, the Z-vector equation is solved by using the Conjugate-Gradient (CG) algorithm. The implementation requires the repeated application of the super-operator, $\mathcal{L} = \mathcal{D} + \mathcal{K}^{1e} - \mathcal{K}^{1d} + \mathcal{K}^{2e} - \mathcal{K}^{2d}$, to residual vectors of Eq. (3.19). We implemented an inexact Krylov subspace approach [124, 125] to accelerate the CG iterations, where the exact $\mathcal{L}$ operator is used until the residual vector becomes smaller than a preset threshold, λ_{thr}. Then an approximate operator, $\mathcal{L}_{\text{approx}}$, is applied. We built $\mathcal{L}_{\text{approx}}$ by neglecting the $\mathcal{K}^{2d}$ term in the definition of $\mathcal{L}$, i.e., $\mathcal{L}_{\text{approx}} = \mathcal{D} + \mathcal{K}^{1e} - \mathcal{K}^{1d} + \mathcal{K}^{2e}$.

We tested the inexact Krylov subspace approach in TDDFT calculations with the DDH functional for the calculation of the first excited state of the NV^- in diamond, as shown in Figure 3.3. As expected, errors on the nuclear forces decrease as the threshold on the norm of the residual vector λ_{thr} is lowered. With $\lambda_{\text{thr}} = 10^{-4}$, the maximum absolute error and the mean absolute error on nuclear forces is 5 meV Å^{-1} and 0.2 meV Å^{-1}, respectively, and the number of CG iterations involving operations with the exact $\mathcal{L}$ is reduced from 31 to 11. As a consequence, the computational cost of the $\mathcal{K}^{2d}$ term is reduced by 64%, and the total wall time for computing VEE and forces is reduced by 15%, as shown by Figure 3.3(b) and (c). In summary, using the inexact Krylov subspace approach can significantly reduce the computational cost of the TDDFT calculations of nuclear forces, and the error can be systematically reduced by decreasing the threshold on the norm of the residual vector.

3.5.2 Using approximations altogether

Finally, we tested the three numerical approximations discussed in the previous subsections altogether in TDDFT calculations with the DDH functional for the calculations of the first excited state of the NV^- in diamond. Compared to the results obtained with the exact TDDFT calculations, when using the three numerical approximations, the error in the VEE is only -9 meV, and the maximum absolute error and the mean absolute error in nuclear

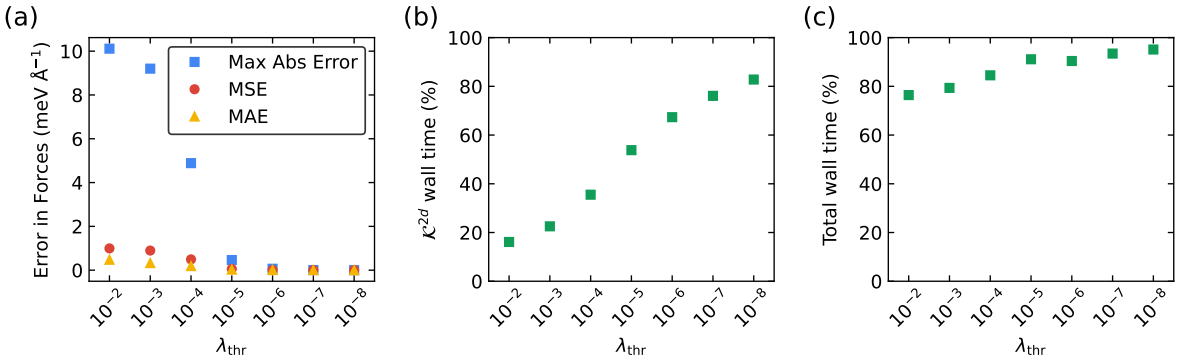

Figure 3.3: Benchmark of the inexact Krylov subspace approach in TDDFT calculations of analytical nuclear forces with the DDH hybrid functional, as a function of the threshold on the norm of the residual vector λ_{thr} for the calculations of the nuclear forces of the first excited state of the NV^- in diamond. (a) Error in the nuclear forces of the first excited state. (b) The fraction of the wall time for the calculations of the $\mathcal{K}^{2d}$ term of Eq. (3.7) when using the inexact Krylov subspace approach with respect to using a conventional approach. (c) The fraction of the total wall time of TDDFT calculations using the inexact Krylov subspace approach relative to the total wall time using a conventional approach.

forces are 10 meV Å^{-1} and 0.7 meV Å^{-1}, respectively. The total wall time for computing VEE and nuclear forces is reduced by 87%. The minimal errors indicate that the parameter settings of the three numerical approximations, i.e., $N_{\text{ACE}} = 4N_{\text{occ}}$ for the ACE operator, $S_{\text{thr}} = 10^{-3}$ for the overlap threshold, and $\lambda_{\text{thr}} = 10^{-4}$ for the threshold on the norm of the residual vector to activate the inexact Krylov subspace approach in the CG solver of the Z-vector equation (Eq. (3.19)), are reasonable choices. These settings can be an effective starting point when tailoring parameters for other systems. In summary, using the ACE operator, near-sightedness, and the inexact Krylov subspace approach together can significantly reduce the computational cost of the TDDFT calculations of the VEE and the nuclear forces, and the balance between the accuracy and cost can be systematically controlled by adjusting the relevant parameters, as shown above.

3.6 Performance and scalability on CPUs and GPUs

We implemented spin-conserving and spin-flip TDDFT for the calculation of VEEs and analytical forces in the WEST code [121], which is a many-body perturbation theory code based on the plane-wave pseudopotential method. In refs. 121, 122, we demonstrated the scaling of the code for full-frequency G_0W_0 calculations using up to 524,288 CPU cores or 25,920 GPUs. The hierarchical parallelization strategy, which leverages the embarrassingly parallel parts of the algorithms, was proven to be key to achieving excellent scaling. The implementation of WEST-TDDFT adopts a similar multilevel parallelization scheme.

Firstly, in our implementation, the processors are partitioned into subgroups, referred to as images, to facilitate the parallel diagonalization of the super-operator $\mathcal{L}$. The diagonalization is carried out iteratively using the Davidson method [138]. Secondly, the processors within each image are partitioned into pools, with each pool computing one spin channel in simulations of spin-polarized systems. Thirdly, the processors within each pool are further partitioned into band groups, with each group being responsible for computing a subset of orbitals. Communications between band groups are required only when a summation over orbitals is carried out, e.g., in Eqs. (3.4), (3.5), (3.6), and (3.7). Finally, as the last parallelization level, the fast Fourier transforms (FFTs) between the direct and reciprocal spaces and the linear algebra operations are carried out using the processors within a band group.

We present an assessment of the performance and scalability of the WEST-TDDFT code on both CPU and GPU nodes using the Perlmutter supercomputer at the National Energy Research Scientific Computing Center (NERSC). Each CPU node of Perlmutter is equipped with two AMD EPYC Milan CPUs. Each GPU node of Perlmutter is equipped with one AMD EPYC Milan CPU and four NVIDIA A100 GPUs. To benchmark the implementation of WEST-TDDFT, we considered the first excited state of the NV^- in diamond, whose ground-state DFT calculation was performed using the Quantum ESPRESSO [139, 140] code (version 7.2), the SG15 optimized norm-conserving Vanderbilt (ONCV) pseudopoten-

tials [141, 142], and the DDH functional [33, 34]. A kinetic energy cutoff of 60 Ry was used for the plane-wave basis set. The Brillouin zone was sampled with the Γ-point. In the TDDFT calculations, we used the numerical approximations discussed in section 3.3, namely the ACE method with $N_{\mathrm{ACE}} = 4N_{\mathrm{occ}}$, the Wannier localization with $S_{\mathrm{thr}} = 10^{-3}$, and the inexact Krylov subspace approach with $\lambda_{\mathrm{thr}} = 10^{-4}$.

The performance of WEST-TDDFT on CPU- and GPU-nodes is presented in Figure 3.4 for the NV^- in conventional $(4 \times 4 \times 4)$ and $(5 \times 5 \times 5)$ supercells of diamond containing 511 and 999 atoms, respectively. The figure displays the total wall clock time, including time spent on input/output (I/O) operations. For the $(4 \times 4 \times 4)$ supercell, we observe an excellent strong scaling up to 128 CPU or GPU nodes. The minor degradation of the parallel efficiency is attributed to the overhead caused by the inter-node message-passing interface (MPI) communications and I/O operations that, at a large node count, become comparable to the computational time. For the $(5 \times 5 \times 5)$ supercell, the GPU version of WEST-TDDFT exhibits near-perfect strong scaling up to 512 nodes (2048 GPUs). This showcases the applicability of WEST-TDDFT to conduct large-scale simulations. Further details on the scalability of WEST-TDDFT can be found in Chapter 3.9.3.

3.7 Results

To validate the implementation of WEST-TDDFT, we computed the VEEs of low-lying excited states of the formaldehyde molecule, and we optimized the geometry of the excited states. We also verified the implementation of the analytical nuclear forces against the calculation of numerical nuclear forces for the excited states of the NV^- in diamond obtained from spin-conserving and spin-flip TDDFT. Details can be found in Chapter 3.9.2. Below, we describe results for spin-defects in several solids.

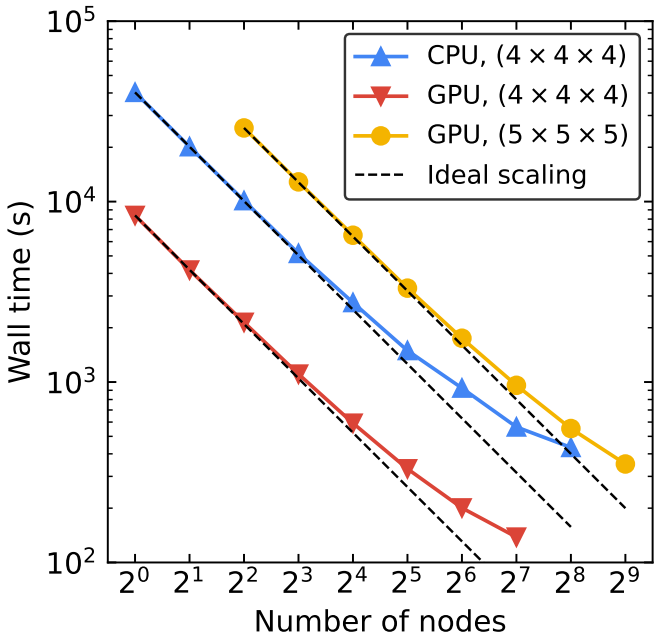

Figure 3.4: Strong scaling of the WEST-TDDFT code on CPU- and GPU-nodes of the NERSC/Perlmutter supercomputing architecture. The scaling tests report the time to compute the vertical excitation energy (VEE) and the nuclear forces for the first excited state of the NV^- in diamond, simulated using the DDH hybrid functional and 60 Ry kinetic energy cutoff. The blue and red triangles represent timings of simulations in a conventional $(4 \times 4 \times 4)$ supercell of diamond containing 511 atoms, carried out on CPU and GPU nodes, respectively. The orange circles represent the timings of simulations in a conventional $(5 \times 5 \times 5)$ supercell of diamond containing 999 atoms carried out on GPU nodes. The timings presented here amount to the total wall clock time, including the time spent on I/O operations. The black dashed lines indicate the ideal strong scaling.

3.7.1 Computational setup

The electronic structures of the defects in diamond, 4H-SiC, and MgO are obtained using DFT and the plane-wave pseudopotential method, as implemented in the Quantum ESPRESSO package [139, 140]. The plane-wave energy cutoff was set to 60 Ry. We used the semilocal functional by Perdew, Burke, and Ernzerhof (PBE) [31] and the DDH functional [33, 34]. The fraction of exact exchange used in the DDH functional was determined by the inverse of the macroscopic dielectric constant of the system, resulting in 18%, 15%, and 36% of exact exchange for diamond, 4H-SiC, and MgO, respectively [33, 126].

We used a $(4\times4\times4)$ supercell containing 511 atoms and a $(5\times5\times2)$ supercell containing 398 atoms for the triplet excited state of the NV^- in diamond and the VV^0 in 4H-SiC, respectively. For singlet excited states, we used a $(3\times3\times3)$ supercell containing 215 atoms and a $(5\times5\times1)$ supercell containing 198 atoms for the NV^- in diamond and the VV^0 in 4H-SiC, respectively. Supercells of different sizes were used in the study of the finite-size effects for the SiV^0 in diamond and V_O^0 in MgO. We used the lattice constant optimized with each specific functional [33, 83]. The Brillouin zone was sampled with the Γ point.

Excited states were computed using the method described in the previous sections. The equilibrium atomic geometries of excited states were obtained by minimizing the nuclear forces below the threshold of 0.01 eV $Å^{-1}$.

3.7.2 NV^- in diamond and VV^0 in 4H-SiC

The NV^- in diamond and the VV^0 in 4H-SiC are prototypical spin defects with numerous quantum technology applications [62–66, 68, 70, 76, 143, 144]. In this work we focus on the kk configuration of the VV^0 in 4H-SiC, where both the silicon and the carbon vacancy are located in the k- site. Although, due to the symmetry of the lattice, there exist three additional configurations of the VV^0, the focus here is to describe the applicability and accuracy of the TDDFT techniques developed and implemented in our work, rather than presenting an exhaustive study of spin defects. Both the NV^- in diamond and the VV^0 in 4H-SiC have C_{3v} symmetry, and the defect single-particle orbitals within the band gap are a_1, and degenerate e_x and e_y orbitals, as shown in Figure 3.5. Many-body electronic states, including the triplet ground state $^3A_2$, the triplet excited state ^3E, and singlet excited states ^1E and $^1A_1$, and the transitions between these states, play an essential role in the operation of the spin defects as qubits, especially in the initialization and readout of the qubit state. Therefore, it is interesting to study their energy and atomic geometries in order to interpret experiments and eventually help design new schemes for quantum technology applications.

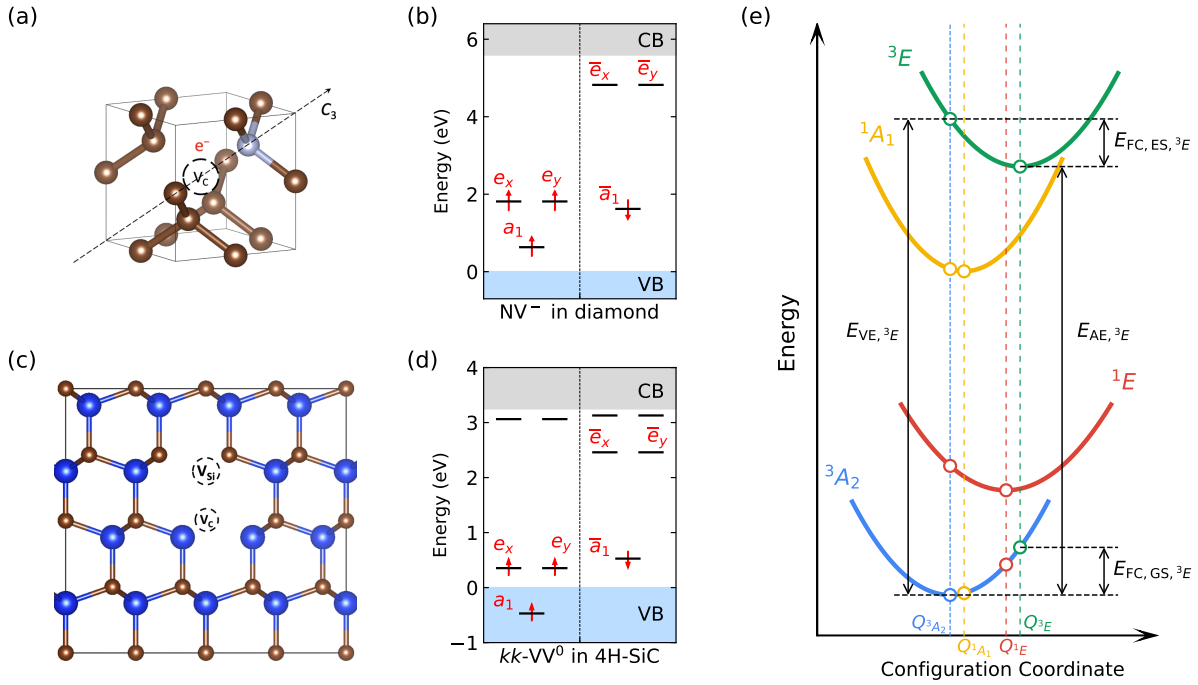

Figure 3.5: Ball and stick representation of (a) the negatively charged nitrogen-vacancy center (NV^-) in diamond and (c) the neutral divacancy center (VV^0) in 4H-SiC (kk configuration), with the vacancies displayed as circles in the middle of the cell, and the carbon, nitrogen, and silicon atoms represented by brown, gray and blue spheres, respectively. Position of the single-particle defect levels for (b) NV^- in diamond and (d) VV^0 in 4H-SiC, labeled according to the irreducible representation of the C_{3v} group and computed by spin unrestricted density functional theory (DFT) calculations with the DDH hybrid functional. (e) Schematic one-dimensional diagram illustrating potential energy surfaces (PESs) of NV^- in diamond and VV^0 in 4H-SiC, including the triplet ground state $^3A_2$, the triplet excited state ^3E, and singlet states ^1E and $^1A_1$. The configuration coordinate of state $^3A_2$ is indicated as $Q_{^3A_2}$. Vertical excitation energy ($E_{\rm VE}$) at the ground state geometry, adiabatic excitation energy ($E_{\rm AE}$), and Franck-Condon shifts in the ground ($E_{\rm FC,GS}$) and excited state ($E_{\rm FC,ES}$) PES are indicated by black arrows for the triplet excited state ^3E. The value of $E_{\rm AE}$ is frequently used to approximate the energy of the zero-phonon line (ZPL) by assuming that the zero-point energies are similar in the electronic ground and excited state.

We first discuss the many-body electronic excited states of the NV^- in diamond, as obtained using TDDFT. The computed VEEs, adiabatic excitation energies (AEEs), Franck-Condon (FC) shifts, and mass-weighted displacements of the many-body electronic excited states are shown in Table 3.1, together with published theoretical and experimental results. Starting from the $M_s = 1$ sublevel of the triplet ground state $^3A_2$ obtained using unre-

stricted Kohn-Sham DFT, we computed the triplet excited state ^3E using spin-conserving TDDFT. The VEEs of state ^3E agree within 0.2 eV with those computed using the so-called ΔSCF approach for both PBE and DDH functionals. Unlike ΔSCF, TDDFT calculations do not require any prior knowledge of the symmetry and the composition of the excited state, and they do not suffer from convergence issues often encountered for (near-)degenerate states within the ΔSCF framework. The VEEs of state ^3E also agree well, within $\sim$0.2 eV, with the results from the quantum defect embedding theory (QDET) [88] and with experiments [143]. The small difference between TDDFT and QDET results and experiments may originate, at least in part, from the use of the DDH functional, which uses a screening constant corresponding to that of the pristine crystal. We expect that adopting a hybrid functional that incorporates the screening effects of both the host crystal and the defect [145] and at the same time taking into account electron-phonon interaction [49, 50] may improve our TDDFT results. The optimized geometry in the excited state using TDDFT analytical nuclear forces and the resulting FC shifts and displacements are in good agreement with ΔSCF results. The ZPL computed by TDDFT differs from the experimental value by 0.05 (0.17) eV with the PBE (DDH) functional.

We also studied the highly correlated singlet excited states ^1E and $^1A_1$ using spin-flip TDDFT. The VEEs computed at the DDH level of theory are overestimated compared with those obtained with QDET and those inferred from experiments. The difference between TDDFT and QDET results may originate from the neglect of double excitations within the TDDFT framework [150].

In addition to VEE, we show in Table 3.1 the FC shifts and displacements resulting from the geometry optimizations of the singlet states. The displacements of the $^1A_1$ state are relatively small, as expected since this state has an electronic composition similar to that of the ground state $^3A_2$: one hole in the a_1 orbital and two holes in the degenerate e_x and e_y orbitals on average. In contrast, the FC shifts and displacements of the ^1E state are

Table 3.1: Computed vertical excitation energy E_{VE} (eV), adiabatic excitation energy E_{AE} (eV), Franck-Condon shift (eV) in the excited ($E_{\mathrm{FC,\ ES}}$) and the ground states ($E_{\mathrm{FC,\ GS}}$), and mass-weighted atomic displacement ΔQ (amu$^{1/2}$ Å) for the negatively charged nitrogen-vacancy center NV^- in diamond.

Method	E_{VE}	E_{AE}	$E_{\mathrm{FC,\ GS}}$	$E_{\mathrm{FC,\ ES}}$	ΔQ
			State ^3E		
TDDFT (PBE)	2.089	1.894	0.175	0.195	0.609
TDDFT (DDH)	2.372	2.112	0.228	0.256	0.659
ΔSCF (PBE, $\overline{a}_1^1\overline{e}_x^{0.5}\overline{e}_y^{0.5}$ [a]) [83]	1.937	1.731	0.180	0.206	0.620
ΔSCF (DDH, $\overline{a}_1^1\overline{e}_x^{0.5}\overline{e}_y^{0.5}$) [83]	2.491	2.230	0.223	0.261	0.635
ΔSCF (PBE, $\overline{a}_1^1\overline{e}_x^1\overline{e}_y^0$ [b]) [83]		1.706	0.203		0.655
ΔSCF (DDH, $\overline{a}_1^1\overline{e}_x^1\overline{e}_y^0$) [83]		2.205	0.248		0.666
QDET [c]	2.162				
Expt. [143]	2.18	1.945 [d]			
			State ^1E		
TDDFT (PBE)	0.512	0.448	0.086	0.064	0.428
TDDFT (DDH)	0.681	0.560	0.079	0.121	0.423
QDET [c]	0.479				
Expt. [146–149]		$0.34 - 0.43$			
			State $^1A_1$		
TDDFT (PBE)	1.336	1.319	0.018	0.017	0.111
TDDFT (DDH)	1.973	1.957	0.018	0.016	0.095
QDET [c]	1.317				
Expt. [146–149]		$1.51 - 1.60$			

[a] The electronic configuration in the hole representation: one hole in the $\overline{a}_1$ orbital, and half a hole in both the $\overline{e}_x$ and the $\overline{e}_y$ orbitals. [b] The electronic configuration in the hole representation: one hole in the $\overline{a}_1$ orbital, and one hole in the $\overline{e}_x$ orbital. [c] The QDET results are obtained with the exact double counting scheme [88] and are converged with respect to the active space size. [d] The computed adiabatic excitation energy is compared with the experimentally measured zero-phonon line (ZPL) energy [143].

larger, although its electronic composition is also not dissimilar from that of the ground state. The reason for that is the coupling with the symmetry broken vibrational modes with e type symmetry. The FC shifts of the ^1E state is about half that of the ^3E state, indicating a weaker electron-phonon coupling for the $^1E \rightarrow {}^3A_2$ transition compared to the $^3E \rightarrow {}^1A_1$ transition, which is consistent with the fact that the experimentally observed multi-phonon inter-system crossing rate is slower for the former process [149, 151, 152]. The optimized geometries of the $^1A_1$ and ^1E states have been further validated through the study of vibrationally resolved optical absorption spectra [150]. The computed absorption line shape is in excellent agreement with the experiment [147], suggesting that spin-flip TDDFT yields an accurate description of the geometries of the highly correlated singlet states.

We now turn to describe the many-body electronic excited states of the VV^0 in 4H-SiC; our results are reported in Table 3.2 together with theoretical and experimental results from previous works. For triplet excited state ^3E, TDDFT predicts VEEs, AEEs, FC shifts, and displacements in fair agreements with ΔSCF results. Both the TDDFT and the ΔSCF results slightly overestimate the experimental ZPL due to finite-size effects [83, 153]. As shown by previous ΔSCF calculations, results obtained with the $(5 \times 5 \times 2)$ supercell used in this work and in the dilute limit differ by ∼0.15 eV [83, 153]. As for the singlet states ^1E and $^1A_1$, spin-flip TDDFT yields an overestimate of their VEEs compared with the constrained random-phase approximation (CRPA) solved by configuration interaction (CI), possibly due to the neglect of double excitations. Unlike the case of the NV^- in diamond, the FC shifts and displacements of the ^1E state are comparable with those of the ^3E state, indicating a comparable electron-coupling strength and multi-phonon inter-system crossing rate for the $^1E \rightarrow {}^3A_2$ and the $^3E \rightarrow {}^1A_1$ transition. These results are consistent with experimental observations for the VV^0 in 3C-SiC [68], which has a similar electronic structure to that of the VV^0 in 4H SiC. In summary, TDDFT can accurately describe the energies and atomic

geometries of many-body electronic excited states of both the NV^- in diamond and the VV^0 in 4H-SiC and enables the study of multi-phonon processes.

3.7.3 SiV^0 in diamond

The SiV^0 in diamond exhibits long spin coherence time together with a near-infrared fluorescence signal and has been proposed as a platform for quantum communication applications [155, 156]. Here, we studied the excited states resulting from the transitions between defect orbitals (so-called *defect excitations*), as well as from transitions between the valence bands (VBs) of diamond and defect orbitals (so-called *bound excitons*). The atomic geometries and electronic structures of the SiV^0 are displayed in Figure 3.6. This defect possesses D_{3d} symmetry, with the e_g type defect orbitals localized in the band gap and the e_u type defect orbitals resonant with the VBs of diamond. The hybridization of the e_u orbitals with the VBs points to the possible impact of finite-size effects on excited states involving transitions from e_u orbitals into e_g orbitals.

Similar to the NV^- in diamond, SiV^0 in diamond has a triplet ground state, $^3A_{2g}$, as shown in Figure 3.6, and in the $M_s = 1$ sublevel e_{gx} and e_{gy} orbitals are filled by two electrons, while $\overline{e}_{gx}$ and $\overline{e}_{gy}$ orbitals are empty. Spin conserving excitations from $\overline{e}_{ux}$ and $\overline{e}_{uy}$ to $\overline{e}_{gx}$ and $\overline{e}_{gy}$ yield three triplet excited states $^3A_{2u}$, ^3E_u, and $^3A_{1u}$, which are all linear combinations of the $\overline{e}_{ux} \rightarrow \overline{e}_{gx}$, $\overline{e}_{ux} \rightarrow \overline{e}_{gy}$, $\overline{e}_{uy} \rightarrow \overline{e}_{gx}$, and $\overline{e}_{uy} \rightarrow \overline{e}_{gy}$ single excitations [157]. Spin-conserving TDDFT can correctly describe the multi-configuration nature of the triplet excited states and yield states with the correct symmetry. To estimate finite-size effects on the computed energy of the triplet excited states $^3A_{2u}$, ^3E_u, and $^3A_{1u}$, we performed TDDFT calculations in supercells with different numbers of atoms; our results for the VEEs are summarized in Figure 3.6. The linear dependence of the VEEs on $1/N_{\text{atom}}$ stems from the dipole-dipole interaction between the localized excitons in periodic images. In contrast, the VEEs of singlet excited states ^1E_g and $^1A_{1g}$ depend weakly on the supercell size

Table 3.2: Computed vertical excitation energy E_{VE} (eV), adiabatic excitation energy E_{AE} (eV), Franck-Condon shifts (eV) in the excited ($E_{\mathrm{FC,\ ES}}$) and the ground states ($E_{\mathrm{FC,\ GS}}$), and mass-weighted atomic displacement ΔQ (amu$^{1/2}$ Å) for the VV^0 in 4H-SiC (kk configuration).

Method	E_{VE}	E_{AE}	$E_{\mathrm{FC,\ GS}}$	$E_{\mathrm{FC,\ ES}}$	ΔQ
			State ^3E		
TDDFT (PBE)	1.413				
TDDFT (DDH)	1.464	1.351	0.097	0.113	0.779
ΔSCF (PBE, $\overline{a}_1^1\overline{e}_x^{0.5}\overline{e}_y^{0.5}$ [a]) [83]	1.233	1.161	0.063	0.072	0.635
ΔSCF (DDH, $\overline{a}_1^1\overline{e}_x^{0.5}\overline{e}_y^{0.5}$) [83]	1.484	1.398	0.075	0.086	0.664
ΔSCF (PBE, $\overline{a}_1^1\overline{e}_x^1\overline{e}_y^0$ [b]) [83]		1.118	0.103		0.770
ΔSCF (DDH, $\overline{a}_1^1\overline{e}_x^1\overline{e}_y^0$) [83]		1.355	0.114		0.787
CI−CPRA [c]	1.13				
Expt. [83]		1.096 [d]			
			State ^1E		
TDDFT (PBE)	0.327	0.253	0.068	0.074	0.548
TDDFT (DDH)	0.424	0.260	0.112	0.164	0.766
CI−CPRA [c]	0.29				
			State $^1A_1$		
TDDFT (PBE)	0.904	0.886	0.021	0.018	0.198
TDDFT (DDH)	1.413	1.392	0.024	0.021	0.208
CI−CPRA [c]	0.88				

[a] The electronic configuration in the hole representation: one hole in the $\overline{a}_1$ orbital, and half a hole in both the $\overline{e}_x$ and the $\overline{e}_y$ orbitals. [b] The electronic configuration in the hole representation: one hole in the $\overline{a}_1$ orbital, and one hole in the $\overline{e}_x$ orbital. [c] Vertical excitation energies are obtained using the model obtained from constrained random-phase approximation (CRPA) solved by configuration interaction (CI) [154]. [d] The computed adiabatic excitation energy is compared with the experimentally measured zero-phonon line (ZPL) energy [83].

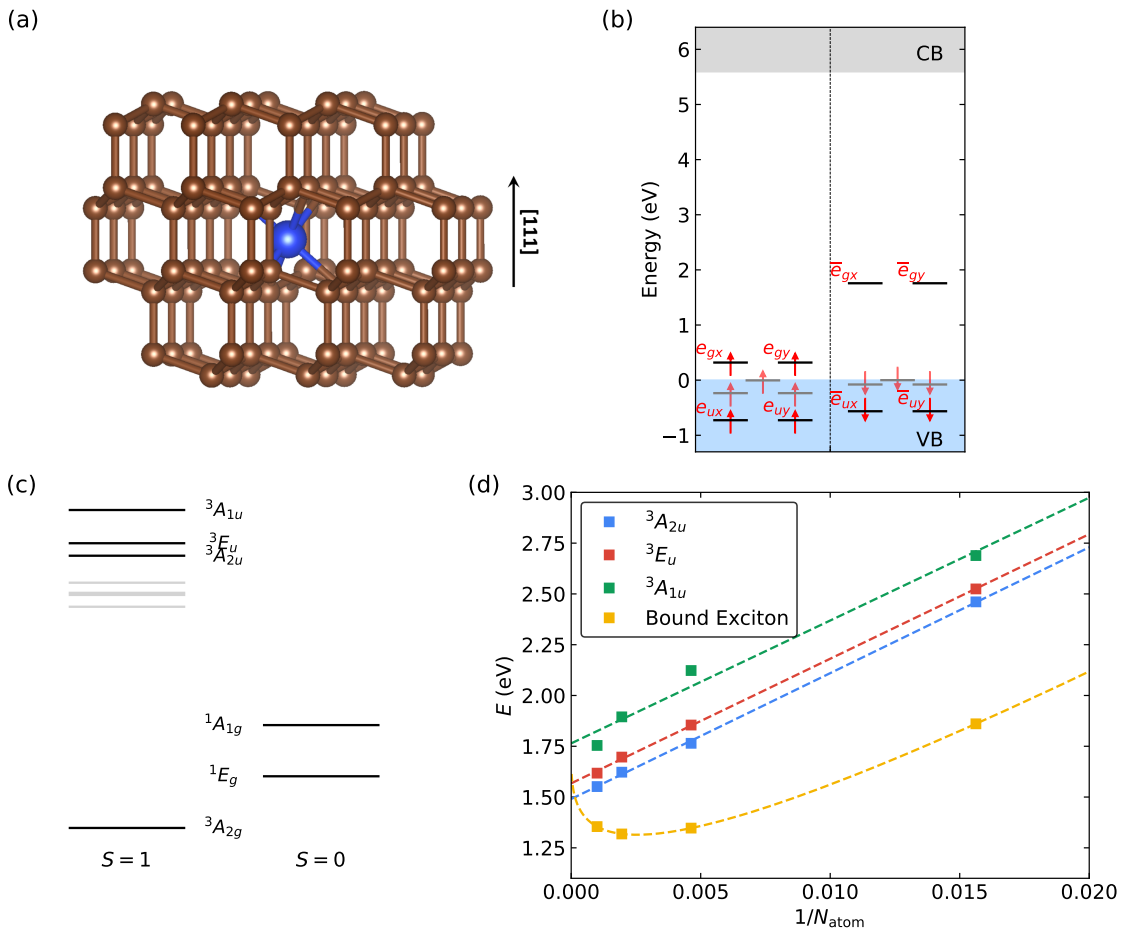

Figure 3.6: (a) Ball and stick representation of the neutral silicon vacancy center (SiV^0) in diamond with the carbon and silicon atoms represented by brown and blue spheres, respectively. (b) Position of the single-particle defect levels for the SiV^0 in diamond, labeled according to the irreducible representation of the D_{3d} point group, and computed by spin unrestricted density functional theory (DFT) calculations with the DDH hybrid functional. (c) Ordering of many-body electronic states computed by TDDFT using the DDH functional in a conventional $(4 \times 4 \times 4)$ supercell containing 511 atoms. Many-body states resulting from transitions between defect orbitals are shown as solid black lines and labeled according to the irreducible representation of the D_{3d} point group. States resulting from transitions of valence bands (VBs) of diamond into the $\overline{e}_{gx}/\overline{e}_{gy}$ orbital are shown as gray lines and labeled as bound excitons, i.e. an electron in the $\overline{e}_{gx}/\overline{e}_{gy}$ orbital bound to a hole in VBs. (d) Vertical excitation energies of the many-body states $^3A_{2u}$, ^3E_u, and $^3A_{1u}$ from defect excitations and the bound exciton state of the transition from the valence band maximum (VBM) to $\overline{e}_{gx}/\overline{e}_{gy}$ computed using TDDFT and the DDH functional in supercells containing different numbers of atoms. Fitting functions are shown as dashed lines. The VEEs of defect excitations $^3A_{2u}$, ^3E_u, and $^3A_{1u}$ are fitted by linear functions of $1/N_{\text{atom}}$, while the fitting function Eq. (3.33) has been used for the VEE of the bound exciton state. Details on the fitting process can be found in Chapter 3.9.5.

Table 3.3: Computed vertical excitation energies E_{VE} (eV) for the neutral silicon vacancy center (SiV^0) in diamond. TDDFT results reported here are extrapolated to the dilute limit.

Method	Cell Size	Triplet			Singlet	
		$^3A_{2u}$	^3E_u	$^3A_{1u}$	^1E_g	$^1A_{1g}$
TDDFT (PBE)	Dilute Limit	1.235	1.280	1.367	0.195	0.377
TDDFT (DDH)	Dilute Limit	1.490	1.568	1.764	0.331	0.657
NEVPT2-DMET(10,12) [93]	$(3 \times 3 \times 3)$	2.39	2.47	2.61	0.51	1.14

since the composition of their respective many-body wavefunctions mainly involve transitions from $e_{gx}(e_{gy})$ orbitals to $\overline{e}_{gx}(\overline{e}_{gy})$ orbitals, which are all within the band gap of diamond (see Chapter 3.9.5). We summarize the VEEs of both triplet and singlet excited states extrapolated to the dilute limit in Table 3.3, together with results from DMET calculations. For triplet states $^3A_{2u}$, ^3E_u, and $^3A_{1u}$ TDDFT predicts much lower VEEs than DMET, closer to the experimental ZPL of 1.31 eV [158]. This discrepancy could be attributed to two factors: (i) the neglect of finite-size effects on VEEs in the DMET calculations and (ii) the unsatisfactory treatment of the hybridization between $e_{ux}(e_{uy})$ orbitals and the VBs of diamond in the DMET calculations. The former could reduce the VEE of the triplet excited states by about 0.3 eV, based on the extrapolation of the $(3 \times 3 \times 3)$ TDDFT results to the dilute limit. A thorough understanding of reason (ii) requires further explorations, which are beyond the scope of this work.

Further, we optimized the geometry of the triplet excited states and approximated the energy of the ZPL as the adiabatic excitation energy by assuming that the zero-point energies are comparable in the electronic ground and excited state. The ZPL obtained in this way is 1.27 eV, in excellent agreement with the experimental value of 1.31 eV [158]. The geometry relaxation in the triplet excited states reduces the symmetry from D_{3d} to C_{2h} due to the elongation of two Si−C bonds by 0.068 Å and the contraction of the other two by 0.029 Å. Further details on the geometry relaxation, including the FC shifts, atomic displacements, and Si−C bond lengths near the defect center, can be found in Chapter 3.9.4. The ability to compute TDDFT analytical nuclear forces also allows for the evaluation of the coupling

between the transition dipole moment and the nuclear vibrational motion in the many-body electronic excited states, and thus for the calculation of the vibrationally resolved photoluminescence spectrum, including the contribution of the vibrational modes breaking the inversion symmetry through the Herzberg-Teller effect [159]. This investigation will be presented in a forthcoming publication.

While the transitions from the $e_{ux}(e_{uy})$ to the $e_{gx}(e_{gy})$ defect states only involve localized orbitals, the transitions from the VBs of diamond into the $e_{gx}(e_{gy})$ defect states involve more delocalized bound exciton orbitals. Bound excitons have been observed experimentally with excitation energies comparable to the ZPL of the triplet defect excited states [160]. We computed the VEE of the bound exciton as the transition from the valence band maximum (VBM) to the $\overline{e}_{gx}(\overline{e}_{gy})$ defect states in supercells of different sizes. Our results are summarized in Figure 3.6(d). In contrast to the triplet defect excited states, the VEE of the bound exciton state has a non-linear dependence on the supercell size, which can be attributed to the combination of the dipole-dipole interaction of excitons in nearby periodic images and the electron-hole interaction in the same exciton. We fitted the VEE using the function

$$E_{\mathrm{VE}}(L) = E_{\mathrm{VE}}(L=\infty) + \frac{A}{L}\exp\left(-\frac{L}{D}\right) - \frac{B}{L^3}, \tag{3.33}$$

where $L \propto N_{\mathrm{atom}}^{1/3}$ is the length of the cubic supercell, A and B are fitting parameters determined by the strength of the electron-hole interaction and the dipole-dipole interaction, respectively. D is a screening parameter, taking into account the fact that the electron-hole interaction no longer depends on L when L is much larger than the radius of the bound exciton. Using $D \in [10, 40]$ Å estimated by a previous study [160], we obtain $E_{\mathrm{VE}}(L = \infty) \in [1.33, 1.50]$ eV, higher than the ZPL of the triplet defect excited states, and in fair agreement with the experimental value of 1.39 eV [160]. Details on the fitting process can be found in Chapter 3.9.5.

In summary, TDDFT with the DDH functional provides a consistent description of lo-

calized defect excitations as well as of bound excitons in SiV^0 in diamond and predicts their energies in good agreement with experiments. Further, the affordable computational cost of TDDFT calculations enables a thorough investigation of finite-size effects.

3.7.4 $V_O{}^0$ in MgO

Oxygen vacancies are abundant in MgO and critically influence its applications in spintronic devices [161–164] and heterogeneous catalysis [165–169]. Here we investigate the excited state and optical properties of the neutral oxygen vacancy, V_O^0, in MgO using TDDFT, with the aim of interpreting its optical absorption and emission processes. In the ground state atomic geometry, the V_O^0 center has O_h symmetry with a s-type defect orbital a_{1g} within the band gap and three p-type defect orbitals t_{1u} resonant with the conduction bands (CBs) of MgO, as shown in Figure 3.7. The measured absorption peak at 5.0 eV was attributed to the V_O^0 center [170, 171]. To interpret the origin of the absorption peak, we computed the VEEs of the low-lying singlet excited states, including the $^1T_{1u}$ state from the $a_{1g} \to t_{1u}$ transition and the bound exciton state from the a_{1g} to the conduction band minimum (CBM) transition. We performed TDDFT calculations with the DDH functional in supercells of different sizes and extrapolated the values of the VEEs to the dilute limit, as shown in Figure 3.7(d). The VEE of the $^1T_{1u}$ state shows a linear dependence on $1/N_{\text{atom}}$ and reaches 5.08 eV at the dilute limit, which is in good agreement with experiments and with previous theoretical studies using the embedded Bethe–Salpeter equation (BSE) [172] and DMET [98] approaches. The $^1A_{1g} \to {}^1T_{1u}$ transition is also a dipole-allowed transition with substantial absorption cross section. The bound exciton state, on the other hand, has a VEE depending non-linearly on the system size. We extrapolated the values of the VEE to the dilute limit using Eq. (3.33). With $D = \infty$, we obtained a charge transition level of 4.81 eV for the $V_O^0 \to V_O^+ + e^-$(at CBM) process. With $D \in [21, 42]$ Å estimated based on the hydrogenic model, we obtained $E_{\text{VE}}(L = \infty) \in [4.41, 4.58]$ eV, which is smaller than the

absorption peak at 5.0 eV. Details on the fitting process can be found in Chapter 3.9.6. We note that the bound exciton corresponds to a dipole-forbidden transition, and thus, it is less likely to account for the absorption peak observed experimentally. Therefore, we conclude that the experimentally observed absorption peak can be attributed to the transition from the ground state $^1A_{1g}$ to the localized defect excited state $^1T_{1u}$, in agreement with previous studies.

The emission peaks at ∼2.3 to 2.4 eV and ∼3.1 to 3.2 eV have been measured experimentally and were suggested to pertain to excitations of the oxygen vacancy in MgO [170, 171]. To unravel their origins, we optimized the geometry of different electronic excited states and computed the FC shifts in the ground and the excited state; we then approximated the emission energy as the VEEs at the ground state geometry minus the FC shifts in both the ground and excited states. The computed absorption energies, emission energies, FC shifts, and mass-weighted displacements are summarized in Table 3.4. All excited states exhibit significant FC shifts and displacements as a result of the local excitation around the vacancy site. The emission energy of the $^1T_{1u}$ state is 4.073 eV, much higher than that of the measured emission peaks. Instead, the emission energy of the $^3T_{1u}$ state is 2.824 eV, only 0.4 to 0.5 eV higher than the measured emission energy of ∼2.3 to 2.4 eV, consistent with the DMET results [98]. Using a larger supercell for excited-state geometry relaxations would further decrease the emission energy and bring it closer to the experimental value. Therefore, we attribute the experimental emission peak of 2.3 to 2.4 eV to the emission from the $^3T_{1u}$ state. We note that the measured emission peak at 2.3 to 2.4 eV has a relatively long lifetime [173], which is consistent with the slow phosphorescence process from the $^3T_{1u}$ state to the $^1A_{1g}$ ground state. The emission energy of the bound exciton state is higher in energy at $\sim 3.04 - 3.21$ eV, and it agrees with the experimental emission peak at 3.1 to 3.2 eV. Therefore, we conclude that the emission peak at 3.1 to 3.2 eV originates from the bound exciton corresponding to the $V_O^+ + e^-(\text{at CBM}) \rightarrow V_O^0$ process. Further characterization of

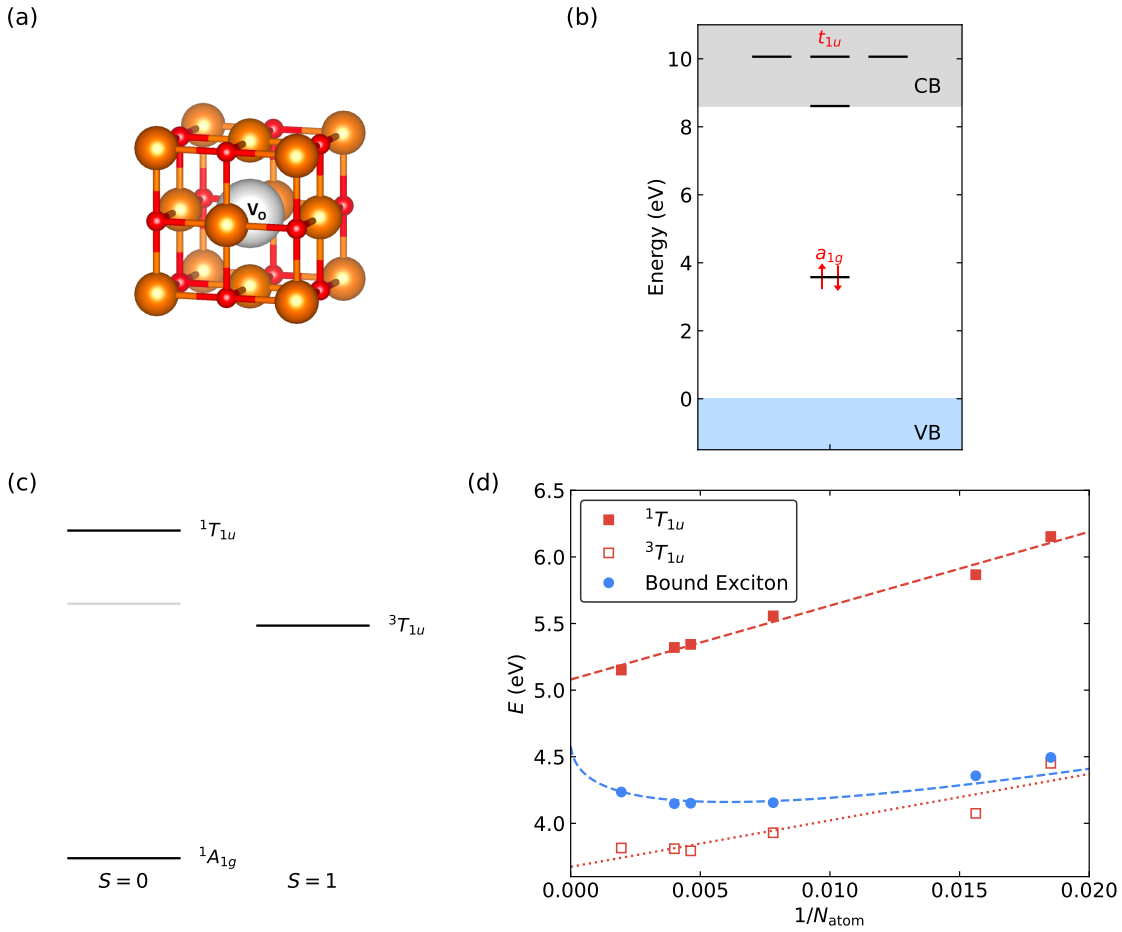

Figure 3.7: (a) Ball and stick representation of the neutral oxygen vacancy center (V_O^0) in magnesium oxide (MgO) with the oxygen and magnesium atoms represented by red and orange spheres, respectively. (b) Position of the single-particle defect levels for V_O^0 in MgO, labeled according to the irreducible representation of the O_h point group and computed by spin-restricted density functional theory (DFT) calculations with the DDH hybrid functional. (c) Ordering of many-body electronic states computed by TDDFT using the DDH functional in a $(3\times3\times3)$ conventional supercell containing 215 atoms. Many-body states resulting from transitions between a_{1g} and t_{1u} defect orbitals are shown as solid black lines and labeled according to the irreducible representation of the O_h point group. The state resulting from transitions from the a_{1g} defect orbital into the conduction band minimum (CBM) is shown as a gray line and labeled as bound exciton state, i.e., an electron in the CBM bound to a hole in the a_{1g} orbital. (d) Vertical excitation energies (VEEs) of the many-body excited states are computed using TDDFT and the DDH functional in supercells with different numbers of atoms. Fitting functions are shown as dashed lines. The VEEs of defect excitations $^1T_{1u}$ and $^3T_{1u}$ are fitted by linear functions of $1/N_{\text{atom}}$, while the fitting function Eq. (3.33) is used for the VEE of the bound exciton state. Details on the fitting process can be found in Chapter 3.9.6.

Table 3.4: Computed absorption energy E_{Abs} (eV), emission energy E_{Emi}, Franck-Condon shifts (eV) in electronic excited states $E_{\mathrm{FC,\ ES}}$ and electronic ground states $E_{\mathrm{FC,\ GS}}$, and mass-weighted atomic displacements ΔQ (amu$^{1/2}$ Å) for the neutral oxygen vacancy center (V_O^0) in magnesium oxide (MgO). Absorption energies are computed using TDDFT with the DDH hybrid functional and extrapolated to the dilute limit. FC shifts and displacements are computed using TDDFT with the DDH functional and a conventional $(3 \times 3 \times 3)$ supercell with 215 atoms.

States	E_{Abs}	E_{Emi}	$E_{\mathrm{FC,\ GS}}$	$E_{\mathrm{FC,\ ES}}$	ΔQ
$^1T_{1u}$	5.080	4.073	0.607	0.400	1.160
$^3T_{1u}$	3.674	2.824	0.419	0.431	1.573
Bound Exciton	$4.41 - 4.58$	$3.04 - 3.21$	0.643	0.732	1.092

the emission peaks would require detailed experimental and theoretical studies on the optical emission spectra.

In summary, in the case of the oxygen vacancy in MgO TDDFT with the DDH functional provides an accurate treatment of excited state geometry relaxation and enables the study of finite-size effects, thus facilitating the interpretation of optical absorption and emission mechanisms of the V_O^0 in MgO. Our calculations predict substantial geometry displacements and FC shifts for the excited states of the V_O^0 in MgO; such a shift has been frequently neglected in previous theoretical studies.

It is worth noting that unlike point defects in diamond and SiC, where the excited state energies from TDDFT calculations using semilocal and hybrid functionals agree with each other within 0.3 eV, for V_O^0 in MgO, using semilocal functionals can underestimate the excited state energies obtained using hybrid functionals and experiments by more than 1 eV. The FC shifts and displacements can also differ (see Table 3.9 for PBE results), depending on the functional. Therefore, it is necessary to use hybrid functionals to study the electronic structure of defects in oxides such as MgO.

3.8 Conclusions

We presented an efficient implementation of spin-conserving and spin-flip TDDFT, including the calculations of analytical nuclear forces based on plane-wave pseudopotential formalism. Our implementation in the WEST code includes several numerical approximations whose impact has been assessed in detail and a multilevel parallelization strategy that enables a strong scaling up to hundreds of CPU and GPU nodes. The numerical approximations introduced here allow for the study of excited states of systems with thousands of atoms using hybrid functionals. We presented results for the NV^- in diamond and the VV^0 in 4H-SiC, showing that spin-conserving and spin-flip TDDFT accurately describe the energy and atomic geometry of triplet and highly-correlated singlet excited states, respectively. In addition, our calculations enable the investigation of multi-phonon processes, including vibrationally resolved optical absorption and emission spectra and inter-system crossing transitions. Our study of the SiV^0 in diamond demonstrates that TDDFT is suitable to describe both defect excitations and bound excitons once finite-size effects are properly taken into account by using our highly scalable implementation. Our TDDFT study of the V_O^0 in MgO points to the key importance of obtaining accurate excited state geometries to correctly interpret absorption and emission mechanisms. In summary, our implementation of TDDFT with analytical nuclear forces provides a valuable tool to study excited states and optical properties of point defects in a variety of semiconductors and insulators.

We are exploring the possibility of extending our TDDFT calculations by incorporating additional hybrid functionals, possibly leading to an improvement in the description of screening effects in solids, especially in low-dimensional hosts such as two-dimensional hexagonal boron nitride (2D-hBN) [145]. Work is in progress to further accelerate TDDFT calculations through the use of density fitting techniques [174, 175], which could enable the direct study of multiple point defects and their interactions in the same supercell. Other interesting future efforts include the implementation of spin-flip TDDFT with the multi-

collinear formalism to reduce numerical instabilities [176, 177] and coupling TDDFT with analytical nuclear forces and molecular dynamics.

3.9 Technical details

3.9.1 Additional Equations for TDDFT

The expression for $u_{v\sigma}(\mathbf{r})$ for spin-conserving TDDFT within the TDA as defined in Eq. (3.20) reads:

$$
\begin{aligned}
u_{v\sigma}(\mathbf{r}) &= \frac{\delta\left[\mathcal{A}^\dagger\left(\mathcal{D}+\mathcal{K}^{1e}-\mathcal{K}^{1d}\right)\mathcal{A}\right]}{\delta\varphi^*_{v\sigma}(\mathbf{r})} \\
&= \varphi_{v\sigma}(\mathbf{r})\sum_{\sigma'}\int \mathrm{d}\mathbf{r}' f^{\mathrm{loc}}_{\mathrm{Hxc},\sigma\sigma'}(\mathbf{r},\mathbf{r}')\Delta\rho^{(x)}_{\sigma'}(\mathbf{r}') \\
&- \alpha_{\mathrm{EXX}}\sum_{v'=1}^{N_{\mathrm{occ},\sigma}} a_{v'\sigma}(\mathbf{r})\int \mathrm{d}\mathbf{r}' v_c(\mathbf{r},\mathbf{r}')a^*_{v'\sigma}(\mathbf{r}')\varphi_{v\sigma}(\mathbf{r}') \\
&+ \alpha_{\mathrm{EXX}}\sum_{v'=1}^{N_{\mathrm{occ},\sigma}}\sum_{v''=1}^{N_{\mathrm{occ},\sigma}} \varphi_{v''\sigma}(\mathbf{r})\int \mathrm{d}\mathbf{r}'' a^*_{v'\sigma}(\mathbf{r}'')a_{v''\sigma}(\mathbf{r}'')\int \mathrm{d}\mathbf{r}' v_c(\mathbf{r},\mathbf{r}')\varphi^*_{v'\sigma}(\mathbf{r}')\varphi_{v\sigma}(\mathbf{r}') \\
&+ a_{v\sigma}(\mathbf{r})\sum_{\sigma'}\int \mathrm{d}\mathbf{r}' f^{\mathrm{loc}}_{\mathrm{Hxc},\sigma\sigma'}(\mathbf{r},\mathbf{r}')\Delta\rho^*_{\sigma'}(\mathbf{r}') \\
&- \sum_{v'=1}^{N_{\mathrm{occ},\sigma}} a_{v'\sigma}(\mathbf{r})\int \mathrm{d}\mathbf{r}'\varphi^*_{v'\sigma}(\mathbf{r}')\varphi_{v\sigma}(\mathbf{r}')\sum_{\sigma'}\int \mathrm{d}\mathbf{r}'' f^{\mathrm{loc}}_{\mathrm{Hxc},\sigma\sigma'}(\mathbf{r}',\mathbf{r}'')\Delta\rho_{\sigma'}(\mathbf{r}'') \\
&+ \varphi_{v\sigma}(\mathbf{r})\sum_{\sigma'}\sum_{\sigma''}\int \mathrm{d}\mathbf{r}'\int \mathrm{d}\mathbf{r}'' g_{\mathrm{xc},\sigma\sigma'\sigma''}(\mathbf{r},\mathbf{r}',\mathbf{r}'')\Delta\rho^*_{\sigma'}(\mathbf{r}')\Delta\rho_{\sigma''}(\mathbf{r}'') \\
&- \alpha_{\mathrm{EXX}}\sum_{v'=1}^{N_{\mathrm{occ},\sigma}} \varphi_{v'\sigma}(\mathbf{r})\int \mathrm{d}\mathbf{r}' v_c(\mathbf{r},\mathbf{r}')a^*_{v'\sigma}(\mathbf{r}')a_{v\sigma}(\mathbf{r}') \\
&+ \alpha_{\mathrm{EXX}}\sum_{v'=1}^{N_{\mathrm{occ},\sigma}} a_{v'\sigma}(\mathbf{r})\int \mathrm{d}\mathbf{r}'\sum_{v''=1}^{N_{\mathrm{occ},\sigma}} a^*_{v''\sigma}(\mathbf{r}')\varphi_{v\sigma}(\mathbf{r}')\int \mathrm{d}\mathbf{r}'' v_c(\mathbf{r}',\mathbf{r}'')\varphi^*_{v'\sigma}(\mathbf{r}'')\varphi_{v''\sigma}(\mathbf{r}'').
\end{aligned}
\tag{3.34}
$$

In Eq. (3.34), $\Delta\rho_\sigma(\mathbf{r}) = \sum_{v=1}^{N_{\mathrm{occ},\sigma}} \varphi^*_{v\sigma}(\mathbf{r}) a_{v\sigma}(\mathbf{r})$, and

$$g^{\mathrm{loc}}_{\mathrm{xc},\sigma\sigma'\sigma''}(\mathbf{r},\mathbf{r}',\mathbf{r}'') = \left.\frac{\delta^2 V^{\mathrm{loc}}_{\mathrm{xc},\sigma}(\mathbf{r})}{\delta\rho_{\sigma'}(\mathbf{r}')\delta\rho_{\sigma''}(\mathbf{r}'')}\right|_{(\rho^0,\nabla\rho^0)} \tag{3.35}$$

is the second-order functional derivative of the exchange-correlation potential with respect to the electron density. The term involving $g^{\mathrm{loc}}_{\mathrm{xc},\sigma\sigma'\sigma''}(\mathbf{r},\mathbf{r}',\mathbf{r}'')$ can be evaluated by using a finite difference approach and written in the following way:

$$\begin{aligned} &\sum_{\sigma'}\sum_{\sigma''}\int \mathrm{d}\mathbf{r}'\int \mathrm{d}\mathbf{r}'' g^{\mathrm{loc}}_{\mathrm{xc},\sigma\sigma'\sigma''}(\mathbf{r},\mathbf{r}',\mathbf{r}'')\Delta\rho^*_{\sigma'}(\mathbf{r}')\Delta\rho_{\sigma''}(\mathbf{r}'') \\ \approx &\sum_k \frac{c_k}{12\epsilon^2} V^{\mathrm{loc}}_{\mathrm{xc},\sigma}\left[\rho^0_\uparrow + k\epsilon\Delta\rho_\uparrow, \rho^0_\downarrow + k\epsilon\Delta\rho_\downarrow\right](\mathbf{r}), \end{aligned} \tag{3.36}$$

where $c_k = -1, 16, -30, 16, -1$ for $k = -2, -1, 0, 1, 2$. Numerical tests have shown that stable results can be achieved by using $\epsilon = 0.01$ [117].

The LR-TDDFT eigenvalue equation in the presence of spin-flip (SF) excitations reads

$$\begin{pmatrix} \mathcal{D}^{\mathrm{SF}} + \mathcal{K}^{1e,\mathrm{SF}} - \mathcal{K}^{1d,\mathrm{SF}} & \mathcal{K}^{2e,\mathrm{SF}} - \mathcal{K}^{2d,\mathrm{SF}} \\ \mathcal{K}^{2e,\mathrm{SF}} - \mathcal{K}^{2d,\mathrm{SF}} & \mathcal{D}^{\mathrm{SF}} + \mathcal{K}^{1e,\mathrm{SF}} - \mathcal{K}^{1d,\mathrm{SF}} \end{pmatrix} \begin{pmatrix} \mathcal{A}^{\mathrm{SF}}_s \\ \mathcal{B}^{\mathrm{SF}}_s \end{pmatrix} = \omega_s \begin{pmatrix} \mathcal{I} & 0 \\ 0 & -\mathcal{I} \end{pmatrix} \begin{pmatrix} \mathcal{A}^{\mathrm{SF}}_s \\ \mathcal{B}^{\mathrm{SF}}_s \end{pmatrix}, \tag{3.37}$$

where $\mathcal{A}^{\mathrm{SF}}_s = \left\{|a^{\mathrm{SF}}_{s,v\sigma}\rangle : v = 1,\ldots,N_{\mathrm{occ},\widetilde{\sigma}}; \sigma = \uparrow,\downarrow\right\}$ and $\mathcal{B}^{\mathrm{SF}}_s = \left\{|b^{\mathrm{SF}}_{s,v\sigma}\rangle : v = 1,\ldots,N_{\mathrm{occ},\widetilde{\sigma}}; \sigma = \uparrow,\downarrow\right\}$ are two sets of orbitals that enter the definition of the linear change of the density matrix with respect to the ground state density matrix, due to the s-th SF excitation:

$$\Delta\rho^{\mathrm{SF}}_{s,\sigma} = \sum_{v=1}^{N_{\mathrm{occ},\widetilde{\sigma}}} |a^{\mathrm{SF}}_{s,v\sigma}\rangle\langle\varphi_{v\widetilde{\sigma}}| + \sum_{v=1}^{N_{\mathrm{occ},\sigma}} |\varphi_{v\sigma}\rangle\langle b^{\mathrm{SF}}_{s,v\widetilde{\sigma}}|.$$

The operators on the left-hand side (LHS) of Eq. (3.37) are defined as

$$\mathcal{D}^{\mathrm{SF}}\mathcal{A}_s^{\mathrm{SF}} = \left\{ \mathcal{P}_\sigma^c \left(H_\sigma^{\mathrm{KS}} - \varepsilon_{v\widetilde{\sigma}} \right) |a_{s,v\sigma}^{\mathrm{SF}}\rangle : v = 1, \ldots, N_{\mathrm{occ},\widetilde{\sigma}}; \sigma = \uparrow, \downarrow \right\}, \tag{3.38}$$

$$\mathcal{K}^{1e,\mathrm{SF}}\mathcal{A}_s^{\mathrm{SF}} = \left\{ \int \mathrm{d}\mathbf{r}' \mathcal{P}_\sigma^c(\mathbf{r},\mathbf{r}') \varphi_{v\widetilde{\sigma}}(\mathbf{r}') \int \mathrm{d}\mathbf{r}'' f_{\mathrm{xc}}^{\mathrm{loc,SF}}(\mathbf{r}',\mathbf{r}'') \sum_{v'=1}^{N_{\mathrm{occ},\widetilde{\sigma}}} \varphi_{v'\widetilde{\sigma}}^*(\mathbf{r}'') a_{s,v'\sigma}^{\mathrm{SF}}(\mathbf{r}'') : \right.$$
$$\left. v = 1, \ldots, N_{\mathrm{occ},\widetilde{\sigma}}; \sigma = \uparrow, \downarrow \right\}, \tag{3.39}$$

$$\mathcal{K}^{2e,\mathrm{SF}}\mathcal{A}_s^{\mathrm{SF}} = \left\{ \int \mathrm{d}\mathbf{r}' \mathcal{P}_\sigma^c(\mathbf{r},\mathbf{r}') \varphi_{v\widetilde{\sigma}}(\mathbf{r}') \int \mathrm{d}\mathbf{r}'' f_{\mathrm{xc}}^{\mathrm{loc,SF}}(\mathbf{r}',\mathbf{r}'') \sum_{v'=1}^{N_{\mathrm{occ},\sigma}} a_{s,v'\widetilde{\sigma}}^{\mathrm{SF}*}(\mathbf{r}'') \varphi_{v'\sigma}(\mathbf{r}'') : \right.$$
$$\left. v = 1, \ldots, N_{\mathrm{occ},\widetilde{\sigma}}; \sigma = \uparrow, \downarrow \right\}, \tag{3.40}$$

$$\mathcal{K}^{1d,\mathrm{SF}}\mathcal{A}_s^{\mathrm{SF}} = \left\{ \alpha_{\mathrm{EXX}} \int \mathrm{d}\mathbf{r}' \mathcal{P}_\sigma^c(\mathbf{r},\mathbf{r}') \sum_{v'=1}^{N_{\mathrm{occ},\widetilde{\sigma}}} a_{s,v'\sigma}^{\mathrm{SF}}(\mathbf{r}') \int \mathrm{d}\mathbf{r}'' v_c(\mathbf{r}',\mathbf{r}'') \varphi_{v'\widetilde{\sigma}}^*(\mathbf{r}'') \varphi_{v\widetilde{\sigma}}(\mathbf{r}'') : \right.$$
$$\left. v = 1, \ldots, N_{\mathrm{occ},\widetilde{\sigma}}; \sigma = \uparrow, \downarrow \right\}. \tag{3.41}$$

$$\mathcal{K}^{2d,\mathrm{SF}}\mathcal{A}_s^{\mathrm{SF}} = \left\{ \alpha_{\mathrm{EXX}} \int \mathrm{d}\mathbf{r}' \mathcal{P}_\sigma^c(\mathbf{r},\mathbf{r}') \sum_{v'=1}^{N_{\mathrm{occ},\sigma}} \varphi_{s,v'\sigma}(\mathbf{r}') \int \mathrm{d}\mathbf{r}'' v_c(\mathbf{r}',\mathbf{r}'') a_{v'\widetilde{\sigma}}^{\mathrm{SF}*}(\mathbf{r}'') \varphi_{v\widetilde{\sigma}}(\mathbf{r}'') : \right.$$
$$\left. v = 1, \ldots, N_{\mathrm{occ},\widetilde{\sigma}}; \sigma = \uparrow, \downarrow \right\}. \tag{3.42}$$

The SF exchange-correlation kernel is defined in Eq. (3.26). Under the TDA, the $\mathcal{K}^{2e,\mathrm{SF}}$ and $\mathcal{K}^{2d,\mathrm{SF}}$ terms in Eq. (3.37) are neglected, yielding $\mathcal{B}_s^{\mathrm{SF}} = 0$, and one solves the eigenvalue problem as defined in Eq. (3.21).

The expression for $u_{v\sigma}(\mathbf{r})$ for spin-flip TDDFT within the TDA reads:

$$
\begin{aligned}
u_{v\sigma}(\mathbf{r}) &= \frac{\delta\left[\mathcal{A}^{\mathrm{SF}\dagger}\left(\mathcal{D}^{\mathrm{SF}}+\mathcal{K}^{1e,\mathrm{SF}}-\mathcal{K}^{1d,\mathrm{SF}}\right)\mathcal{A}^{\mathrm{SF}}\right]}{\delta\varphi^{*}_{v\sigma}(\mathbf{r})} \\
&= \varphi_{v\sigma}(\mathbf{r})\sum_{\sigma'}\int \mathrm{d}\mathbf{r}' f^{\mathrm{loc}}_{\mathrm{Hxc},\sigma\sigma'}(\mathbf{r},\mathbf{r}')\Delta\rho^{(x)}_{\sigma'}(\mathbf{r}') \\
&- \alpha_{\mathrm{EXX}}\sum_{v'=1}^{N_{\mathrm{occ},\widetilde{\sigma}}} a^{\mathrm{SF}}_{v'\sigma}(\mathbf{r}')\int \mathrm{d}\mathbf{r}' v_c(\mathbf{r},\mathbf{r}')a^{\mathrm{SF}*}_{v'\sigma}(\mathbf{r}')\varphi_{v\sigma}(\mathbf{r}') \\
&+ \alpha_{\mathrm{EXX}}\sum_{v'=1}^{N_{\mathrm{occ},\sigma}}\sum_{v''=1}^{N_{\mathrm{occ},\sigma}} \varphi_{v''\sigma}(\mathbf{r})\int \mathrm{d}\mathbf{r}'' a^{\mathrm{SF}*}_{v'\widetilde{\sigma}}(\mathbf{r}'')a^{\mathrm{SF}}_{v''\widetilde{\sigma}}(\mathbf{r}'')\int \mathrm{d}\mathbf{r}' v_c(\mathbf{r},\mathbf{r}')\varphi^{*}_{v'\sigma}(\mathbf{r}')\varphi_{v\sigma}(\mathbf{r}') \\
&+ a^{\mathrm{SF}}_{v\widetilde{\sigma}}(\mathbf{r})\int \mathrm{d}\mathbf{r}' f^{\mathrm{loc,SF}}_{\mathrm{xc}}(\mathbf{r},\mathbf{r}')\Delta\rho^{\mathrm{SF}*}_{\widetilde{\sigma}}(\mathbf{r}') \\
&- \sum_{v'=1}^{N_{\mathrm{occ},\widetilde{\sigma}}} a^{\mathrm{SF}}_{v'\sigma}(\mathbf{r})\int \mathrm{d}\mathbf{r}' \varphi^{*}_{v'\widetilde{\sigma}}(\mathbf{r}')\varphi_{v\sigma}(\mathbf{r}')\int \mathrm{d}\mathbf{r}'' f^{\mathrm{loc,SF}}_{\mathrm{xc}}(\mathbf{r}',\mathbf{r}'')\Delta\rho^{\mathrm{SF}}_{\sigma}(\mathbf{r}'') \\
&+ \varphi_{v\sigma}(\mathbf{r})\int \mathrm{d}\mathbf{r}'\int \mathrm{d}\mathbf{r}'' g^{\mathrm{loc,SF}}_{\mathrm{xc},\sigma}(\mathbf{r},\mathbf{r}',\mathbf{r}'')\sum_{\sigma'}\Delta\rho^{\mathrm{SF}*}_{\sigma'}(\mathbf{r}')\Delta\rho^{\mathrm{SF}}_{\sigma'}(\mathbf{r}'') \\
&- \alpha_{\mathrm{EXX}}\sum_{v'=1}^{N_{\mathrm{occ},\sigma}} \varphi_{v'\sigma}(\mathbf{r})\int \mathrm{d}\mathbf{r}' v_c(\mathbf{r},\mathbf{r}')a^{\mathrm{SF}*}_{v'\widetilde{\sigma}}(\mathbf{r}')a^{\mathrm{SF}}_{v\widetilde{\sigma}}(\mathbf{r}') \\
&+ \alpha_{\mathrm{EXX}}\sum_{v'=1}^{N_{\mathrm{occ},\widetilde{\sigma}}} a^{\mathrm{SF}}_{v'\sigma}(\mathbf{r})\int \mathrm{d}\mathbf{r}' \sum_{v''=1}^{N_{\mathrm{occ},\widetilde{\sigma}}} a^{\mathrm{SF}*}_{v''\sigma}(\mathbf{r}')\varphi_{v\sigma}(\mathbf{r}')\int \mathrm{d}\mathbf{r}'' v_c(\mathbf{r}',\mathbf{r}'')\varphi^{*}_{v'\widetilde{\sigma}}(\mathbf{r}'')\varphi_{v''\widetilde{\sigma}}(\mathbf{r}'').
\end{aligned}
\tag{3.43}
$$

Here $\Delta\rho^{\mathrm{SF}}_{\sigma}(\mathbf{r}) = \sum_{v=1}^{N_{\mathrm{occ},\widetilde{\sigma}}}\varphi^{*}_{v\widetilde{\sigma}}(\mathbf{r})a^{\mathrm{SF}}_{v\sigma}(\mathbf{r})$. We have used the following definition for the functional derivative of the spin-flip exchange-correlation kernel with respect to the electron density [102, 104]:

$$g_{\mathrm{xc},\sigma}^{\mathrm{loc,SF}}(\mathbf{r},\mathbf{r}',\mathbf{r}'') = \begin{cases} -\left.\dfrac{V_{\mathrm{xc},\uparrow}^{\mathrm{loc}}(\mathbf{r}'') - V_{\mathrm{xc},\downarrow}^{\mathrm{loc}}(\mathbf{r}'')}{\left[\rho_\uparrow(\mathbf{r}'') - \rho_\downarrow(\mathbf{r}'')\right]^2}\right|_{(\rho^0,\nabla\rho^0)} \delta(\mathbf{r}'',\mathbf{r})\delta\left(\mathbf{r}'',\mathbf{r}'\right) \\ \quad + \left.\dfrac{f_{\mathrm{xc},\uparrow\uparrow}^{\mathrm{loc}}(\mathbf{r}'',\mathbf{r}) - f_{\mathrm{xc},\downarrow\uparrow}^{\mathrm{loc}}(\mathbf{r}'',\mathbf{r})}{\rho_\uparrow(\mathbf{r}'') - \rho_\downarrow(\mathbf{r}'')}\right|_{(\rho^0,\nabla\rho^0)} \delta\left(\mathbf{r}'',\mathbf{r}'\right), \quad \sigma = \uparrow \\ \left.\dfrac{V_{\mathrm{xc},\uparrow}^{\mathrm{loc}}(\mathbf{r}'') - V_{\mathrm{xc},\downarrow}^{\mathrm{loc}}(\mathbf{r}'')}{\left[\rho_\uparrow(\mathbf{r}'') - \rho_\downarrow(\mathbf{r}'')\right]^2}\right|_{(\rho^0,\nabla\rho^0)} \delta(\mathbf{r}'',\mathbf{r})\delta\left(\mathbf{r}'',\mathbf{r}'\right) \\ \quad + \left.\dfrac{f_{\mathrm{xc},\uparrow\downarrow}^{\mathrm{loc}}(\mathbf{r}'',\mathbf{r}) - f_{\mathrm{xc},\downarrow\downarrow}^{\mathrm{loc}}(\mathbf{r}'',\mathbf{r})}{\rho_\uparrow(\mathbf{r}'') - \rho_\downarrow(\mathbf{r}'')}\right|_{(\rho^0,\nabla\rho^0)} \delta\left(\mathbf{r}'',\mathbf{r}'\right), \quad \sigma = \downarrow \end{cases} . \tag{3.44}$$

3.9.2 Verification and Validation of the Implementation of WEST-TDDFT

Formaldehyde Molecule

We verified the implementation of time-dependent density functional theory (TDDFT) in the WEST code (referred to as WEST-TDDFT hereafter) by applying it to the formaldehyde molecule, which is routinely used as a benchmark for TDDFT. Geometry relaxation was performed in excited states $^1A''$, $^1B_2$, and $^3A''$ with the Tamm-Dancoff approximation (TDA), and the resulting atomic geometries and the adiabatic excitation energies are summarized in Table 3.5 and compared with the TDDFT-TDA results reported in literature [17]. The Quantum ESPRESSO code [139, 140] was employed for the ground-state DFT calculations, with the PBE functional [31] and the SG15 optimized norm-conserving Vanderbilt (ONCV) pseudopotentials [141, 142]. The dimensions of the supercell were set to 20 Å$\times$ 20 Å$\times$ 20 Å. The energy cutoff of the plane-wave basis was set to 90 Ry. The force convergence criterion for geometry relaxation was set as 0.01 eV Å^{-1}. As shown in Table 3.5, the results obtained using WEST-TDDFT agree very well with the TDDFT results reported in literature [17].

Table 3.5: Equilibrium structures and adiabatic excitation energies, denoted as E_{AE} (in eV), for formaldehyde were calculated using WEST-TDDFT and compared with values from the literature [17]. Both sets of calculations employed the Tamm-Dancoff approximation (TDA) and the PBE functional. Bond lengths are provided in Å, while angles are in degrees. Φ represents the out-of-plane angle.

State	R_{CO}	R_{CH}	$\angle_{\mathrm{HCH}}$	Φ	E_{AE}	Reference
$^1A_1$ (Ground state)	1.2065	1.1162	115.98	0		WEST-TDDFT
	1.211	1.118	116.1	0		Ref. 17
$^1A''$	1.3040	1.1009	117.13	30.63	3.544	WEST-TDDFT
	1.308	1.103	116.8	30.0	3.53	Ref. 17
$^1B_2$	1.2019	1.1133	122.03	0	5.776	WEST-TDDFT
	1.204	1.115	119.0	0	5.70	Ref. 17
$^3A''$	1.3028	1.1057	113.19	42.77	2.686	WEST-TDDFT
	1.305	1.108	113.7	43.2	2.67	Ref. 17

NV^- in Diamond

To verify our implementation of WEST-TDDFT, we compared TDDFT-TDA gradients of the vertical excitation energy obtained from the analytical expressions to those calculated from numerical differentiation for the triplet excited state ^3E (Table 3.6) and singlet excited states ^1E and $^1A_1$ (Table 3.7) of the NV^- in diamond. The triplet excited state ^3E was studied using spin-conserving TDDFT while the singlet excited states ^1E and $^1A_1$ were studied using spin-flip TDDFT. The NV^- center was simulated in a conventional $(2 \times 2 \times 2)$ supercell of diamond containing 63 atoms. The derivatives of the vertical excitation energy were calculated with respect to the atomic coordinates of carbon atoms C29, C42, and C56, which are the three carbon atoms connected to the vacancy site. The gradients of the ^3E state were computed at the optimized geometry of the ^3E state, and the gradients of the ^1E and $^1A_1$ states were computed at the optimized geometry of the ^1E state; both geometries were obtained using TDDFT with the PBE functional. The numerical gradients were computed using a finite difference approach with a displacement of 0.007136 Å. The Quantum ESPRESSO code [139, 140] was employed for the ground-state DFT calculations, with the LDA [30], PBE [31] or DDH [33, 34] functional, the SG15 ONCV pseudopotentials [141, 142],

Table 3.6: Analytical and numerical gradients of the vertical excitation energy of the ^3E excited state of the NV^- in diamond obtained using TDDFT with the LDA, PBE, and DDH functional. C29, C42, and C56 are three carbon atoms connected to the vacancy site. The gradients are provided in Ry bohr^{-1}.

	Atom	Analytical gradients			Numerical gradients		
		X	Y	Z	X	Y	Z
				State ^3E			
	C29	−0.022872	0.006882	0.020531	−0.022847	0.006893	0.020535
LDA	C42	−0.001743	−0.046582	0.001106	−0.001742	−0.046578	0.001111
	C56	−0.020777	0.007246	0.023305	−0.020791	0.007248	0.023315
	C29	−0.028021	0.010382	0.015042	−0.028024	0.010373	0.015040
PBE	C42	0.000684	−0.046292	−0.001324	0.000750	−0.046226	−0.001381
	C56	−0.015312	0.010708	0.028343	−0.015318	0.010704	0.028353
	C29	−0.038475	0.017117	0.008861	−0.038528	0.017107	0.008816
DDH	C42	0.001024	−0.049392	−0.001741	0.001049	−0.049284	−0.001756
	C56	−0.009310	0.017345	0.038643	−0.009267	0.017337	0.038696

and a plane-wave energy cutoff of 60 Ry. To prevent the numerical instabilities in the spin-flip TDDFT calculations, we set values of $f_{\text{xc}}^{\text{loc,SF}}$ to zero on a grid point $\mathbf{r}_0$ if the absolute value of the spin density $\rho_{\uparrow}^0(\mathbf{r}_0) - \rho_{\downarrow}^0(\mathbf{r}_0)$ on this point is smaller than 1×10^{-3}. As shown in Table 3.6 and Table 3.7, the analytical and numerical gradients agree very well with each other.

3.9.3 Details on the Scalability of WEST-TDDFT

We present an assessment of the performance and scalability of the WEST-TDDFT code on both CPU and GPU nodes, using the Perlmutter supercomputer at the National Energy Research Scientific Computing Center (NERSC). The CPU nodes of Perlmutter are equipped with two AMD EPYC Milan CPUs, with a theoretical peak double-precision (FP64) performance of 5.0 TFLOPS (tera floating-point operations per second) per node. The GPU nodes of Perlmutter are equipped with one AMD EPYC Milan CPU and four NVIDIA A100 GPUs, with a theoretical peak FP64 performance of 39.0 TFLOPS per node, or 78.0 TFLOPS if the acceleration provided by the tensor cores is used. The latter are specialized computing units

Table 3.7: Analytical and numerical gradients of the vertical excitation energy of the ^1E and $^1A_1$ excited states of the NV^- in diamond obtained using TDDFT with the LDA, PBE, and the DDH functional. C29, C42, and C56 are three carbon atoms connected to the vacancy site. The gradients are provided in Ry bohr^{-1}.

	Atom	Analytical gradients			Numerical gradients		
		X	Y	Z	X	Y	Z
				State ^1E			
	C29	0.002100	0.002938	0.002176	0.002100	0.002946	0.002175
LDA	C42	0.008544	−0.014794	−0.009486	0.008533	−0.014795	−0.009471
	C56	−0.002373	0.003749	−0.001157	−0.002368	0.003764	−0.001141
	C29	0.004743	0.002861	0.006857	0.004695	0.002894	0.006824
PBE	C42	0.014139	−0.024152	−0.014744	0.014091	−0.023985	−0.014677
	C56	−0.006685	0.003664	−0.003715	−0.006630	0.003676	−0.003677
	C29	0.008305	0.003743	0.013414	0.008263	0.003796	0.013369
DDH	C42	0.020372	−0.035543	−0.020950	0.020291	−0.035246	−0.020892
	C56	−0.012993	0.004753	−0.006982	−0.012924	0.004808	−0.006935
				State $^1A_1$			
	C29	−0.009928	0.000453	−0.017409	−0.009918	0.000466	−0.017420
LDA	C42	0.008165	−0.001599	−0.007678	0.008194	−0.001603	−0.007695
	C56	0.017676	0.000242	0.009756	0.017684	0.000260	0.009758
	C29	−0.008408	0.005775	−0.014338	−0.008413	0.005788	−0.014333
PBE	C42	0.009275	−0.003203	−0.009050	0.009423	−0.003439	−0.009179
	C56	0.014471	0.005658	0.008310	0.014469	0.005670	0.008314
	C29	−0.005726	0.009158	−0.012240	−0.005730	0.009176	−0.012243
DDH	C42	0.010072	−0.003079	−0.009980	0.010186	−0.003292	−0.010082
	C56	0.012301	0.009101	0.005671	0.012300	0.009121	0.005673

optimized for matrix multiplications. Comparing the workflows of full-frequency G_0W_0 and TDDFT implemented in WEST, we observe a higher utilization rate of the tensor core in the former because its implementation involved more matrix multiplication operations.

To benchmark the implementation of WEST-TDDFT, we considered the first excited state of the NV^- in diamond, whose ground-state DFT calculations were performed using the Quantum ESPRESSO [139, 140] code (version 7.2), the SG15 optimized norm-conserving Vanderbilt (ONCV) pseudopotentials [141, 142], and the DDH functional [33, 34]. A kinetic energy cutoff of 60 Ry was used for the plane-wave basis set. The Brillouin zone was sampled at the *Gamma* point. In the TDDFT calculations, we used the numerical approximations discussed in Chapter 3.3, namely the ACE method with $N_{\mathrm{ACE}} = 4N_{\mathrm{occ}}$, the Wannier localization with $S_{\mathrm{thr}} = 10^{-3}$, and the inexact Krylov subspace approach with $\lambda_{\mathrm{thr}} = 10^{-4}$.

The performance of the CPU version of WEST-TDDFT is presented in Figure 3.8 (a) for the NV^- center in a conventional $(4 \times 4 \times 4)$ supercell of diamond containing 511 atoms. The figure displays the total wall clock time, including time spent on I/O operations, and breaks it down into the time required to compute energy or forces. For the part of the code that computes forces (see blue upward triangles), we observe very good strong scaling up to 128 nodes, i.e., a scaling that closely aligns with the ideal one (indicated by the black dashed line). For the part of the code that computes energies (see red downward triangles), we observe good scaling up to 32 nodes, after which the parallel efficiency drops because the computational time becomes small and comparable to the overheads caused by internode MPI communications and I/O operations. Nonetheless, the overall strong scaling of WEST-TDDFT (corresponding to the time required to compute both energies and forces, and represented by orange circles), remains close to ideal, as the computation of forces is approximately one order of magnitude more expensive than the computation of energy.

In Figure 3.8 (b), we examine the performance of the GPU version of WEST-TDDFT for the same test system of 511 atoms. Again, the code exhibits nearly ideal scaling up to 128

GPU nodes (512 GPUs), primarily due to the highly efficient implementation of the forces. Similar to the CPU case, the scaling of the energy part, which has a lower computation-to-communication ratio, is inferior to that of the forces. Comparing Figure 3.8 (a) and (b), we observe that the GPU version of WEST-TDDFT achieves a 4.8× overall speedup over its CPU counterpart on the same number of nodes, with the computation of the energy and the forces accelerated by 3.7× and 5.2×, respectively. The higher speedup achieved in computing the forces is due to the larger amount of computations involved in this part. We note that the attained speedup falls short of the theoretical speedup estimated by considering the ratio between the theoretical peak performance of the GPU and CPU nodes. This discrepancy is primarily attributed to (i) the communication overhead when summing over the bands, which becomes necessary each time the operators on the left-hand side of Eq. (3.1) are applied, and (ii) the overhead associated with reading the ground state wavefunctions from the file system and writing the excited state wavefunctions to the file system. The scalability of the GPU version of WEST-TDDFT is further demonstrated in Figure 3.8 (c) for the NV^- center in a $(5 \times 5 \times 5)$ supercell of diamond containing 999 atoms. Remarkably, WEST-TDDFT scales to 512 GPU nodes (2048 GPUs), with the forces part of the code exhibiting near-perfect strong scaling.

3.9.4 Excited-State Geometry Relaxation of the SiV^0 in Diamond

The geometry relaxation was carried out in the triplet excited state for SiV^0 in diamond using TDDFT-TDA with the PBE and DDH functional. We used $(3 \times 3 \times 3)$, $(4 \times 4 \times 4)$, and $(5 \times 5 \times 5)$ conventional supercells of diamond that contain 215, 511, and 999 atoms, respectively. Results on relaxed geometries are summarized in Table 3.8. The zero-phonon line (E_{ZPL}) and the Franck-Condon shift in electronic excited states ($E_{\mathrm{FC,\ ES}}$) computed using TDDFT with the DDH functional agree well with the ΔSCF results reported in Ref. 157.

Franck-Condon shifts in electronic excited states $E_{\mathrm{FC,\ ES}}$ and electronic ground states

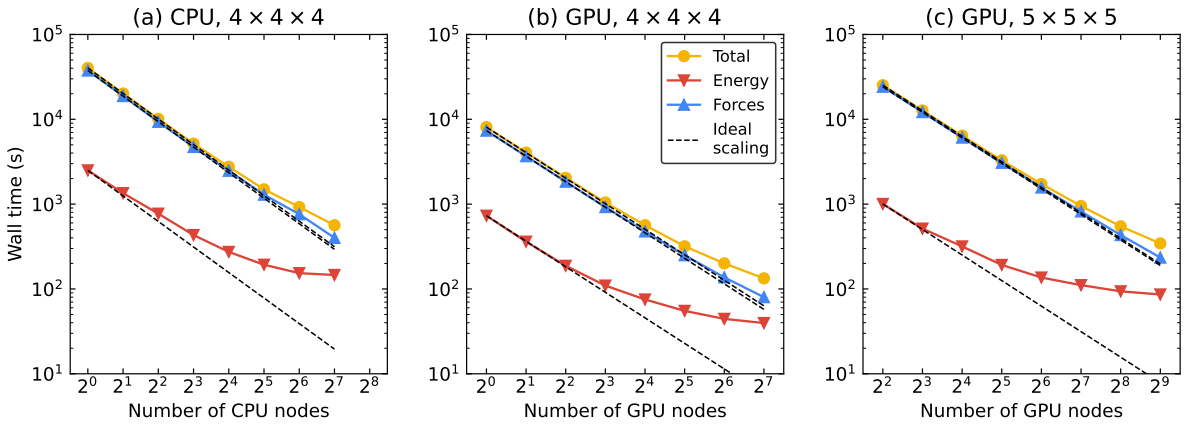

Figure 3.8: Strong scaling of the WEST-TDDFT code on CPU and GPU nodes of NERSC/Perlmutter supercomputing architecture. The scaling tests were carried out on the electronic properties of the first excited state of the NV^- center in diamond, simulated using the DDH functional and 60 Ry of kinetic energy cutoff. (a) NV^- in a conventional $(4 \times 4 \times 4)$ supercell of diamond. The calculations were carried out on CPU nodes. (b) NV^- in a conventional $(4 \times 4 \times 4)$ supercell of diamond. The calculations were carried out on GPU nodes. (c) NV^- in a conventional $(5 \times 5 \times 5)$ supercell of diamond. The calculations were carried out on GPU nodes. The red downward triangles and blue upward triangles represent the time measured to compute the vertical excited state energy and forces, respectively. The yellow circles represent the total wall clock time, including the time spent on I/O operations. The black dashed lines indicate ideal strong scaling.

$E_{\mathrm{FC,\,GS}}$, and mass-weighted atomic displacements ΔQ computed using TDDFT with the PBE functional exhibit non-negligible finite-size effects, while those obtained with the DDH functional do not. This discrepancy stems from different degrees of localization of the excited state orbitals obtained with the PBE and DDH functional. The exciton is more delocalized with the PBE functional, and its radius increases as the cell size increases, and as a consequence, the magnitude of geometry displacements decreases. The exciton obtained with the DDH functional is almost fully localized within the $(3 \times 3 \times 3)$ supercell, and increasing the cell size brings a negligible change to the magnitude of geometry displacements.

Table 3.8: Computed zero-phonon line energies E_{ZPL} (eV), Franck-Condon shifts (eV) in electronic excited states $E_{\mathrm{FC,\ ES}}$ and electronic ground states $E_{\mathrm{FC,\ GS}}$, mass-weighted atomic displacements ΔQ (amu$^{1/2}$ Å), and Si−C bond lengths (Å) for SiV^0 in diamond.

Method	Cell size	E_{ZPL}	$E_{\mathrm{FC,\ GS}}$	$E_{\mathrm{FC,\ ES}}$	ΔQ	d (Si−C)
TDDFT (PBE)	$(3\times3\times3)$	1.501	0.236	0.265	0.510	1.965, 2.051
TDDFT (PBE)	$(4\times4\times4)$	1.299	0.145	0.142	0.412	1.966, 2.029
TDDFT (PBE)	$(5\times5\times5)$	1.124	0.079	0.086	0.289	1.970, 2.005
TDDFT (DDH)	$(3\times3\times3)$	1.518	0.314	0.338	0.581	1.952, 2.052
TDDFT (DDH)	$(4\times4\times4)$	1.403	0.298	0.294	0.590	1.953, 2.050
ΔSCF (HSE) [157]	$(4\times4\times4)$	1.34		0.258		
Expt. [158]		1.31				

3.9.5 Extrapolation of Vertical Excitation Energies of the SiV^0 in Diamond

Defect Excitation

The vertical excitation energies (VEEs) for excited states based on transitions among defect orbitals are summarized in Figure 3.9 and Figure 3.10 for triplet and singlet excited states, respectively. The VEEs were computed using TDDFT with the PBE and DDH functional at the optimized ground state atomic geometry and were extrapolated to the dilute limit using linear functions of $1/N_{\mathrm{atoms}}$, where N_{atoms} is the number of atoms in the supercell. The conventional $(2\times2\times2)$, $(3\times3\times3)$, $(4\times4\times4)$, and $(5\times5\times5)$ diamond supercells were used in the calculations of VEEs, which contains 63, 215, 511, and 999 atoms, respectively.

The VEEs of singlet excited states ^1E_g and $^1A_{1g}$ depend weakly on N_{atoms} since the composition of their respective many-body wavefunctions mainly involve transitions from $e_{gx}(e_{gy})$ orbitals to $\overline{e}_{gx}(\overline{e}_{gy})$ orbitals, which are all within the band gap of diamond. In contrast, the VEEs of triplet excited states $^3A_{2u}$, ^3E_u and $^3A_{1u}$ exhibit a linear dependence on $1/N_{\mathrm{atoms}}$, which stems from the dipole-dipole interaction between the localized excitons in periodic images. The triplet excited states computed with the DDH functional show a clearer linear relationship for VEEs than those with the PBE functional. This may be due to more localized excitons computed with the DDH functional, which are better described

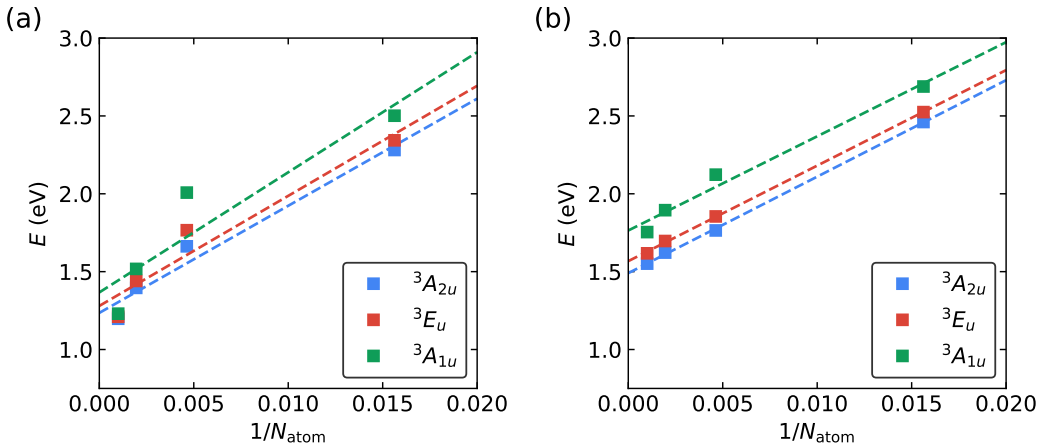

Figure 3.9: Vertical excitation energies (VEEs) of the triplet excited states ${}^3A_{2u}$ (blue), ${}^3E_u$ (red) and ${}^3A_{1u}$ (green) for the SiV^0 in diamond as a function of the number of atoms N_{atoms} in the supercell. The VEEs were obtained using spin-conserving TDDFT calculations with (a) the PBE functional and (b) the DDH functional. Dashed lines show linear extrapolations of VEEs as a function of $1/N_{\text{atoms}}$.

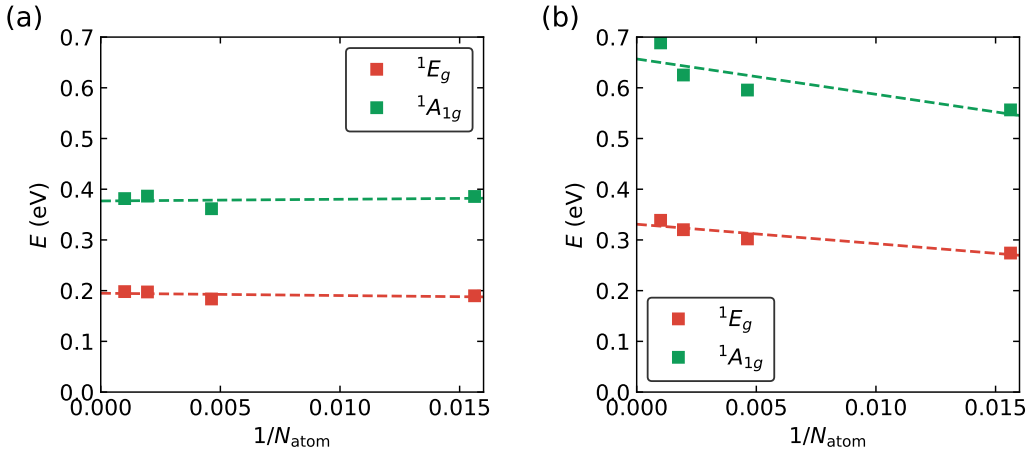

Figure 3.10: Vertical excitation energies (VEEs) of the singlet excited states ${}^1E_g$ (red) and ${}^1A_{1g}$ (green) for the SiV^0 in diamond as a function of the number of atoms N_{atoms} in the supercell. The VEEs were obtained using spin-flip TDDFT calculations with (a) the PBE functional and (b) the DDH functional. Dashed lines show linear extrapolations of VEEs as a function of $1/N_{\text{atoms}}$.

by the model accounting for the dipole-dipole interaction in periodic images.

Bound Exciton

To extrapolate the VEE of the bound exciton state, which is based on the transition from the valence band maximum (VBM) to the $\overline{e}_{gs}/\overline{e}_{gy}$ defect orbitals, we used the fitting function

$$E_{\mathrm{VE}}(L) = E_{\mathrm{VE}}(L=\infty) - \frac{A}{L}\exp\left(-\frac{L}{D}\right) + \frac{B}{L^3}. \tag{3.45}$$

where $L \propto N_{\mathrm{atoms}}^{1/3}$ is the length of the cubic supercell, A and B are fitting parameters determined by the strength of the electron-hole interaction and the dipole-dipole interaction, respectively. D is a screening parameter related to the fact that the electron-hole interaction does not depend on L if L is much larger than the radius of the bound exciton.

To obtain the fitting parameter B, we decompose the VEE into two terms. The first term is $e_{e_g} - e_{\mathrm{VBM}}$, which can be approximately viewed as the fundamental gap for the bound exciton. The second term is $e_{e_g} - e_{\mathrm{VBM}} - E_{\mathrm{VE}}$, which can be approximately viewed as the exciton binding energy, i.e. the difference between the fundamental gap and the optical gap. Figure 3.11 shows the VEE, the fundamental gap, and the exciton binding energy as functions of supercell size. The fundamental gap $e_{e_g} - e_{\mathrm{VBM}}$ shows a linear dependence on $1/L^3$, and the slope yields $B = 331.8$ eV Å^3 for the PBE functional and $B = 398.3$ eV Å^3 for the DDH functional.

To obtain the fitting parameter D, which is the effective screening length for the bound exciton, we adopted the model proposed in Ref. 160. The screening length is expressed as

$$D = \alpha \frac{m_e \varepsilon_\infty}{m^*} D_{\mathrm{H}}, \tag{3.46}$$

where $D_{\mathrm{H}} = 1.9$ Å is the screening length of the hydrogen atom obtained from DFT calculations [160], $m^* = 0.7m_e$ ($2.12m_e$) is the effective mass of light (heavy) hole in VBM, $\varepsilon_\infty = 5.7$ is the dielectric constant of diamond. $\alpha = 1.87$ is derived from the comparison with experiments to account for the fact that the hole orbital is expelled from the central

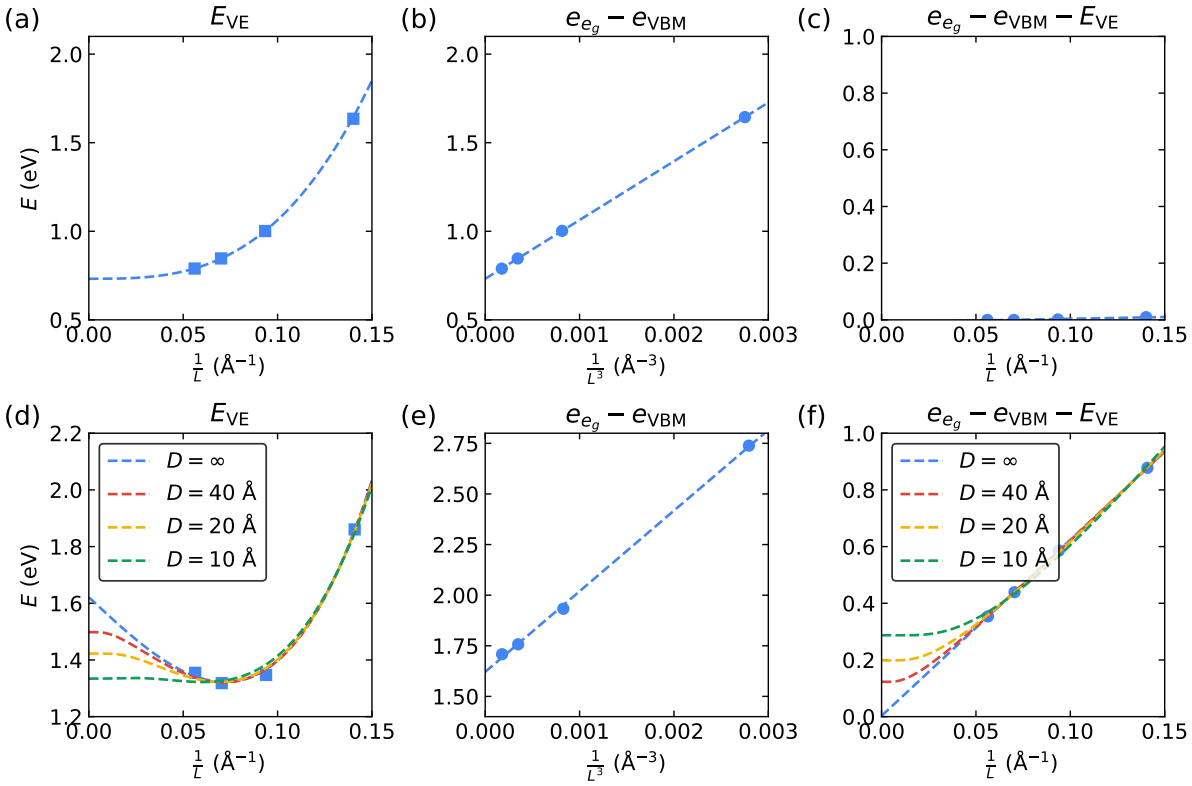

Figure 3.11: Extrapolation of the vertical excitation energy E_{VE} for the bound exciton of SiV^0 in diamond to the dilute limit. E_{VE} obtained from TDDFT with the PBE functional and the DDH functional are displayed in (a) and (d) as a function of $\frac{1}{L}$. The values of E_{VE} are fitted using Eq. (3.45), and the fitting lines are shown as dashed lines. The energy difference of the defect orbital e_g and the valence band maximum (VBM), $e_{e_g} - e_{\mathrm{VBM}}$, obtained using the PBE functional and the DDH functional are displayed in (b) and (e) as a function of $\frac{1}{L^3}$. The exciton binding energy, $e_{e_g} - e_{\mathrm{VBM}} - E_{\mathrm{VE}}$, obtained using the PBE functional and the DDH functional are displayed in (c) and (f) as a function of $\frac{1}{L}$. Details on the fitting process can be found in Section 3.9.5.

region of the defect as the e_g orbital of the electron already occupies this region [160]. With these parameters, the screening length is estimated as $D \in [10, 40]$ Å.

To obtain the fitting parameter A, we fitted the exciton binding energy $e_{e_g} - e_{\mathrm{VBM}} - E_{\mathrm{VE}}$ as $\frac{A}{L}\exp\left(-\frac{L}{D}\right)$. With $D = \infty$, the exciton binding energy was fitted as a function versus against $1/L$, and the slope yields $A = 0.12$ eV Å for the PBE functional and $A = 6.21$ eV Å for the DDH functional. The intercept of the linear function is almost zero, pointing to the fact that the exciton binding energy is zero for an infinite large exciton whose screening length

is $D = \infty$. It is worth noting that the exciton binding energy predicted by TDDFT with the PBE functional is approximately zero because the Coulomb interaction between the electron and the hole of the exciton is absent with the PBE functional, which points to the necessity of using the DDH functional in TDDFT calculations. By setting $D = \infty$ in Eq. (3.45), we obtained $E_{\mathrm{VE}}(L = \infty) = 1.621$ eV, which corresponds to the charge transition level of the $\mathrm{SiV}^- + h^+(\text{at VBM}) \rightarrow \mathrm{SiV}^0$ process. With $D \in [10, 40]$ Å, we obtained $A \in [6.41, 8.65]$ eV Å, which yields $E_{\mathrm{VE}}(L = \infty) \in [1.33, 1.50]$ eV.

3.9.6 Extrapolation of Vertical Excitation Energies of the $V_O{}^0$ in MgO

Defect Excitation

The vertical excitation energies (VEEs) for excited states based on transitions among defect orbitals are summarized in Figure 3.12 for triplet and singlet excited states. The VEEs were computed using TDDFT with the PBE functional and the DDH functional at the optimized ground state atomic geometry and were extrapolated to the dilute limit as linear functions of $1/N_{\mathrm{atoms}}$, where N_{atoms} is the number of atoms in the supercell. The primitive $(3 \times 3 \times 3)$, $(4 \times 4 \times 4)$, and $(5 \times 5 \times 5)$ MgO supercells containing 53, 127, and 249 atoms, and the conventional $(2 \times 2 \times 2)$, $(3 \times 3 \times 3)$, and $(4 \times 4 \times 4)$ MgO supercells containing 63, 215, and 511 atoms were used in the calculations of VEEs.

The VEEs of singlet and triplet excited states ${}^1T_{1u}$ and ${}^3T_{1u}$ exhibit a linear dependence on $1/N_{\mathrm{atoms}}$, which stems from the dipole-dipole interaction between the localized excitons in periodic images.

Bound Exciton

The VEE of the bound exciton state of $\mathrm{V_O^0}$ in MgO, which is based on the transition from the a_{1g} defect orbital to the conduction band minimum (CBM), is extrapolated using the

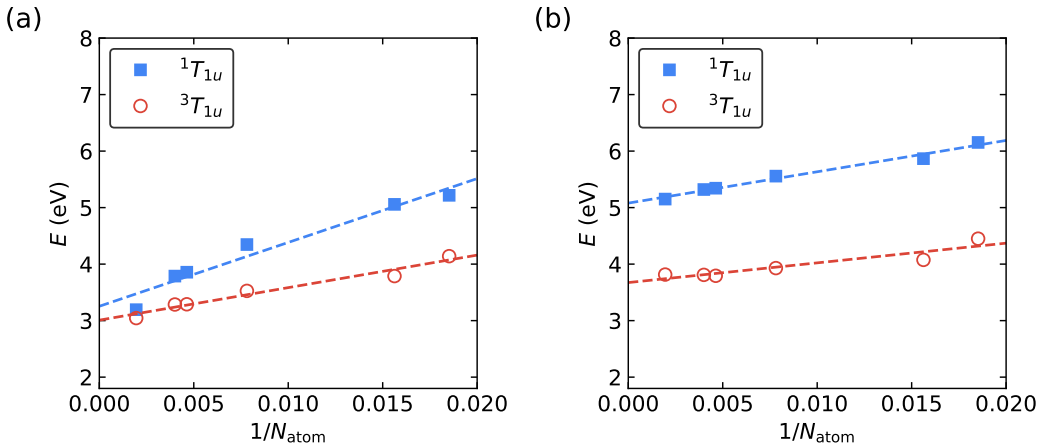

Figure 3.12: Vertical excitation energies (VEEs) of the singlet and triplet excited states $^1T_{1u}$ (blue squares) and $^3T_{1u}$ (red circles) for the V_O^0 in MgO as a function of the number of atoms, N_{atoms}, in the supercell. The VEEs were obtained using TDDFT calculations with (a) the PBE functional and (b) the DDH functional. Dashed lines show linear extrapolations of VEEs based on $1/N_{\text{atoms}}$.

same strategy as the one used for the SiV^0 in diamond, as summarized in Section 3.9.5. For conventional supercells, L is simply the length of the cubic supercell. For primitive supercells, L is defined as $L = (N_{\text{atoms}}/8)^{1/3} L_0$, where $L_0 = 4.26$ Å is the lattice constant of MgO obtained with the DDH functional. $A = 10.60$ eV Å was obtained for the DDH functional by fitting the exciton binding energy $e_{\text{CBM}} - e_{a_{1g}} - E_{\text{VE}}$ as a linear function of $1/L$ with the intercept fixed as zero. $B = 462.2$ eV Å^3 was obtained for the DDH functional by fitting $e_{\text{CBM}} - e_{a_{1g}}$ as a linear function of $1/L^3$. The screening length is estimated as $D \in [21, 42]$ Å using Eq. (3.46), with $\varepsilon_\infty = 2.96$ [33], $m^* = 0.4 m_e$ [178], and an estimated $\alpha \in [1.5, 3]$. With these parameters, the vertical excitation energy of the bound exciton state is estimated to be $[4.41, 4.58]$ eV for the DDH functional.

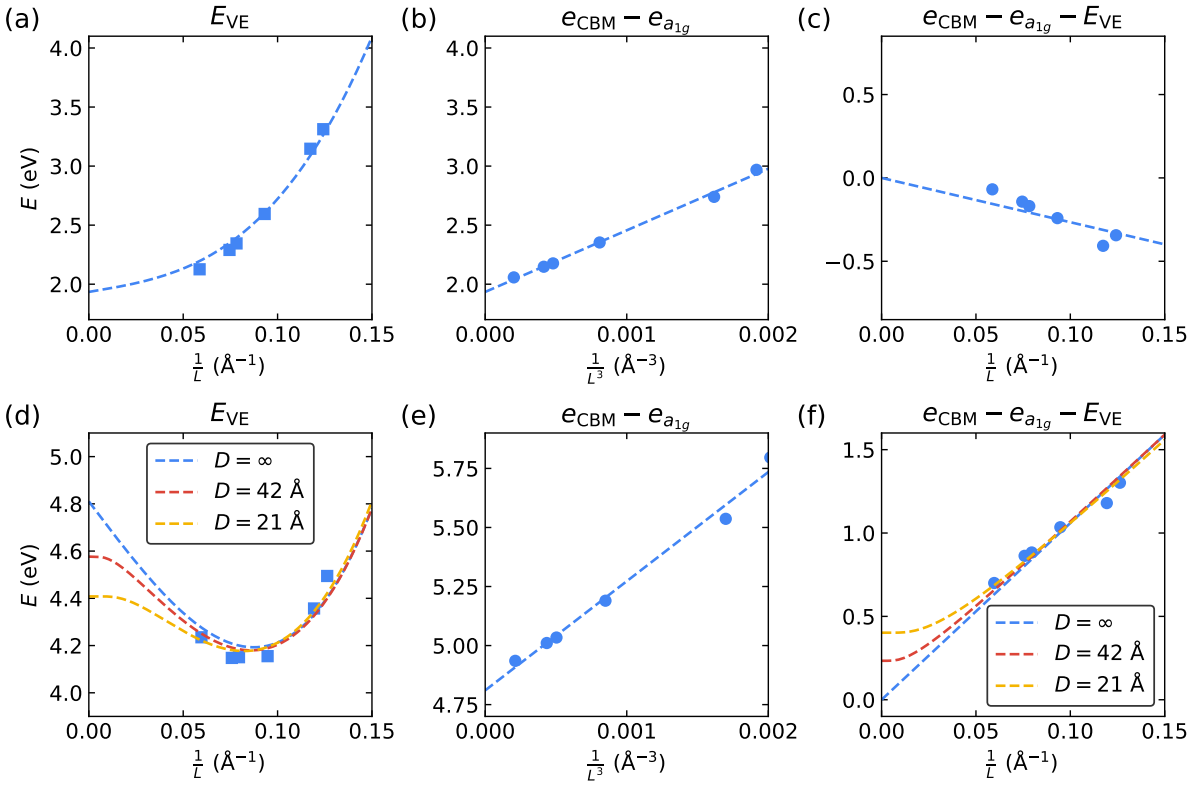

Figure 3.13: Extrapolation of the vertical excitation energy E_{VE} for the bound exciton of V_O^0 in MgO to the dilute limit. E_{VE} obtained from TDDFT with the PBE functional and the DDH functional are displayed in (a) and (d) as a function of $\frac{1}{L}$. The values of E_{VE} are fitted using Eq. (3.45), and the fitting lines are shown as dashed lines. The energy difference of the conduction band minimum (CBM) and the defect orbital a_{1g}, $e_{\mathrm{CBM}} - e_{a_{1g}}$, obtained using the PBE functional and the DDH functional are displayed in (b) and (e) as a function of $\frac{1}{L^3}$. The exciton binding energy, $e_{\mathrm{CBM}} - e_{a_{1g}} - E_{\mathrm{VE}}$, obtained using the PBE functional and the DDH functional are displayed in (c) and (f) as a function of $\frac{1}{L}$. Details on the fitting process can be found in Section 3.9.6.

Table 3.9: Computed absorption energy E_{Abs} (eV), emission energy E_{Emi}, Franck-Condon shifts (eV) in electronic excited states $E_{\mathrm{FC,\,ES}}$ and electronic ground states $E_{\mathrm{FC,\,GS}}$, and mass-weighted atomic displacements ΔQ (amu$^{1/2}$ Å) for V_O^0 in MgO. Absorption energies were computed using TDDFT with the PBE functional and extrapolated to the dilute limit. FC shifts and displacements were computed using TDDFT with the PBE functional and a conventional $(3 \times 3 \times 3)$ supercell with 215 atoms.

States	E_{Abs}	E_{Emi}	$E_{\mathrm{FC,\,GS}}$	$E_{\mathrm{FC,\,ES}}$	ΔQ
$^1T_{1u}$	3.254	2.307	0.410	0.537	1.694
$^3T_{1u}$	3.008	2.387	0.263	0.358	2.224
Bound Exciton	1.934	1.444	0.182	0.308	0.659

CHAPTER 4

PHOTOLUMINESCENCE SPECTRA OF POINT DEFECTS IN SEMICONDUCTORS: VALIDATION OF FIRST-PRINCIPLES CALCULATIONS

This chapter is adapted with permission from Y. Jin, M. Govoni, G. Wolfowicz, S. E. Sullivan, F. J. Heremans, D. D. Awschalom, and G. Galli. Physical Review Materials 5(8), 084603 (2021). https://doi.org/10.1103/PhysRevMaterials.5.084603.

Optically and magnetically active point defects in semiconductors are interesting platforms for the development of solid-state quantum technologies. Their optical properties are usually probed by measuring photoluminescence spectra, which provide information on excitation energies and the interaction of electrons with lattice vibrations. In this Chapter, we present a combined computational and experimental study of photoluminescence spectra of defects in diamond and SiC, aimed at assessing the validity of theoretical and numerical approximations used in first-principles calculations, including the use of the Franck-Condon principle and the displaced harmonic oscillator approximation. We focus on prototypical examples of solid-state qubits, the divacancy centers in SiC and the nitrogen-vacancy in diamond, and we report computed photoluminescence spectra as a function of temperature that are in very good agreement with the measured ones. As expected we find that the use of hybrid functionals leads to more accurate results than semilocal functionals. Interestingly, our calculations show that constrained density functional theory (CDFT) and time-dependent hybrid DFT perform equally well in describing the excited state potential energy surface of triplet states; our findings indicate that CDFT, a relatively cheap computational approach, is sufficiently accurate for the calculations of photoluminescence spectra of the defects studied here. Finally, we find that only by correcting for finite-size effects and extrapolating to the

dilute limit, one can obtain a good agreement between theory and experiment. Our results provide a detailed validation protocol of first-principles calculations of photoluminescence spectra, necessary both for the interpretation of experiments and for robust predictions of the electronic properties of point defects in semiconductors.

4.1 Introduction

The last two decades have witnessed the rapid development of quantum information technologies based on solid-state platforms, in particular optically addressable spin-defects in semiconductors and insulators [27, 179–181]. The optoelectronic properties of point defects used to realize qubits are most often probed by measuring photoluminescence (PL) spectra, which yield information about excitation energies and the interaction of the excited electrons with lattice vibrations.

A PL experiment collects the photons emitted when an excited electron radiatively decays to the ground state (GS), and PL spectra of defects usually exhibit a narrow zero-phonon line (ZPL) and a broad phonon side band (PSB); the latter originates from decay processes that involve structural relaxation and thus the coupling of electrons and phonons. The strength of such coupling can be inferred from the Debye-Waller factor (DWF) [182] that is proportional to the ratio between the emission intensity of the ZPL and that of the entire spectrum. Applications that require photon coherence or interference benefit from point defects whose PL signal exhibits a high DWF, indicating a weak coupling between phonons and electrons. The average number of phonons emitted during an electronic transition is instead quantified by the Huang-Rhys factor (HRF) [60, 182], which can be estimated from measured spectra from the logarithm of the DWF.

As for many properties of condensed systems, Density Functional Theory (DFT) has turned out to be a valuable tool to compute PL spectra, which are used to interpret experiments as well as to provide predictions of the fingerprints of specific defects in materi-

als [77–79]. For example, first principles spectra based on DFT have been recently reported for nitrides, e.g., GaN [183, 184], AlN [185], and hexagonal born nitride (h-BN) [186–191], diamond [59, 82, 114, 115, 192–198], silicon carbide (SiC) [199–202], and monolayers of transition metal dichalcogenides (TMDC) [203]. These studies have been performed with several useful computational approaches; however, a systematic assessment of the theoretical and numerical approximations adopted in PL calculations has not yet been conducted.

In this work, we present a joint theoretical and experimental study of the PL spectra of prototypical spin defects in diamond and SiC. We focus on the negatively charged nitrogen-vacancy (NV^-) in diamond [62, 63, 65, 147, 182, 204] and the neutral divacancy ($V_{Si}V_C^0$, abbreviated as VV^0) centers in hexagonal 4H-SiC, which have been recently suggested as promising platforms for quantum sensors [64, 68, 69, 153]. While the NV^- center has just one possible geometrical configuration in the GS, the VV^0 centers may attain four different geometries due to the layered structure of 4H-SiC, giving rise to different PL signals. We discuss the comparison between theoretical and experimental PL spectra as a function of temperature, as well as HRFs and DWFs, and we present a detailed assessment of the theoretical and numerical approximations involved in first-principles calculations. These approximations include the choice of the density functional, the method adopted to describe excited state (ES) potential energy surfaces, finite supercell size, and approximations based on the Franck-Condon (FC) principle and the displaced harmonic oscillator (DHO) approximation.

We compare constrained DFT (CDFT) [81] calculations of ES potential energy surfaces of triplet states with those carried out with time-dependent DFT (TDDFT), which enable the description of the ES as a linear combination of multiple Slater determinants. In our TDDFT calculations, we use hybrid functionals with the fraction of exact exchange determined by the dielectric constant of the system; based on recent studies, these calculations are expected to yield results in good agreement with the solutions of the Bethe-Salpeter equation [107, 132].

So far, TDDFT has only been employed to describe spin defects with cluster models and atomic-centered basis sets [110–112, 114, 115] and here we present a comparison between CDFT and TDDFT calculations carried out for the same supercell and using the same plane-wave basis sets and density functional. We also investigate finite size effects that affect defect-host interactions and present results for PL line shapes converged to supercells with more than 10,000 atoms, following the approach proposed by Alkauskas et al. [59, 82, 159]. Finally, we provide a qualitative assessment of the accuracy of the FC principle and the displaced harmonic oscillator (DHO) approximation. By conducting fully converged hybrid functional calculations for the electronic properties, we obtain good agreement with measured spectra over a wide temperature range, with small differences between PL line shapes obtained with phonons computed with semilocal or hybrid functionals.

The rest of the paper is organized as follows. In Chapter 4.2 we discuss the methodology for computing PL spectra using the Huang-Rhys (HR) theory within the generating function formulation, highlighting all theoretical and numerical approximations. In Chapter 4.3, we give the details of first-principles calculations and experiments. In Chapter 4.4, results on the chosen defects in SiC and diamond, including ZPLs, HRFs, DWFs, and PL line shapes are discussed. Conclusions are given in Chapter 4.5.

4.2 Theory and computational methodology

Based on Fermi's golden rule and the FC principle, the PL spectrum generated by the optical transitions from the ES to the GS potential energy surfaces is expressed as [59]:

$$L(\hbar\omega, T) = \frac{n\omega^3}{3\pi\epsilon_0 c^3 \hbar} \left|\boldsymbol{\mu}_{eg}\right|^2 \sum_i \sum_j P_{ej}(T) \left|\left\langle \Theta_{ej} \mid \Theta_{gi} \right\rangle\right|^2 \delta\left(E_{\mathrm{ZPL}} + E_{ej} - E_{gi} - \hbar\omega\right), \tag{4.1}$$

where $\boldsymbol{\mu}_{eg}$ is the electronic transition dipole moment; n is the refractive index of the material; $|\Theta^{gi}\rangle$ ($|\Theta^{ej}\rangle$) is the i-th (j-th) nuclear wavefunction of the system in the GS (ES) with

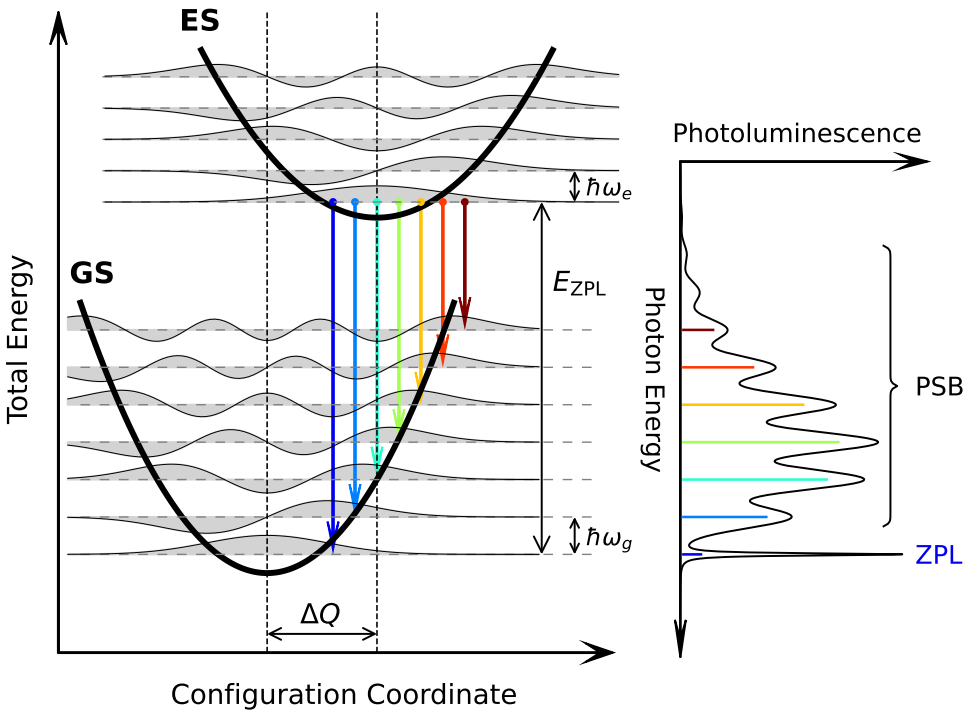

Figure 4.1: Schematic diagram illustrating optical processes leading to photoluminescence (PL) spectra. For simplicity, only one phonon mode is depicted in the diagram. Ground state (GS) and excited state (ES) potential energy curves are approximated by harmonic functions with frequency ω_g and ω_e, respectively. Vibrational energy levels and wavefunctions are shown as horizontal dashed lines and gray areas, respectively. ΔQ is the mass-weighted displacement between the local minimum of the GS and the ES energy curves. Colored arrows represent optical transitions at 0 K. The zero-phonon line (ZPL) originates from the transition between the 0-th vibrational level of the ES to the 0-th vibrational level of the GS. All other transitions contribute to the phonon sideband (PSB).

vibrational energy E_{gi} (E_{ej}); and E_{ZPL} is the energy of the ZPL (see Figure 4.1). The thermal distribution function of the vibrational energy in the ES is

$$P_{ej}(T) = \frac{e^{-\frac{E_{ej}}{k_B T}}}{\sum_j e^{-\frac{E_{ej}}{k_B T}}}, \tag{4.2}$$

where k_B is the Boltzmann constant. For an ordered solid, under the harmonic approximation, we express the nuclear wavefunctions as products of vibrational wavefunctions:

$$|\Theta_{gi}\rangle = \prod_k |\phi_{kn_k^{gi}}\rangle, \quad |\Theta_{ej}\rangle = \prod_k |\phi_{kn_k^{ej}}\rangle, \tag{4.3}$$

where n_k^{gi} (n_k^{ej}) is the number of k-th phonons in the i-th (j-th) vibrational state of the GS (ES), and $|\phi_{kn}\rangle$ is the n-th excited state of the k-th phonon mode. The vibrational energies in the GS and ES are

$$E_{gi} = \sum_k n_k^{gi} \hbar\omega_k^g, \quad E_{ej} = \sum_k n_k^{ej} \hbar\omega_k^e, \tag{4.4}$$

where ω_k^g (ω_k^e) is the frequency of k-th phonon in the GS (ES). Note that by definition, Eq. (4.4) does not include the zero point energy, which is included in the term E_{ZPL}.

A commonly used approximation is the so-called displaced harmonic oscillator (DHO) approximation, or HR theory [60], where Eq. (4.1) is simplified by assuming that the potential energy surface of the ES and the GS are identical except for a rigid displacement due to the difference in their equilibrium structures, i.e., $\omega_k^g = \omega_k^e$ (the superscript g and e will hence be omitted), and:

$$\left|\langle \Theta_{ej} \mid \Theta_{gi} \rangle\right|^2 = \prod_k e^{-S_k} (S_k)^{n_k^{gi} - n_k^{ej}} \left(\frac{n_k^{ej}!}{n_k^{gi}!}\right) \left[L_{n_k^{ej}}^{n_k^{gi} - n_k^{ej}}(S_k)\right]^2, \tag{4.5}$$

where S_k is the partial HRF and accounts for the average number of k-th phonons that participate in the transition. L_m^{n-m} are the associated Laguerre polynomials [61]. For the calculations of PL line shapes, only the phonons of the GS are computed and used within the DHO approximation. At zero temperature, Eq. (4.1) may be further approximated by setting to zero the vibrational energy in the ES (i.e., we only consider $j = 0$, and $n_k^{e0} = 0$), namely:

$$L(\hbar\omega, T = 0) \propto \omega^3 \sum_i \left[\prod_k \frac{e^{-S_k}}{n_k^{gi}!} (S_k)^{n_k^{gi}}\right] \delta\left(E_{ZPL} - E_{gi} - \hbar\omega\right). \tag{4.6}$$

To avoid the evaluation of the overlap integrals entering Eq. (4.5) and the sum over all vibrational states of the GS and the ES, we adopt the generating function approach [205, 206] to compute PL spectra. In the DHO approximation, Eq. (4.1) can be obtained as the Fourier transform of the generating function $G(t,T)$:

$$L(\hbar\omega,T) \propto \omega^3 \int_{-\infty}^{\infty} \mathrm{d}t G(t,T) e^{i\omega t - \frac{\lambda}{\hbar}|t| - i\frac{E_{\mathrm{ZPL}}}{\hbar}t}, \tag{4.7}$$

where

$$G(t,T) = \exp\left\{ -\sum_k S_k \left[\left(1 - e^{i\omega_k t}\right) + \bar{n}_k(T) \left(2 - e^{i\omega_k t} - e^{-i\omega_k t}\right) \right] \right\}, \tag{4.8}$$

and λ accounts for the broadening of the line shape. $\bar{n}_k(T)$ is the average occupation number of the k-th phonon mode:

$$\bar{n}_k(T) = \frac{1}{e^{\frac{\hbar\omega_k}{k_B T}} - 1}. \tag{4.9}$$

In practice, one may write Eq. (4.8) as the following alternative expression:

$$G(t,T) = e^{S(t) - S(0) + C(t,T) + C(-t,T) - 2C(0,T)}, \tag{4.10}$$

where $S(t) = \sum_k S_k e^{i\omega_k t}$ and $C(t,T) = \sum_k \bar{n}_k(T) S_k e^{i\omega_k t}$ are evaluated as the Fourier transforms of the spectral densities:

$$S(\hbar\omega) = \sum_k S_k \delta\left(\hbar\omega - \hbar\omega_k\right), \tag{4.11}$$

$$C(\hbar\omega,T) = \sum_k \bar{n}_k(T) S_k \delta(\hbar\omega - \hbar\omega_k). \tag{4.12}$$

In Eqs. (4.11)–(4.12), the δ-functions are replaced by Gaussian functions with ω-dependent broadening to account for a continuum of vibrational modes participating in the optical

transition (see Chapter 4.4.2).

At zero temperature, we have $\bar{n}_k(T=0) \approx 0$ and $C(\hbar\omega, T=0) \approx 0$, and Eq. (4.7) is equivalent to Eq. (4.6) with the δ-function replaced by a Lorentzian function with a broadening λ. In order to evaluate Eq. (4.7), the partial HRF S_k, E_{ZPL}, and phonon frequencies ω_k are required as input. We compute S_k as:

$$S_k = \frac{\omega_k \Delta Q_k^2}{2\hbar}, \tag{4.13}$$

where ΔQ_k is the mass-weighted displacement along the k-th mode, evaluated as:

$$\Delta Q_k = \sum_{\alpha=1}^{N} \sum_{i=x,y,z} \sqrt{M_\alpha} \Delta \mathbf{R}_{\alpha i} \boldsymbol{e}_{k,\alpha i}. \tag{4.14}$$

In Eq. (4.14), $\mathbf{e}_{k,\alpha i}$ is the eigenvector of the k-th phonon mode on the α-th atom in the i-th direction; M_α is the mass of the α-th atom, and $\Delta \mathbf{R}_{\alpha i} = (\mathbf{R}_{\alpha i})_e - (\mathbf{R}_{\alpha i})_g$ is the displacement between the ES and the GS equilibrium atomic structures in the i-th direction. Within the harmonic approximation, ΔQ_k may be equivalently computed as [59]:

$$\Delta Q_k = \frac{1}{\omega_k^2} \sum_{\alpha=1}^{N} \sum_{i=x,y,z} \frac{\mathbf{F}_{\alpha i}}{\sqrt{M_\alpha}} \boldsymbol{e}_{k,\alpha i}. \tag{4.15}$$

Here $\mathbf{F}_{\alpha i}$ is the GS force on the α-th atom in the i-th direction evaluated at the ES equilibrium structure.

In this work, we simulate PL spectra at finite temperatures using Eq. (4.7), with parameters computed from first principles. In particular, we use DFT to obtain the GS equilibrium atomic structure, $\mathbf{R}_g$, the GS forces, $\mathbf{F}$, the phonon modes, $\mathbf{e}$, and the phonon frequencies ω; the ES equilibrium atomic structure, $\mathbf{R}_e$, is obtained with CDFT and, in some cases validated by carrying out TDDFT calculations. The resulting PL line shapes are then compared with measured PL spectra at finite temperatures. Below, we report our results and we sys-

tematically investigate the validity of the chosen theoretical and numerical approximations, including the use of the FC and the DHO approximations, which are at the core of the HR theory.

4.3 Technical details

4.3.1 First principles calculations

The electronic structures of the defects in diamond and 4H-SiC are obtained using DFT and the plane-wave pseudopotential method, as implemented in the Quantum Espresso package [139, 207, 208]. The plane-wave energy cutoff was set to 80 Ry. We used SG15 ONCV norm-conserving pseudopotentials [141, 142] and the semi-local functional by Perdew, Burke, and Ernzerhof (PBE) [31], the dielectric dependent hybrid (DDH) functional [33] and the screened hybrid functional by Heyd, Scuseria, and Ernzerhof (HSE) [209, 210]. The fraction of exact exchange used in the DDH functional was determined by the inverse of the macroscopic dielectric constant of the system, resulting in 18% and 15% of exact exchange for diamond and 4H-SiC [33, 126], respectively. The macroscopic dielectric constants were computed by including the full response of the electronic density to the perturbing external electric field at the level of hybrid functional, and the fraction of exact exchange was self-consistently determined from the dielectric constant [33].

We used a $(4 \times 4 \times 4)$ supercell with 512 atomic sites and a $(5 \times 5 \times 2)$ supercell with 400 atomic sites for the NV^- center in diamond and VV^0 centers in 4H-SiC, respectively. In the cases of VV^0 centers in 4H-SiC, convergence tests were carried out with large supercells (up to $(8 \times 8 \times 2)$). We used the lattice constant optimized with each specific functional (see Table 4.4). The Brillouin zone was sampled with the Γ point.

The paramagnetic ESs were computed using the CDFT (also called ΔSCF) method, where one electron is promoted from the highest occupied to the lowest unoccupied state

in the same spin channel (see Chapter 4.6.2 for details of CDFT calculations). The energy E_{ZPL} was computed as the difference between the total energy of the relaxed ES (with CDFT) and the total energy of the GS. The CDFT method has been shown to yield reliable results for systems with localized electronic states, e.g., the NV^- center in diamond [81] and VV^0 centers in 4H-SiC [153, 202, 211]. We also performed TDDFT calculations within the Tamm-Dancoff approximation to assess the accuracy of our CDFT results. We obtained the ES low-lying energies and eigenvectors by iteratively diagonalizing the linearized Liouville operator, as implemented in the WEST code [44, 121]. Due to the higher computational cost of TDDFT calculations, we used a $(3 \times 3 \times 3)$ supercell and a $(5 \times 3\sqrt{3} \times 1)$ supercell for the NV^- center in diamond and VV^0 centers in 4H-SiC, respectively.

Phonon modes of bulk and defective solids were computed using the frozen phonon approach, with configurations generated with the PHONOPY package [45] and a displacement of 0.01 Å from equilibrium structures. Phonon calculations for pristine bulk systems were carried out with the PBE, DDH, and HSE functionals, but those for defective solids were performed only with PBE due to the high computational cost of hybrid functionals. We then approximated the values of hybrid-DFT phonons by using a scaling factor equal to the ratio of hybrid-DFT and PBE phonon results in the pristine bulk systems. We verified that this approximation yields accurate phonon frequencies for bulk systems (see Chapter 4.6.4 for details). We evaluated finite size effects on computed PL line shapes, HRFs, and spectral densities following the force constant matrix embedding approach proposed by Alkauskas et al. [59, 82, 159] (see Chapter 4.6.5).

4.3.2 Experiments

The SiC experiments were realized in a confocal microscopy setup (0.67 NA objective) with the sample in a closed-cycle cryostat at 10 K unless mentioned otherwise. The sample was diced from a commercial high-purity semi-insulating 4H-SiC wafer (Cree) containing intrin-

sic concentrations of VV^0 ($10^{15} - 10^{16}$ cm^{-3}). The sample was excited within the VV^0 absorption sideband with a 908 nm laser (QPhotonics, ∼100 mW), and the resulting PL was filtered using several 1000 nm long-pass filters. The PL was then measured using a spectrometer with a 300 g/mm grating blazed for 1.2 µm and an InGaAs camera (Teledyne Princeton Instruments) with a spectral resolution of ∼0.3 nm. Careful calibration was performed to correct for the entire setup transmission and the camera response using a NIST-calibrated tungsten-halogen white light source (StellarNet). Optically detected magnetic resonance at a weak static magnetic field (<20 G) with microwave excitation was delivered using a printed circuit board was used to obtain independent contrast (i.e., the difference in PL with and without microwave excitation) for the various VV^0 sites. The DWF was calculated as the ratio of the integrated intensity of the ZPL to the total integrated intensity. Though most of the PL is within our detection bandwidth (900-1600 nm), the sideband may be very slightly underestimated due to weak emission extending beyond this range.

Similarly, for the NV^- center in diamond, the PL spectra were taken on an ensemble of NV^- centers using a home-built confocal microscope with a flow cryostat (Janis - LakeShore Cryotronics) for temperature studies. The sample was an IB diamond (Sumitomo) with a high nitrogen concentration synthesized via high-pressure / high-temperature growth. The sample was electron irradiated (2 MeV, 10^{17} cm^{-2}) and annealed (850 °C, 2 hr), resulting in a high density of NV^- centers. The NV^- center ensemble was photo-excited within the absorption sideband using 532 nm light, and the PL measurements were collected using a high-resolution spectrometer with a visible camera (Teledyne Princeton Instruments) with ∼0.1 nm spectral resolution. The spectrum intensity was also calibrated using a tungsten halogen light source (Ocean Optics) to correct for transmission losses in the experimental setup.

4.4 Results and discussions

4.4.1 Zero-phonon lines

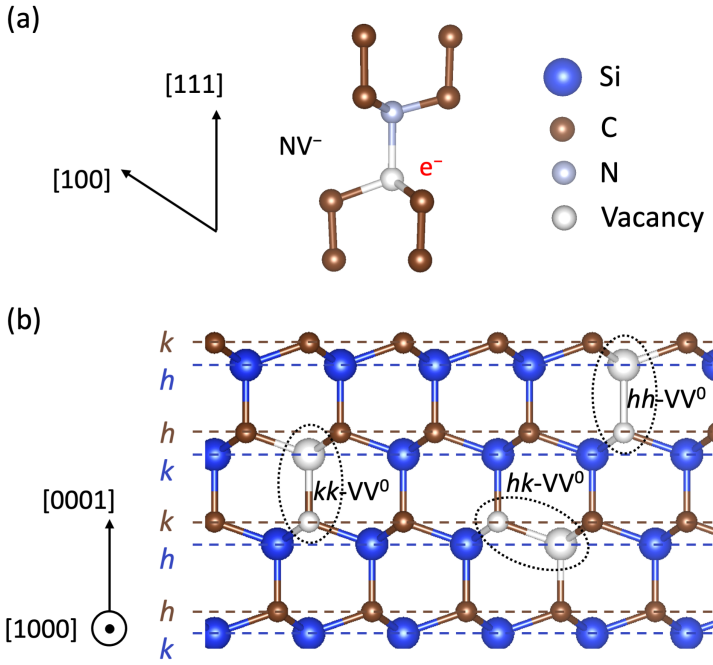

Figure 4.2: Ball and stick representation of the defect centers studied in this work. (a) NV^- center in diamond. (b) Divacancy ($V_{Si}V_C^0$) centers in 4H-SiC. The planes are labeled with h and k according to the symmetry of lattice sites. Three non-equivalent configurations (hh, kk and hk) of the $V_{Si}V_C^0$ centers are shown. The kh configuration was not investigated computationally, due to the lower quality of the experimental spectrum for this configuration.

The NV^- center in diamond is composed of a nitrogen impurity and an adjacent carbon vacancy (V_C) with an additional electron, as shown in Figure 4.2(a) [62, 63]. It has C_{3v} symmetry, and three defect orbitals are present within the band gap of diamond: the a_1 orbital and the two-fold degenerate e orbitals, as shown in Figure 4.3(a). Defect orbitals are mainly localized on three carbon atoms around the V_C (see Figure 4.9).

The neutral divacancy center in 4H-SiC is composed of a silicon vacancy (V_{Si}) and an adjacent carbon vacancy (V_C) and is denoted as $V_{Si}V_C^0$ [68, 69]. We consider the 4H polytype of SiC, 4H-SiC, with ABCB stacking along the c-axis. 4H-SiC contains two nonequivalent

hexagonal (h) and quasi-cubic (k) sites for each type of atom, as shown in Figure 4.2(b). Therefore, the VV^0 center can occur in four distinct configurations (hh, kk, hk, and kh), and the experimentally measured PL ensemble is a mixture of contributions from all configurations. Experimentally, we used microwave-assisted spectroscopy to separate the PL of different configurations. In our computational study, we considered the hh, kk, and hk configurations denoted as hh-VV^0, kk-VV^0 and hk-VV^0. The first two c-axis orientated defects (hh-VV^0 and kk-VV^0) have C_{3v} symmetry, with an a_1 state and two sets of degenerate e states within the band gap of 4H-SiC (see Figure 4.3(b)). The a_1 orbital and lower e orbitals are mainly localized on three carbon atoms around the V_{Si} (see Figure 4.9). For NV^-, hh-VV^0 and kk-VV^0, we studied the optical transition between the a_1 orbital and the (lower) e orbitals, which corresponds to the transition between the $^3A_2$ and the ^3E many-body states. For the hk configuration, which has C_{1h} symmetry, we studied the a' and the a'' transition accounting for the transition between the $^3A''$ and the $^3A'$ state.

We computed E_{ZPL} using the PBE, DDH, and HSE functionals in the DHO approximation (note that the zero-point energy contributions of the GS and ES phonons cancel out within the DHO approximation). Triplet ESs were computed using CDFT with electronic configuration $a_1^1 e_x^2 e_y^1$ (see Chapter 4.6.2 for details of CDFT calculations). Results for all defect systems at different levels of theory are summarized in Table 4.1. The PBE functional underestimates the measured E_{ZPL} of the NV^- by 0.24 eV, while the DDH and HSE functionals overestimate it by 0.26 eV. In the case of VV^0 centers, particular attention must be exercised to account for finite-size effects. For small cells (e.g. $(5 \times 5 \times 2)$ supercell), the experimental order of the ZPL of the various defect configurations was not reproduced. Hence we computed E_{ZPL} at the PBE level of theory for $(5\times5\times2)$ and $(8\times8\times2)$ supercells; we then used the difference between these two values to estimate the converged hybrid-DFT E_{ZPL} starting from our results obtained with $(5 \times 5 \times 2)$ supercells. The converged results reproduce the experimental trend. Similar to our results for diamond, we find that the PBE

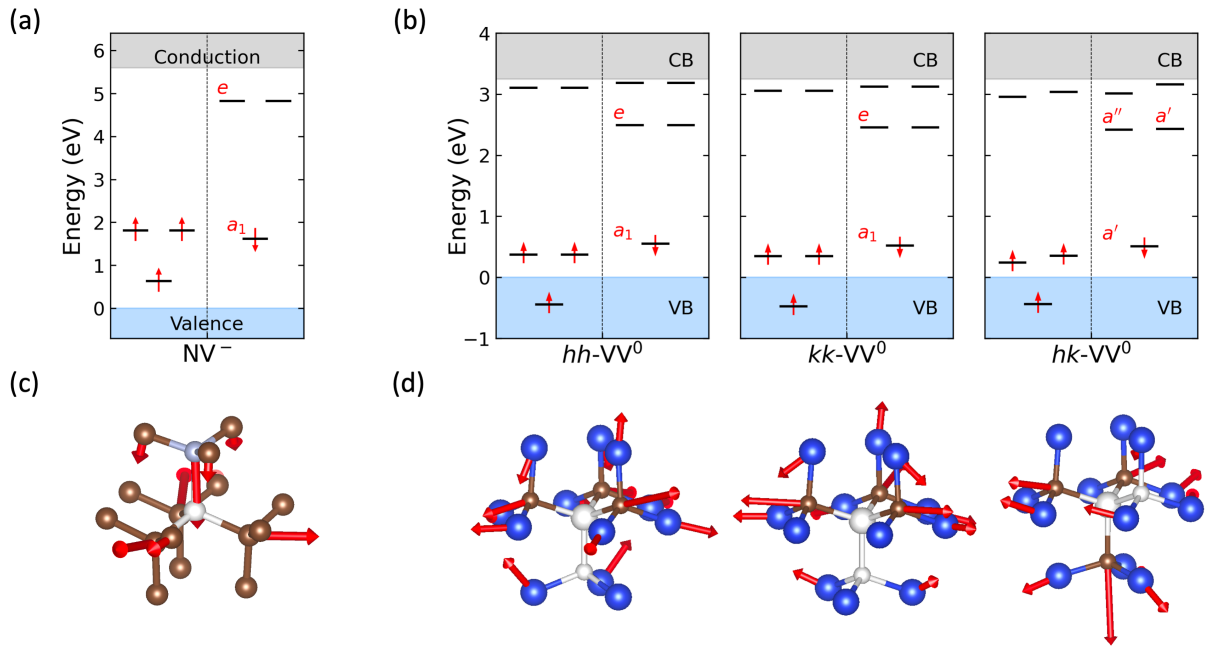

Figure 4.3: Ground state (GS) electronic structure of (a) NV^- center in diamond and (b) VV^0 centers in 4H-SiC at the DDH level of theory. Displacements between the excited state (ES) and the GS equilibrium structures of the NV^- center in diamond and the VV^0 centers in 4H-SiC are shown in (c) and (d), respectively. The red arrows represent mass-weighted displacements (ΔQ) of each atom with the magnitude being amplified by a factor of 10. The ΔQ of the NV^- center is mainly localized on the nitrogen atom and three nearest neighbor carbon atoms around the carbon vacancy. The ΔQ of the VV^0 centers is mainly localized on three nearest neighbor carbon atoms and nine next nearest neighbor silicon atoms around the silicon vacancy, as well as three nearest neighbor silicon atoms around the carbon vacancy.

functional underestimates the measured E_{ZPL} of the VV^0 centers by ~0.16 eV, while the DDH (HSE) yields an overestimate of ~0.11 eV (~0.12 eV). Table 4.1 summarizes our results and previously reported theoretical predictions of E_{ZPL}. We note that although the E_{ZPL} obtained with the HSE functional is generally in good agreement with experiments, theoretical results exhibit a variance up to 0.3 eV due to different choices of pseudopotentials, supercell sizes, and sampling of the reciprocal space.

Table 4.1: Energy of the zero-phonon line (E_{ZPL}, eV) for spin-conserving transitions computed using different levels of theory and a $(4\times4\times4)$ supercell for the NV^- center in diamond, and a $(5\times5\times2)$ supercell for the VV^0 centers in 4H-SiC. The extrapolation value of the E_{ZPL} with the finite size corrections is reported in parentheses. The finite size corrections are calculated as the difference of E_{ZPL} values between the $(8\times8\times2)$ and the $(5\times5\times2)$ supercell at the PBE level of theory. Previous theoretical predictions on E_{ZPL} are also shown.

Hosts	Defects	This work			Previous Theoretical Work			Expt.
		PBE	DDH	HSE	PBE	DDH	HSE	
Diamond	NV^-	1.706	2.205	2.205	1.72[a], 1.706[b]	2.22[a]	2.23[a], 1.955[b]	1.945 [62]
4H-SiC	hh-VV^0	1.086 (0.937)	1.346 (1.196)	1.371 (1.221)	1.03[a], 0.92[c]	1.30[a]	1.33[a], 1.056[c], 1.13[d], 1.14[e]	1.095
	kk-VV^0	1.105 (0.951)	1.355 (1.201)	1.372 (1.218)	0.94[c]		1.044[c], 1.14[d]	1.096
	hk-VV^0	1.075 (0.979)	1.355 (1.259)	1.365 (1.269)	0.97[c]		1.103[c], 1.21[d]	1.149

[a]Ref. [126]: Calculations were carried out using the Quantum Espresso package with ONCV pseudopotentials (PPs). The plane-wave energy cutoff was set to 75 Ry. The Brillouin zone was sampled with the Γ point. A $(4\times4\times4)$ ($(5\times3\sqrt{3}\times1)$) supercell was used for NV^- (hh-VV^0). [b]Ref. [81]: Calculations were carried out using the VASP code with PAW PPs. The plane-wave energy cutoff was set to 420 eV. The Brillouin zone was sampled with the Γ point. A $(4\times4\times4)$ supercell was used for NV^-. [c]Ref. [153]: Calculations were carried out using the VASP code with PAW PPs. The Brillouin zone was sampled with the Γ point. A $(10\times10\times3)$ ($(8\times8\times3)$) supercell was used for PBE (HSE) calculations. HSE E_{ZPL} was computed with PBE structure. [d]Ref. [211]: Calculations were carried out using the VASP code with PAW PPs. The plane-wave energy cutoff was set to 400 eV. The Brillouin zone was sampled using a $2\times2\times2$ k-point mesh. A $(4\times3\times1)$ supercell was used for VV^0. [e]Ref. [202]: Calculations were carried out using the VASP code with PAW PPs. The plane-wave energy cutoff was set to 400 eV. The Brillouin zone was sampled with the Γ point. A $(5\times5\times2)$ supercell was used for VV^0. HSE E_{ZPL} was computed with PBEsol structure.

To estimate the accuracy of CDFT for the ES potential energy surface, we compared results obtained with CDFT and TDDFT for NV^-, hh-VV^0, and kk-VV^0 at the DDH level of theory. TDDFT enables the description of the ES as a linear combination of multiple Slater determinants. In our TDDFT calculations, we use hybrid functionals with the fraction of exact exchange determined by the dielectric constant of the system; based on recent studies, these calculations are expected to yield results in good agreement with the solutions of the Bethe Salpeter equation [107, 132]. Previous TDDFT studies of these defect systems used cluster models and atomic-centered basis sets [110, 111, 114]. Here, we consistently compared TDDFT and CDFT calculations performed with the same basis set and pseudopotential, in the same cell and with the same functional. After obtaining the equilibrium structure of the ES using the CDFT approach, we selected several configurations along the linear path connecting equilibrium atomic structures of the GS and the ES and carried out single-point DFT, CDFT, and TDDFT calculations, from which configuration coordinate diagrams were obtained, as shown in Figure 4.4. The comparison between TDDFT and CDFT results was carried out using the configuration $a_1^1 e_x^{1.5} e_y^{1.5}$ in CDFT because we could not converge the configuration $a_1^1 e_x^2 e_y^1$ when using the DDH functional. The difference between CDFT calculations at the PBE level using the $a_1^1 e_x^2 e_y^1$ and $a_1^1 e_x^{1.5} e_y^{1.5}$ electronic configurations is $\sim$0.04 eV; assuming an energy difference of the same order of magnitude at the DDH level, we deemed the CDFT/TDDFT comparison with the $a_1^1 e_x^{1.5} e_y^{1.5}$ configuration to be a meaningful one. We found that the TDDFT energies of the ^3E states are 0.1 (0.04) eV smaller than CDFT energies for NV^- (VV^0); the minimum of the TDDFT curve is close to that of the CDFT curve, with a difference smaller than 6% for all three systems. An analysis of our TDDFT results shows that the spin-conserving transition between the a_1 and the e orbitals contributes to more than 95% to the whole transition to the ^3E state, indicating that the ^3E state can be well-described by a single Slater determinant. This finding is in good agreement with that of a previous TDDFT study using a cluster model, atom-centered basis sets, and

the PBE0 functional [110]. We note that the quality of the agreement between TDDFT and CDFT depends on the functional and the system. For example, we found a difference of ∼0.2 eV in the excitation energy and a difference greater than 12% in the configuration coordinate of the minimum between TDDFT and CDFT results when using the PBE functional (see Figure 4.11). In addition, in the case of defect systems with singlet GS and ES, we expect non-negligible differences between TDDFT and CDFT results, since the accurate description of a singlet ES requires a linear combination of at least two Slater determinants [187, 212]. In that case, the use of quantum embedding theories (QDET) should be preferable to describe strongly correlated states [86, 87, 92].

To understand the effect of lattice vibrations on optical transitions, we analyzed in detail the mass-weighted displacement ΔQ computed at different levels of theory (see Chapter 4.6.3). The magnitude of the displacement follows the relation: HSE > DDH > PBE, and the difference of the results obtained with different functionals can be up to 10%. The same trend can also be found for energies of bulk phonons and can be understood by noting that the bonds in the diamond and SiC crystals turn out to be stiffer with HSE than with DDH, which are in turn stiffer than with PBE, as reflected in the difference of predicted lattice constants (see Table 4.4). ΔQ is localized on the neighboring atoms of the defect center, as shown in Figure 4.3(c) and (d), consistent with the localization of defect orbitals involved in the optical transition. We also found that the symmetry of the ES is reduced from C_{3v} to C_{1h} for NV^-, hh-VV^0 and kk-VV^0, and hence in principle both a_1 type and e type phonons could participate in the optical process. Although the average symmetry of the ES structure turns out to be C_{3v} due to the dynamic Jahn-Teller effect [194, 213], here we used the ES equilibrium structure with C_{1h} symmetry to include the coupling with e type phonons. Hence, the ES configuration used is $a_1^1 e_x^2 e_y^1$.

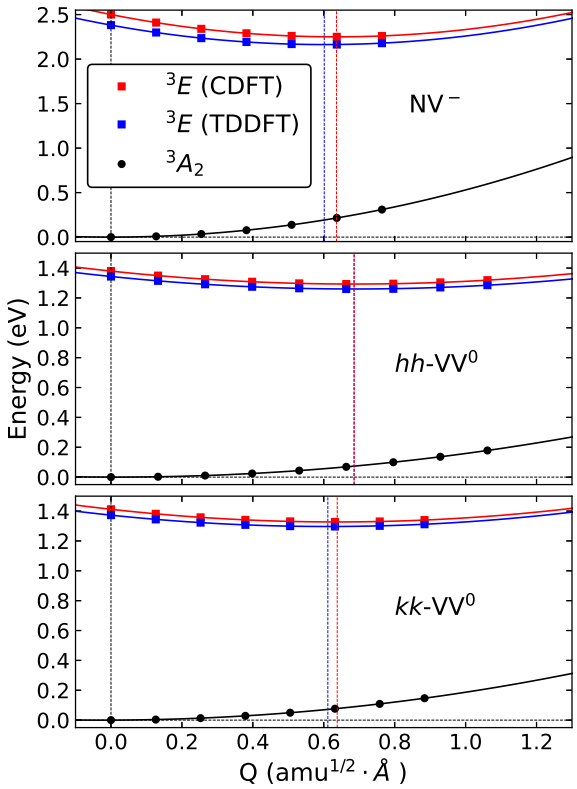

Figure 4.4: Configuration coordinate diagrams describing the total energies of the $^3A_2$ ground state (GS) and the ^3E excited state (ES) along the relaxation path resulting from CDFT with electronic configuration $a_1^1 e_x^{1.5} e_y^{1.5}$ for the NV^- center in diamond and the *hh*-VV^0 and the *kk*-VV^0 centers in 4H-SiC. Calculations are performed at the DDH level of theory. Dashed vertical lines denote the locations of the local minimum by fitting the energy curves with quadratic functions. The energy of the effective phonon obtained from the fitting process is 66.4 meV for the $^3A_2$ state and 72.0 (71.1) meV for the ^3E state when computed with CDFT (TDDFT) for NV^-. The energy of the effective phonon is 36.8 meV for the $^3A_2$ state and 39.3 (38.6) meV for the ^3E state when computed with CDFT (TDDFT) for *hh*-VV^0. The energy of the effective phonon is 38.7 meV for the $^3A_2$ state and 41.7 (41.2) meV for the ^3E state when computed with CDFT (TDDFT) for *kk*-VV^0.

Table 4.2: Huang-Rhys factors (HRFs) for spin-conserving transitions computed using Eq. (4.13) with different levels of theory. PBE$-\Delta Q$ denotes that ΔQ used in Eq. (4.13) is computed using Eq. (4.15) with forces and phonons computed at the PBE level. PBE$-ph$ denotes that phonons used in Eq. (4.13) are computed at the PBE level. Similar notations are used for DDH and HSE. Only one digit was kept for HRFs computed with the largest supercells, considering the uncertainty introduced in the extrapolation procedure (see Chapter 4.6.5). Experimental HRFs for VV^0 centers are estimated as the negative logarithm of the Debye-Waller factor (DWF).

Hosts	Defects	Cell Size	PBE$-\Delta Q$	DDH$-\Delta Q$		HSE$-\Delta Q$		Expt.
			PBE$-ph$	PBE$-ph$	DDH$-ph$	PBE$-ph$	HSE$-ph$	
Diamond	NV^-	$(4 \times 4 \times 4)$	2.94	3.20	3.32	3.46	3.64	3.49 [147]
		$(12 \times 12 \times 12)$	3.0	3.2	3.3	3.5	3.7	3.49 [147]
4H-SiC	hh-VV^0	$(5 \times 5 \times 2)$	2.55	2.55	2.64	2.72	2.86	3.30
		$(16 \times 16 \times 5)$	3.0	3.0	3.0	3.2	3.3	3.30
	kk-VV^0	$(5 \times 5 \times 2)$	2.51	2.53	2.62	2.68	2.81	2.80
		$(16 \times 16 \times 5)$	2.6	2.6	2.7	2.8	2.9	2.80
	hk-VV^0	$(5 \times 5 \times 2)$	2.26	2.46	2.54	2.53	2.66	2.58
		$(16 \times 16 \times 5)$	2.5	2.7	2.8	2.8	2.9	2.58

4.4.2 Huang-Rhys factor and spectral density of the electron-phonon coupling

Table 4.2 summarizes HRFs computed using Eq. (4.13) at different levels of theory and includes combinations of mass-weighted displacements, ΔQ_k, computed with DDH or HSE and phonons computed with PBE. We used a scaling factor (see Chapter 4.6.4) to approximate DDH (HSE) phonon frequencies using PBE results; the factor was evaluated from the ratio of frequencies of bulk systems optical phonons computed at different levels of theory, an approximation that introduces a root-mean-square error (RMSE) of only 0.4 meV for bulk 4H-SiC.

We find that the HRFs computed with the PBE functional are smaller than those computed with hybrid functionals, consistent with the magnitude of the structural relaxations upon optical excitation (see Table 4.5). In addition, the HRFs computed with hybrid functionals are larger when phonons are obtained at the DDH (HSE) level, consistent with the fact that the phonon frequencies computed with hybrid functionals are higher than those obtained at the PBE level of theory.

The spectral densities of electron-phonon coupling (Eq. (4.11)) are computed with the $(4 \times 4 \times 4)$ supercell for NV^- and the $(5 \times 5 \times 2)$ supercell for VV^0 centers and are shown in Figure 4.5(a) and (c). The hybrid-DFT peak intensity is higher than that computed with PBE, consistent with the values of the HRF. As for spectral densities at the level of hybrid functionals, we find that peak positions are shifted to higher energies, compared with the PBE results, when phonons are computed with hybrid functionals.

To evaluate finite size effects on the HRFs and spectral densities, we need to compute ΔQ_k for large supercells with either Eq. (4.14) or Eq. (4.15). For the smallest supercell, Eq. (4.14) and Eq. (4.15) yield results that differ by less than 3% (see Figure 4.14); hence, for larger supercells, we used Eq. (4.15) which converges more rapidly as a function of the distance from the defect center because inter-atomic interactions in diamond and 4H-SiC are short-ranged [59, 82, 159]. Previous work on NV^- has shown that forces on atoms that are

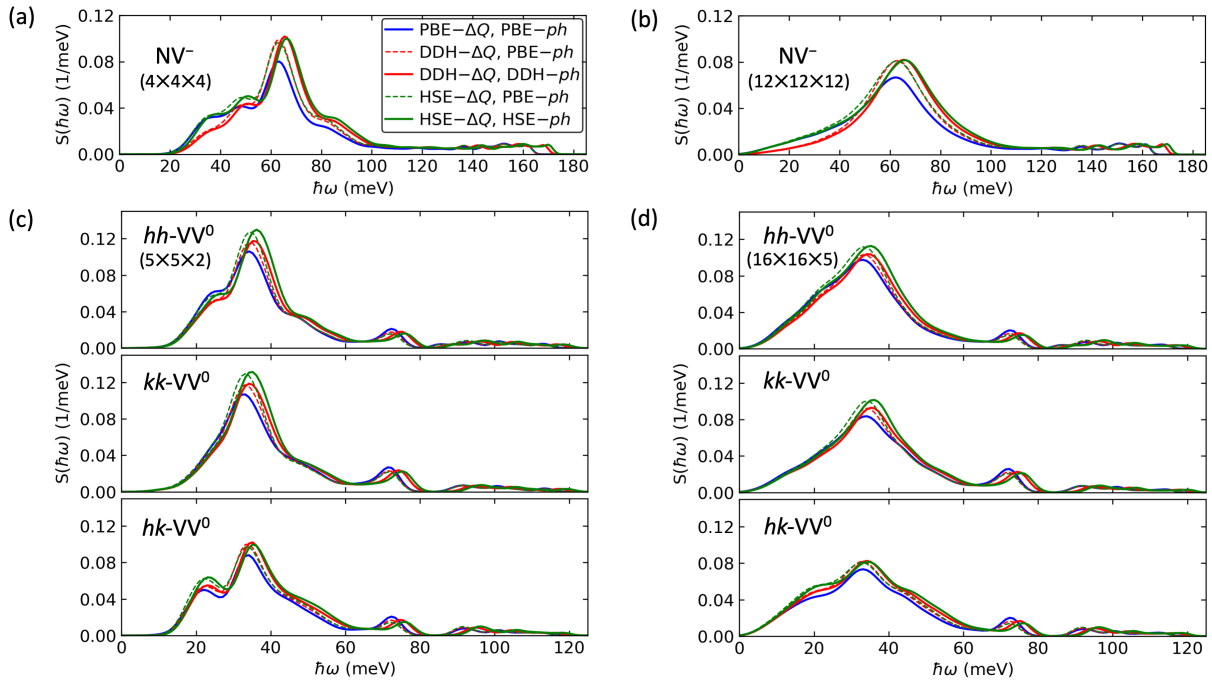

Figure 4.5: Spectral densities of the electron-phonon coupling, $S(\hbar\omega)$, for defect systems computed at different levels of theory. The labels follow the same notation as in Table 4.2. Gaussian functions with varying standard deviation (σ) were used to broaden the δ-function in Eq. (4.11). For the NV^- center (VV^0 centers), σ is chosen to vary linearly from 6 (3.5) meV for the lowest-energy phonon to 1.5 (1.5) meV for the highest-energy phonon.

separated from the defect by more than 5 Å yield a negligible contribution to the HRF [82]. For VV^0 centers, we compared results for the HRF and spectral density using forces from a $(7 \times 7 \times 2)$ supercell and those from a $(5 \times 5 \times 2)$ supercell (see Figure 4.15). We found a difference of less than 5% in the HRFs, and the spectral densities are almost identical. To obtain phonon frequencies and modes for large supercells, we employed the force constant matrix embedding approach [59], and details can be found in Chapter 4.6.5.

The HRFs computed in the dilute limit for NV^- ($(12\times12\times12)$ supercell) and VV^0 centers ($(16 \times 16 \times 5)$ supercell) differ by 2% and 5–15% respectively, relative to those obtained with $(4 \times 4 \times 4)$ and $(5 \times 5 \times 2)$ supercells. Computed HRFs for NV^- are in close agreement with previous theoretical predictions [59, 82, 194] and experiments [147]. Computed HRFs for VV^0 centers are also in close agreement with our experiments. A previous theoretical work

by Hashemi et al. [202] reported an HRF of 2.75 for *hh*-VV^0. This value falls in the range of our results computed with the $(5\times5\times2)$ supercell and is 15% smaller than our experimental value likely due to finite size effects not being fully taken into account in Ref. [202]. In the dilute limit, we found that the spectral densities are smoother and exhibit a linear tail below 20 meV, reflecting the coupling with long-range acoustic phonons. Detailed analysis of spectral densities and vibrational modes can be found in Chapter 4.6.6.

4.4.3 Photoluminescence line shapes and Debye-Waller factors

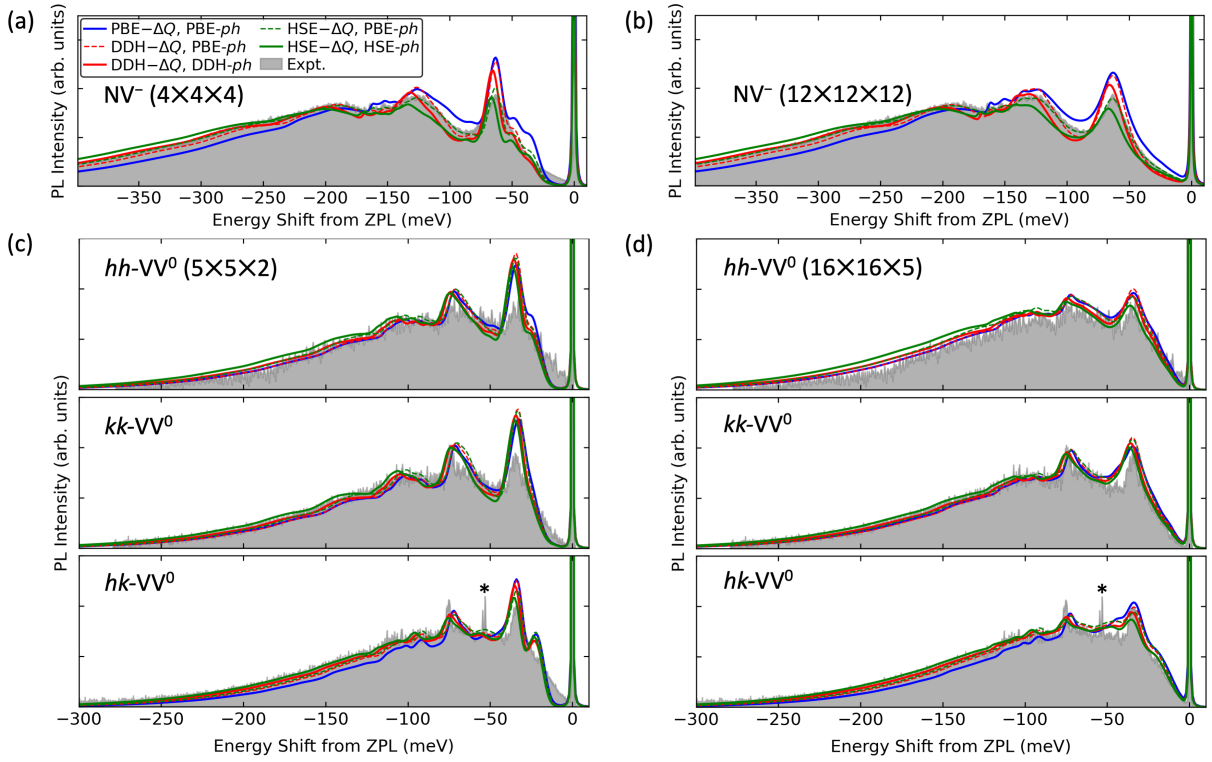

Figure 4.6: Photoluminescence (PL) line shapes computed at different levels of theory at low temperature (8 K for the NV^- center in diamond and 10 K for VV^0 centers in 4H-SiC). The labels follow the same notation as in Table 4.2. We used $\lambda = 0.3$ (0.1) meV in Eq. (4.8) for the NV^- center (VV^0 centers) to reproduce the experimental broadening of the zero-phonon line. The experimental data for the NV^- center in diamond are from Ref. [59]. The small peak marked with a star '$*$' in the experimental curve is the ZPL of another center and should be disregarded in the comparison between theory and experiment presented here. The intensity of the experimental line shapes has been scaled to match the peaks of the computed line shapes.

In Figure 4.6 we show the PL line shapes computed using the generating function approach (Eq. (4.7)) with HRFs computed at different levels of theory and different supercell sizes, compared with the experiment. The spectra consist of a sharp ZPL and a structured PSB. The broadening of the PSB is ∼500 meV for NV^- and ∼300 meV for VV^0 centers. Note that the PL line shapes computed with small supercells show sharper peaks and a gap of 5-10 meV between the ZPL and the PSB. The peaks located at 30 (23) meV from the ZPL for NV^- (hk-VV^0) also stem from finite size effects. In our calculations, the contribution of the e type phonons is computed using the HR theory, which was shown to represent an accurate approximation in the recent work by Razinkovas et al. [82]. These authors computed the contribution of e type phonons to the PL and absorption line shapes for NV^- by explicitly solving the multi-mode $E \otimes e$ Jahn-Teller problem; they showed that if the HRF of e type phonons lies between 0.5 and 1.0, then the HR theory yields reasonable results for the PL line shape. For the NV^- and VV^0 centers, we find an HRF of e type phonons of about 0.5 and 1.0, respectively, indicating that the HR theory should be accurate.

We find that computed and measured line shapes agree well, both in terms of the peak positions and intensity of line shapes, when calculations are performed with the largest supercells ($(12 \times 12 \times 12)$ for NV^- and $(16 \times 16 \times 5)$ supercell for VV^0 centers). When computing phonons with the PBE functional, we find that the PSB is dominated by coupling with the 63 meV phonon for NV^-, close to the experimental value 64 meV [147]. The PSB also shows peaks at 122 meV, 135 meV, 150 meV, and 161 meV from the ZPL, in good agreement with the experimental values 122 meV, 138 meV, 153 meV, and 163 meV [147]. As for the relative intensity of peaks, the best agreement with the experiment is obtained using HSE for the calculation of ΔQ and PBE phonons, respectively. When phonons are computed at the DDH (HSE) level, the 63 meV peak is shifted to 66 (67) meV, and the 161 meV peak to 168 (170) meV. Overall, the agreement with the experiment is good in all cases.

Similar conclusions can be drawn for the VV^0 centers. When computing phonons with

PBE, we obtain peak positions at 34 meV and 72 meV from the ZPL in the PSB, in good agreement with experiments. Calculated PSB also exhibits small peaks located at 90 meV from the ZPL, originating from the coupling with high-energy phonons. As for the relative intensity of peaks, those computed with DDH ΔQ or HSE ΔQ are in slightly better agreement with experiments than with PBE, but generalizations to other defects or materials are difficult to make. When computing phonons with the DDH or HSE functionals, the peaks are slightly shifted to lower energy by 1–3 meV, depending on the peak, and the agreement with experiments is improved, although again, in all cases, we find good agreement with the measured spectra. We emphasize that the ability to resolve phonon side bands is important in order to build predictive capabilities to identify fingerprints of defects using first principle calculations.

From the PL line shape, we can obtain the DWF, which is defined as the ratio of the emitted light from the ZPL to the total emitted light. At very low temperatures, the DWF is computed as DWF $= e^{-S} = e^{-\sum_k S_k}$. In Table 4.3, we report the DWFs evaluated for the largest supercells. The experimental and theoretical DWFs (see Chapter 4.3.2) are in good agreement, and in the case of the VV^0 centers, we find that the computed DWFs show the trend hh-VV^0 < kk-VV^0, consistent with experiments. The relation kk-VV^0 < hk-VV^0 can be reproduced at the PBE level of theory. The computed DWF for hh-VV^0 ranges from 3.6% to 5.3%, smaller than that previously reported, 6.39% [202], likely due to an incomplete finite size extrapolation in Ref. [202]. We also note that a recent experiment on VV^0 centers reported DWFs of 9% and 10% for kk-VV^0 and hk-VV^0 [214], which we consider here to be overestimates, based on our computed and measured spectra. Overall, when using hybrid functionals to compute the GS and ES electronic structure, we obtain good agreement with experiments, with small differences between results for phonons obtained with PBE or hybrid functionals, provided an extrapolation to the dilute limit is performed.

Table 4.3: Computed Debye-Waller factor (DWF) (%) for spin-conserving transitions using different levels of theory. Results computed with the ($12 \times 12 \times 12$) supercell for the NV^- center in diamond and ($16 \times 16 \times 5$) supercell for VV^0 centers in 4H-SiC are shown. We used the same notation as in Table 4.2 to denote different levels of theory.

Hosts		Diamond	4H-SiC		
Defects		NV^-	hh-VV^0	kk-VV^0	hk-VV^0
PBE$-\Delta Q$	PBE$-ph$	5.0	5.2	7.1	8.5
DDH$-\Delta Q$	PBE$-ph$	4.1	5.3	7.2	6.8
	DDH$-ph$	3.7	4.8	6.6	6.1
HSE$-\Delta Q$	PBE$-ph$	3.0	4.2	6.3	6.2
	HSE$-ph$	2.5	3.6	5.5	5.4
Expt.		3.2 [59]	3.69	6.11	7.54

4.4.4 Temperature dependent photoluminescence line shapes

In Figure 4.7(a), we show PL line shapes as a function of temperature for NV^-. We included the temperature effect on the phonon population and the line shape broadening using Eq. (4.7). We tuned the parameter λ to obtain the best agreement with the experiment; this parameter describes the broadening of the line shape and is related to the lifetime of the ES and the variation of the local environment of the defect in the experimental samples. The values of λ obtained in our fit to experimental data are reported in the inset of Figure 4.7(a). We approximated λ with a quadratic function of T for NV^-, consistent with the findings of Ref. [215] for $T \geq 100$ K. We note that the ZPL width was shown to depend on T^5 due to the dynamic Jahn-Teller effect of the ^3E ES for $T \leq 80$ K [213, 216]. The T^5 temperature dependence was not considered in our work due to the lack of experimental data.

Overall, the calculated temperature-dependent PL line shapes agree well with the experiments. As the temperature increases, the ZPL width increases due to the decrease in the lifetime of the ES. The intensity of the PSB in the 30 meV range around the ZPL also increases, indicating an increasing population of the higher vibrational levels of the ES long-range modes. The increasing population causes the broadening and the small shift of the first peak of the PSB (about 63 meV lower than ZPL) towards lower energies, as observed

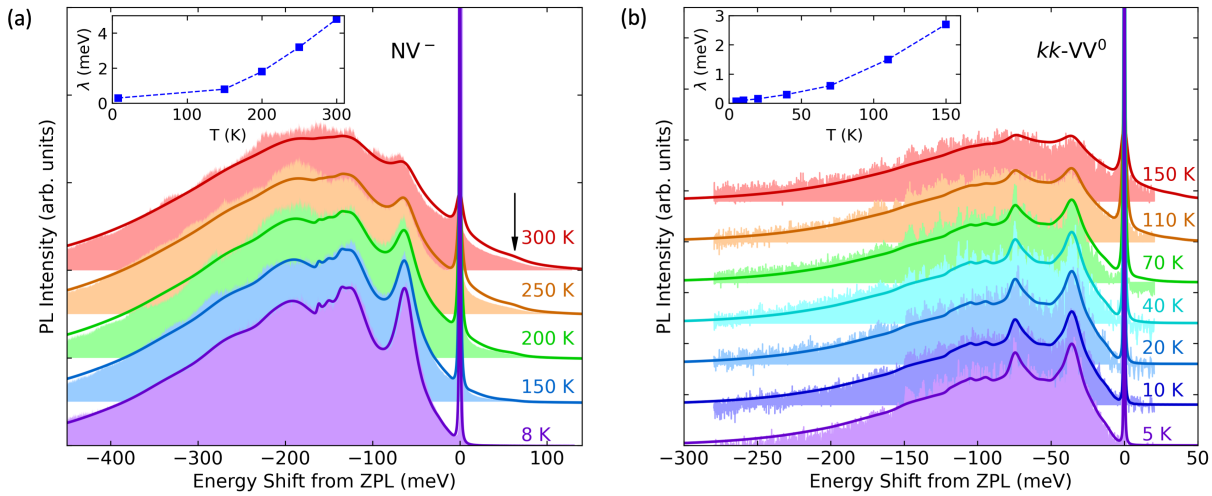

Figure 4.7: Computed photoluminescence (PL) line shapes (solid lines) of (a) the NV^- center in diamond and (b) the kk-VV^0 center in 4H-SiC as a function of temperature. The best agreement with experiments is obtained when Huang-Rhys factors (HRFs) are calculated with HSE$-\Delta Q$ and PBE$-ph$ (DDH$-\Delta Q$ and DDH$-ph$) for the NV^- center (kk-VV^0 center) (see Table 4.2). The experimental line shapes of the NV^- center are averaged over twenty measurements at 8 K and 300 K and over two measurements at 150 K, 200 K, and 250 K in (a). The 8 K data for the NV^- center in diamond in (a) is from Ref. [59]. The broadening parameter λ used in Eq. (4.8) for the theoretical line shapes is shown in the insets as a function of temperature. The black arrow in (a) indicates a shoulder at approximately 60 meV.

both theoretically and experimentally. As for the PSB with energy higher than the ZPL, we find that a shoulder peak at about 60 meV becomes increasingly more intense as the temperature increases, due to the coupling with the quasi-local mode in the ES. Temperature effects on the electronic structure, atomic structure, and lattice parameters were neglected in our calculations. These effects are assumed to be relatively small considering the $\sim$3 meV shift of the ZPL from 8 K to 300 K observed in experiments.

The measured and computed temperature-dependent PL line shapes for kk-VV^0 (Figure 4.7(b)) are in general good agreement. Also in this case, we observe a broadening of the ZPL and the PSB and the increase of the intensity around the ZPL as the temperature increases. The chosen broadening parameter λ turns out to be a non-linear function of the temperature. Our temperature-dependent results show that converged calculations can

successfully discern features in the PSB also as a function of T.

4.4.5 Displaced harmonic oscillator and the Franck-Condon approximations

We have presented results for PL line shapes obtained using the generating function approach (Eq. (4.8)), which in turn was derived using the FC and the DHO approximations. The former assumes that the transition dipole moment $|\boldsymbol{\mu}_{eg}|$ is independent of changes in the atomic structure, and the latter assumes that the vibrational modes of the GS and the ES are identical except for a displacement. We present below an analysis of the validity of these two approximations using a one-dimensional (1D) model, where just one effective phonon mode is considered. Previous studies have shown that the 1D model provides an accurate description of defect systems with strong electron-phonon coupling (HRF $\gg 1$) and serves as a valuable approximation to cases with weak or intermediate electron-phonon coupling [78, 183]. The systems considered in this work, e.g., NV^- and kk-VV^0, yield HRF ≈ 3 (intermediate electron-phonon coupling); hence, the use of the 1D model appears to be justified, although the Herzberg-Teller (HT) effect of symmetry forbidden vibrational modes and the Duschinsky rotation effect between vibrational modes of the GS and the ES [217] are not captured by the model.

In the 1D model, we considered one effective phonon mode which includes only vibrations projected along the direction of the configuration coordinate Q, which connects the equilibrium atomic structures of the GS and the ES (see Figure 4.1). The frequency of such an effective phonon mode is calculated as the weighted average over all phonon frequencies in either the GS or the ES:

$$\Omega^2_{\{e,g\}} = \frac{\sum_k \omega^2_{\{e,g\};k} \Delta Q^2_k}{\sum_k \Delta Q^2_k}. \tag{4.16}$$

At the PBE level of theory, we obtain: for NV^-, $\Omega_g = 63.06$ meV, $\Omega_e = 66.38$ meV, and $\Delta Q = \sqrt{\sum_k \Delta Q^2_k} = 0.653$ amu$^{0.5}$ Å; for kk-VV^0, $\Omega_g = 38.11$ meV, $\Omega_e = 43.45$ meV, and $\Delta Q = 0.763$ amu$^{0.5}$ Å. With these parameters, we can also compute the HRF for the 1D

model as HRF $= \frac{\Omega_g \Delta Q^2}{2\hbar}$. We obtained 3.22 (2.65) for NV^- (kk-VV^0), close to the HRF from the all-phonon calculation with the $(4 \times 4 \times 4)$ $((5 \times 5 \times 2))$ supercell, which is 2.94 (2.51).

Figure 4.8(a) shows the PL spectra of NV^- and kk-VV^0 computed using the 1D model with (i) actual Ω_g different from Ω_e, (ii) Ω_g the same as Ω_e, and (iii) Ω_e the same as Ω_g. We find that for the NV^- center, the approximation (iii) yields 2.3% and 3.1% relative error at $T = 10$ K and at $T = 300$ K relative to (i). This result agrees with those reported by Razinkovas et al. [82]. In the case of the kk-VV^0 center, the approximation (iii) yields a 6.0% and 9.5% relative error at $T = 10$ K and $T = 300$ K, respectively, arising from the greater difference between Ω_g and Ω_e. The error caused by using (iii) increases as a function of T, since the number of excited vibrational states contributing to the PL spectrum increases. Since excited vibrational states are more likely to be populated in kk-VV^0 than in NV^-, due to the smaller effective phonon frequency, the error is larger for the former. The DHO approximation used in the calculations of PL line shapes in Chapter 4.4.3 corresponds to case (iii). Our analysis of the 1D model suggests that the DHO approximation used in our calculations is fairly accurate. In general, we expect the DHO approximation to be valid for defects in rigid materials with relatively small structural displacements upon optical transitions at low temperatures.

To use the 1D model to examine the validity of the FC approximation, we first write Eq. (4.1) without using the FC principle:

$$L(\hbar\omega, T) \propto \omega^3 \sum_i \sum_j P_{ej}(T) |\langle \Theta_{ej} | \boldsymbol{\mu}_{eg} | \Theta_{gi} \rangle|^2 \delta \left(E_{\mathrm{ZPL}} + E_{ej} - E_{gi} - \hbar\omega \right). \tag{4.17}$$

Within the 1D effective phonon approximation we have:

$$\langle \Theta_{ej} | \boldsymbol{\mu}_{eg} | \Theta_{gi} \rangle = \int dQ \phi^*_{n^{ej}}(Q) \boldsymbol{\mu}_{eg}(Q) \phi_{n^{gi}}(Q). \tag{4.18}$$

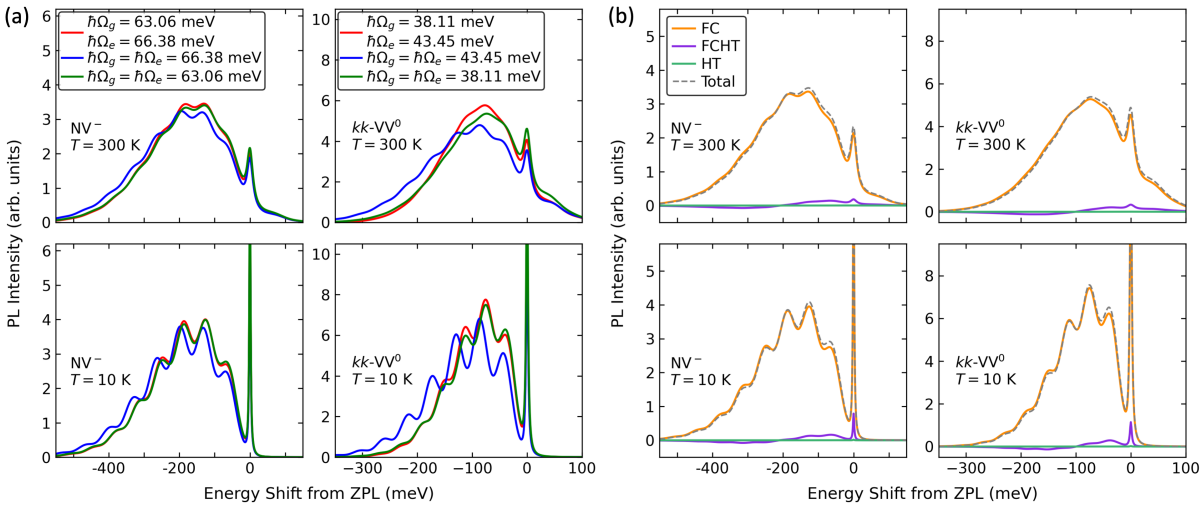

Figure 4.8: PL line shapes evaluated within the 1D model for the NV$^-$ center in diamond and the kk-VV^0 center in 4H-SiC at $T = 10$ K and $T = 300$ K. (a) Analysis of the displaced harmonic oscillator (DHO) approximation. Red lines denote the line shapes computed with both the ground state (GS) and the excited state (ES) frequency. Blue (green) lines denote the line shapes computed with DHO approximation using the ES (GS) frequency. (b) 'FC', 'FCHT', and 'HT' denote the contribution to the PL given by the Franck-Condon, Franck-Condon Herzberg-Teller, and the Herzberg-Teller terms, respectively. 'Total' denotes the sum of three terms. The zero-phonon line is broadened using a Lorentzian function with scale parameter λ, and the phonon sideband is broadened using a Gaussian function with standard deviation σ. For the NV$^-$ center, $\lambda = 2$ (10) meV and $\sigma = 25$ (30) meV were used at $T = 10$ (300) K. For the kk-VV^0 center, $\lambda = 2$ (8) meV and $\sigma = 15$ (20) meV were used at $T = 10$ (300) K.

Here we use the same notations for nuclear wavefunctions and vibrational states as in Eq. (4.3). The quantity $\boldsymbol{\mu}_{eg}(Q) = \langle\psi_e(Q)|\hat{\boldsymbol{\mu}}|\psi_g(Q)\rangle$ is the transition dipole moment between electronic wavefunctions obtained at fixed values of the configuration coordinate Q, where ψ_e (ψ_g) is the electronic wavefunction of the system in the ES (GS). To first order in Q we can further approximate Eq. (4.18) as:

$$\langle\Theta_{ej}|\boldsymbol{\mu}_{eg}|\Theta_{gi}\rangle \approx \boldsymbol{\mu}_{eg}(Q=0)\langle\phi_{n^{ej}}|\phi_{n^{gi}}\rangle + \left.\frac{d\boldsymbol{\mu}_{eg}}{dQ}\right|_{Q=0}\langle\phi_{n^{ej}}|Q|\phi_{n^{gi}}\rangle \tag{4.19}$$

We have numerically computed the electronic transition dipole moment as a function of Q and verified that the dependence is linear with a relative change of about 10% between the

equilibrium atomic structures of GS and ES for both NV^- and kk-VV^0 (see Figure 4.20).

After introducing Eq. (4.19) in Eq. (4.17) we recognize the usual FC term and the terms beyond the FC approximation. The latter can be grouped into two categories: the Franck-Condon Herzberg-Teller (FCHT), and the Herzberg-Teller (HT) term, depending on whether one or two derivatives of the electronic transition dipole moment with respect to Q are present, respectively (see Eq. (4.32)–(4.34)). Figure 4.8(b) shows the FC, FCHT, and HT contributions to the PL line shape for both NV^- and kk-VV^0, at $T = 10$ K and $T = 300$ K. We find that the FC term is the dominant one and that the FCHT and HT contributions are smaller than 5% and 0.1% of the total intensity, respectively. These results indicate that the FC approximation used in Chapter 4.4.3 is accurate. We note that the validity of the FC approximation depends on the symmetry and the strength of electron-phonon coupling of the defect center. For negatively-charged silicon vacancy centers in diamond, the HT term may not be negligible [159, 196]. We suggest that computing the relative error caused by neglecting FCHT and HT contributions using the 1D model is a useful first step in assessing the validity of the FC approximation.

4.5 Conclusions

In summary, we presented a detailed comparison of measured and computed PL spectra of defects in diamond and SiC, aimed at assessing the validity of theoretical and numerical approximations used in first-principles calculations. As expected, our results show that the best agreement between theory and experiments is obtained when using hybrid functionals, instead of PBE, although the qualitative differences between the PL line shapes of the different configurations of the VV^0 centers are reproduced with PBE as well. We find minor differences between the results obtained with the hybrid functionals HSE and DDH: the values of the ZPL obtained with the two functionals are almost identical (note that our HSE results slightly differ from previous ones reported in the literature for the case of the

NV^-) and the values of the HRF differ by less than 10%. We also find minor differences between spectral densities computed at the PBE and DDH level of theory, indicating that the major improvement of hybrid functionals over PBE is in the determination of the electronic structure of the system. Our findings show that results for the triplet ES obtained with CDFT and TDDFT are similar at the DDH level of theory for NV^- and VV^0 centers, suggesting that the relatively cheap CDFT method is accurate for the calculations of their PL spectra. In addition, by using a 1D model, we provided a qualitative assessment of the approximation arising from the use of the FC principle and of the DHO approximation, finding that both of them are justified. Finally, we emphasize the importance of finite size scaling to obtain theoretical results in agreement with experiments for HRFs and PL line shapes, especially for the contribution of quasi-local and long-range acoustic phonon modes. The protocol established in our work shows that accurate results for PL spectra may be obtained at a given temperature using the generating function approach, with phonons extrapolated to the dilute limit, and by using hybrid functionals to compute the GS and ES potential energy surfaces of the defects, with the ES computed with constrained DFT. A 1D model can be used to evaluate the accuracy of the FC and DHO approximations. This protocol, validated here for NV^- and VV^0 centers, leads to robust predictions of the overall line shape, including PSBs, which can be used to aid the identification and characterization of optically active defects.

4.6 Technical details

4.6.1 Bulk diamond and 4H-SiC

Bulk properties, including lattice constants and band gaps, are computed for diamond and 4H-SiC at different levels of theory and summarized in Table 4.4. Band gaps computed at the level of DDH or HSE are in good agreement with experiments. The best agreement with

the experimental lattice constants is obtained using the PBE and the HSE functional for diamond and 4H-SiC, respectively. We observe that bonds predicted by HSE are stiffer than the ones obtained with DDH, which are, in turn, stiffer than PBE ones.

4.6.2 Details of CDFT calculations

The Kohn-Sham orbitals of defect states computed with DFT using the DDH functional are reported in Figure 4.9. For the NV^- in diamond, the a_1 orbital and e orbitals are mainly localized on the three carbon atoms that are first neighbors of the carbon vacancy (V_C). For VV^0 centers in 4H-SiC, the a_1 orbital and the lower-energy e orbitals are mainly localized on the three carbon atoms that are first neighbors of the silicon vacancy (V_{Si}).

At the PBE level of theory, we examined several ways for constraining occupations in CDFT calculations to accurately represent the optical transition from the a_1 to the degenerate e orbitals in the kk-VV^0 in 4H-SiC. The triplet ground state (GS) can be denoted as configuration $a_1^2 e_x^1 e_y^1$. After applying a spin conserving excitation, the triplet excited state (ES) is in the configuration $a_1^1 e_x^2 e_y^1$ (equivalent to $a_1^1 e_x^1 e_y^2$). When the latter configuration is constrained within CDFT, the system ES is forced to have C_{1h} symmetry, which corresponds to the actual local minimum on the adiabatic ES potential energy surface. A commonly adopted strategy to enforce C_{3v} symmetry, and therefore simulate an ES whose atomic structure relaxation is not coupled to e type phonons, is to constrain CDFT with

Table 4.4: Bulk properties of diamond and 4H-SiC computed using PBE, DDH, and HSE functionals. Experimental values are also shown.

Diamond	PBE	DDH	HSE	Expt.
a (Å)	3.568	3.55 [33]	3.543 [126]	3.567 [218]
E_g (eV)	4.19	5.59	5.42	5.48 [219]
4H-SiC	PBE	DDH[b]	HSE[b]	Expt. [220]
a (Å)	3.095	3.087	3.074	3.073
c (Å)	10.133	10.089	10.074	10.053
E_g (Å)	2.27	3.28	3.19	3.23

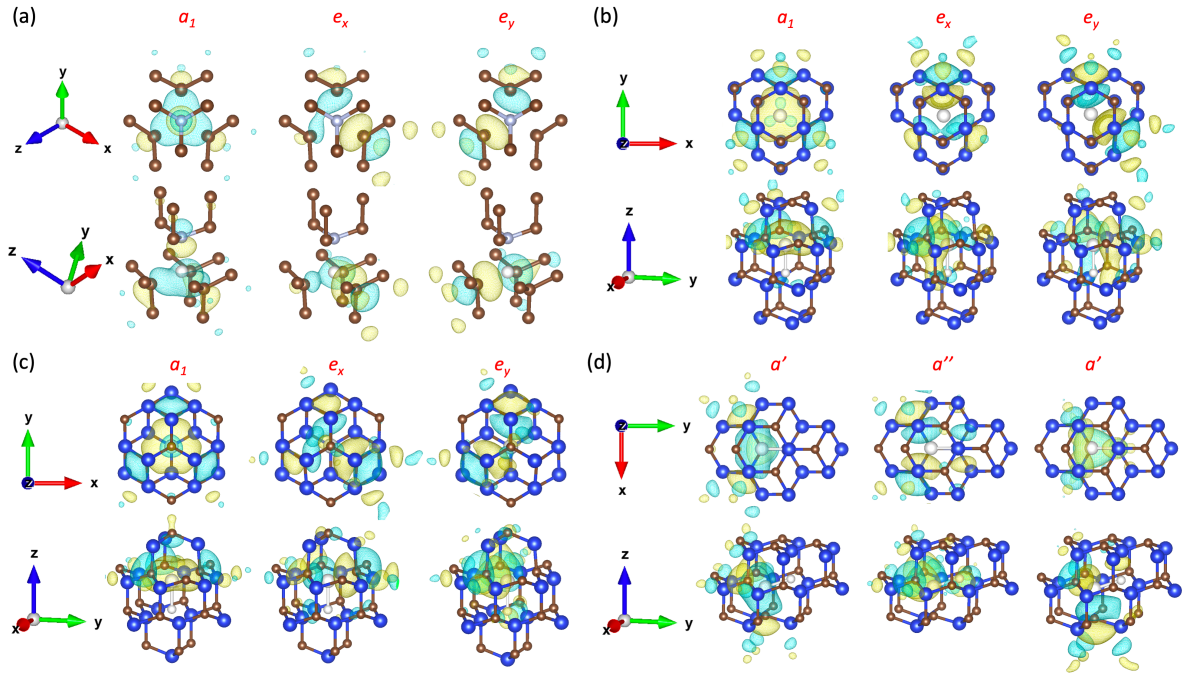

Figure 4.9: Isosurfaces of the square of module of Kohn-Sham orbitals associated to defect states for (a) NV^- in diamond, (b) hh-VV^0 in 4H-SiC, (c) kk-VV^0 in 4H-SiC, and (d) hk-VV^0 in 4H-SiC. The isosurface level is set to 0.015 e/Å^3. The color (yellow or light below) represents the sign $(+/-)$ of the orbital. Blue, brown, silver and white spheres denote Silicon, Carbon, Nitrogen atoms, and vacancies. The $+x$, $+y$, and $+z$ axes are shown using the compass for both the top view and the side view.

the configuration $a_1^1 e_x^{1.5} e_y^{1.5}$. The energy of the ZPL (E_{ZPL}) and the atomic displacement computed for the ES with C_{3v} symmetry are 0.04 eV (4%) greater and 18% smaller than the ones computed for the ES with C_{1h} symmetry. As a result, the computed HRFs, the spectral densities of electron-phonon coupling, and PL line shapes are significantly different depending on the chosen constrained occupations, as shown in Figure 4.10. To correctly describe the coupling with e type phonons in the optical process, $a_1^1 e_x^2 e_y^1$ occupations should be used for CDFT calculations.

At the DDH/HSE level of theory, we observed that the self-consistent cycle within CDFT could not converge by using the configuration $a_1^1 e_x^2 e_y^1$. In such cases, we performed CDFT calculations with the configuration $a_1^1 e_x^{1.5} e_y^{1.5}$, which did not show convergence issues. We then added a correction term to determine the energy of the ZPL (E_{ZPL}) and the equilibrium

structure of the ES based on the results obtained at the PBE level of theory:

$$
\begin{aligned}
E_{\mathrm{ZPL}}\left(a_1^1 e_x^2 e_y^1, \mathrm{DDH/HSE}\right) &= E_{\mathrm{ZPL}}\left(a_1^1 e_x^{1.5} e_y^{1.5}, \mathrm{DDH/HSE}\right) \\
&\quad + \left[E_{\mathrm{ZPL}}\left(a_1^1 e_x^2 e_y^1, \mathrm{PBE}\right) - E_{\mathrm{ZPL}}\left(a_1^1 e_x^{1.5} e_y^{1.5}, \mathrm{PBE}\right)\right], \\
\mathbf{R}\left(a_1^1 e_x^2 e_y^1, \mathrm{DDH/HSE}\right) &= \mathbf{R}\left(a_1^1 e_x^{1.5} e_y^{1.5}, \mathrm{DDH/HSE}\right) \\
&\quad + \left[\mathbf{R}\left(a_1^1 e_x^2 e_y^1, \mathrm{PBE}\right) - \mathbf{R}\left(a_1^1 e_x^{1.5} e_y^{1.5}, \mathrm{PBE}\right)\right],
\end{aligned}
\tag{4.20}
$$

where $E_{\mathrm{ZPL}}\left(a_1^1 e_x^{1.5} e_y^{1.5}, \mathrm{PBE/DDH/HSE}\right)$ and $\mathbf{R}\left(a_1^1 e_x^{1.5} e_y^{1.5}, \mathrm{PBE/DDH/HSE}\right)$ denote the E_{ZPL} and the equilibrium structure of the ES obtained with the configuration $a_1^1 e_x^{1.5} e_y^{1.5}$ at the PBE/DDH/HSE level.

The comparison between TDDFT and CDFT results with the DDH functional was carried out with the configuration $a_1^1 e_x^{1.5} e_y^{1.5}$ in CDFT also because of the convergence issues with the configuration $a_1^1 e_x^2 e_y^1$. We checked that the energy difference between the CDFT calculations with different occupations at the PBE level is small ($\sim$0.04 eV). Hence, we concluded that our TDDFT/CDFT comparison with DDH is meaningful and accurate to $\sim$0.04 eV.

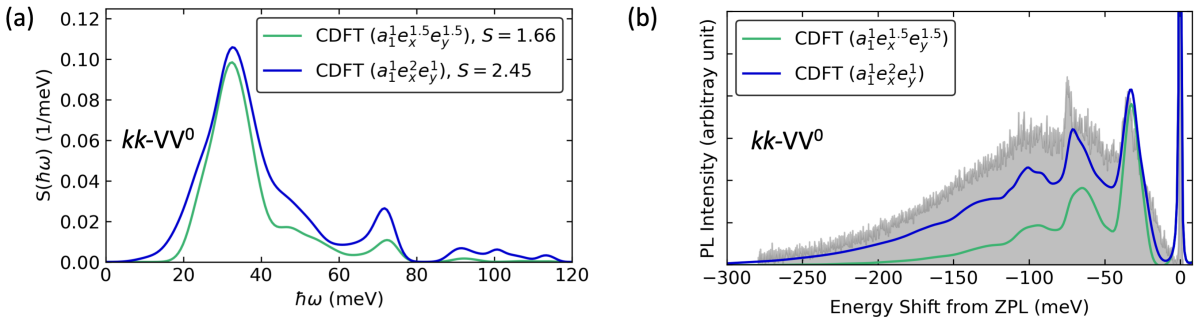

Figure 4.10: Influence of the occupations in CDFT excited-state (ES) calculations on the results. (a) Computed spectral densities of electron-phonon coupling $S(\hbar\omega)$ for the kk-VV^0 center in 4H-SiC. The total Huang-Rhys factor (HRF, S) is given in the legend. (b) Computed photoluminescence (PL) line shapes for the kk-VV^0 center in 4H-SiC. The gray area represents the experimental PL line shape measured at 10 K. Calculations were performed with ($5 \times 5 \times 2$) supercell at the PBE level of theory.

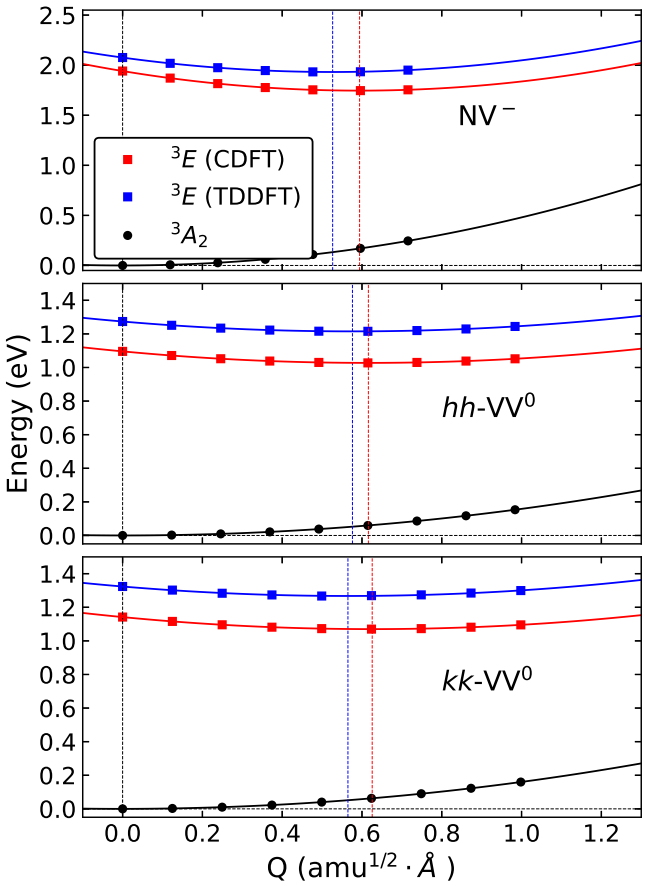

Figure 4.11: Configuration coordinate diagrams describing the total energies of the $^3A_2$ ground state (GS) and the ^3E excited state (ES) along the relaxation path resulting from CDFT with the electronic configuration $a_1^1 e_x^{1.5} e_y^{1.5}$ for the NV^- center in diamond and the hh-VV^0 and the kk-VV^0 centers in 4H-SiC. Calculations are performed at the PBE level of theory. Dashed vertical lines denote the locations of the local minimum by fitting the energy curves with quadratic functions.

4.6.3 Atomic displacements upon optical excitation

Total atomic displacement ΔR and mass-weighted atomic displacement ΔQ are computed for all defect systems at different levels of theory and summarized in Table 4.5.

$$\Delta R = \left(\sum_{\alpha=1}^{N} \sum_{i=x,y,z} \Delta \mathbf{R}_{\alpha i}^2 \right)^{1/2}, \quad \Delta Q = \left(\sum_{\alpha=1}^{N} \sum_{i=x,y,z} M_\alpha \Delta \mathbf{R}_{\alpha i}^2 \right)^{1/2}. \tag{4.21}$$

Here $\Delta\mathbf{R}_{\alpha i} = (\mathbf{R}_{\alpha i})_e - (\mathbf{R}_{\alpha i})_g$ is the atomic displacement of the α-th atom in the i-th direction between the equilibrium structures of the ES and the GS. M_α is the mass of the α-th atom.

One can notice that the magnitude of ΔR and ΔQ follows the relation: HSE > DDH > PBE, which can be related to the stiffness of the bonds. For VV^0 centers in 4H-SiC, ΔR and ΔQ follow the relation: hh-VV^0 > kk-VV^0 > hk-VV^0 in most cases. The same relation is followed by the HRFs, as discussed in Chapter 4.4.2.

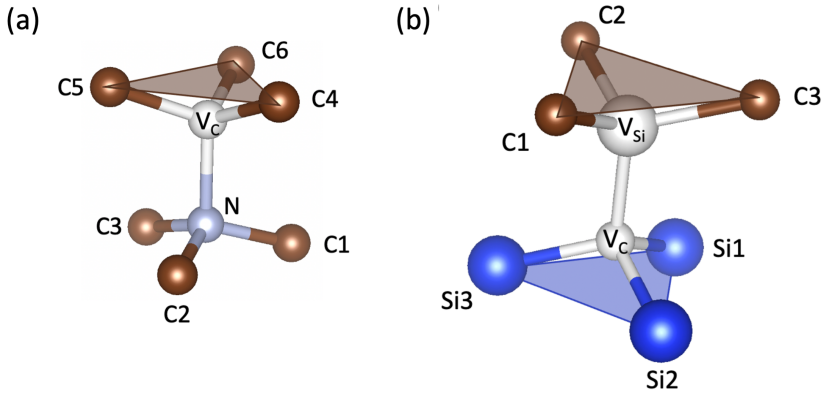

Figure 4.12: Atomic structure of (a) the NV^- center in diamond and (b) the kk-VV^0 center in 4H-SiC. Carbon, nitrogen, and silicon atoms are represented using brown, silver, and blue spheres. Vacancy sites are represented using white spheres. Labels of atoms are used in Table 4.6 and Table 4.7.

We examined the atomic displacements of neighbor atoms upon optical excitation for the NV^- center in diamond and the kk-VV^0 center in 4H-SiC. For the NV^- center, the

Table 4.5: Displacements ΔR (Å) and mass-weighted displacements ΔQ (amu$^{0.5}$ Å) between the equilibrium structures of the ground state (GS) and the excited state (ES) computed at different levels of theory.

Hosts	Defects	PBE		DDH		HSE	
		ΔR	ΔQ	ΔR	ΔQ	ΔR	ΔQ
Diamond	NV^-	0.187	0.653	0.191	0.666	0.200	0.697
4H-SiC	hh-VV^0	0.186	0.785	0.195	0.816	0.200	0.834
	kk-VV^0	0.185	0.763	0.192	0.787	0.198	0.813
	hk-VV^0	0.183	0.759	0.190	0.785	0.200	0.835

Table 4.6: Distances (Å) between neighbor atoms around the NV^- center in diamond in the equilibrium structures of the ground state (GS) and the excited state (ES). N is the nitrogen substituent, and C1, C2, and C3 are the three carbon atoms connected to it. C4, C5, and C6 are three carbon atoms adjacent to the carbon vacancy site, as shown in Figure 4.12.

Atom pairs	PBE		DDH		HSE	
	GS	ES	GS	ES	GS	ES
N−C1	1.472	1.491	1.463	1.482	1.460	1.479
N−C2	1.472	1.490	1.463	1.481	1.460	1.478
N−C3	1.472	1.490	1.463	1.481	1.460	1.478
C4−C5	2.664	2.762	2.639	2.749	2.631	2.744
C4−C6	2.664	2.808	2.639	2.795	2.631	2.790
C5−C6	2.664	2.762	2.639	2.749	2.631	2.744

distances between three carbon atoms around the V_C were computed for both the GS and the ES and summarized in Table 4.6. In the GS structure, three pairs of carbon atoms around the V_C have the same distances due to the C_{3v} symmetry. In the ES structure, all distances and bond lengths are increased because the e defect orbitals are more delocalized than a_1 orbitals. One pair of carbon atoms has longer distances while the other two pairs have shorter distances, indicating that the symmetry is reduced from C_{3v} to C_{1h}. The length of three nitrogen-carbon bonds also shows a similar behavior, but the magnitude of the asymmetric stretching is much smaller. This is consistent with the fact that the defect orbitals are mainly localized on the carbon atoms around the V_C.

For the kk-VV^0 center, the distance between three carbon atoms around the V_{Si} and the distance between three silicon atoms around the V_C were computed for both the GS and the ES and summarized in Table 4.7. In the GS structure, three pairs of carbon atoms and silicon atoms have the same distances due to the C_{3v} symmetry. In the ES structure, all distances and bond lengths are increased because the e defect orbitals are more delocalized than a_1 orbitals. The magnitude of the stretching is greater for carbon pairs than silicon pairs, which is consistent with the localization of defect orbitals. One pair of carbon atoms and silicon atoms has a longer distance while the other two pairs have shorter distances, indicating that the symmetry is reduced from C_{3v} to C_{1h}.

Table 4.7: Distances (Å) between atoms around the kk-VV^0 center in 4H-SiC in the equilibrium structures of the ground state (GS) and the excited state (ES). C1, C2, and C3 are three closet carbon atoms adjacent to the silicon-vacancy site, while Si1, Si2, and Si3 are three closet silicon atoms adjacent to the carbon vacancy site, as shown in Figure 4.12.

Atom pairs	PBE		DDH		HSE	
	GS	ES	GS	ES	GS	ES
C1−C2	3.334	3.456	3.317	3.448	3.289	3.424
C1−C3	3.334	3.465	3.317	3.457	3.289	3.433
C2−C3	3.334	3.456	3.317	3.448	3.289	3.424
Si1−Si2	3.103	3.114	3.099	3.108	3.082	3.088
Si1−Si3	3.103	3.147	3.099	3.140	3.082	3.120
Si2−Si3	3.103	3.114	3.099	3.108	3.082	3.088

4.6.4 Phonons at the level of hybrid functionals

For bulk diamond and 4H-SiC, phonons were calculated with PBE, DDH, and HSE functionals using the $(4 \times 4 \times 4)$ supercell for diamond and the $(5 \times 5 \times 2)$ supercell for 4H-SiC. Vibrational densities of states computed with different functionals are reported in Figure 4.13 for 4H-SiC.

Since it is computationally prohibitive to carry out phonon calculations for defect systems with hybrid functional, we first carried out phonon calculations at the PBE level of theory, and then we assumed that the force constant matrix at the DDH or HSE level is just the one at PBE level multiplied by a constant. Under this hypothesis, the phonon eigenmodes obtained at the PBE level of theory would also diagonalize the dynamical matrix at the DDH/HSE level of theory, and the phonon frequencies at the DDH/HSE level of theory would be proportional to the ones evaluated at PBE:

$$\omega_{k,\mathrm{HSE}} = f_{\mathrm{HSE-PBE}} \cdot \omega_{k,\mathrm{PBE}}, \tag{4.22}$$

where f is a scaling factor, evaluated as the ratio of the highest phonon frequency computed with DDH/HSE to that computed with PBE for the pristine systems (see Table 4.8). The validity of the approximation was examined for bulk pristine systems by computing

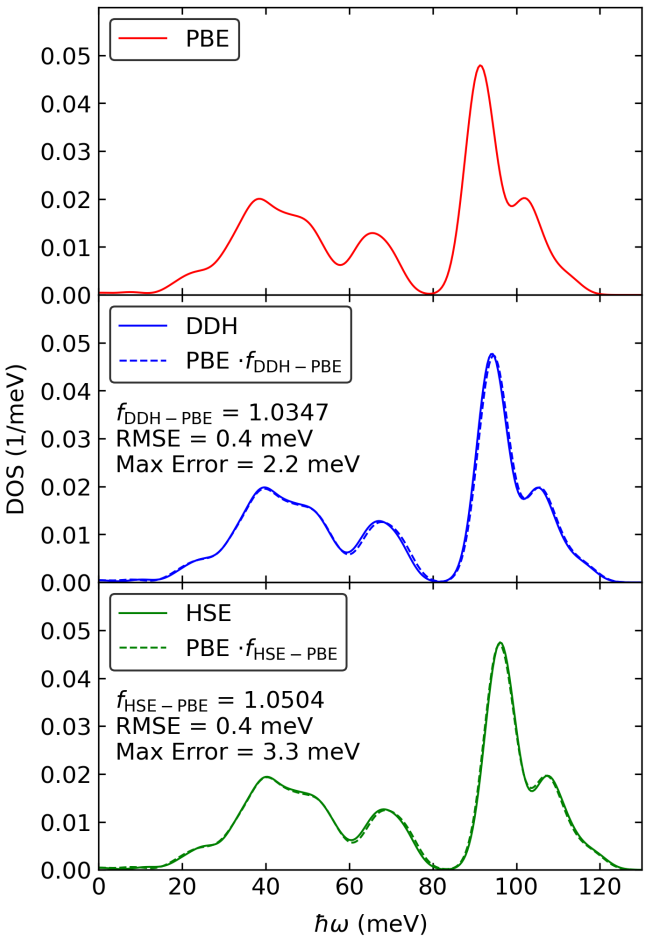

Figure 4.13: Vibrational density of state of bulk 4H-SiC computed at the different levels of theory. Gaussian function with standard deviation $\sigma = 3$ meV was used for broadening. Solid lines represent the results from direct first-principles calculations, and the dashed lines represent the results from approximation defined by Eq. (4.22).

DDH/HSE phonon frequencies using Eq. (4.22). The maximum error, root mean square error (RMSE), and vibrational densities of state were displayed in Figure 4.13. The overall agreement between the vibrational density of state plots computed with Eq. (4.22) is in very close agreement with those from direct first-principles calculations. The maximum error is about 2 to 3 meV, and the RMSE is less than 1 meV, validating the hypothesis. The same scaling factors were used to approximate the DDH/HSE level phonon frequencies for defect systems.

4.6.5 *Extrapolating to the dilute limit*

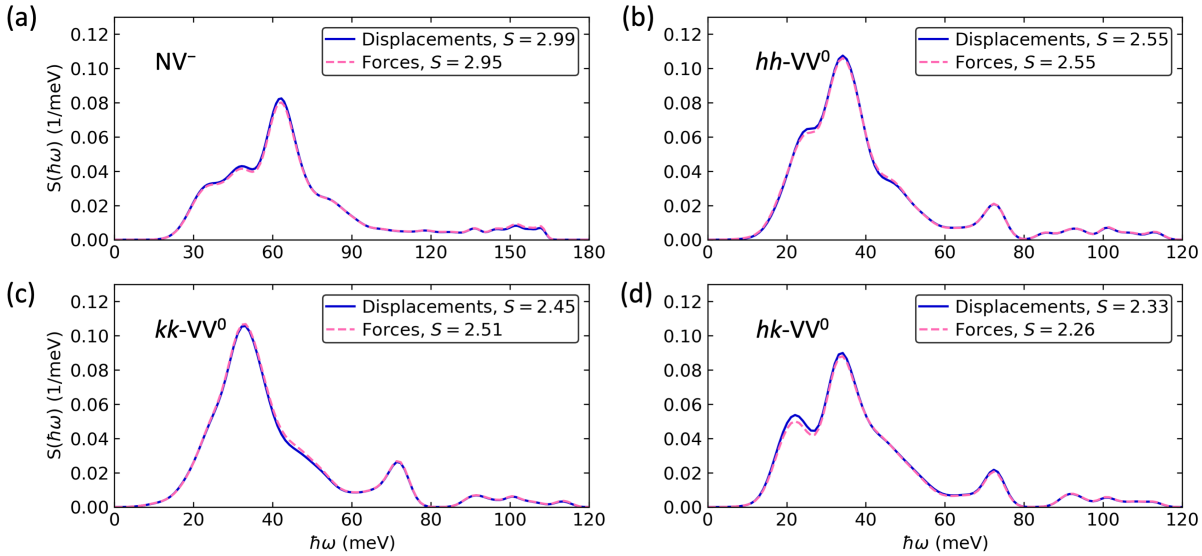

Figure 4.14: Spectral densities of electron-phonon coupling for (a) NV^- center in diamond, (b) *hh*-VV^0, (c) *kk*-VV^0, and (d) *hk*-VV^0 center in 4H-SiC. Calculations are carried out with the $(4 \times 4 \times 4)$ supercell for NV^- and the $(5 \times 5 \times 2)$ supercell for VV^0 centers at the PBE level of theory. Solid blue lines denote results computed using Eq. (4.23), and dashed red lines denote results computed using Eq. (4.24). Total Huang-Rhys factors (HRFs, S) are also given in the legend.

Mass-weighted atomic displacements of the k-th phonon mode, ΔQ_k, are required to compute HRFs. Either the atomic displacements computed between the equilibrium structures of the GS and ES (Eq. (4.23)) or GS forces evaluated at the equilibrium structure of the ES (Eq. (4.24)) can be used to compute ΔQ_k [59, 82].

$$\Delta Q_k = \sum_{\alpha=1}^{N} \sum_{i=x,y,z} \sqrt{M_\alpha} \Delta \mathbf{R}_{\alpha i} \boldsymbol{e}_{k,\alpha i}, \tag{4.23}$$

Table 4.8: Scaling factors of phonon frequencies at different levels of theories defined in Eq. (4.22) for diamond and 4H-SiC.

	$f_{\mathrm{DDH-PBE}}$	$f_{\mathrm{HSE-PBE}}$
Diamond	1.0400	1.0514
4H-SiC	1.0347	1.0504

$$\Delta Q_k = \frac{1}{\omega_k^2} \sum_{\alpha=1}^{N} \sum_{i=x,y,z} \frac{\mathbf{F}_{\alpha i}}{\sqrt{M_\alpha}} \boldsymbol{e}_{k,\alpha i}. \tag{4.24}$$

Here, $\mathbf{e}_{k,\alpha i}$ is the eigenvector of the k-th phonon mode on the α-th atom in the i-th direction. M_α is the mass of the α-th atom, and $\Delta\mathbf{R}_{\alpha i} = (\mathbf{R}_{\alpha i})_e - (\mathbf{R}_{\alpha i})_g$ is the displacement between the ES and the GS equilibrium atomic structures in the i-th direction. $\mathbf{F}_{\alpha i}$ is the GS force on the α-th atom in the i-th direction evaluated at the ES equilibrium structure. These two approaches are equivalent under the harmonic approximation:

$$\Delta\mathbf{F} = \mathbf{H} \cdot \Delta\mathbf{R}. \tag{4.25}$$

Here, $\mathbf{H}$ is the Hessian matrix or the force constant matrix. We used both approaches to compute HRFs and spectral densities of electron-phonon coupling for the NV^- center in diamond with the $(4 \times 4 \times 4)$ supercell and the VV^0 centers with $(5 \times 5 \times 2)$ supercells, as shown in Figure 4.14. The differences in HRFs computed with the two approaches are within 3%, and the spectral densities are almost identical, indicating that the harmonic approximation works well for these defect systems and validating the use of Eq. (4.24) in our work.

To compute HRFs and spectral densities for supercells larger than $(4 \times 4 \times 4)$ for NV^- and $(5 \times 5 \times 2)$ VV^0 centers, both (i) ΔQ_k and (ii) phonons for these supercells are needed. For (i) ΔQ_k, since direct first-principles calculations with these supercells are prohibitive, we used the hypothesis that the forces quickly decay to zero as a function of the distance to the defect center, and the forces computed with the smallest supercell ($(4 \times 4 \times 4)$ for NV^- and $(5 \times 5 \times 2)$ VV^0 centers) are the same as those computed with the larger supercell. Previous work shows that forces 5 Å away from the defect center contribute negligibly to the HRF for the NV^- in diamond [82]. Here, we want to ensure that for VV^0 centers in 4H-SiC, forces computed with the smallest $(5 \times 5 \times 2)$ supercell are sufficient to represent the forces in larger supercells. For this purpose, $(7 \times 7 \times 2)$ supercells were used to model the VV^0 centers. HRFs

and spectral densities were computed using forces computed with $(7 \times 7 \times 2)$ supercells and compared with those computed using forces computed with $(5 \times 5 \times 2)$ supercells, as shown in Figure 4.15. The differences in HRFs are less than 5%, and the spectral densities are almost identical, indicating that forces computed using $(5 \times 5 \times 2)$ supercells are sufficient to evaluate ΔQ_k for larger supercells.

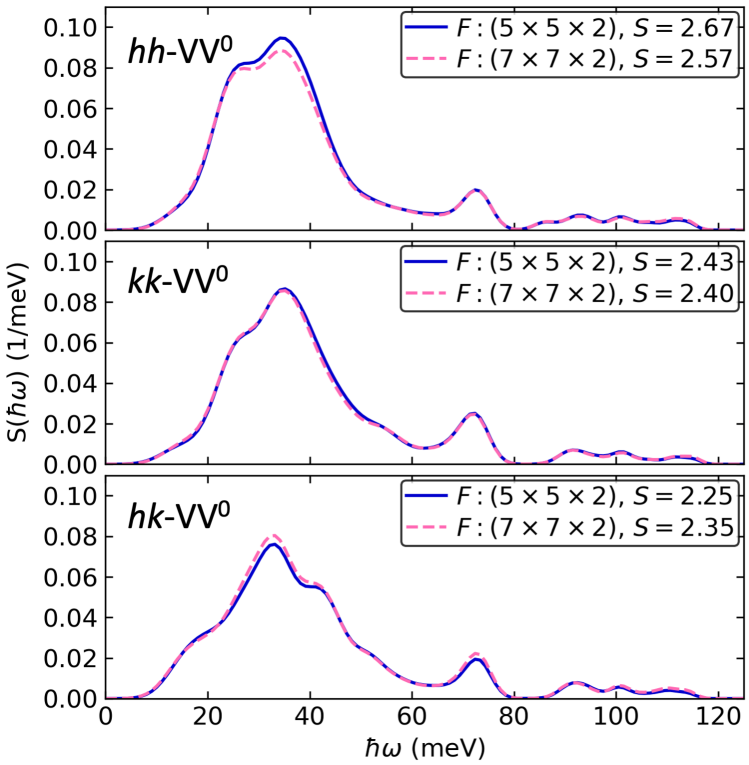

Figure 4.15: Spectral densities of electron-phonon coupling for hh-VV^0, kk-VV^0 and hk-VV^0 centers in 4H-SiC for a $(7 \times 7 \times 2)$ supercell. Calculations are carried out using either the forces computed with a $(5 \times 5 \times 2)$ supercell (solid blue lines) or a $(7 \times 7 \times 2)$ supercell (dashed red lines) at the PBE level of theory. Total Huang-Rhys factors (HRFs, S) are also given in the legend.

We used the force constant matrix embedding scheme proposed by Alkauskas et al. [59, 82, 159] to compute (ii) phonons for supercells larger than $(4 \times 4 \times 4)$ for the NV^- center in diamond and $(5 \times 5 \times 2)$ for VV^0 centers in 4H-SiC. The method is based on the short-range property of the force constant matrix in semiconductors: when the position of one atom changes in a fixed electronic state, the induced force on neighboring atoms decays rapidly

to zero as a function of the distance from this atom. It enables the construction of the force constant matrix of larger supercells using the one computed with the smallest supercells. The force constant matrix is defined as

$$\Phi_{i,j}(\alpha,\beta) = \frac{\partial F_{\alpha i}}{\partial r_{\beta j}}, \tag{4.26}$$

where $F_{\alpha i}$ is the force that acts on atom α in the Cartesian direction i and $r_{\beta j}$ is the displacement of atom β from the equilibrium position in the Cartesian direction j. The force constant matrix of a large defect supercell is constructed as follows. If atoms n and m are separated by a distance larger than a chosen cutoff radius r_{c1}, then the force constant matrix element is set to zero. If both atoms are separated from the defect center by a distance smaller than the cutoff radius r_{c2}, then the force constant matrix element from the actual defect supercell is used. For all other atom pairs, the force constant matrix elements of the bulk system are used. To fulfill the acoustic sum rule, we use the same approach as the one used in Ref [82]:

$$\Phi_{i,i}(\alpha,\alpha) = -\sum_{\beta\neq\alpha} \Phi_{i,i}(\beta,\alpha). \tag{4.27}$$

To obtain components for the embedding process, $(4 \times 4 \times 4)$ supercells were used to compute the force constant matrix for both pristine bulk diamond and the NV^- center in diamond, and $(5 \times 5 \times 2)$ supercells were used to compute the force constant matrix for VV^0 centers in 4H-SiC, and a $(8 \times 8 \times 3)$ supercell with 1536 sites were used to compute the force constant matrix for pristine bulk 4H-SiC. As for the cutoff radius, $r_{c1} = 5$ Å and $r_{c2} = 5$ Å was used for the NV^- in diamond and $r_{c1} = 9.45$ Å and $r_{c2} = 6.75$ Å was used for VV^0 centers in 4H-SiC. The choice of cutoff radii was carefully examined. Taking the kk-VV^0 center in 4H-SiC modeled by the $(5 \times 5 \times 2)$ supercell as the example, HRF and the error of the phonon energies are computed using the force constant matrix from the embedding scheme with different choice of cutoff radius, as shown in Figure 4.16. It can be concluded

that $r_{c1} = 9.45$ Å and $r_{c2} = 6.75$ Å is a good choice: the HRF is only 5% away from the reference value, and the root mean square error (RMSE) of phonon energies is 0.4 meV. Our test on larger supercells points out the existence of an uncertainty of ∼0.2 in the HRF due to the choice of r_{c1}, and we only kept 1 digit for these HRFs.

We examined the convergence of partial HRFs and the spectral density as a function of the supercell size for the kk-VV^0 center in 4H-SiC, as shown in Figure 4.17. By extrapolating to the dilute limit, modes at 23, 33, and 72 meV split into many closely spaced modes, with a simultaneous decrease of their absolute contributions to the total HRF, indicating the existence of quasi-local vibrational modes.

We also examined the computed highest and lowest phonon energy for different supercells. At the PBE level of theory, we find that the lowest phonon energy is 34 meV (11 meV) for the NV^- center in diamond when the $(4 \times 4 \times 4)$ $((12 \times 12 \times 12))$ supercell is used. The lowest phonon energy is 11 meV (5 meV) for VV^0 centers in 4H-SiC when the $(5 \times 5 \times 2)$ $((16 \times 16 \times 5))$ supercell is used. The computed highest phonon energy depends weakly on the supercell size. At the PBE level theory, we find that the highest phonon energy is 162∼163 meV for the NV^- center in diamond, basically the same as the highest bulk phonon energy, 163 meV. The highest phonon energy is 115 meV for VV^0 centers in 4H-SiC, very close to that of the highest bulk phonon energy, 114 meV.

4.6.6 Detailed analysis of spectral densities and vibrational modes

The spectral density of the NV^- center in diamond is dominated by a peak at about 63 meV, which originates from the coupling with a quasi-local vibrational mode [59]. Coupling with other (quasi-)local vibrational modes leads to detailed structures above 130 meV. In the case of VV^0 centers, our calculations showed two peaks at about 34 meV and 72 meV together with detailed structures above 90 meV. The overall intensity of hh-VV^0 is larger than that of kk-VV^0, which is in turn larger than that of hk-VV^0, consistent with the magnitude of

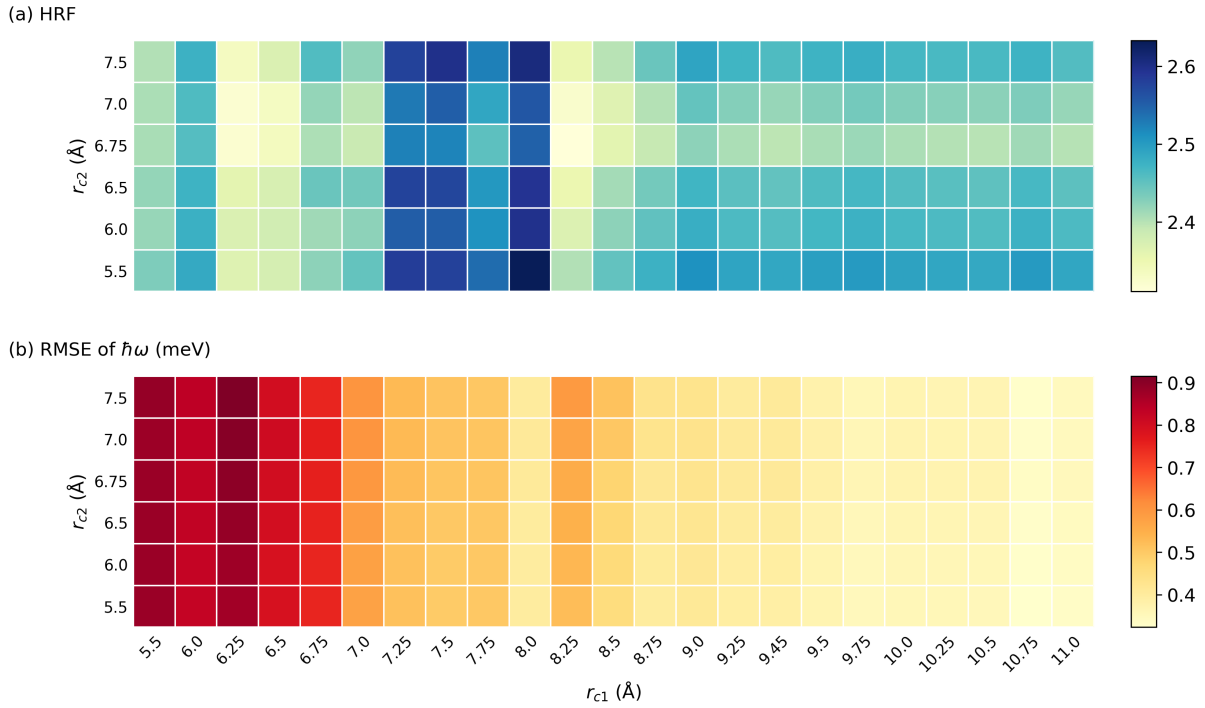

Figure 4.16: (a) Huang-Rhys factor (HRF) as a function of the cutoff radius r_{c1} and r_{c2}. (b) Root mean square error (RMSE) of phonon energies $\hbar\omega$ with those computed from the first-principles calculations as a function of the cutoff radius r_{c1} and r_{c2}. $(5\times5\times2)$ supercell was used for these calculations. Forces and force constant matrix computed at the PBE level of theory were used.

the HRF. We examined the convergence of the HRF and the spectral densities as a function of the supercell size for kk-VV^0 (see Figure 4.17). By extrapolating to the dilute limit, we found that modes at 23, 33, and 72 meV split into many closely spaced ones, with a simultaneous decrease of their absolute contributions, indicating the existence of quasi-local vibrational modes. The same behavior was also observed for hh-VV^0 and hk-VV^0. Spectral densities of hh-VV^0 and kk-VV^0 are similar, with two small differences: (i) the shoulder peak at 23 meV is more pronounced for hh-VV^0; (ii) hh-VV^0 has a small peak at about 86 meV not present for kk-VV^0. The hk-VV^0 spectrum shows an apparent shoulder peak at 22 meV.

We performed phonon (vibrational) modes analysis for VV^0 centers in 4H-SiC to comprehend their relationship with the defect center using the same approach as the one used to

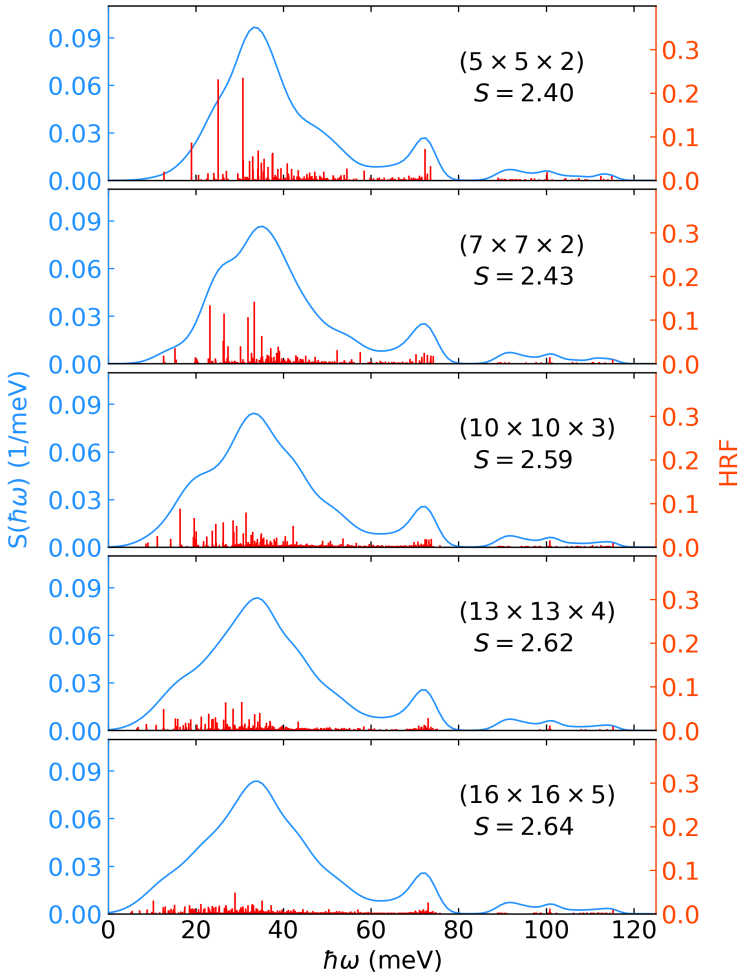

Figure 4.17: Convergence of the spectral density of electron-phonon coupling $S(\hbar\omega)$ and Huang-Rhys factors (HRFs) with respect to the supercell size for the kk-VV^0 center in 4H-SiC computed at the PBE level of theory. Supercells range in size from $(5 \times 5 \times 2)$ (400 atomic sites) to $(16 \times 16 \times 5)$ (10240 atomic sites). Blue lines refer to spectral densities, and the red vertical bars represent the partial HRFs for each phonon mode.

study the NV^- and the SiV^- centers in diamond by Alkauskas et al. [59, 159]. The quasi-local and local vibrational modes were qualitatively characterized by computing the inverse partition ratio (IPR) and localization ratio β_k. the IPR for the k-th vibrational modes is defined as

$$\mathrm{IPR}_k = \frac{1}{\sum_{\alpha=1}^{N} \left(\sum_{i=x,y,z} \mathbf{e}_{k,\alpha i}^2 \right)^2}. \tag{4.28}$$

The IPR reflects the effective number of atoms that participate in a phonon mode; IPR = 1

indicates that only one atom vibrates, while IPR = N indicates all N atoms in the supercell vibrate with the same amplitude. β_k is defined as

$$\beta_k = \frac{N}{\mathrm{IPR}_k}, \tag{4.29}$$

and describes the inverse fraction of atoms in the supercell that vibrate for a given phonon mode; $\beta_k \gg 1$ for quasi-local and local modes. Here we analyzed the vibrational modes for hh-VV^0, kk-VV^0 and hk-VV^0 centers in 4H-SiC by computing IPR and β_k for different supercell sizes, as shown in Figure 4.18 together with results for the pristine 4H-SiC. Three inverted peaks with the energy ∼23 meV, 33 meV, and 72 meV can be identified in the IPR plots with IPRs significantly smaller than those for the pristine 4H-SiC. IPRs for these peaks increase as the supercell size increases, which is a signature of quasi-local modes. The quasi-local modes can also be identified in the β plots as isolated peaks. These quasi-local modes are made of a continuum of vibrations and have significant localization on the atoms around the defect center (see Figure 4.19). The 23 meV quasi-local mode involves asymmetric stretching of three nearest neighbor silicon atoms around $\mathrm{V_C}$. The 33 meV quasi-local mode involves symmetric stretching of three nearest neighbor silicon atoms around $\mathrm{V_C}$. The 72 meV mode involves both symmetric and asymmetric vibrations of three nearest neighbor carbon atoms and nine next nearest neighbor silicon atoms around $\mathrm{V_{Si}}$. Several other inverted peaks with energy at 86 meV, 100 meV, 110 meV, and 115 meV can be identified in the IPR plots with IPRs around 10, indicating the existence of local vibrational modes. Their contributions to the PL line shape are much smaller compared with the quasi-local vibrational modes.

With the knowledge of vibrational modes, we can interpret the observed difference among the spectral densities of VV^0 centers in 4H-SiC. The 23 meV peak in the spectral density originates from the coupling with the mode involving asymmetric vibrations of three nearest neighbor silicon atoms around $\mathrm{V_C}$ where two silicon atoms vibrate with an amplitude smaller than the other silicon atom. We computed the difference of mass-weighted displacements

among these silicon atoms and obtained 0.15 amu$^{0.5}$ Å for hh-VV^0 and 0.07 amu$^{0.5}$ Å for kk-VV^0. This fact indicates that the coupling with the 23 meV mode is stronger for hh-VV^0 and explains the observation that the 23 meV shoulder peak is more notable in the spectral densities for hh-VV^0 than kk-VV^0. For hk-VV^0, the 22 meV mode is more localized with more considerable variance compared with hh-VV^0 and kk-VV^0, as can be seen from the figure of β. It is consistent with the more prominent feature of the 22 meV shoulder peak in the spectral density.

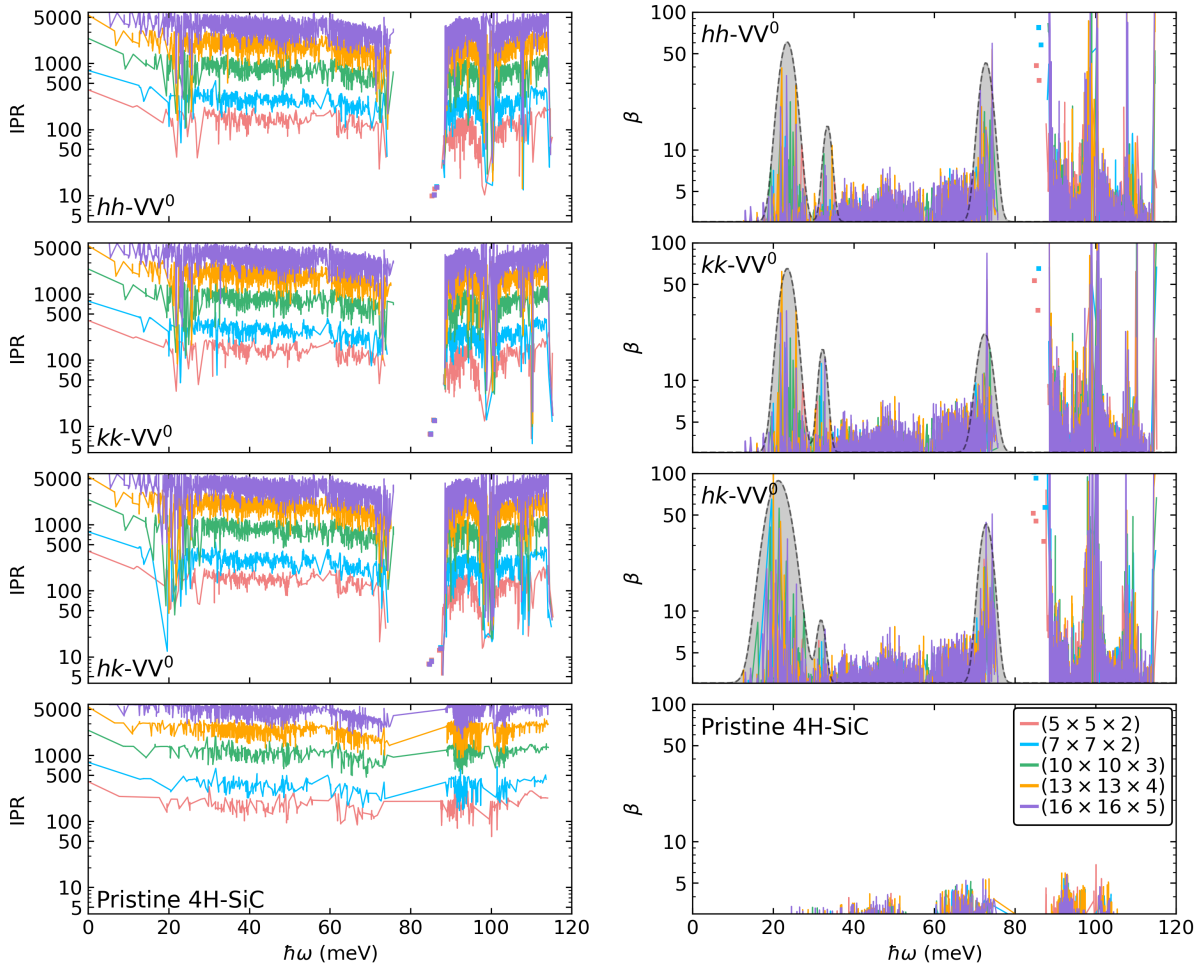

Figure 4.18: Inverse partition ratio (IPR) and localization ratio (β) as a function of phonon energies computed using supercells of different sizes for hh-VV^0, kk-VV^0, and hk-VV^0 centers in 4H-SiC and pristine 4H-SiC. The shaded region denotes the quasi-local vibrational modes.

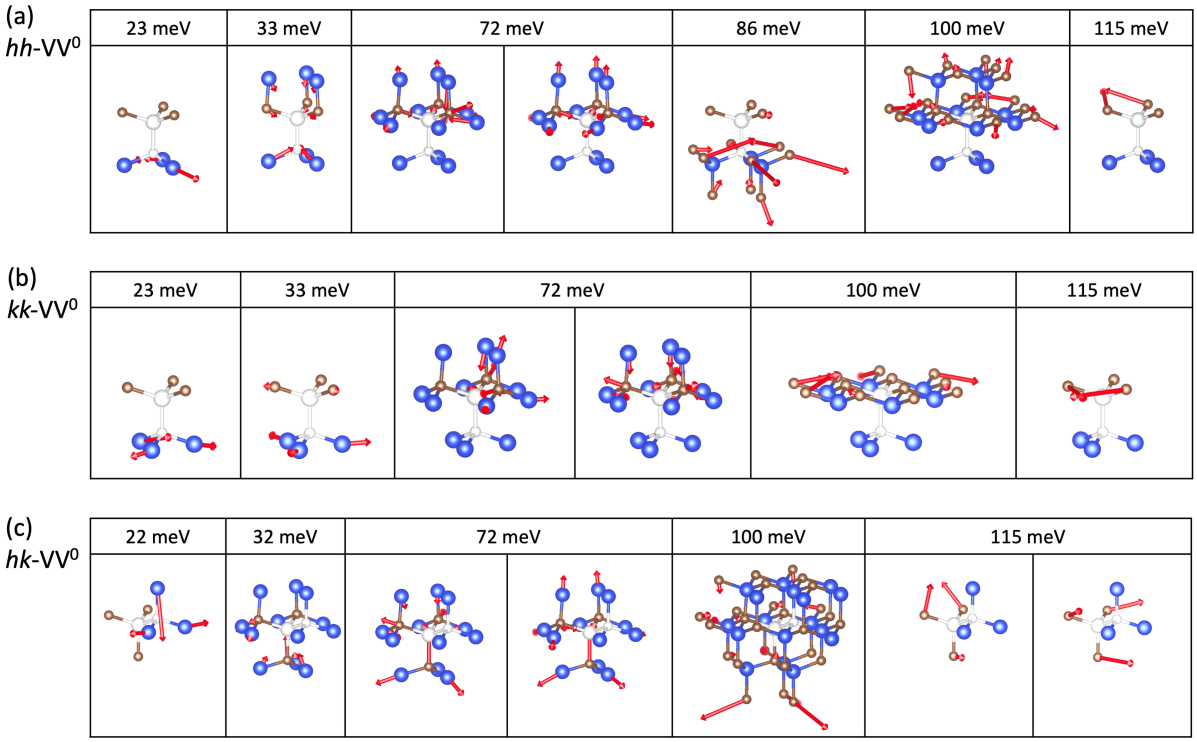

Figure 4.19: Displacement patterns of vibrational modes of (a) hh-VV^0, (b) kk-VV^0, and (c) hk-VV^0 centers in 4H-SiC. Vectors are amplified by a factor of 10. Vibrational modes with energy smaller than 80 meV are quasi-local modes while those with energy greater than 80 meV are local modes.

4.6.7 Calculations of transition dipole moment and radiative lifetime

To validate the Franck-Condon (FC) approximation using the 1D model, we computed the electronic transition dipole moment between the ES and the GS, $|\boldsymbol{\mu}_{eg}|$, for the actual defect systems along the 1D configuration coordinate. By approximating the optical transition from the ES to the GS as a transition between single-particle states, we have that

$$\boldsymbol{\mu}_{eg} = -\frac{e\hbar^2}{(\varepsilon_f - \varepsilon_i)m}\langle\psi_f|\boldsymbol{\nabla}|\psi_i\rangle, \tag{4.30}$$

where e is the charge of the electron, m is the mass of the electron, $\hbar$ is the Planck constant, ψ_f and ψ_i are Kohn-Sham orbitals of defect levels involved in the optical transition, and ε_f and ε_i are the corresponding energies. To validate the correctness of the calculation,

we compared the radiative lifetime $\tau_{\rm rad}$ at the PBE level of theory. $\tau_{\rm rad}$ is related to the radiative emission rate $\Gamma_{\rm rad}$ by

$$\Gamma_{\rm rad} = \frac{1}{\tau_{\rm rad}} = \frac{nE_{\rm ZPL}^3 |\boldsymbol{\mu}_{eg}|^2}{3\pi\epsilon_0 c^3 \hbar^4}, \tag{4.31}$$

where $n = 2.4$ and $n = 2.6473$ are the refractive index of diamond and 4H-SiC, respectively. $E_{\rm ZPL} = 1.945$ eV and $E_{\rm ZPL} = 1.096$ eV are the experimental ZPL energies of the NV^- center in diamond and the kk-VV^0 center in 4H-SiC, respectively. ϵ_0 is the vacuum permittivity, and c is the speed of light in vacuum. For the NV^- in diamond, the computed lifetime is 12.4 ns (10.3 ns) when the equilibrium atomic structure of GS (ES) is used. It is in good agreement with a previous theoretical result of 12.2 ns [221] and the experimental result of 12 ns [62]. For the kk-VV^0 in 4H-SiC, the computed lifetime is 36.8 ns (31.4 ns) when the equilibrium atomic structure of the GS (ES) is used. It is in good agreement with a previous theoretical result 38.49 ns [222].

We have numerically computed the electronic transition dipole moment $|\boldsymbol{\mu}|$ as a function of the configuration coordinate Q for the NV^- center in diamond and the kk-VV^0 center in 4H-SiC, as shown in Figure 4.20. A linear dependence with a relative change of about 10% between the equilibrium atomic structures of GS and ES can be found. The derivative of $|\boldsymbol{\mu}|$ with respect to Q is then used to compute the Franck-Condon Herzberg-Teller (FCHT) and Herzberg-Teller (HT) terms of the PL line shape using the one-dimensional (1D) model:

$$L_{\rm FC}(\hbar\omega, T) \propto \omega^3 \sum_i \sum_j P_{ej}(T) \left|\boldsymbol{\mu}_{eg}^0\right|^2 \left|\langle \phi_{n^{ej}} | \phi_{n^{gi}} \rangle\right|^2 \delta\left(E_{\rm ZPL} + E_{ej} - E_{gi} - \hbar\omega\right), \tag{4.32}$$

$$\begin{aligned} L_{\rm FCHT}(\hbar\omega, T) \propto 2\omega^3 \sum_i \sum_j P_{ej}(T) \boldsymbol{\mu}_{eg}^0 \frac{d\boldsymbol{\mu}_{eg}^0}{dQ} \langle \phi_{n^{ej}} | \phi_{n^{gi}} \rangle \langle \phi_{n^{gi}} | Q | \phi_{n^{ej}} \rangle \\ \times \delta\left(E_{\rm ZPL} + E_{ej} - E_{gi} - \hbar\omega\right), \end{aligned} \tag{4.33}$$

$$L_{\mathrm{HT}}\left(\hbar\omega, T\right) \propto \omega^3 \sum_i \sum_j P_{ej}\left(T\right) \left|\frac{d\boldsymbol{\mu}_{eg}^0}{dQ}\right|^2 \left|\left\langle \phi_{n^{gi}} \middle| Q \middle| \phi_{n^{ej}} \right\rangle\right|^2 \delta\left(E_{\mathrm{ZPL}} + E_{ej} - E_{gi} - \hbar\omega\right). \tag{4.34}$$

Here $\boldsymbol{\mu}_{eg}^0$ is $\boldsymbol{\mu}_{eg}$ at $Q = 0$, and $\frac{d\boldsymbol{\mu}_{eg}^0}{dQ}$ is the derivative of $\boldsymbol{\mu}_{eg}$ at $Q = 0$.

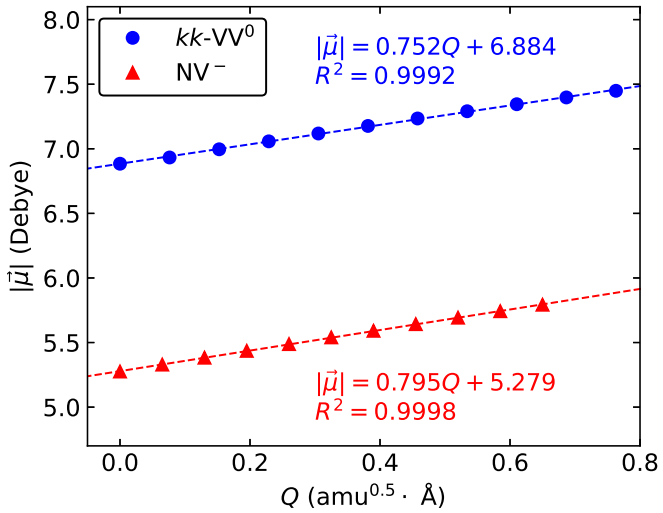

Figure 4.20: Norm of the calculated transition dipole moment $|\boldsymbol{\mu}|$ between the ground state and the excited state as a function of the configuration coordinate Q for the NV^- center in diamond and the kk-VV^0 center in 4H-SiC. Calculations are performed at the PBE level of theory with a $(4 \times 4 \times 4)$ supercell for the NV^- center in diamond and a $(7 \times 7 \times 2)$ supercell for the kk-VV^0 center in 4H-SiC. The parameters of the linear fits are reported in the figure.

CHAPTER 5

VIBRATIONALLY RESOLVED OPTICAL EXCITATIONS OF THE NITROGEN-VACANCY CENTER IN DIAMOND

This chapter is adapted with permission from Y. Jin, M. Govoni, and G. Galli. npj Computational Materials, 8(1), 238 (2022). https://doi.org/10.1038/s41524-022-00928-y.

A comprehensive description of the optical cycle of spin defects in solids requires an understanding of the electronic and atomistic structure of states with different spin multiplicities, including singlet states, which are particularly challenging from a theoretical standpoint. We present a general framework, based on spin-flip time-dependent density function theory, to determine the excited state potential energy surfaces of the many-body singlet states of spin defects; we then predict the vibrationally resolved absorption spectrum between singlet shelving states of a prototypical defect, the nitrogen-vacancy center in diamond. Our results, which are in very good agreement with experiments, provide an interpretation of the measured spectra and reveal the key role of specific phonons in determining absorption processes and the notable influence of non-adiabatic interactions. The insights gained from our calculations may be useful in defining strategies to improve infrared absorption-based magnetometry and optical pumping schemes. The theoretical framework developed here is general and applicable to a variety of other spin defects and materials.

5.1 Introduction

Spin defects in semiconductors and insulators have attracted considerable attention in the last decade as promising platforms to realize quantum technologies [27]. For example, it has been shown that simple point defects such as the negatively charged nitrogen-vacancy (NV^-) in diamond [182] may be used as quantum bits (qubits), where the qubit initialization and

readout are realized through an optical spin-polarization cycle between the triplet ground state, a triplet excited state and two shelving singlet states [73, 148, 151, 223]. The ability to initialize and readout the NV^- center in diamond has led to numerous proposals for quantum technology applications [62, 63], including quantum sensing [65, 66] and communication [67], and possibly quantum computation [71, 72].

While the optical and magnetic properties of the triplet ground and the first triplet excited state of the NV^- center have been extensively investigated using density functional theory (DFT) [59, 63, 81–83, 110, 194, 224], robust first-principles predictions of the properties of the singlet shelving states are not yet available. The reason is two-fold: the description of the electronic structure of these singlet states requires a higher level of theory than DFT to account for their strongly correlated (multiconfigurational) nature; in addition, the determination of their atomistic structure requires techniques capable of optimizing complex excited state potential energy surfaces (PESs), beyond DFT with constrained occupations (ΔSCF). Important progress has been reported in using high-level theories to investigate the electronic structure of the shelving singlets of the NV^- center, at fixed geometries; these theories include many-body perturbation theory (GW and the solution of the Bethe-Salpeter Equation (BSE) [225]), quantum chemistry methods, e.g., complete active space self-consistent field (CASSCF) [226], the diagonalization of effective Hamiltonian derived within the constrained random phase approximation (CRPA) [154], and a quantum embedding theory (QDET) [85–88, 92, 95]. However, all these approaches have been limited to the evaluation of vertical excitation energies at given geometries and the PESs of the singlet states, and their vibrationally resolved optical spectra have not been predicted from first principles. In a pioneering work, Thiering and Gali [73] investigated optical transitions and inter-system crossings involving singlet states based on a model Hamiltonian parameterized by DFT calculations. However, they included parameters fitted to experiments, e.g., the energy spacing between the singlet states, and overall, they obtained a fair agreement between

experiments and computed absorption spectra.

With the goal of providing a comprehensive description of the optical cycle of the NV^- center, we investigate the electronic and atomistic structure of the singlet states involved in the optical cycle. We present a general framework based on the implementation of spin-flip time-dependent density function theory (TDDFT) [39, 44, 100, 101, 103–105] using a plane-wave basis set, which allows for a robust determination of the excited states PESs. We use both the semi-local functional by Perdew, Burke, and Ernzerhof (PBE) [31] and dielectric dependent hybrid (DDH) functionals [33] and we evaluate analytical forces acting on the nuclei [17, 102]. By computing many-body electronic states, equilibrium geometries, and phonons of the singlet states, we successfully predict the infrared vibrationally resolved absorption spectrum [147] between singlet shelving states using the Huang-Rhys (HR) theory [59, 60, 82, 83]. Our results, which are in very good agreement with experiments, provide an interpretation of the measured spectra and reveal the key role of specific phonons in determining absorption processes, and the notable influence of non-adiabatic interactions. The insights gained from our calculations may be useful in defining strategies to improve infrared-absorption-based magnetometry [227–230] and optical pumping schemes. The theoretical framework developed and used here is general and applicable to a variety of other spin defects and materials.

The rest of the paper is organized as follows. We first present our electronic structure calculations of the many-body electronic states of the NV^- center at a fixed geometry, followed by the determination of their PESs. We then discuss electron-phonon coupling and finally present the vibrationally resolved optical absorption spectrum of the spin-defect. We close the paper with a discussion and summary of all the results.

5.2 Methodology

5.2.1 Electronic structure calculations

The ground state electronic structure of the NV^- center in diamond was obtained using DFT and the plane-wave pseudopotential method, as implemented in the Quantum Espresso package [139, 207, 208]. We used SG15 ONCV norm-conserving pseudopotentials [141, 142] and the semi-local functional by Perdew, Burke, and Ernzerhof (PBE) [31] and the dielectric dependent hybrid (DDH) functional [33]. The fraction of exact exchange used in the DDH functional is the inverse of the macroscopic dielectric constant of the system as reported in Ref. [33, 126]. The plane-wave energy cutoff was set to 85 Ry when using the PBE functional and to 60 Ry for the DDH functional. We used a $(3 \times 3 \times 3)$ supercell containing 216 atomic sites for the NV^- center in diamond, with the lattice constant optimized for each functional [83]. The convergence of our results for VEEs with respect to the supercell size is reported in Chapter 5.5.1. The Brillouin zone of the supercell was sampled with the Γ point.

Excited states were computed using the TDDFT method within the Tamm-Dancoff approximation. We obtained the energies and eigenvectors of low-lying excited states by iterative diagonalization of the linearized Liouville operator, as implemented in the WEST code [44, 121]. An approximated non-collinear kernel was included in the spin-flip TDDFT calculations [100, 101, 103]. Analytical forces on nuclei in TDDFT were evaluated using the Lagrangian formulation by Hütter [17]. The equilibrium atomic geometries of excited states were obtained by minimizing the nuclear forces below the threshold of 0.01 eV/Å.

5.2.2 Phonon calculations

Phonon modes of the NV^- center were computed using the frozen phonon approach, with configurations generated with the PHONOPY package [45] and a displacement of 0.01 Å from equilibrium geometries of the $^3A_2$ and $^1A_1$ states, respectively. To compute the phonon

modes of the $^3A_2$ state, DFT self-consistent calculations were conducted at displaced configurations. As for the phonon modes of the $^1A_1$ state, a DFT self-consistent calculation, and an additional TDDFT excited state calculation were performed at each displaced configuration. Phonon calculations were performed only with the PBE functional due to the high computational cost of hybrid DFT calculations. We estimated hybrid-DFT phonons by using a scaling factor [83]. Phonon modes are extrapolated to the dilute limit, approximated by a $(12 \times 12 \times 12)$ supercell cell with 13824 atomic sites, using the force constant matrix embedding approach proposed by Alkauskas et al. [59, 82].

5.2.3 Huang-Rhys factors and spectral functions

We write the absorption line shape as [221]

$$\sigma_{\text{abs}}(\hbar\omega, T) \propto (\hbar\omega) A_{\text{abs}}(\hbar\omega - E_{\text{ZPL}}, T), \tag{5.1}$$

where E_{ZPL} is the energy of the zero-phonon line, and $\hbar\omega$ is the energy of the absorbed photon. T is the temperature. To be consistent with experiment [147], $T = 10$ K was used in the calculation of absorption line shape. The absorption spectral function is computed using the generating function approach [59, 205, 206]

$$A_{\text{abs}}(\hbar\omega, T) = \frac{1}{2\pi} \int_{-\infty}^{\infty} \mathrm{e}^{\mathrm{i}\omega t} G_{\text{abs}}(t, T) \mathrm{e}^{-\frac{\lambda|t|}{\hbar}} \mathrm{d}t, \tag{5.2}$$

where $\lambda = 0.1$ meV was used in our calculation to account for the broadening of the line shape. The generating function is written as

$$\begin{aligned} G_{\text{abs}}(t, T) = \exp\Bigg[& \int_{-\infty}^{\infty} S(\hbar\omega) e^{-\mathrm{i}\omega t} \mathrm{d}(\hbar\omega) - \sum_k S_k \\ & + \int_{-\infty}^{\infty} C(\hbar\omega, T) e^{-\mathrm{i}\omega t} \mathrm{d}(\hbar\omega) + \int_{-\infty}^{\infty} C(\hbar\omega, T) e^{\mathrm{i}\omega t} \mathrm{d}(\hbar\omega) - 2 \sum_k \overline{n}_k(T) S_k \Bigg], \end{aligned} \tag{5.3}$$

where $\overline{n}_k(T)$ is the average occupation number of the kth phonon mode. $S(\hbar\omega)$ and $C(\hbar\omega, T)$ are the spectral densities of electron-phonon coupling,

$$S(\hbar\omega) = \sum_k S_k \delta(\hbar\omega - \hbar\omega_k), \quad C(\hbar\omega, T) \ = \sum_k \overline{n}_k(T) S_k \delta(\hbar\omega - \hbar\omega_k). \tag{5.4}$$

In actual calculations, the δ functions are replaced by Gaussian functions, and the broadening σ_k is varied linearly from 6 to 2 meV with the phonon energy, to account for the continuum of phonon modes participating in the optical transition. The HR factor S_k is computed as

$$S_k = \frac{\omega_k \Delta Q_k^2}{2\hbar}. \tag{5.5}$$

where ΔQ_k is the mass-weighted displacement along the kth mode, evaluated as

$$\Delta Q_k = \frac{1}{\omega_k^2} \sum_{\alpha=1}^{N} \sum_{i=x,y,z} \frac{\mathbf{F}_{\alpha i}}{\sqrt{M_\alpha}} \mathbf{e}_{k,\alpha i}. \tag{5.6}$$

Here, M_α is the mass of the αth atom. For the ${}^1E \rightarrow {}^1A_1$ absorption, $\mathbf{F}$ represents the forces of the ${}^1A_1$ state evaluated at the equilibrium geometry of the ${}^1E$ state. ω_k ($\mathbf{e}_k$) is the frequency (eigenvector) of the kth phonon mode of the ${}^1A_1$ state.

Similarly, the PL line shape of the ${}^3A_2 \rightarrow {}^3E$ transition can be computed as [221]

$$I(\hbar\omega, T) \propto (\hbar\omega)^3 A_{\text{emi}}(E_{\text{ZPL}} - \hbar\omega, T). \tag{5.7}$$

Here, the emission spectral function is calculated using the generating function built on HR factors computed with forces of the ${}^3A_2$ state, evaluated at the equilibrium structure of the ${}^3E$ state and with the phonons of the ${}^3A_2$ state. To be consistent with the experiment [59], $T = 8$ K was used in the calculation of the PL line shape.

5.3 Results

5.3.1 Many-body electronic states and vertical excitation energies

As is well known, the NV^- center in diamond is composed of a nitrogen impurity and an adjacent carbon vacancy (V_C) (see Figure 5.1). The defect has C_{3v} symmetry, with three orbitals within the band gap of diamond (one a_1 and twofold-degenerate e orbitals), localized on three carbon sites in the vicinity of V_C. Hereafter, we denote the spin up (down) defect orbitals as a_1, e_x, e_y ($\overline{a}_1$, $\overline{e}_x$, $\overline{e}_y$). The low-lying many-body triplet states are denoted as $^3A_2$ (ground state) and ^3E and the singlet states as ^1E and $^1A_1$ [75, 76]. In the $m_s = 1$ sublevel of the $^3A_2$ ground state, a_1, e_x, e_y and $\overline{a}_1$ are occupied by four electrons, while $\overline{e}_x$, $\overline{e}_y$ are empty, and its electronic configuration is represented by the Slater determinant $|\overline{e}_x\overline{e}_y\rangle$ in the hole notation. Similarly, phonons modes of the NV^- center are also labeled as a_1, a_2, and e type according to the C_{3v} point group.

We computed the vertical excitation energies (VEEs) of the triplet ^3E and singlet states ^1E and $^1A_1$ with respect to the $^3A_2$ ground state using TDDFT and the semi-local functional PBE (TDDFT@PBE) and hybrid functional DDH (TDDFT@DDH), with the aim of establishing the accuracy of the chosen electronic structure methods, before proceeding with structural optimizations. Our results are shown in Figure 5.2, together with those of other calculations [88, 154, 225, 226] and inferred experimental values [143, 146, 149, 231]. Irrespective of the functional, TDDFT correctly predicts the ordering of singlet and triplet excited states. However, at the PBE level of theory, TDDFT underestimates the energies of the ^3E and the $^1A_1$ states with respect to the $^3A_2$ ground state compared to experiment; the agreement is improved when using the hybrid functional DDH, where the inclusion of a portion of Hartree-Fock exact exchange interaction provides a more accurate description of excitonic effects. The latter yields the energy of ^3E in good accord with GW-BSE results [225], but those of the ^1E and $^1A_1$ states differ, likely due to the fact that, in contrast to

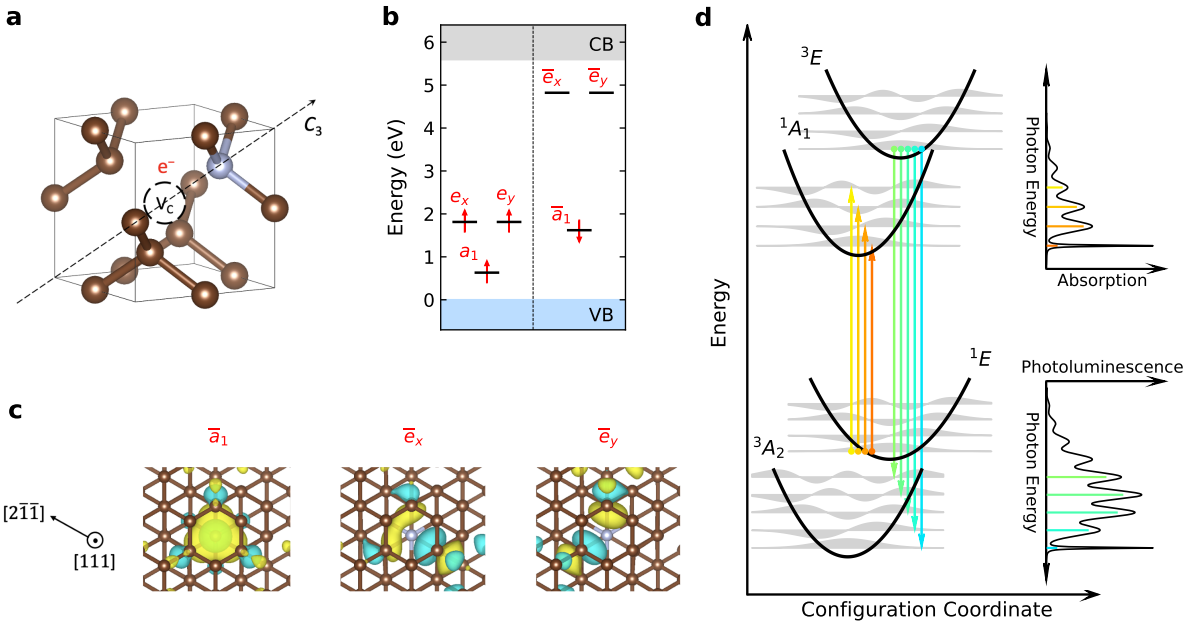

Figure 5.1: Description of the NV^- center in diamond. **a** Ball and stick representation, with the vacancy depicted as a circle in the middle of the diamond cage, and the carbon and nitrogen atoms represented by brown and gray spheres, respectively. The defect has C_{3v} symmetry, with a threefold rotation axis (C_3) parallel to the $\langle 111 \rangle$ axis of diamond. **b** Position of the single-particle defect levels in the band gap of diamond, labeled according to the irreducible representation of the C_{3v} group, and computed by spin unrestricted density functional theory calculations with the DDH hybrid functional [33]. **c** Isosurfaces of the square moduli of the single particle orbitals associated with the defect levels. The color (yellow/light blue) represents the sign (+/−) of the orbital. **d** Schematic diagram illustrating optical processes leading to the photoluminescence (PL) of the $^3E \rightarrow {}^3A_2$ transition and the absorption of the $^1E \rightarrow {}^1A_1$ transition (see text). For ease of graphical representation, the potential energy surfaces are shown as parabolas. Vibrational wavefunctions are schematically shown in gray. Colored arrows represent optical transitions at 0 K. PL and absorption line shapes containing sharp zero-phonon lines and broad phonon side bands are shown as insets.

GW-BSE, in TDDFT an approximate non-collinear spin-flip kernel is introduced to describe spin-flip excitations.

In spite of the correct ordering, the VEEs obtained at the TDDFT@DDH level of theory are an overestimate, especially for singlets, relative to the experimental values. To understand the origin of this discrepancy we compared the many-body wavefunctions obtained with TDDFT with those computed with QDET [88]; the latter includes double and higher

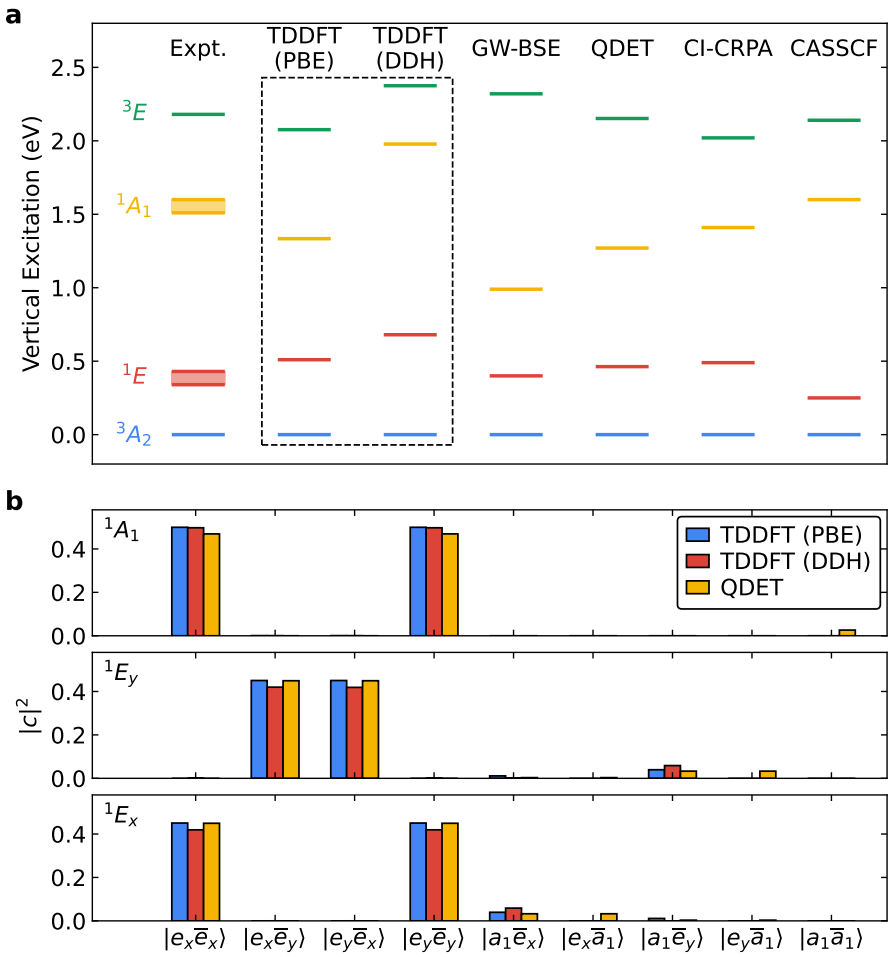

Figure 5.2: Many-body electronic states of the NV^- center in diamond. **a** Vertical excitation energies (VEEs) of the low-lying many-body electronic states at the ground state geometry, computed using time dependent density functional theory (TDDFT). The experimentally inferred VEE of the ^3E state and zero-phonon absorption energies of the $^1A_1$ and ^1E states are from Ref. [143, 146, 149, 231]. We also report theoretical results obtained using *GW* and the Bethe-Salpeter Equation (BSE) [225]; results obtained from the quantum defect embedding theory (QDET) [88]; results obtained from the constrained random-phase approximation solved by configuration interaction (CI-CRPA) [154]; and quantum chemistry results for clusters from complete active space self-consistent field (CASSCF) [226] calculations. **b** Contribution of Slater determinants of single excitation ($|e_x\bar{e}_x\rangle$, $|e_x\bar{e}_y\rangle$, $|e_y\bar{e}_x\rangle$, $|e_y\bar{e}_y\rangle$, $|a_1\bar{e}_x\rangle$ and $|a_1\bar{e}_x\rangle$) and double excitation ($|e_x\bar{a}_1\rangle$, $|e_y\bar{a}_1\rangle$ and $|a_1\bar{a}_1\rangle$) with respect to the $^3A_2$ ground state represented by Slater determinant $|\bar{e}_x\bar{e}_y\rangle$ to the wavefunction of the singlet states, as obtained from TDDFT and QDET [88] calculations. Slater determinants are denoted in the hole notation, and their contributions to the total wavefunction are given in terms of the coefficients defined in Eq. (5.8) (see text). Both TDDFT and QDET calculations are performed at the geometry of the $^3A_2$ ground state with C_{3v} symmetry.

order excitations from the $^3A_2$ ground state, which is represented by the Slater determinant $|\overline{e}_x\overline{e}_y\rangle$ in our spin unrestricted DFT calculations. These excitations are not included in the TDDFT calculations presented here (and also not included in the GW-BSE calculations of Ref. [225]. In QDET, the defect states are described by an effective many-body Hamiltonian diagonalized exactly by full configuration interaction (CI), and hence, the many-body wavefunction contains higher-order excitations. The Hamiltonian includes the interaction of the defect and the solid where it is embedded through an effective dielectric screening. The many-body electronic wavefunctions $|\Phi_i\rangle$ are written as linear combinations of Slater determinants $|\Psi_n\rangle$:

$$|\Phi_i\rangle = \sum_n c_n^i |\Psi_n\rangle \,, \tag{5.8}$$

where $|c_n^i|^2$ represents the contribution of the n-th Slater determinant to the i-th many-body electronic wavefunction. The Slater determinants with contributions to the total wavefunction larger than 1% are reported in Figure 5.2 and in Table 5.2 for the three singlet states, for both QDET and spin-flip TDDFT calculations. Note that we use $^1A_1^{(0)}$, $^1E_x^{(0)}$ and $^1E_y^{(0)}$ to denote states with $C_{3\mathrm{v}}$ symmetry, and in Chapter 5.3.2 we use $^1A_1$ and ^1E to denote singlet states in geometrical configurations where the $C_{3\mathrm{v}}$ symmetry is not preserved. As shown in Figure 5.2, the major contributions to the many-body electronic states $^1A_1^{(0)}$, $^1E_x^{(0)}$ and $^1E_y^{(0)}$ come from linear combinations of Slater determinants with only single excitations, which are accounted for when using spin-flip TDDFT, and yield contributions similar to QDET. However, QDET calculations show an additional, nonnegligible ($\sim$ 3%) contribution to the total wavefunction coming from determinants containing double excitations that cannot be described by TDDFT: $|a_1\overline{a}_1\rangle$, $|e_x\overline{a}_1\rangle$, and $|e_y\overline{a}_1\rangle$, for $^1A_1^{(0)}$, $^1E_x^{(0)}$ and $^1E_y^{(0)}$, respectively.

By adding the contributions of double excitations to our spin-flip TDDFT results, using perturbation theory, we find that the energies of the $^1A_1$ and ^1E states decrease by $0.2 \sim 0.3$ eV, resulting in a better agreement with experiment and QDET values (see Chapter 5.5.2).

Hence, we conclude that the absence of double excitations in the TDDFT description leads to a moderate overestimate of the energy of singlets relative to QDET results. In summary, TDDFT calculations yield results for VEEs in good (albeit not perfect) agreement with those of QDET and experiments, and account for the majority of excitations entering the many-body wavefunction of the NV^- center, giving us confidence that the geometries of singlet manifolds obtained using spin-flip TDDFT and all single excitations are reliable.

5.3.2 Potential energy surfaces of electronic excited states

Having established the accuracy of TDDFT in describing VEEs, we proceed to optimize the geometry of the system in each excited state using TDDFT forces acting on nuclei. The PESs of singlets are computed by carrying out calculations on two specific geometrical paths, described by collective variables (CVs) defined below. We then define an effective Hamiltonian for ionic and electronic degrees of freedom, including electron-phonon interaction, and we investigate the non-adiabatic coupling between many-body electronic states and lattice vibrations.

We start by describing the optimized geometrical configurations of excited electronic states, quantified in terms of mass-weighted atomic displacements and Franck-Condon shifts (see Chapter 5.5.3). We find that the optimized geometry of the triplet excited state ^3E exhibits a significant displacement of $\sim$0.6 amu$^{0.5}$ Å and a Franck-Condon shift of $\sim$200 meV, relative to the geometry of the ground state. These results obtained with TDDFT forces are consistent with our previous study, where geometry optimization of the triplet excited state was obtained with ΔSCF, and results were validated against photoluminescence (PL) measurements [83]. The singlet states cannot be simulated with ΔSCF. Hence, we optimize their geometry using forces computed with spin-flip TDDFT and a plane-wave basis set. The two singlet states have rather different optimized configurations: that of the $^1A_1$ state is similar to the optimized geometry of the ground state (with a negligible atomic displacement

of $\sim$0.1 amu$^{0.5}$ Å and a Franck-Condon shift of 17 meV), while the ^1E state exhibits a displacement of $\sim$0.4 amu$^{0.5}$ Å and a Franck-Condon shift of 60$\sim$100 meV.

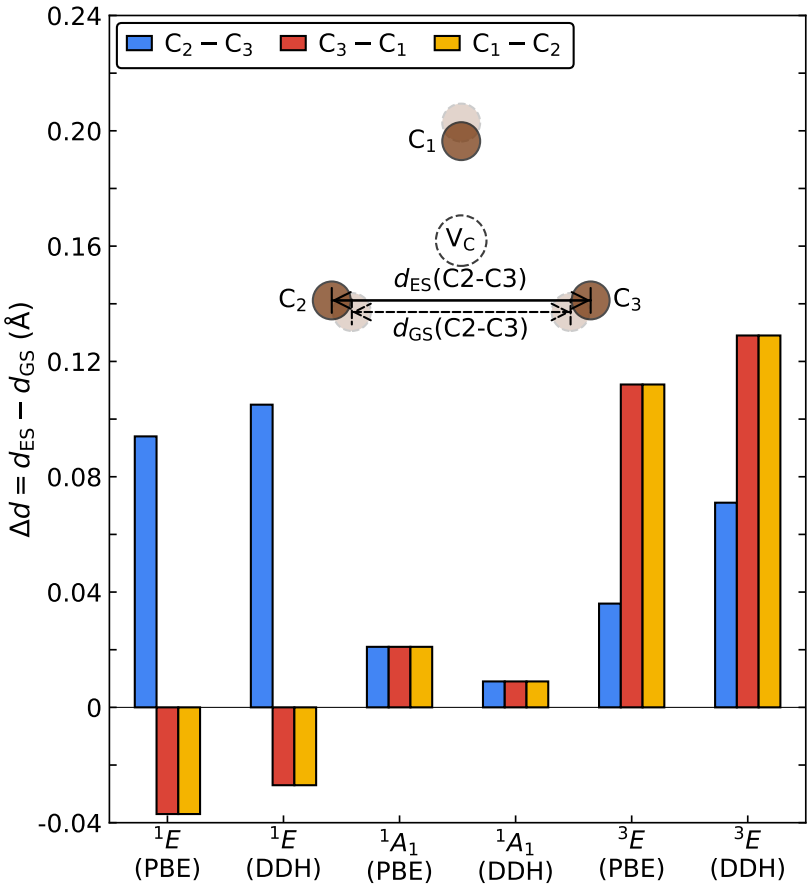

Figure 5.3: Geometrical configurations of many-body states of the NV$^-$ center in diamond. Differences of the distances between the three carbon atoms (C_1, C_2 and C_3) around the vacancy site (V_C), as obtained in the excited states (ES) and ground state (GS): $\Delta d = d_{ES} - d_{GS}$. The differences are reported for the ^1E, $^1A_1$ and ^3E excited states (ESs) and are computed using TDDFT with PBE or DDH functionals. Note that $\Delta d(C_1{-}C_2)$, $\Delta d(C_2{-}C_3)$ and $\Delta d(C_3{-}C_1)$ for the ^3E state differ, due to the coupling of the electronic state to both a_1 and e type phonon modes (see text). For the $^1A_1$ state, $\Delta d(C_1{-}C_2)$, $\Delta d(C_2{-}C_3)$ and $\Delta d(C_3{-}C_1)$ are instead all equal within $\sim$ 0.02 Å, implying that in this case the equilibrium geometry preserves the C_{3v} symmetry and is close to that of the $^3A_2$ ground state. $\Delta d(C_1{-}C_2)$, $\Delta d(C_2{-}C_3)$ and $\Delta d(C_3{-}C_1)$ of the ^1E state differ, due to a significant coupling with e type phonon modes, leading to symmetry breaking.

We then computed the variation of the distances (Δd) of the three carbon atoms close to V_C in the excited states (d_{ES}), relative to the ground state (d_{GS}); these are shown in

Figure 5.3. We find an asymmetric displacement pattern for the ^1E singlet, suggesting the existence of three equivalent equilibrium geometries, compatible with the C_{3v} symmetry of the defect, which we characterized in terms of two CVs, Q_α, and Q_β. Q_β defines a direction connecting two of the three geometrical configurations, and Q_α is perpendicular to Q_β. The three geometrical configurations form an equilateral triangle on the plane defined by Q_α and Q_β. The minimum of the $^1A_1$ singlet PES on the plane of Q_α and Q_β is located at the center of the triangle (defined by $Q_\alpha = 0$, $Q_\beta = 0$) and is very close to the actual minimum of the $^1A_1$ singlet with a negligible displacement of 0.08 amu$^{1/2}$ Å. Using the CVs Q_α and Q_β, we computed the total energies of the singlet many-body states along two paths, using TDDFT@PBE: path 1, parallel to Q_α, with $Q_\beta = 0$, which connects one of the local minima and the center of the triangle; path 2, parallel to Q_β, with $Q_\alpha = 0$, and crossing the triangle center (see Figure 5.6). For values of Q_α and Q_β different from zero, and along both paths 1 and 2, we find that the wavefunctions of the $^1A_1$ and ^1E singlets, as computed using TDDFT, are linear combinations of the states with C_{3v} symmetry previously identified as $^1A_1^{(0)}$, $^1E_x^{(0)}$ and $^1E_y^{(0)}$. For the $^1A_1$ singlet, the wavefunction is given by a linear combination of the $^1A_1^{(0)}$ component, mixed with a small amount (<10%) of the $^1E_x^{(0)}$ component along path 1 (or $^1E_y^{(0)}$ component along path 2). The magnitude of the mixing between states with C_{3v} symmetry increases as the absolute value of Q_α and Q_β increases. While the wavefunction of the ^1E singlet on path 1 can still be approximately identified as the so-called "pure" state $^1E_x^{(0)}$ or $^1E_y^{(0)}$, on path 2, the wavefunction is given by a linear combination with approximately equal weights of the $^1E_x^{(0)}$ and $^1E_y^{(0)}$ components. The mixing of components found in our calculations points to the non-adiabatic coupling occurring in the system, which requires further analysis, as we discuss next.

To analyze in detail the PESs of the singlet states, we define an effective Hamiltonian that includes electron-phonon (non-adiabatic) coupling [73, 232], and where the nuclei are represented in terms of the CVs defined above, and the electrons in the basis of the three

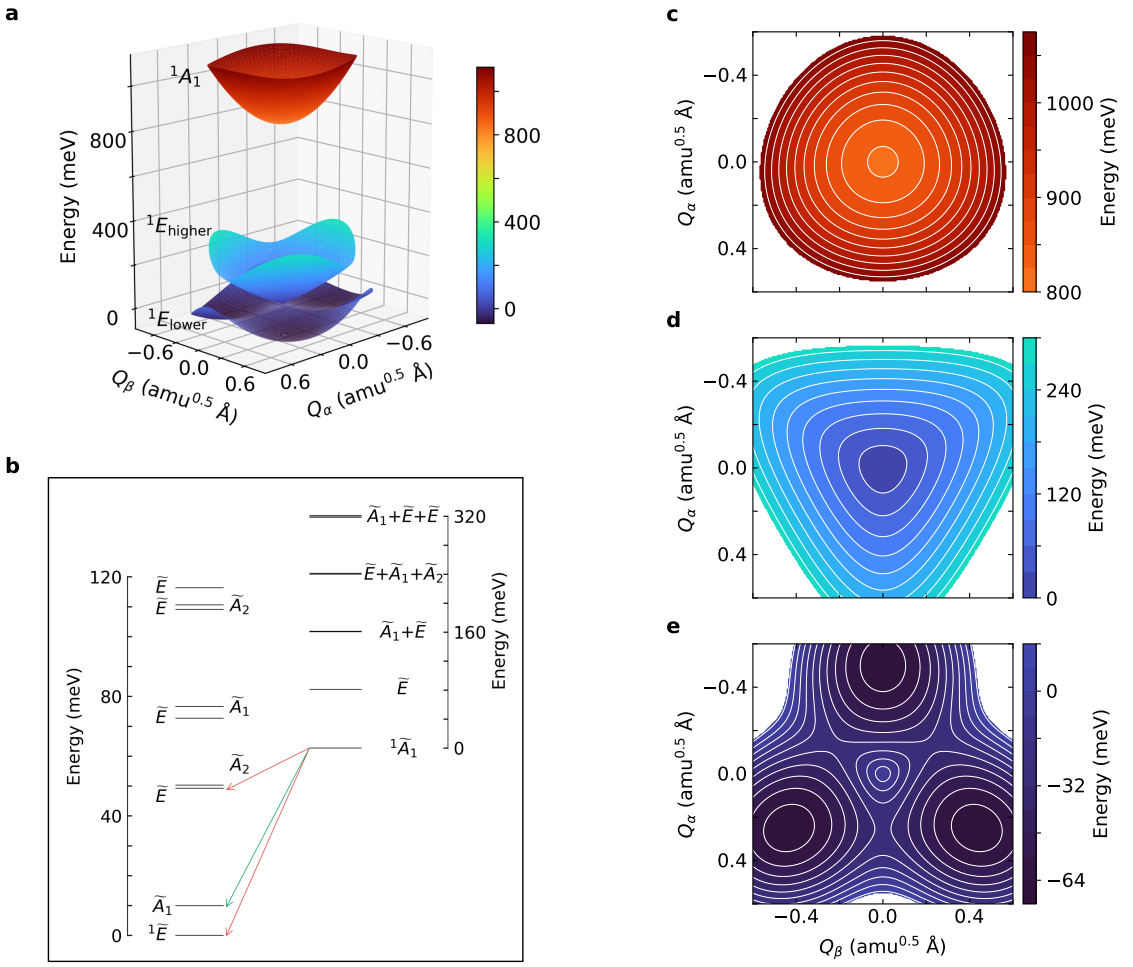

Figure 5.4: Potential energy surfaces (PESs) and vibronic energy levels of the many-body electronic states of the NV$^-$ center in diamond. **a** Adiabatic PESs of the lower and higher branches of the ^1E and $^1A_1$ states. The Q_α, Q_β configuration coordinates (see text) represent the collective motion of effective phonon modes with e symmetry. Contour plots of the PESs are shown in **c-e**. The PES of the ^1E lower branch (**e**) has the "tricorn Mexican hat" shape with three minima and three saddle points, and is connected to the higher branch (**d**) through a cusp. The PES of the $^1A_1$ singlet (**c**) slightly deviates from a perfect two-dimensional paraboloid. **b** The vibronic levels of the ^1E (left) and $^1A_1$ (right) states, whose vibronic ground states are labeled as $^1\widetilde{E}$ and $^1\widetilde{A}_1$, respectively. The energy differences of vibronic levels of the $^1A_1$ from bottom to top are found to be 80.8 meV, 79.7 meV, 78.8 meV, and 77.3 meV, respectively. The selection rules for the photoluminescence (PL) are indicated as arrows: red arrows represent the optically active $^1\widetilde{A}_1 \rightarrow {}^1\widetilde{E}$ transition resulting in the zero-phonon line (ZPL) and the $^1\widetilde{A}_1 \rightarrow \widetilde{E}$ transition resulting in the phonon sideband shifted by 49.3 meV from the ZPL; the green arrow represents the $^1\widetilde{A}_1 \rightarrow \widetilde{A}_1$ transition, shifted by 10.0 meV from the ZPL, and can be activated by uniaxial stress. In the plot, the values of the ZPL and sidebands are not given on the same energy scale for clarity.

singlet states ${}^1A_1^{(0)}$, ${}^1E_x^{(0)}$ and ${}^1E_y^{(0)}$ at $Q_\alpha = 0$ and $Q_\beta = 0$:

$$\hat{H} = \hat{H}_{\mathrm{e}} + \hat{H}_{\mathrm{ph}} + \hat{H}_{\mathrm{e-ph}}. \tag{5.9}$$

Here $\hat{H}_{\mathrm{e}} = \sum_i E_i \hat{c}_i^\dagger \hat{c}_i$ is the electronic Hamiltonian, and $\hat{c}_i^\dagger$ ($\hat{c}_i$) is the creation (annihilation) operator of the i-th many-body electronic state with $E_i = (\Lambda, 0, 0)$ for $|\Phi_i\rangle = \left(|\,{}^1A_1^{(0)}\rangle, |\,{}^1E_x^{(0)}\rangle, |\,{}^1E_y^{(0)}\rangle\right)$; $\Lambda = 821\,\mathrm{meV}$ is the energy gap between the ${}^1A_1^{(0)}$ and degenerate ${}^1E_x^{(0)}$ and ${}^1E_y^{(0)}$ electronic states obtained with TDDFT@PBE.
$\hat{H}_{\mathrm{ph}} = \sum_{\lambda=\alpha,\beta} \hbar\omega_e \left(\hat{b}_\lambda^\dagger \hat{b}_\lambda + \frac{1}{2}\right)$ is the Hamiltonian of the 2D harmonic oscillator written in terms of Q_α and Q_β, with an effective phonon energy of $\hbar\omega_e$, and $\hat{b}_\lambda^\dagger$ ($\hat{b}_\lambda$) is the creation (annihilation) operator of phonon λ. The electron-phonon coupling term reads

$$\hat{H}_{e-ph} = \sum_{ij} \sum_{\lambda=\alpha,\beta} g_{ij,\lambda} \hat{c}_i^\dagger \hat{c}_j \left(\hat{b}_\lambda^\dagger + \hat{b}_\lambda\right), \tag{5.10}$$

where $g_{ij,\lambda}$ is the linear electron-phonon coupling strength between electronic state i, j and phonon mode λ. Details on our first-principles calculation of the electron-phonon coupling strength and the analysis of the Hamiltonian of Eq. (5.9) in terms of pseudo- and dynamical Jahn-Teller effects are given in Chapter 5.5.4.

To obtain the adiabatic PESs of the singlet states we write $\hat{b}_\lambda = \sqrt{\frac{\omega_e}{2\hbar}} \left(\hat{Q}_\lambda + \frac{\mathrm{i}}{\omega_e}\hat{\Pi}_\lambda\right)$, where $\hat{\Pi}_\lambda$ is the momentum operator. Treating Q_λ and Π_λ as classical coordinates allows us to separate the kinetic and potential energy terms in the Hamiltonian, and hence to obtain the adiabatic PESs, which are displayed in Figure 5.4 **c-e**. We obtained the parameters of the Hamiltonian, including the effective phonon energy $\hbar\omega_e = 63\,\mathrm{meV}$ and the electron-phonon coupling strength $g_{ij,\lambda}$, by fitting the PESs obtained with the Hamiltonian Eq. (5.9) to our first-principles calculations, without introducing any empirical parameters (see Figure 5.7). The lower branch of the PES of the ${}^1E$ singlet exhibits a "tricorn Mexican hat" shape with three minima and three saddle points and is connected to the higher branch through a cusp.

The PES of the $^1A_1$ singlet slightly deviates from a perfect two-dimensional paraboloid, and the anharmonicity is most apparent along the path connecting its minimum to the minima on the lower branch of the ^1E state PES.

By solving the effective Hamiltonian Eq. (5.9) considering quantized vibrations, instead of classical coordinates, we obtain the vibronic levels of the two singlet states, as shown in Figure 5.4 **b**. We find that the vibronic levels with major electronic contribution from the ^1A singlet state are well approximated by harmonic vibrational levels, being almost equidistant with an energy gap of $\sim$ 80 meV. The energy gap is 17 meV higher than the energy of the effective phonon defined in Eq. (5.9), as a result of the non-adiabatic coupling. The non-adiabatic coupling also results in noticeable anharmonicity: the energy difference between adjacent vibronic levels with a major contribution coming from $^1A_1$ decreases as the quantum number increases. On the other hand, the vibronic levels with major electronic contribution from the ^1E singlet state are substantially different from those of a quantum harmonic oscillator. Our calculations identify an $^1\widetilde{A}_1$ state 10 meV above the vibronic ground state ($^1\widetilde{E}$), which likely corresponds to the state detected experimentally at about 14 to 16 meV [151, 152, 233, 234], and discussed in Ref. [73]. Such a state is not accessible under equilibrium conditions but can be reached when the crystal is under uniaxial stress. We also find degenerate $^1\widetilde{E}$ vibronic levels at 49.3 meV above the vibronic ground state; the transition into these states might be the origin of the phonon sideband at 42.6 meV observed in the low-temperature experimental PL spectrum of the $^1A_1 \rightarrow {}^1E$ transition [146].

Finally we note that, unlike the $^1E \rightarrow {}^1A_1$ absorption line shape, the calculation of the $^1A_1 \rightarrow {}^1E$ PL line shape would require an evaluation of all the phonon modes of the ^1E state, whose PES is strongly anharmonic, as well as an explicit treatment of the non-adiabatic coupling including all phonon modes [82]. While possible in principle, these calculations are beyond the scope of the present work.

5.3.3 *Optical spectra*

We now turn to the discussion of our calculations of the vibrationally resolved absorption spectrum for the transition between singlet states, which we compare with experiments, and with the PL spectrum for the transition between triplet states.

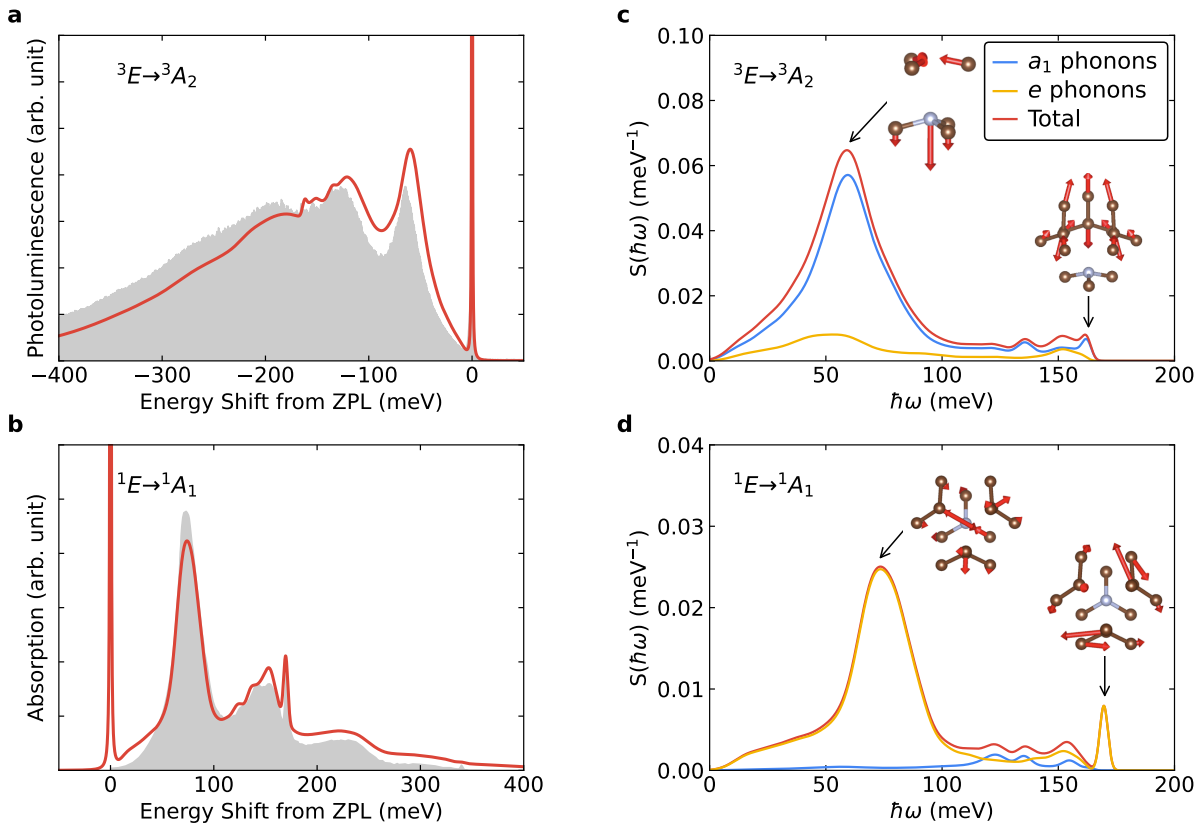

Figure 5.5: Optical spectra and spectral densities. **a** Photoluminescence (PL) line shapes of the $^3E \rightarrow {}^3A_2$ transition and **b** absorption line shapes of the $^1E \rightarrow {}^1A_1$ transition. The red lines are theoretical results, while the gray area represents experimental spectra from Ref. [59, 147]. Spectral densities $S(\hbar\omega)$ of the $^3E \rightarrow {}^3A_2$ (**c**) and the $^1E \rightarrow {}^1A_1$ transitions (**d**). Contributions from a_1 and e type phonon modes are shown as blue and yellow lines, respectively. The quasi-local (local) a_1 mode at 60 meV (162 meV) of the $^3A_2$ state that strongly couples with the $^3E \rightarrow {}^3A_2$ transition is shown in the inset of **a**. The quasi-local (local) e mode at 73 meV (170 meV) of the $^1A_1$ state that strongly couples with the $^1E \rightarrow {}^1A_1$ transition is shown in the inset of **c**. Results reported here are based on phonons computed at the PBE level of theory and optimized geometries computed at the DDH level of theory and are extrapolated to the dilute limit, approximated by a $(12 \times 12 \times 12)$ supercell with 13824 atomic sites. A comparison of results obtained using different functionals is given in Chapter 5.5.5.

Having computed the forces acting on nuclei with spin-flip TDDFT and all phonon modes in the $^1A_1$ state, we calculated the vibrationally resolved absorption spectrum of the transition between the ^1E and $^1A_1$ singlets using the HR theory. At T $\sim$ 0 K, transitions occur from the lowest vibronic level of the ^1E state whose vibronic wavefunction is localized in the local minimum of the PES, into vibronic levels of the $^1A_1$ singlet state; these levels are all well approximated by harmonic vibrational levels; hence, the use of the HR theory is justified.

Our results are compared with experiment [147] in Figure 5.5. The agreement is very good (see Chapter 5.5.5 for a comparison of results obtained using different functionals), and we successfully predicted the main peak at 73 meV and the sharp peak at 170 meV. Note that the energy of the main peak is 7 meV smaller than the distance between vibronic levels of the $^1A_1$ state obtained from the effective Hamiltonian Eq. (5.9), pointing at the importance of including all phonon modes in the calculation of optical spectra. The level of agreement obtained here indicates that our first-principles calculations based on spin-flip TDDFT provide an improved description of the atomic geometries and vibrational properties of the singlet states. Such properties are not accessible in ΔSCF, and hence, their calculations require the implementation of TDDFT forces. In addition, we emphasize the importance of including the anharmonicity of the PES of the $^1A_1$ singlet in the calculation of the HR factors and spectral functions (see Chapter 5.5.7).

Note that the phonon sideband of the absorption line shape for the $^1E \rightarrow {}^1A$ transition decays much faster compared with that of the PL spectrum for the $^3E \rightarrow {}^3A_2$ transition (shown in Figure 5.5 **a** for comparison). Indeed, the computed Debye-Waller factor (the ratio of the zero-phonon line (ZPL) relative to the entire line shape) of the $^1E \rightarrow {}^1A$ absorption line shape is 34%, in good agreement with the inferred experimental value of $\sim$ 40% [147], and is 10 times larger than that of the $^3E \rightarrow {}^3A_2$ PL line shape. The large Debye-Waller factor suggests that the ZPL is more absorptive than the phonon sideband and hence better

suited for infrared-absorption-based magnetometry measurements than the phonon sideband wavelengths [147].

It is interesting to analyze the main differences between singlet absorption and triplet PL spectra in terms of the spectral density of the electron-phonon coupling in the two cases, $S(\hbar\omega)$, as shown in Figure 5.5 **c** and **d**. The main contribution to the $S(\hbar\omega)$ of the ${}^1E \rightarrow {}^1A_1$ transition comes from the coupling of the electronic states with e type phonon modes; instead, the main contribution in the case of the ${}^3E \rightarrow {}^3A_2$ transition originates from the coupling with a_1 type phonon modes. In more detail, we find that $S(\hbar\omega)$ of the ${}^1E \rightarrow {}^1A_1$ transition exhibits a broad peak at 73 meV and a sharp peak at 170 meV, resulting from the coupling of the electronic states with a quasi-local and a local e type phonon mode, displayed in the inset of Figure 5.5 **d**. The 170 meV e type local mode exists only in the ${}^1A_1$ state and has an energy higher than that of the optical phonons of diamond. It couples weakly to the vibrations of the diamond lattice, resulting in a sharp peak in both $S(\hbar\omega)$ and the adsorption spectrum. The $S(\hbar\omega)$ of the ${}^1E \rightarrow {}^1A_1$ transition is generally shifted to higher energy relative to that of the ${}^3E \rightarrow {}^3A_2$ transition, originating from an increase of the energy of the phonons of the ${}^1A_1$ state compared with those of the ${}^3A_2$ state. Previous work suggested that such an increase of phonon energies might be caused by the contribution of the double excitation configurations $|a_1\overline{a}_1\rangle$ in the wavefunction of the ${}^1A_1$ state [147]. However, our work suggests that the non-adiabatic coupling of the ${}^1A_1$ and ${}^1E$ singlet states is more likely responsible for the increase in phonon energies. A detailed comparison of the phonon modes of the ${}^1A_1$ and ${}^3A_2$ states can be found in Chapter 5.5.6.

5.4 Discussion

In summary, we studied the many-body electronic states of the NV^- center in diamond, including singlet states, using first-principles calculations based on TDDFT with semi-local and hybrid functionals, and we computed vibrationally resolved optical spectra. We showed

that TDDFT with analytical forces can be successfully applied to predict optical spectra of spin defects in solids, providing a robust description of both the electronic structure and atomic geometries of the many-body electronic states. In particular, TDDFT predicts the same energy ordering as the experiment and the correct characteristics of the many-body electronic states, similar to those obtained using higher-level methods, although the neglect of double excitations results in a slight overestimate of excitation energies relative to experiments. The computed vibrationally resolved absorption spectrum of the ${}^1E \rightarrow {}^1A_1$ transition is in very good agreement with the experiment, thanks to an improved description of the atomic geometries and phonons of the singlet states obtained in our work. Our results show the key role played by non-adiabatic coupling in determining optical transitions. For example, we found that the equilibrium geometry of the ${}^1A_1$ state is similar to that of the ${}^3A_2$ ground state; however, the e type phonons of the former have significantly higher energy than those of the ground state, due to the non-adiabatic coupling of the former with the ${}^1E$ states. Such coupling is also responsible for the anharmonicity of the ${}^1A_1$ state PES, which should be taken into account in obtaining absorption spectra in quantitative agreement with the experiment. Interestingly, solving the effective Hamiltonian for the non-adiabatic coupling yields optically forbidden $\widetilde{A}_1$ and optically allowed $\widetilde{E}$ vibronic levels above the ${}^1\widetilde{E}$ ground vibronic state, consistent with PL measurements. Our study provides first principles predictions of the basic properties of the NV^- center in diamond, which are important for a comprehensive understanding of the optical spin-polarization cycle of this defect and, hence, of its functionalities for quantum technology applications. In particular, the techniques presented here enable the modeling, from first principles, of the phonon sideband of the optical absorption process between singlet states, which has been used for infrared absorption-based magnetometry. The strategy applied here to the NV^- center in diamond is general and paves the way to the study of shelving states and optical spectra in other spin defects and materials.

Table 5.1: Convergence of vertical excitation energies (VEEs) with respect to the size of the supercell. VEEs (eV) of many-body excited states relative to the $^3A_2$ ground state of the NV^- center in diamond computed using TDDFT at the PBE level of theory. Results obtained with the $(2 \times 2 \times 2)$, the $(3 \times 3 \times 3)$ and the $(4 \times 4 \times 4)$ supercells are shown.

Excited state	$(2 \times 2 \times 2)$	$(3 \times 3 \times 3)$	$(4 \times 4 \times 4)$
^3E	1.978	2.076	2.095
$^1A_1$	1.283	1.334	1.341
^1E	0.504	0.510	0.512

5.5 Technical details

5.5.1 Supercell size convergence

To check convergence with respect to the size of the supercell, we performed TDDFT calculations at the PBE level of theory for supercells with up to 512 atomic sites, corresponding to a supercell with $(4 \times 4 \times 4)$ repetitions of the unit cell. Vertical excitation energies (VEEs) of many-body excited states are summarized in Table 5.1. We found that the difference in the VEEs calculated with the $(3 \times 3 \times 3)$ and the $(4 \times 4 \times 4)$ supercells is less than 0.02 eV, indicating that the $(3 \times 3 \times 3)$ supercell already yields relatively well-converged results.

5.5.2 Analysis of vertical excitation energies

We attribute the overestimate of the VEE of the $^1A_1$ state to the neglect of the double excitation Slater determinant $|a_1\bar{a}_1\rangle$. Here, we provide a simple estimate of the error based on perturbation theory: the coupling strength between the double excitation Slater determinant and the singlet state, $\langle a_1\bar{a}_1|\hat{H}|\,^1A_1\rangle$, can be estimated using the coefficient of the configuration $|a_1\bar{a}_1\rangle$, $c^{\,^1A_1}_{a_1\bar{a}_1}$ predicted by QDET calculations [88], and the energy difference, $E_{^1A_1} - E_{a_1\bar{a}_1}$; the correction to the energy of the singlet state, $E^{(2)}_{^1A_1}$, can then be estimated using the coupling strength and the difference $E_{^1A_1} - E_{a_1\bar{a}_1}$. Here $\hat{H}$ is the many-body electronic Hamiltonian.

QDET results [88] indicate that the weight of the $|e_x\bar{e}_x\rangle$ and $|e_y\bar{e}_y\rangle$ configurations in the

Table 5.2: Contribution of Slater determinants to the many-body electronic states of the NV^- center in diamond. Contribution of single and double excitation Slater determinants (%) to the many-body electronic states, as obtained from TDDFT and QDET calculations. Slater determinants are denoted in the hole notation, and the contributions are given in terms of the coefficients defined in Eq. (5.8).

		TDDFT@PBE			TDDFT@DDH			QDET		
	Slater det.	^1E_x	^1E_y	$^1A_1$	^1E_x	^1E_y	$^1A_1$	^1E_x	^1E_y	$^1A_1$
Single Excitations	$\|e_x\bar{e}_x\rangle$	45.1	–	50.0	41.9	–	49.8	44.9	–	46.9
	$\|e_x\bar{e}_y\rangle$	–	45.1	–	–	41.9	–	–	44.9	–
	$\|e_y\bar{e}_x\rangle$	–	45.1	–	–	41.9	–	–	44.9	–
	$\|e_y\bar{e}_y\rangle$	45.1	–	50.0	41.9	–	49.8	44.9	–	46.9
	$\|a_1\bar{e}_x\rangle$	4.0	1.1	–	5.9	–	–	3.3	–	–
	$\|a_1\bar{e}_y\rangle$	1.1	4.0	–	–	5.9	–	–	3.3	–
Double Excitations	$\|e_x\bar{a}_1\rangle$	–	–	–	–	–	–	3.3	–	–
	$\|e_y\bar{a}_1\rangle$	–	–	–	–	–	–	–	3.3	–
	$\|a_1\bar{a}_1\rangle$	–	–	–	–	–	–	–	–	2.6

$^1A_1$ state is $\left|c^{\,^1A_1}_{e_x\bar{e}_x}\right|^2 + \left|c^{\,^1A_1}_{e_y\bar{e}_y}\right|^2 = 0.938$ (see Table 5.2), while the weight of $|a_1\bar{a}_1\rangle$ and other configurations with higher energies amounts to 0.062 [88]. For simplicity we assume the weight of $|a_1\bar{a}_1\rangle$ configuration is 0.062, corresponding to $\left|c^{\,^1A_1}_{a_1\bar{a}_1}\right| = 0.25$ [88]. The energy of the $|a_1\bar{a}_1\rangle$ configuration relative to the $^3A_2$ ground state is 7.33 eV, estimated using Kohn-Sham orbital energies at the DDH level of theory. It is thus 5.36 eV higher than the $^1A_1$ state. Within perturbation theory, the coefficient of the $|a_1\bar{a}_1\rangle$ configuration is

$$\left|c^{\,^1A_1}_{a_1\bar{a}_1}\right| \approx 0.25 \approx \left|\frac{\langle a_1\bar{a}_1|\hat{H}|\,^1A_1\rangle}{E_{^1A_1} - E_{a_1\bar{a}_1}}\right|. \tag{5.11}$$

With the estimated $E_{^1A_1} - E_{a_1\bar{a}_1} = -5.36$ eV, we have $|\langle a_1\bar{a}_1|\hat{H}|\,^1A_1\rangle| \approx 1.34$ eV. Therefore, the second-order correction to the energy is

$$E^{(2)}_{^1A_1} = \frac{|\langle a_1\bar{a}_1|\hat{H}|\,^1A_1\rangle|^2}{E_{^1A_1} - E_{a_1\bar{a}_1}} \approx -0.34 \text{ eV}. \tag{5.12}$$

Using this correction to estimate the energy of the $^1A_1$ state we obtain 1.64 eV, which

is in good agreement with the experimentally inferred zero-phonon absorption energy of $1.51 \sim 1.60$ eV [146] and the QDET VEE value of 1.270 eV [88].

Similarly, including the $|e_x\overline{a}_1\rangle$ Slater determinant in the expansion of the many-body wavefunction brings the VEE of the ^1E_x state closer to the experimental and high-level theoretical results. For the ^1E_x state, we have $E_{^1E_x} - E_{e_x\overline{a}_1} = -5.53$ eV, and $\left|c^{^1E_x}_{e_x\overline{a}_1}\right| = 0.18$ from QDET results. Hence, we can estimate $\langle e_x\overline{a}_1|\hat{H}|\,^1E_x\rangle \approx 1.00$ eV and an energy correction $E^{(2)}_{^1E_x} \approx -0.18$ eV. Using this energy correction, the energy of the ^1E_x state becomes 0.50 eV, in much better agreement with the experimentally inferred zero-phonon absorption energy of $0.34 \sim 0.43$ eV [149, 231] and the QDET VEE value of 0.463 eV [88]. For the ^1E_y state, including the $|e_y\overline{a}_1\rangle$ configuration, brings the value of VEE to 0.50 eV.

For completeness, we note that QDET and TDDFT calculations are built on spin-unpolarized and spin-polarized ground state Kohn-Sham orbitals, respectively, and this difference has been neglected in our comparison.

5.5.3 Geometry Relaxation

To quantify the magnitude of geometry relaxation in excited states, we computed the mass-weighted atomic displacement between geometries of excited states and the $^3A_2$ ground state, ΔQ, and the Franck-Condon (FC) shift, E_{FC}, for many-body excited states, as shown in Table 5.3. TDDFT results obtained at the PBE level are generally similar to those obtained at the DDH level. For the ^3E excited state, TDDFT and constrained-occupations DFT (ΔSCF) yield comparable results. For the $^1A_1$ singlet state, TDDFT predicts a minor displacement and FC shift, indicating that the geometry of the $^1A_1$ state is close to that of the $^3A_2$ ground state. On the other hand, a more significant displacement and FC shift are found for the ^1E state, indicating that its geometry is significantly displaced from that of the $^3A_2$ ground state.

Table 5.3: Geometry relaxation in excited states. Mass-weighted displacement ΔQ (amu$^{0.5}$ Å) between the equilibrium geometries of the $^3A_2$ ground state (GS) and the excited states (ES), and the Franck-Condon (FC) shift E_{FC} (meV) in the ESs. Equilibrium geometries of the ESs are obtained using TDDFT or constrained occupations DFT (ΔSCF) with PBE and DDH functionals.

State	Method	Configuration[a]	ΔQ[b]	E_{FC}[c]
^3E	TDDFT (PBE)	$\overline{a}_1\overline{e}$	0.583	187
^3E	TDDFT (DDH)	$\overline{a}_1\overline{e}$	0.634	255
^3E	ΔSCF (PBE)	$\overline{a}_1\overline{e}$	0.625	219
^3E	ΔSCF (DDH)[d]	$\overline{a}_1\overline{e}$	0.635	246
$^1A_1$	TDDFT (PBE)	$e\overline{e}$	0.111	17
$^1A_1$	TDDFT (DDH)	$e\overline{e}$	0.094	17
^1E	TDDFT (PBE)	$e\overline{e}$	0.415	64
^1E	TDDFT (DDH)	$e\overline{e}$	0.413	105

[a] Electronic configuration of many-body states in the hole notation.

[b] $\Delta Q = \left(\sum_{\alpha=1}^{N_{\mathrm{atoms}}} \sum_{i=x,y,z} M_\alpha (\mathbf{R}_{\alpha i,\mathrm{ES}} - \mathbf{R}_{\alpha i,\mathrm{GS}})^2\right)^{0.5}$, where M_α is the mass of the αth atom, $\mathbf{R}_{\alpha i,\mathrm{ES}}$ ($\mathbf{R}_{\alpha i,\mathrm{GS}}$) is the equilibrium atomic structure of the ES (GS).

[c] $E_{\mathrm{FC}} = E_{\mathrm{ES@GS}} - E_{\mathrm{ES@ES}}$, where $E_{\mathrm{ES@GS}}$ is the total energy of ES at the equilibrium geometry of the GS, and $E_{\mathrm{ES@ES}}$ is the total energy of ES at the equilibrium geometry of the ES.

[d] The $\overline{a}_1\overline{e}_x^{0.5}\overline{e}_y^{0.5}$ configuration was used to converge the ΔSCF (DDH) calculation.

5.5.4 Non-adiabatic coupling between singlet states

The electron-phonon coupling entering the effective Hamiltonian reads

$$\hat{H}_{e-ph} = \sum_{ij} \sum_{\lambda=\alpha,\beta} g_{ij,\lambda} \hat{c}_i^\dagger \hat{c}_j \left(\hat{b}_\lambda^\dagger + \hat{b}_\lambda\right), \tag{5.13}$$

where $g_{ij,\lambda}$ is the linear electron-phonon coupling strength between electronic state i, j and phonon mode λ. Considering $C_{3\mathrm{v}}$ symmetry and using e_x and e_y vibrational modes as collective variables (CVs, which we call Q_α, Q_β), the electron-phonon coupling strength can

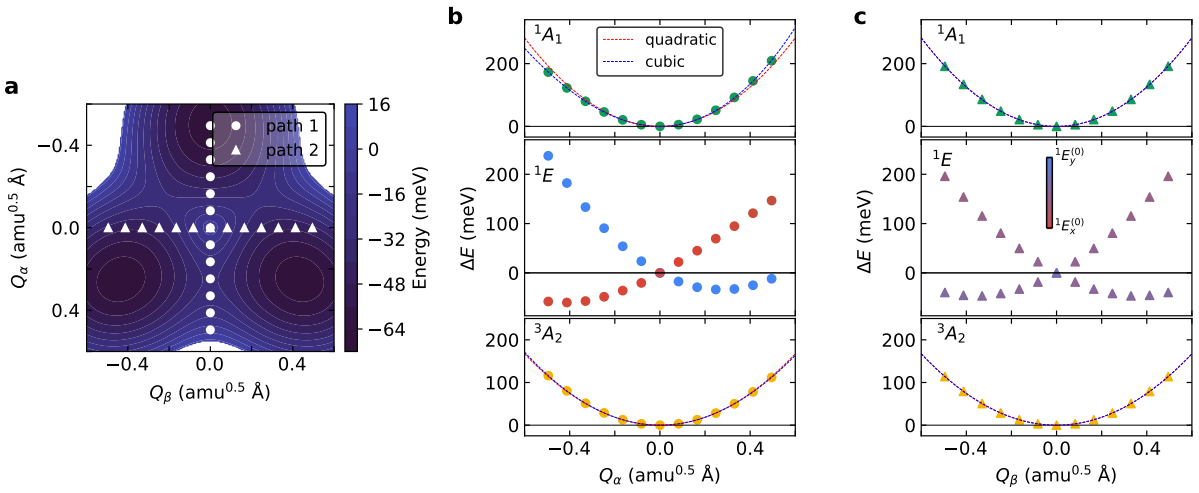

Figure 5.6: Potential energy curves (PECs) of the NV^- center in diamond. **a** Adiabatic potential energy surface (PES) of the lower branch of the ^1E state. Q_α, Q_β configuration coordinates represent the collective motion of effective e phonon modes. **b-c** PECs of the $^1A_1$ state (up panel), the ^1E states (middle panel) and the $^3A_2$ state (bottom panel) along path 1 and path 2 defined in **a**. Relative change in total energy, ΔE, computed at the PBE level of theory as a function of Q_α and Q_β is reported. The color of the ^1E states represents the weight of $^1E_x^{(0)}$ and $^1E_y^{(0)}$ configuration. The PECs of the $^1A_1$ and $^3A_2$ states are fitted by quadratic functions (red dashed lines) and cubic functions (blue dashed lines).

be simplified as

$$g_{ij,\alpha} = \begin{pmatrix} 0 & \widetilde{G} & 0 \\ \widetilde{G} & G & 0 \\ 0 & 0 & -G \end{pmatrix}, \quad g_{ij,\beta} = \begin{pmatrix} 0 & 0 & \widetilde{G} \\ 0 & 0 & -G \\ \widetilde{G} & -G & 0 \end{pmatrix}. \tag{5.14}$$

$\widetilde{G}$ is the coupling strength between the $^1A_1$ and the ^1E states,

$$\widetilde{G} = \sqrt{\frac{\hbar}{2\omega_e}} \left\langle {}^1A_1 \left| \frac{\partial V}{\partial Q_\alpha} \right| {}^1E_x \right\rangle = \sqrt{\frac{\hbar}{2\omega_e}} \left\langle {}^1A_1 \left| \frac{\partial V}{\partial Q_\beta} \right| {}^1E_y \right\rangle, \tag{5.15}$$

and G is the coupling strength between the ${}^1E_x$ and ${}^1E_y$ states,

$$G = \sqrt{\frac{\hbar}{2\omega_e}}\left\langle {}^1E_x\left|\frac{\partial V}{\partial Q_\alpha}\right|{}^1E_x\right\rangle = -\sqrt{\frac{\hbar}{2\omega_e}}\left\langle {}^1E_y\left|\frac{\partial V}{\partial Q_\alpha}\right|{}^1E_y\right\rangle = -\sqrt{\frac{\hbar}{2\omega_e}}\left\langle {}^1E_x\left|\frac{\partial V}{\partial Q_\beta}\right|{}^1E_y\right\rangle. \tag{5.16}$$

Here, V is the potential energy of the many-body system. The dependence of $\widetilde{G}$ and G on Q_α and Q_β is neglected.

We computed the potential energy curves (PECs) of many-body electronic states along path 1 ($Q_\beta = 0$) and path 2 ($Q_\alpha = 0$) using TDDFT with the PBE functional, as shown in Figure 5.6. Along path 1, we observe a local minimum for $Q_\alpha < 0$, a cusp at $Q_\alpha = 0$ and 60 meV higher than the minimum, and a saddle point for $Q_\alpha > 0$ with a barrier height of 26 meV. The PEC of the ${}^1A_1$ state has a curvature that corresponds to an effective phonon energy of 81 meV, which is 19 meV higher than that of the ${}^3A_2$ ground state. The PEC of the ${}^1A_1$ state is also slightly anharmonic, as shown by the quality of a cubic function fit (blue dashed line) compared to a quadratic one (red dashed line).

By fitting the adiabatic PECs along path 1 and path 2 obtained by solving the effective Hamiltonian, to the PECs from first-principles calculations, we obtained the parameters for the effective Hamiltonian, i.e. $\hbar\omega_e = 63.0$ meV, $\widetilde{G} = 133.2$ meV, and $G = 62.4$ meV, as shown in Figure 5.7.

The non-adiabatic coupling can be analyzed in terms of the pseudo Jahn-Teller (PJT) interaction between the ${}^1A_1$ and the ${}^1E$ states with strength $\widetilde{G}$, together with the dynamic Jahn-Teller (DJT) interaction between two ${}^1E$ states with strength G [73, 232]. Here, we investigate the contribution of the PJT and DJT effect separately by setting either G or $\widetilde{G}$ to zero along path 1 (Figure 5.8) and path 2 (Figure 5.9), respectively. The DJT effect only couples two ${}^1E$ states. Along path 1 (path 2), the DJT effect shifts the local minima of the ${}^1E$ states away from the $Q_\alpha = 0$ ($Q_\beta = 0$) point and results in the presence of a cusp. On the other hand, the PJT effect couples ${}^1A_1$ and ${}^1E$ states. It increases the curvature of the ${}^1A_1$ PES; it also decreases the curvature of the lower branch of the ${}^1E$ PESs that

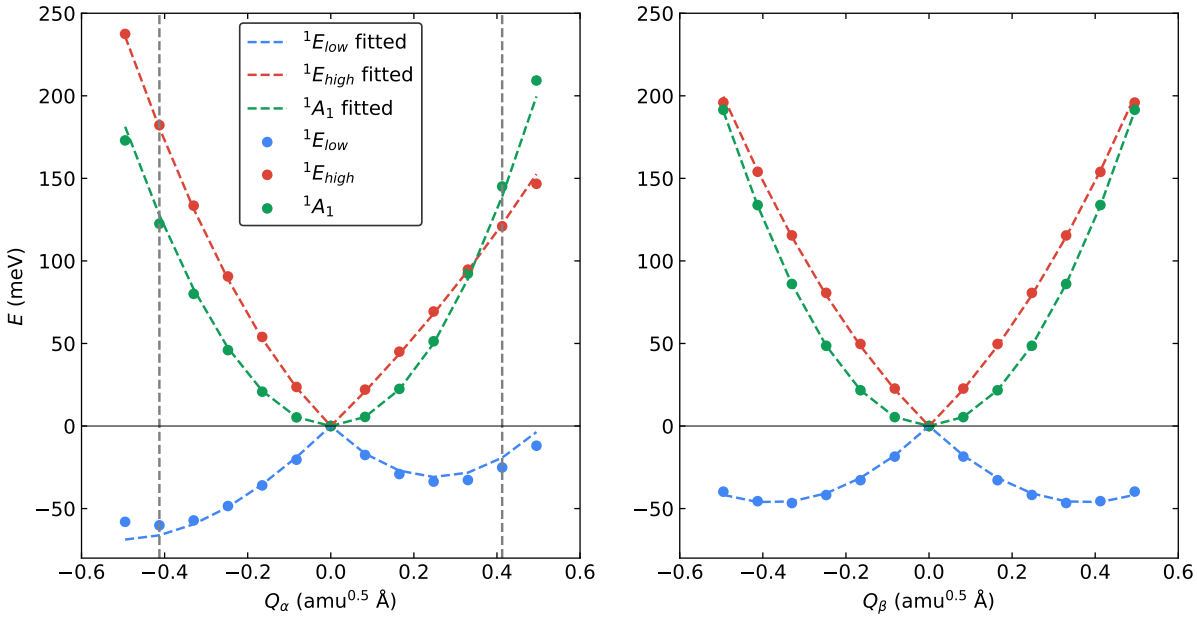

Figure 5.7: Fitting of the potential energy curves (PECs) of the NV^- center in diamond. Potential energy curves (PECs) are obtained from first-principles calculations (dots) and by solving the effective Hamiltonian (dashed lines) along path 1 and path 2, as defined in Figure 5.6. Minima of the $^1A_1$ state is arbitrarily shifted to 0 meV. The parameters of the effective Hamiltonian (see Eq. (5.9) are obtained by best fitting the first-principles results.

can be characterized as ^1E_x (^1E_y) state along path 1 (path 2), and is accompanied by the mixing of ^1E_x (^1E_y) wavefunctions with the $^1A_1$ wavefunction. Either the PJT or the DJT effect taken separately can preserve the axial symmetry of the PESs; preservation of the axial symmetry is the typical result when electron-phonon coupling is considered only at the linear order. When the PJT and the DJT effects are considered at the same time, the axial symmetry of the PESs is reduced to C_{3v} symmetry.

5.5.5 Huang-Rhys factors and spectral densities

We compared the Huang-Rhys factors (HRFs) and Debye-Waller factors (DWFs) obtained using TDDFT at the PBE and the DDH level, as shown in Table 5.4. Due to the unaffordable cost of computing phonon modes at the DDH level of theory, we approximated the DDH phonons as PBE phonons whose phonon energies are multiplied by a constant factor [83].

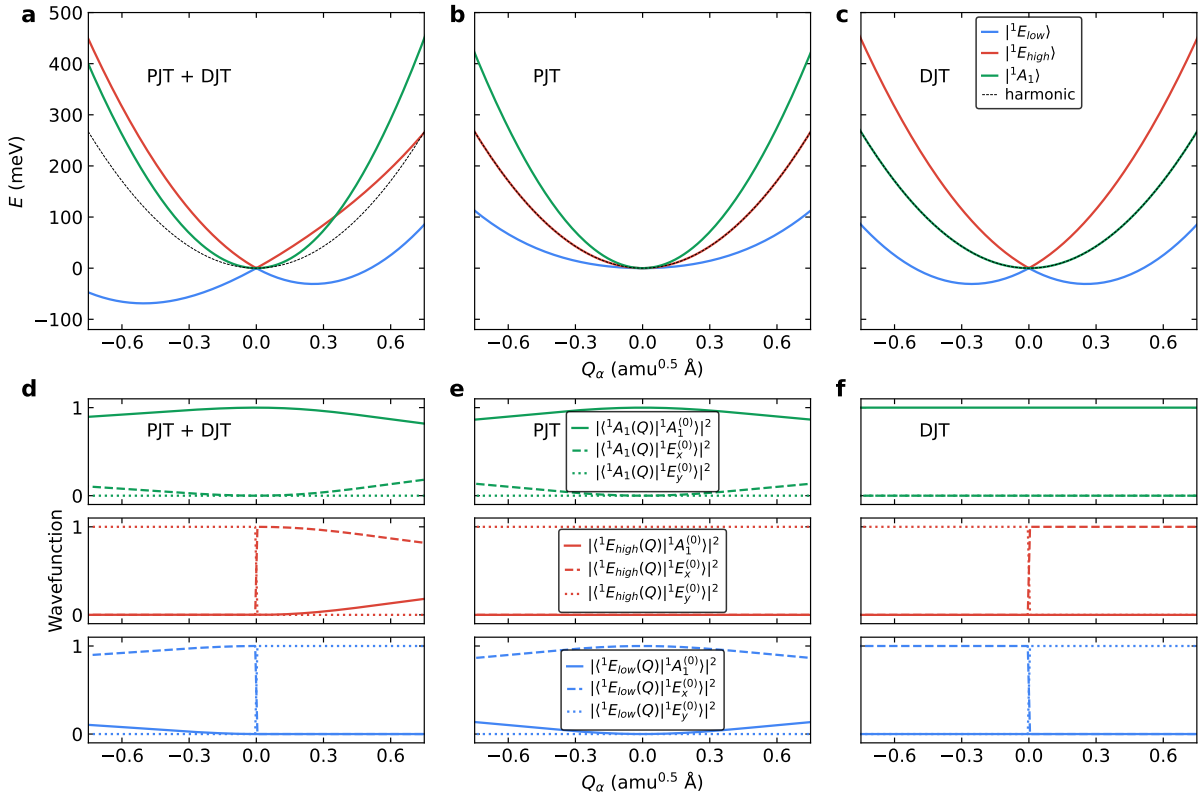

Figure 5.8: Dynamic Jahn-Teller (DJT) and pseudo Jahn-Teller (PJT) effect. Potential energy curves (PECs) of the $^1A_1$ and ^1E states along the path with $Q_\beta = 0$ obtained by solving the effective Hamiltonian for non-adiabatic coupling, considering (**a**) both the PJT and the DJT effect, (**b**) only the PJT effect, and (**c**) only the DJT effect. Minima of the $^1A_1$ curve are arbitrarily shifted to 0 meV for a better comparison. Decomposition of the wavefunctions of the ^1A and ^1E states onto the wavefunctions at $Q_\alpha = 0$ are displayed in the bottom panel, considering (**d**) both the PJT and the DJT effect, (**e**) only the PJT effect, and (**f**) only the DJT effect.

For both the $^3E \rightarrow {}^3A_2$ transition and the $^1E \rightarrow {}^1A_1$ transition, the best agreement with experiment is obtained when the displacement computed at the DDH level of theory (DDH$-\Delta Q$) was used. Using phonons computed at the PBE level of theory (PBE$-ph$) or DDH level of theory (DDH$-ph$) only results in minor changes.

Spectral density of electron-phonon coupling, $S(\hbar\omega)$, computed at different levels of theory are shown in Figure 5.10. Peak positions of the spectral densities computed with DDH$-ph$ are generally right-shifted relative to those obtained with PBE. For the $^3E \rightarrow {}^3A_2$ transition, all spectral densities have a similar shape, while the one computed with DDH$-\Delta Q$

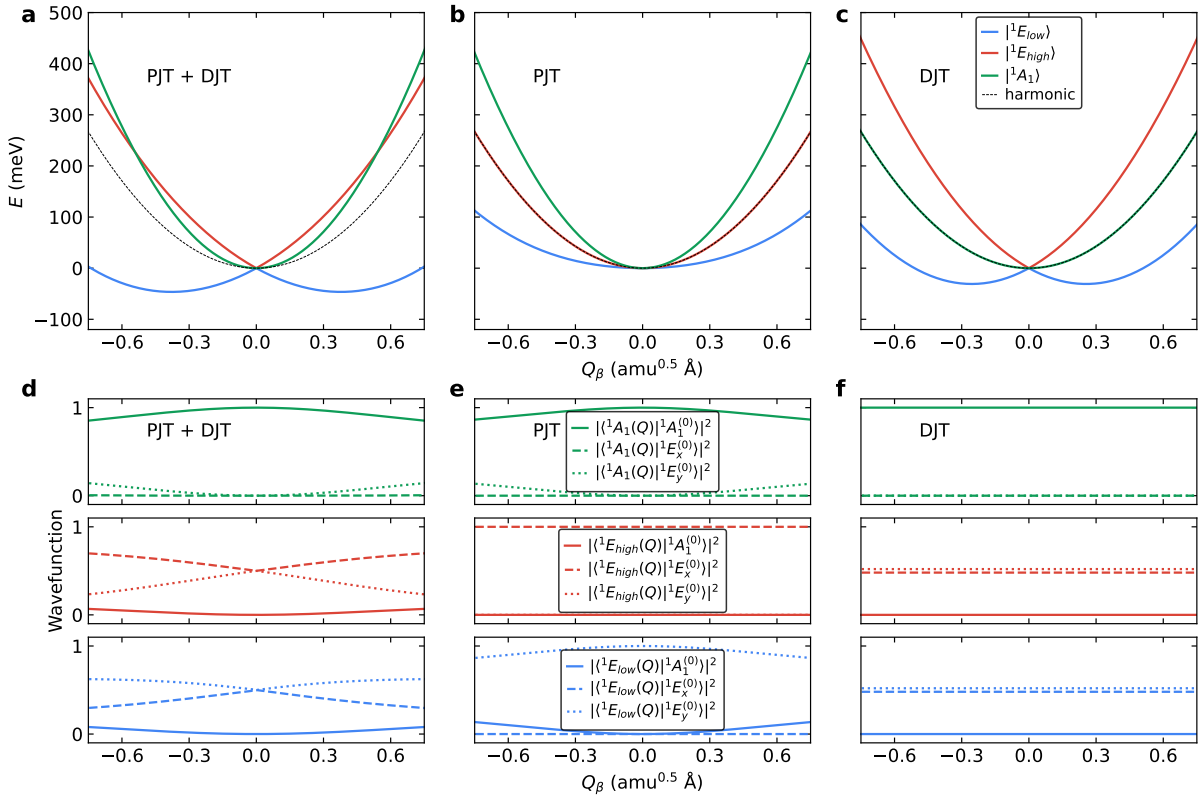

Figure 5.9: Dynamic Jahn-Teller (DJT) and pseudo Jahn-Teller (PJT) effect. Potential energy curves (PECs) of the $^1A_1$ and ^1E states along the path with $Q_\alpha = 0$ considering (**a**) both the PJT and the DJT effect, (**b**) only the PJT effect, and (**c**) only the DJT effect. Minima of the $^1A_1$ curve are arbitrarily shifted to 0 meV for a better comparison. Decomposition of the wavefunctions of the $^1A_1$ and ^1E states onto the wavefunctions at $Q_\beta = 0$ are displayed in the bottom panel, considering (**d**) both the PJT and the DJT effect, (**e**) only the PJT effect, and (**f**) only the DJT effect.

has higher intensities than the one computed with PBE$-\Delta Q$. The opposite is found for the $^1E \rightarrow {}^1A_1$ transition, where the spectral densities computed with DDH$-\Delta Q$ have smaller intensities than the one computed with PBE$-\Delta Q$. The spectral density for the $^1E \rightarrow {}^1A_1$ transition is dominated by the coupling with e type phonons, while the one of the $^3E \rightarrow {}^3A_2$ transition is dominated by the coupling with the a_1 type phonons. When using PBE phonons, we find that the spectral density for the $^1E \rightarrow {}^1A_1$ transition has a broad (sharp) peak at 73 meV (170 meV), resulting from the coupling with a quasi-local (local) e type phonon mode. Instead, the spectral density for the $^3E \rightarrow {}^3A_2$ transition mainly couples with the

Table 5.4: Computed Huang-Rhys factors (HRFs) and Debye-Waller factors (DWFs). Total HRFs and DWFs (%) for $^3E \rightarrow {}^3A_2$ and $^1E \rightarrow {}^1A_1$ transitions computed at different levels of theory are compared with experiments [147]. Here, DDH$-\Delta Q$, PBE$-ph$ denotes results based on the Huang-Rhys theory, evaluated using ΔQ computed at the DDH level and the phonon modes computed at the PBE level of theory. The DWF is calculated as DWF $= \mathrm{e}^{-\mathrm{HRF}}$. These results are obtained in the dilute limit, approximated by a ($12 \times 12 \times 12$) supercell with 13824 atomic sites.

	$^3E \rightarrow {}^3A_2$		$^1E \rightarrow {}^1A_1$	
	HRF	DWF(%)	HRF	DWF(%)
PBE$-\Delta Q$, PBE$-ph$	2.44	8.7	1.42	24
DDH$-\Delta Q$, PBE$-ph$	2.97	5.1	1.08	34
DDH$-\Delta Q$, DDH$-ph$	3.08	4.6	1.13	32
Expt. [147]	3.49	3.2	$\sim$0.9	$\sim$40

quasi-local a_1 type phonon mode, resulting in a broad peak at 60 meV. The 162 meV a_1 type local phonon mode is present in both the $^1A_1$ and $^3A_2$ states, but it does not contribute to the spectral density for the $^1E \rightarrow {}^1A_1$ transition. However, the 170 meV e type local phonon mode is only present in the $^1A_1$ state. The 170 meV e mode has an energy higher than the optical phonons of diamond and couples weakly to the vibrations of the diamond lattice. The spectral density of the $^1E \rightarrow {}^1A_1$ transition generally shifts to higher energy direction compared to that of the $^3E \rightarrow {}^3A_2$ transition, implying an increase of phonon energies in the $^1A_1$ state compared with those of the $^3A_2$ state.

The photoluminescence (PL) spectrum of the $^3E \rightarrow {}^3A_2$ transition and the absorption spectrum of the $^1E \rightarrow {}^1A_1$ transition computed at difference levels of theory are shown in Figure 5.11. For both computed spectra, we obtained a better agreement with experiments when DDH$-\Delta Q$ was used. For the PL of the $^3E \rightarrow {}^3A_2$ transition, we obtained the best agreement with experiments when DDH$-ph$ was used, while for the absorption of the $^1E \rightarrow {}^1A_1$ transition, the best agreement was obtained when PBE$-ph$ was used. However, the difference caused by the choice of level of theory used for phonons and overall negligible.

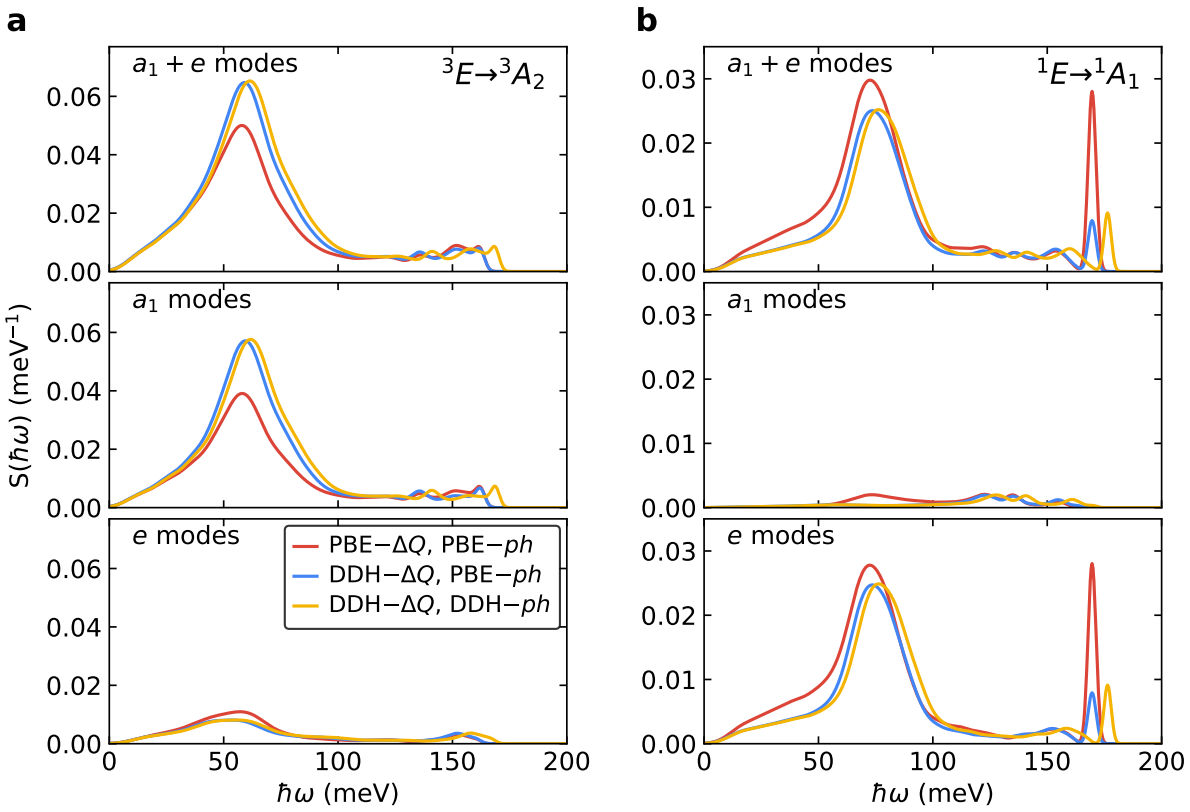

Figure 5.10: Spectral densities of electron-phonon coupling. Spectral densities of electron-phonon coupling $S(\hbar\omega)$ for the $^3E \rightarrow {}^3A_2$ transition (**a**) and the $^1E \rightarrow {}^1A_1$ transition (**b**). Contributions of the a_1 type and e type phonon modes are shown in the middle and the bottom panels, respectively. Here, DDH$-\Delta Q$, PBE$-ph$ denotes results based on the Huang-Rhys theory, evaluated using ΔQ computed at the DDH level and the phonon modes computed at the PBE level of theory. These results are obtained in the dilute limit, approximated by a $(12 \times 12 \times 12)$ supercell with 13824 atomic sites.

5.5.6 Phonons of the $^3A_2$ and $^1A_1$ states

To quantify the differences between the phonons of the $^3A_2$ ground state and the phonons of the $^1A_1$ singlet state, we computed the atomic displacements between equilibrium geometries obtained for the $^3E \rightarrow {}^3A_2$ and for the $^1E \rightarrow {}^1A_1$ transitions. We then project the displacements onto the phonon modes of the $^3A_2$ state and the $^1A_1$ state and computed spectral densities of electron-phonon coupling $S(\hbar\omega)$, as shown in Figure 5.12. For both the $^3E \rightarrow {}^3A_2$ and the $^1E \rightarrow {}^1A_1$ transition, the contributions of the e type phonon modes

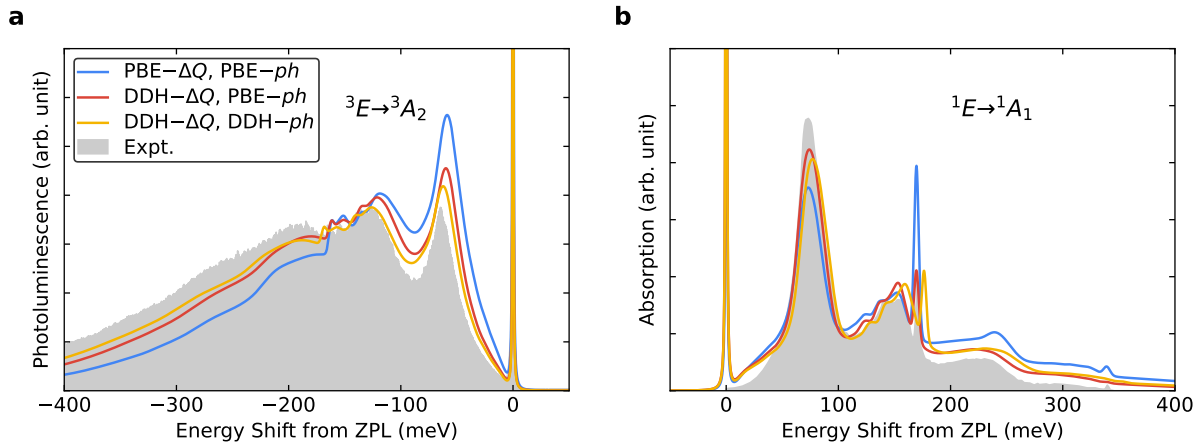

Figure 5.11: Optical spectra. Photoluminescence (PL) spectra of the $^3E \rightarrow {}^3A_2$ transition (**a**) and absorption spectra of the $^1E \rightarrow {}^1A_1$ transition (**b**). Theoretical results are shown as solid lines, while experimental results [59, 147] are shown as shaded areas. Here, DDH$-\Delta Q$, PBE$-ph$ denotes the line shapes based on the Huang-Rhys theory, evaluated using ΔQ computed at the DDH level and the phonon modes computed at the PBE level of theory. These results are obtained in the dilute limit, approximated by a $(12 \times 12 \times 12)$ supercell with 13824 atomic sites.

shift to higher energies when the phonon modes of the $^1A_1$ state are used, while the contributions of the a_1 type phonon modes remain almost unchanged. This finding implies that the a_1 type mode of the $^1A_1$ and the $^3A_2$ state are quite similar, which is consistent with the fact that the two states have similar geometries. The e-type mode of the $^1A_1$ state has energies apparently higher than those of the $^3A_2$ state, consistent with the analysis based on non-adiabatic coupling between singlet states.

5.5.7 Treatment of anharmonic effects

The non-adiabatic interaction between singlet states results in a noticeable anharmonicity of the PES of the $^1A_1$ state, which needs to be carefully taken into account in the calculations of the absorption line shape of the $^1E \rightarrow {}^1A_1$ transition. The formalism used to describe the optical process relies on the HR theory, which assumes that the harmonic approximation holds. Since the anharmonic effect is small, we can still use the HR theory and introduce an-

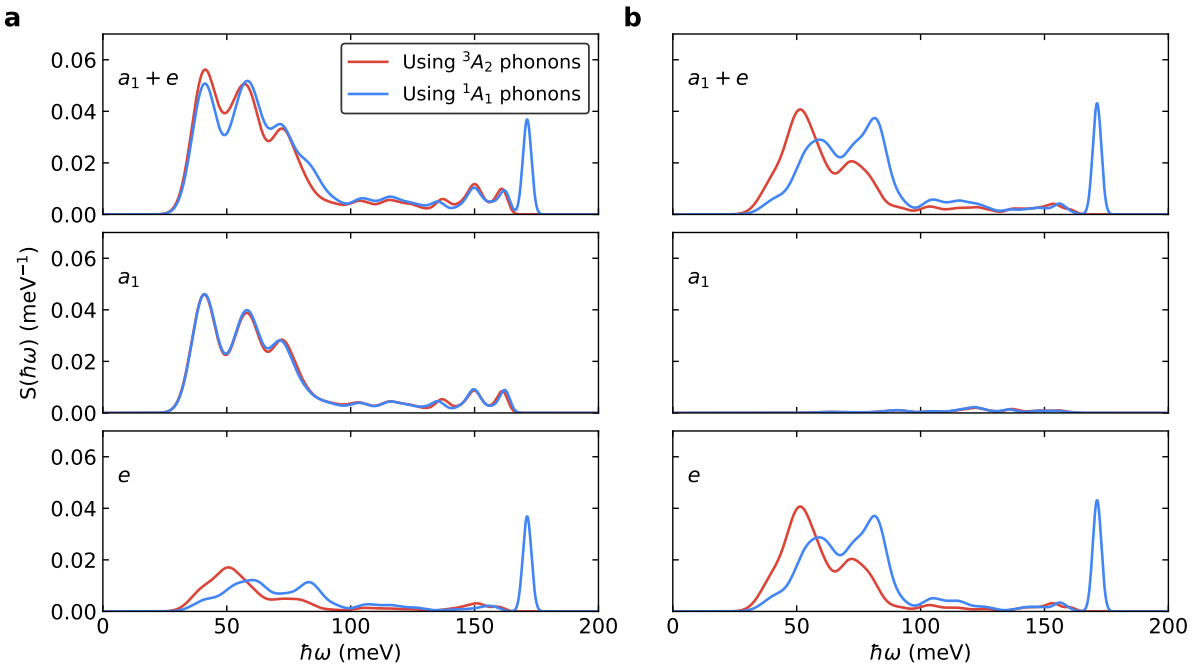

Figure 5.12: Spectral densities of electron-phonon coupling computed using different sets of phonon modes. Spectral densities $S(\hbar\omega)$ of the $^3E \rightarrow {}^3A_2$ transition (**a**) and the $^1E \rightarrow {}^1A_1$ transition (**b**). Red and blue lines are the spectral densities computed using the phonon modes of the $^3A_2$ state and the $^1A_1$ state, respectively. The entire spectral densities, contributions of the a_1 type phonons, and contributions of the e type phonons are shown in the upper, middle, and bottom panels, respectively. The partial Huang-Rhys factors used to evaluate the spectral densities are computed using atomic displacements between different states, which are obtained at the PBE level of theory with the $(3 \times 3 \times 3)$ supercell with 216 atomic sites.

harmonicity perturbatively. Following Ref. [235], the spectral function for optical absorption, including the lowest order of anharmonic effects, reads:

$$A_{\text{abs, an}}(\hbar\omega, T) = \frac{1}{2\pi\hbar} \int_{-\infty}^{\infty} \mathrm{e}^{\mathrm{i}\omega t} G_{\text{abs, an}}(t, T) \mathrm{e}^{-\frac{\lambda|t|}{\hbar}} \mathrm{d}t, \tag{5.17}$$

Table 5.5: Comparison of Huang-Rhys factors (HRFs) computed using forces and actual displacements. Total HRFs of the $^1E \rightarrow {}^1A_1$ transition computed using either $\Delta Q_{k,F}$ ($\sum_k S_{k,F}$) or ΔQ_k ($\sum_k S_k$) for the $(3 \times 3 \times 3)$ supercell. The ratio $r = \frac{a_3 \Delta Q}{a_2}$ reported here is computed based on fitting the results of the one-dimensional configurational coordinate diagrams (see Figure 5.13). Here, DDH$-\Delta Q$, PBE$-ph$ denotes the line shapes based on the Huang-Rhys theory, evaluated using ΔQ computed at the DDH level and the phonon modes computed at the PBE level of theory.

	PBE$-\Delta Q$, PBE$-ph$	DDH$-\Delta Q$, PBE$-ph$
$\sum_k S_{k,F}$	1.33	1.03
$\sum_k S_k$	1.63	1.59
$\frac{\sum_k S_{k,F}}{\sum_k S_k}$	0.816	0.648
r	-0.065	-0.120
$(1 + 3r)$	0.805	0.640

where $G_{\text{abs, an}}(\hbar\omega, T)$ is the generating function including the lowest order of anharmonic effects

$$G_{\text{abs, an}}(t,T) = \exp\left[\mathrm{i}t\left(2\sum_k S_k \omega_k r_k\right)\right] \exp\left[(1+3r_k)\left(\int_{-\infty}^{\infty} S(\hbar\omega)\mathrm{e}^{-\mathrm{i}\omega t}\mathrm{d}(\hbar\omega) - \sum_k S_k + \int_{-\infty}^{\infty} C(\hbar\omega,T)\mathrm{e}^{-\mathrm{i}\omega t}\mathrm{d}(\hbar\omega) + \int_{-\infty}^{\infty} C(\hbar\omega,T)\mathrm{e}^{\mathrm{i}\omega t}\mathrm{d}(\hbar\omega) - 2\sum_k \overline{n}_k(T) S_k\right)\right]. \tag{5.18}$$

Here, we have expanded the potential energy to the third order with respect to the kth phonon mode

$$V_k(Q_k) = a_{k2} Q_k^2 + a_{k3} Q_k^3. \tag{5.19}$$

and we have defined r_k as the unitless ratio between the third and the second-order coefficients of the expansion

$$r_k = \frac{a_{k3}}{a_{k2}} \Delta Q_k \,. \tag{5.20}$$

It is evident that the anharmonicity affects the line shape in two ways. Firstly, it shifts the position of the zero-phonon line and also the phonon sidebands from E_{ZPL} to $E_{\text{ZPL}} -$

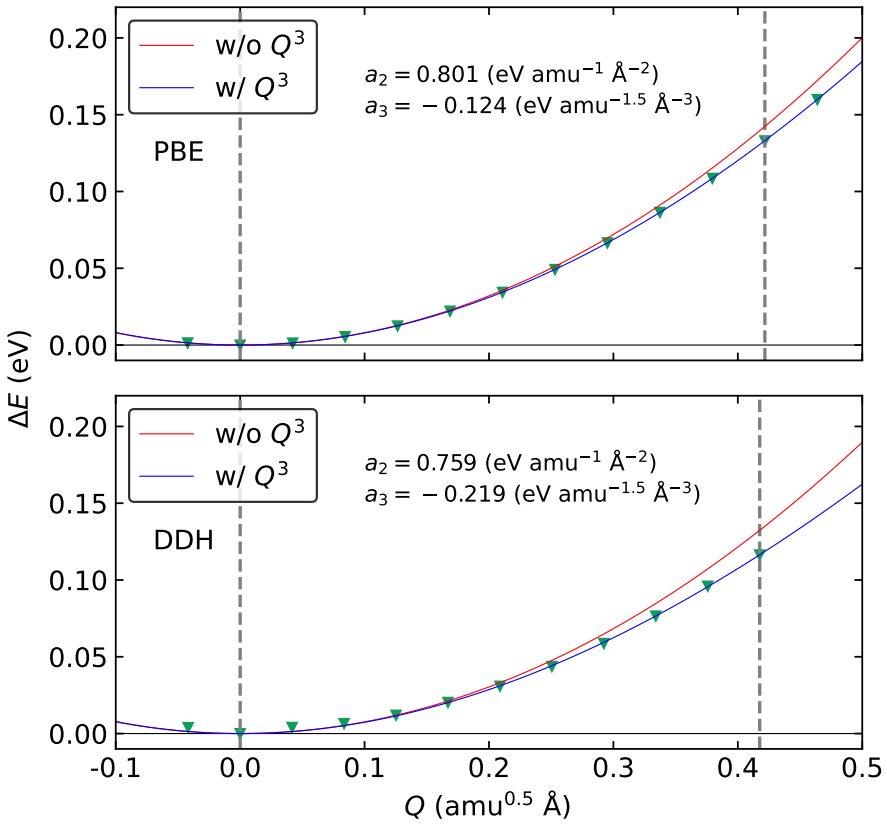

Figure 5.13: Anharmonic effects of the potential energy curves (PECs). The PECs of the $^1A_1$ state along the linear path connecting the equilibrium geometries of the $^1A_1$ state and the ^1E state computed using TDDFT with PBE (top panel) and DDH (bottom panel) functional. The energy difference relative to the local minimum, ΔE, is fitted as a function of Q as $\Delta E = a_2 Q^2 + a_3 Q^3$. Blue lines are obtained with the fitted function, while the red lines are obtained neglecting the $a_3 Q^3$ term.

$2\sum_k S_k(\hbar\omega_k) r_k$. Further, it scales the HRFs. The anharmonic HR factor can be defined as

$$S_{k,\mathrm{an}} = (1 + 3r_k) S_k. \tag{5.21}$$

The latter effect is responsible for changing the line shape of the transition.

In the following, we show an efficient method to compute the anharmonic HR factor. We first compute, at the equilibrium atomic geometry of the ^1E state, the force $\mathbf{F}_\alpha$ associated with the $^1A_1$ PES and exerted on atom α. We then compute the effective displacement

associated to the kth phonon, $\Delta Q_{k,F}$, as

$$\Delta Q_{k,F} = \frac{1}{\omega_k^2} \sum_{\alpha=1}^{N} \frac{\mathbf{F}_\alpha \cdot \mathbf{e}_{k,\alpha}}{\sqrt{M_\alpha}} = \frac{1}{\omega_k^2} \langle \widetilde{\mathbf{F}} | \mathbf{e}_k \rangle = \frac{\widetilde{\mathbf{F}}_k}{\omega_k^2}, \tag{5.22}$$

where M_α is the mass of the αth atom, and ω_k and $\mathbf{e}_{k,\alpha}$ are the energy and eigenvector of the kth phonon mode, respectively. $\widetilde{\mathbf{F}}_\alpha = \mathbf{F}_\alpha / \sqrt{M_\alpha}$. If we use the definition of $\widetilde{\mathbf{F}}_k$ in terms of a derivative of the potential, and we express the potential as in Eq. (5.19), we obtain:

$$\widetilde{\mathbf{F}}_k = -\frac{\partial V_k(Q_k)}{\partial Q_k}\bigg|_{Q_k=\Delta Q_k} = -2a_{k2}\Delta Q_k - 3a_{k3}\Delta Q_k^2 = -\omega_k^2 \Delta Q_k \left(1 + \frac{3a_{k3}}{2a_{k2}}\Delta Q_k\right), \tag{5.23}$$

where we used the fact that $a_{k2} = \frac{1}{2}\omega_k^2$. Here, ΔQ_k is the actual displacement directly evaluated using the atomic displacements between the equilibrium geometry of the $^1A_1$ and the ^1E states. Then, the HRF can be evaluated as

$$\begin{aligned} S_{k,F} &= \frac{\omega_k \Delta Q_{k,F}^2}{2\hbar} \\ &= \frac{\omega_k}{2\hbar}\left(\frac{\widetilde{\mathbf{F}}_k}{\omega_k^2}\right)^2 \\ &= \frac{\omega_k \Delta Q_k^2}{2\hbar}\left(1 + \frac{3a_{k3}}{2a_{k2}}\Delta Q_k\right)^2 \\ &= S_k\left(1 + 3\frac{a_{k3}}{a_{k2}}\Delta Q_k + O\left(a_{k3}^2\right)\right) \\ &\approx S_k(1 + 3r_k), \end{aligned} \tag{5.24}$$

which is exactly the anharmonic HR factor $S_{k,\mathrm{an}}$ (Eq. (5.21)). In the last step, we neglected the term containing a_{k3}^2. Therefore, by evaluating the HRFs using $\Delta Q_{k,F}$ computed using Eq. (5.22), we automatically include anharmonic effects to the lowest order. We also note that if anharmonic effects are negligible, then by definition, $S_{k,F} = S_k$.

Table 5.5 reports the total HRFs computed using either forces or displacements. We also

report the unitless ratio r of Eq. (5.20) evaluated based on the cubic fitting of the PECs of the $^1A_1$ along the one-dimensional configurational coordinate diagram connecting the equilibrium geometries of the $^1A_1$ and ^1E states. By comparing $\frac{\sum_k S_{k,F}}{\sum_k S_k}$ with $(1+3r)$, we can conclude that anharmonic effects are included when calculating HRFs using $\Delta Q_{k,F}$.

CHAPTER 6

FIRST-PRINCIPLES SIMULATION OF SPIN-DEFECTS FOR QUANTUM INFORMATION SCIENCE

In this chapter, we introduce two studies in which we employ first-principles methods to explore spin-defects relevant to quantum information science (QIS). Specifically, our investigations focus on the photo-ionization processes of neutral divacancy centers in 4H-SiC and the substitutional nitrogen in diamond, aiming to interpret experimental observations and inform the design of future experiments.

6.1 First-principles study of photo-ionization and stimulated emission processes of divacancy centers in 4H-SiC

This chapter is adapted with permission from C. P. Anderson, E. O. Glen, C. Zeledon, A. Bourassa, Y. Jin, Y. Zhu, ..., and D. D. Awschalom. Sci. Adv., 8(5), eabm5912 (2022). by American Association for the Advancement of Science (2022). https://doi.org/10.1126/sciadv.abm5912.

6.1.1 Introduction

Single-shot readout of individual defects in SiC can be realized through spin-to-charge conversion, a process that translates the defect's spin state into a stable charge state. Utilizing this method, we can achieve readout fidelity exceeding 80% without the need for pre-selection or post-selection techniques, thereby facilitating a high signal-to-noise ratio crucial for measuring extended spin coherence times. In our study, we employed a first-principles approach to examine the spin-to-charge conversion mechanisms of neutral divacancy centers (VV^0) in 4H-SiC, with a particular focus on analyzing charge transition levels and photo-ionization

cross sections. Our findings align closely with experimental data and offer valuable insights for refining experimental protocols related to spin-to-charge conversion operations.

6.1.2 Theory and methods

Energetics

We computed the energy of the ionization threshold ($E^{\mathrm{VBM}}_{q+1/q}$) from VV^0 to VV^- using Kohn-Sham density functional theory (DFT):

$$E^{\mathrm{VBM}}_{q+1/q} = E^{q}_{\mathrm{tot}} - E^{q+1}_{\mathrm{tot}} + \Delta V(q) - \Delta V(q+1) - \varepsilon(\mathrm{VBM}) \tag{6.1}$$

where $q = -1$ for VV^- and $q + 1 = 0$ for VV^0, E_{tot} is the total energy of the supercell containing the defect, ΔV is a correction term to the total energy as derived by Freysoldt et al. in the case of charged defects [236], and $\varepsilon_{\mathrm{VBM}}$ is the position of valence band maximum (VBM) as determined by the highest occupied Kohn-Sham eigenvalue.

Cross sections

The cross section of the stimulated emission as a function of the photon energy $\hbar\omega$ and temperature T is given by [221]:

$$\sigma_{\mathrm{s}}(\hbar\omega, T) = \frac{4\pi^2\alpha}{n}\hbar\omega r_{\mathrm{s}}^2 A_{\mathrm{s}}\left(\hbar\omega - E_{\mathrm{ZPL}}, T\right). \tag{6.2}$$

Here, α is the fine-structure constant, n is the refractive index, r_{s}^2 is the square of the optical matrix element for the transition ${}^3E$ to ${}^3A_2$ of VV^0 at a given photon polarization, and E_{ZPL} is the energy of the zero-phonon line (ZPL). $A_{\mathrm{s}}(\hbar\omega, T)$ is the electron-phonon spectral function for stimulated emission, which is the same as that of the spontaneous emission

(photoluminescence) [82, 83]:

$$A_{\mathrm{s}}(\hbar\omega, T) = \sum_{a}\sum_{b} P_{e_a}(T) \left|\left\langle \Theta_{e_a} \mid \Theta_{g_b} \right\rangle\right|^2 \delta\left(\hbar\omega - E_{e_a} + E_{g_b}\right). \tag{6.3}$$

Here, Θ_{e_a} $\left(\Theta_{g_b}\right)$ is the a-th (b-th) nuclear wave function of the system in the excited state ^3E (ground state $^3A_2$) with vibrational energy E_{e_a} $\left(E_{g_b}\right)$, and $P_{e_a}(T)$ is the distribution function of the vibrational energies at finite temperature in the excited state. We compute the spectral function by using the displaced harmonic oscillator approximation and the generating function approach [83].

Similarly, the ionization cross section is given by:

$$\sigma_{\mathrm{i}}(\hbar\omega, T) = \frac{4\pi^2\alpha}{n}\hbar\omega \sum_{j} r_{i,j}^2 A_{\mathrm{i}}\left(\hbar\omega - E_{i,j}, T\right). \tag{6.4}$$

Here, $r_{i,j}^2$ is the square of the optical matrix element between the initial state (^3E state of VV^0), and all possible final states (^2E state of VV^- with a hole in the valence band) for a given photon polarization direction. The summation over j includes all valence states of the defective system. $E_{i,j}$ is the energy difference between the initial and final states. $A_{\mathrm{i}}(\hbar\omega, T)$ is the electron-phonon spectral function for ionization, which can be computed in the same way as $A_{\mathrm{s}}(\hbar\omega, T)$. We computed the ionization cross section as a convolution [221]:

$$\sigma_{\mathrm{i}}(\hbar\omega, T) = \hbar\omega \int_{-\infty}^{\infty} \frac{1}{\hbar\omega'} \tilde{\sigma}_{\mathrm{i}}\left(\hbar\omega'\right) A_{\mathrm{i}}\left(\hbar\omega - \hbar\omega'\right) d\left(\hbar\omega'\right), \tag{6.5}$$

where

$$\tilde{\sigma}_{\mathrm{i}}(\hbar\omega) = \frac{4\pi^2\alpha}{n}\hbar\omega \sum_{j} r_{i,j}^2 \delta\left(\hbar\omega - E_{\mathrm{i},j}\right). \tag{6.6}$$

Here, we replace the δ function with a Gaussian function.

Optical matrix elements

Optical matrix elements are key ingredients for the accurate description of both the stimulated-emission and ionization cross sections. Here, we compute optical matrix elements, assuming that the wavefunctions of the single-particle orbitals of the defective crystal are the same irrespective of the orbital occupation. Hence, the optical matrix elements between two many-electron wavefunctions can be computed from the matrix elements between single-particle orbitals [221]. For example, the optical matrix elements entering the stimulated emission cross section for the $m_s = 1$ sublevel of the ^3E and the $^3A_2$ state of VV^0 are given by:

$$\begin{aligned} \boldsymbol{r}_s &= \left\langle {}^3E_{x/y}, m_s = 1 \left| \sum_e \boldsymbol{r}_e \right| {}^3A_2, m_s = 1 \right\rangle \\ &= \left\langle \bar{a}_1 \bar{e}_{x/y} \left| \sum_e \boldsymbol{r}_e \right| \bar{e}_{y/x} \bar{e}_{x/y} \right\rangle = \left\langle \bar{a}_1 | \boldsymbol{r} | \bar{e}_{y/x} \right\rangle \end{aligned} \tag{6.7}$$

where we use the hole representation for many-electron wavefunctions. A similar expression is obtained for the $m_s = 1$ and $m_s = -1$ sublevels, where we assume that the spin-up and spin-down orbitals are identical.

The ionization optical matrix elements are calculated in a way similar to those of the stimulated emission. The optical matrix element from the $m_s = 1$ and $m_s = -1$ sublevels of the ^3E state of VV^0 into the $m_s = \frac{1}{2}$ and $m_s = -\frac{1}{2}$ sublevels of the ^2E state of $VV^-$with a hole in the valence band are given by:

$$\begin{aligned} \boldsymbol{r}_{i,j} &= \left\langle {}^3E_{x/y}, m_s = 1 \left| \sum_e \boldsymbol{r}_e \right| \left({}^2E_{x/y}, m_s = \frac{1}{2} \right) + \bar{\phi}_j \right\rangle \\ &= \left\langle \bar{a}_1 \bar{e}_{x/y} \left| \sum_e \boldsymbol{r}_e \right| \bar{e}_{x/y} \bar{\phi}_j \right\rangle \\ &= \left\langle \bar{a}_1 | \boldsymbol{r} | \bar{\phi}_j \right\rangle , \end{aligned} \tag{6.8}$$

and

$$\begin{aligned}\boldsymbol{r}_{i,j} &= \left\langle {}^3E_{x/y}, m_s = -1 \left| \sum_e \boldsymbol{r}_e \right| \left({}^2E_{x/y}, m_s = -\frac{1}{2} \right) + \phi_j \right\rangle \\ &= \left\langle a_1 e_{x/y} \left| \sum_e \boldsymbol{r}_e \right| e_{x/y} \phi_j \right\rangle \\ &= \left\langle a_1 | \boldsymbol{r} | \phi_j \right\rangle .\end{aligned} \tag{6.9}$$

In an analogous fashion, the optical matrix element from the $m_s = 0$ sublevel of the ${}^3E$ state of VV^0 into the $m_s = \frac{1}{2}$ and $m_s = -\frac{1}{2}$ sublevels of the ${}^2E$ state of $VV^-$with a hole in the valence band are given by:

$$\begin{aligned}\boldsymbol{r}_{i,j} &= \left\langle {}^3E_{x/y}, m_s = 0 \left| \sum_e \boldsymbol{r}_e \right| \left({}^2E_{x/y}, m_s = \frac{1}{2} \right) + \phi_j \right\rangle \\ &= \frac{1}{\sqrt{2}} \left\langle a_1 \bar{e}_{x/y} \left| \sum_e \boldsymbol{r}_e \right| \bar{e}_{x/y} \phi_j \right\rangle + \frac{1}{\sqrt{2}} \left\langle \bar{a}_1 e_{x/y} \left| \sum_e \boldsymbol{r}_e \right| \bar{e}_{x/y} \phi_j \right\rangle \\ &= \frac{1}{\sqrt{2}} \left\langle a_1 | \boldsymbol{r} | \phi_j \right\rangle ,\end{aligned} \tag{6.10}$$

and

$$\begin{aligned}\boldsymbol{r}_{i,j} &= \left\langle {}^3E_{x/y}, m_s = 0 \left| \sum_e \boldsymbol{r}_e \right| \left({}^2E_{x/y}, m_s = -\frac{1}{2} \right) + \bar{\phi}_j \right\rangle \\ &= \frac{1}{\sqrt{2}} \left\langle a_1 \bar{e}_{x/y} \left| \sum_e \boldsymbol{r}_e \right| e_{x/y} \bar{\phi}_j \right\rangle + \frac{1}{\sqrt{2}} \left\langle \bar{a}_1 e_{x/y} \left| \sum_e \boldsymbol{r}_e \right| e_{x/y} \bar{\phi}_j \right\rangle \\ &= \frac{1}{\sqrt{2}} \left\langle \bar{a}_1 | \boldsymbol{r} | \bar{\phi}_j \right\rangle\end{aligned} \tag{6.11}$$

Hence, the cross section is the same for all three sublevels of the ${}^3E$ state of VV^0. To investigate the effect of photon polarization, we express the photon wavevector in polar coordinates (Fig. 6.1) [237] with the z direction parallel to the c axis of 4H-SiC as:

$$\mathbf{q} = (\sin\theta\cos\varphi, \sin\theta\sin\varphi, \cos\theta), \tag{6.12}$$

and two polarization vectors in the $x-y$ plane and the $\mathbf{q}-z$ plane as

$$\boldsymbol{e}_{\parallel} = (-\sin\varphi, \cos\varphi, 0), \tag{6.13}$$

and

$$\boldsymbol{e}_{\perp} = (-\cos\theta\cos\varphi, -\cos\theta\sin\varphi, \sin\theta). \tag{6.14}$$

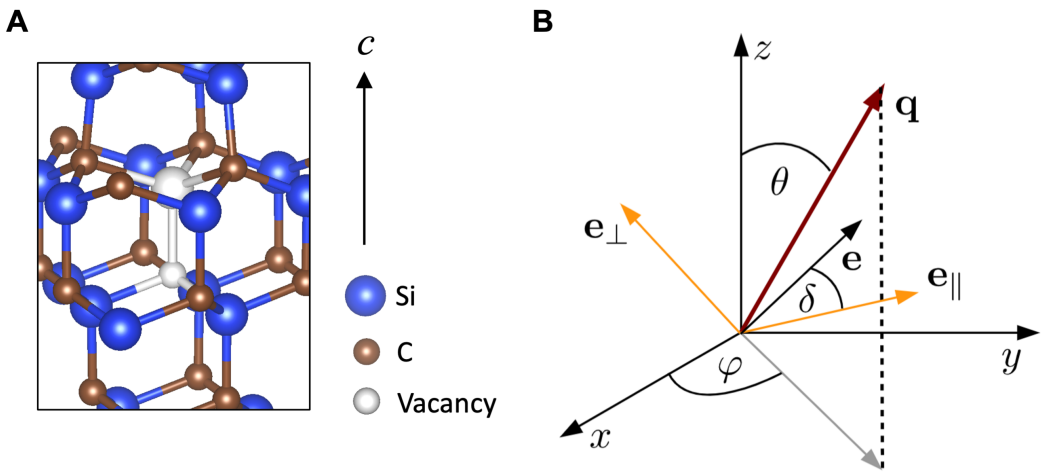

Figure 6.1: Schematic representation of the system. (A) Structure of the hh divacancy center in 4H-SiC. The 3-fold rotational axis of the divacancy center is parallel to the c-axis, as shown in the plot. (B) Polarization for a photon with wavevector $\mathbf{q}$, defined by the angles θ and φ in polar coordinates. The z-axis is chosen such that it aligns with the c-axis of 4H-SiC. $\mathbf{e}_{\parallel}$ is the component of the photon polarization vector that lies in the $x-y$ plane; $\mathbf{e}_{\perp}$ is the out-of-plane component of the photon polarization; both $\mathbf{e}_{\parallel}$ and $\mathbf{e}_{\perp}$ are perpendicular to $\mathbf{q}$. Any polarization direction $\mathbf{e}$ can be expressed as a linear combination of $\mathbf{e}_{\parallel}$ and $\mathbf{e}_{\perp}$.

As a result, any polarization vector can be expressed as a linear combination of $\boldsymbol{e}_{\parallel}$ and $\boldsymbol{e}_{\perp}$

$$\mathbf{e} = \cos\delta\boldsymbol{e}_{\parallel} + \sin\delta\boldsymbol{e}_{\perp} \tag{6.15}$$

and the square of the optical matrix element r^2 becomes

$$r^2 = |\boldsymbol{e}\cdot\boldsymbol{r}|^2 = \left|\cos\delta\boldsymbol{e}_{\parallel}\cdot\boldsymbol{r} + \sin\delta\boldsymbol{e}_{\perp}\cdot\boldsymbol{r}\right|^2, \tag{6.16}$$

where the angle δ is defined in Fig. 6.1.

6.1.3 Computational parameters

Energetics of the ionization of VV^0 to VV^-

We carried out DFT calculations with the Quantum ESPRESSO code [139, 207, 208] and a dielectric dependent hybrid (DDH) functional [33, 34], using a fraction of exact exchange equal to 0.15, corresponding to the inverse of the experimental dielectric constant of 4H-SiC in the direction parallel to the c-axis (see Fig. 6.1) [126]. We used supercells with 400 atoms ($5 \times 5 \times 2$) and sampled the supercell Brillouin zone with the Γ point. We employed SG15 ONCV pseudopotentials [141, 142] and a plane-wave basis with a kinetic energy cut-off of 80 Ry. We used constrained occupations in DFT calculations to evaluate the excited states of the VV0 defect, and we computed the Freysoldt correction term with the `sxdefectalign` package [236]. However, larger cell sizes are required to converge the computed values of the ZPL, and here we report the values of the ZPL energy extrapolated to the values obtained with a 1024 atom-site supercell ($8 \times 8 \times 2$) [83].

Table 6.1: Comparison between DFT results and experiment. Experimental values of each transition are calculated using the measured fundamental gap (3.285 eV), experimental ZPL (1.096 eV), and experimental threshold of ionization (1.31 eV) reported in Ref. [238].

Transition	Computed (DFT, eV)	Measured (eV)
${}^3A_2 \rightarrow {}^3E$ (ZPL)	1.196	1.096
${}^3A_2 \rightarrow {}^2E$	2.090	1.98
${}^3E \rightarrow {}^2E$	1.029	0.88

Cross section

We used the refractive index $n = 2.55$ of 4H-SiC [220] in our calculation of ionization and stimulated-emission cross sections, and in Fig. 6.3, we aligned the computed (1.196 eV) and

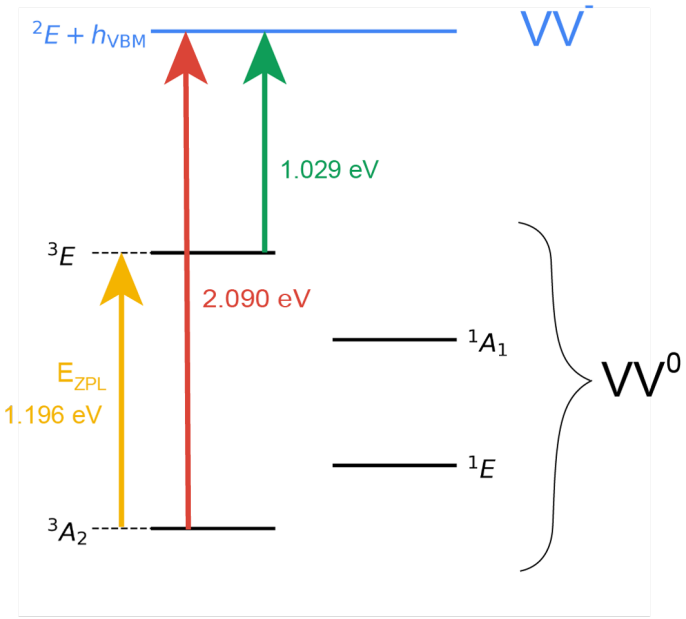

Figure 6.2: Schematic representation of the ionization of VV^0 to VV^-, where the energy of the transitions from many-body states (black lines) are indicated. $^3A_2$ and ^3E are the ground and excited triplet states of VV^0 respectively and ^2E corresponds to the ground state of VV^-; $^1A_1$ and ^1E, the singlet states of VV^0 are also indicated.

the experimental (1.096 eV) ZPL energies for the stimulated cross section and the computed (1.029 eV) and the experimental (0.88 eV) onset for the ionization cross section.

We computed spectral functions (Eq. (6.3)) using the generating function approach and the displaced harmonic oscillator approximation. We used Gaussian functions with a standard deviation of 5 meV to broaden the δ function entering the expression of the spectral densities (Eqs. (11) and (12) of Ref. [83]. In the case of the stimulated emission, we broadened the ZPL with $\lambda = 0.002$ meV (Eq. (8) of Ref. [83], with the temperature set to 0 K in all calculations. We used Gaussian functions with a standard deviation of 30 meV to broaden the δ function entering Eq. (6.6) (ionization cross section).

We computed the phonon modes of defective solids using the frozen phonon approach and a $(5 \times 5 \times 2)$ supercell, with configurations generated with the `PHONOPY` package [45] and a displacement of 0.01 Å from equilibrium positions. We extrapolated our results to the

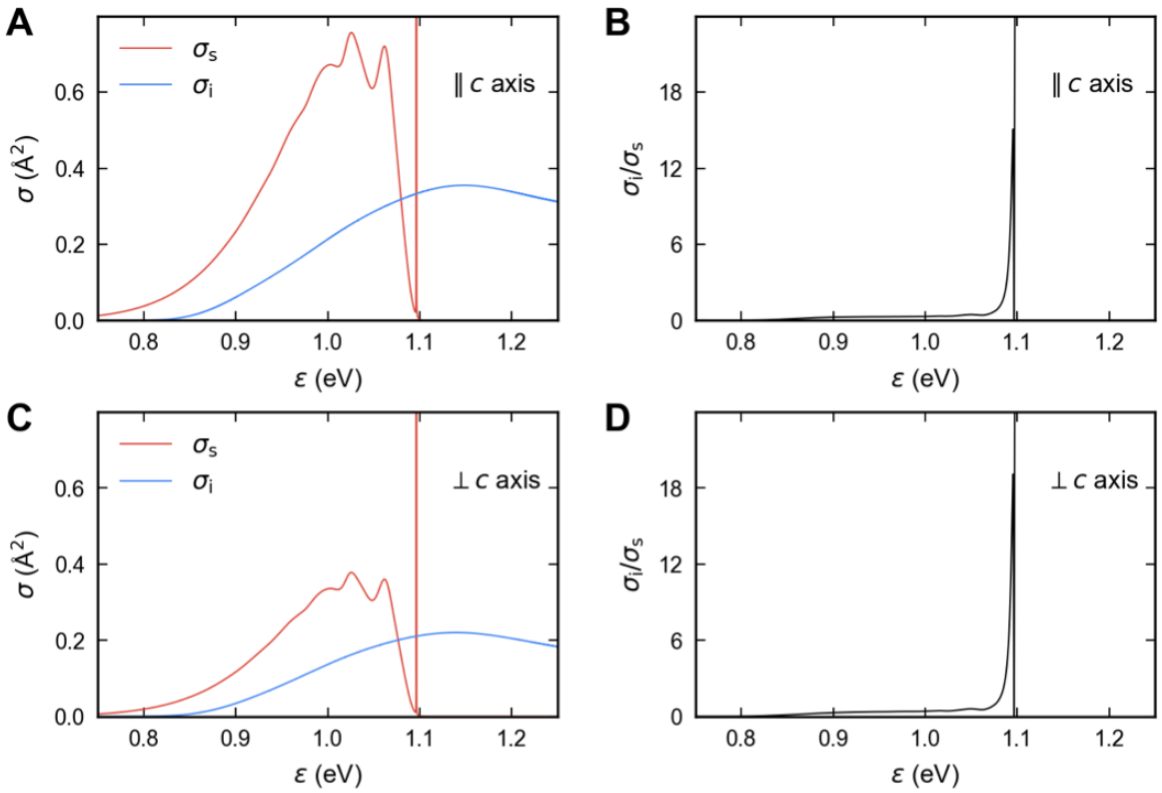

Figure 6.3: Computed stimulated emission (σ_s), ionization (σ_i) cross sections and their ratio. Computed cross sections with the light parallel (A) and perpendicular (C) to the c axis of 4H-SiC averaged over all possible polarization directions. The ratio of the stimulated emission and ionization cross sections with the light parallel (B) and perpendicular (D) to the c axis of 4H-SiC averaged over all possible polarization directions.

($16 \times 16 \times 5$) supercell values, as proposed in Ref. [83]. The ground-state phonons of the hh-VV^0 defect (hh-VV^-) were used in the calculation of spectral functions of the stimulated emission (ionization). We used equal occupations of the e_x and the e_y orbitals in the phonon calculations for hh-VV^- to maintain the C_{3v} symmetry of the point defect.

Optical matrix elements

We computed optical matrix elements between Kohn-Sham orbitals for hh-VV^0 in its ground state $^3A_2$ as

$$\langle \psi_a | \boldsymbol{r} | \psi_b \rangle = \frac{\left\langle \psi_a | [\widehat{H}, \boldsymbol{r}] | \psi_b \right\rangle}{\varepsilon_a - \varepsilon_b}. \tag{6.17}$$

Here, $\hat{H}$ is the Kohn-Sham Hamiltonian; ε_a (ε_b) is the energy of the Kohn-Sham orbital with single particle wavefunction ψ_a (ψ_b), and the contribution of the non-local potential to the commutator is explicitly taken into account. Calculations were performed with the WEST code [121] at the PBE level of theory [31]. We checked convergence as a function of the supercell size by carrying out calculations with a $(5 \times 5 \times 2)$ supercell with 400 atomic sites up to a $(9 \times 9 \times 2)$ supercell with 1296 atomic sites (see Fig. 6.5 for details).

6.1.4 Results

Polarization dependence

To determine the dependence of stimulated emission and ionization spectra on the light polarization, we considered the two limiting cases of light propagation along the z-axis, parallel to the 3-fold rotational axis of the defect, which has C_{3v} symmetry, and that of propagation along the x-axis (Fig. 6.1). In the case of propagation along the z-axis, we did not observe any polarization dependence of either the stimulated emission or the ionization cross sections (Fig. 6.4A), due to the symmetry of the defect orbitals in the $x - y$ plane orthogonal to the defect 3-fold rotational axis. In the case of light propagation within the $x - y$ plane, we observed instead a strong polarization dependence of the cross sections (Fig. 6.4C). For out-of-plane polarization parallel to the defect axis, the stimulated emission vanishes, and the cross-section ratio displays a pronounced pole.

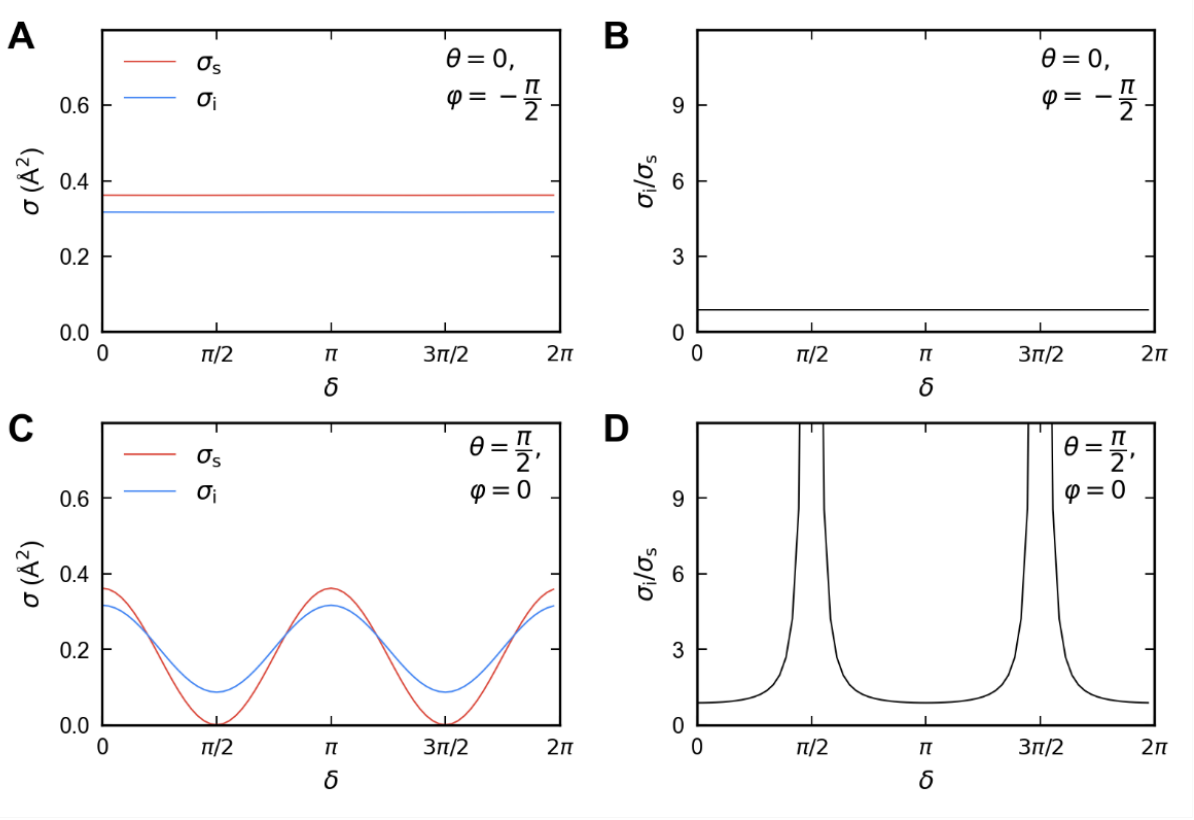

Figure 6.4: Computed stimulated emission (σ_s), ionization (σ_i) cross sections and their ratio at 1151 nm. (A) Computed cross sections at $\theta = 0$ and $\varphi = -\frac{\pi}{2}$ (light parallel to the z axis) (C) and at $\theta = \frac{\pi}{2}$ and $\varphi = 0$ (light perpendicular to the x axis) as a function of the polarization angle δ. (B) The ratio of the stimulated emission cross sections and ionization cross sections at $\theta = 0$ and $\varphi = -\frac{\pi}{2}$ (light parallel to the z axis) (D) and at $\theta = \frac{\pi}{2}$ and $\varphi = 0$ (light perpendicular to the x axis) as a function of the polarization angle δ.

Convergence of calculations

To investigate the finite-size effects on computed optical matrix elements and thus on the cross sections, we performed calculations using supercells with sizes increasing from $(5\times5\times2)$ to $(9 \times 9 \times 2)$ (Fig. 6.5). We observed an increase of the stimulated emission cross section and a decrease of the ionization cross section as a function of supercell size and reached convergence for the $(9 \times 9 \times 2)$ supercell.

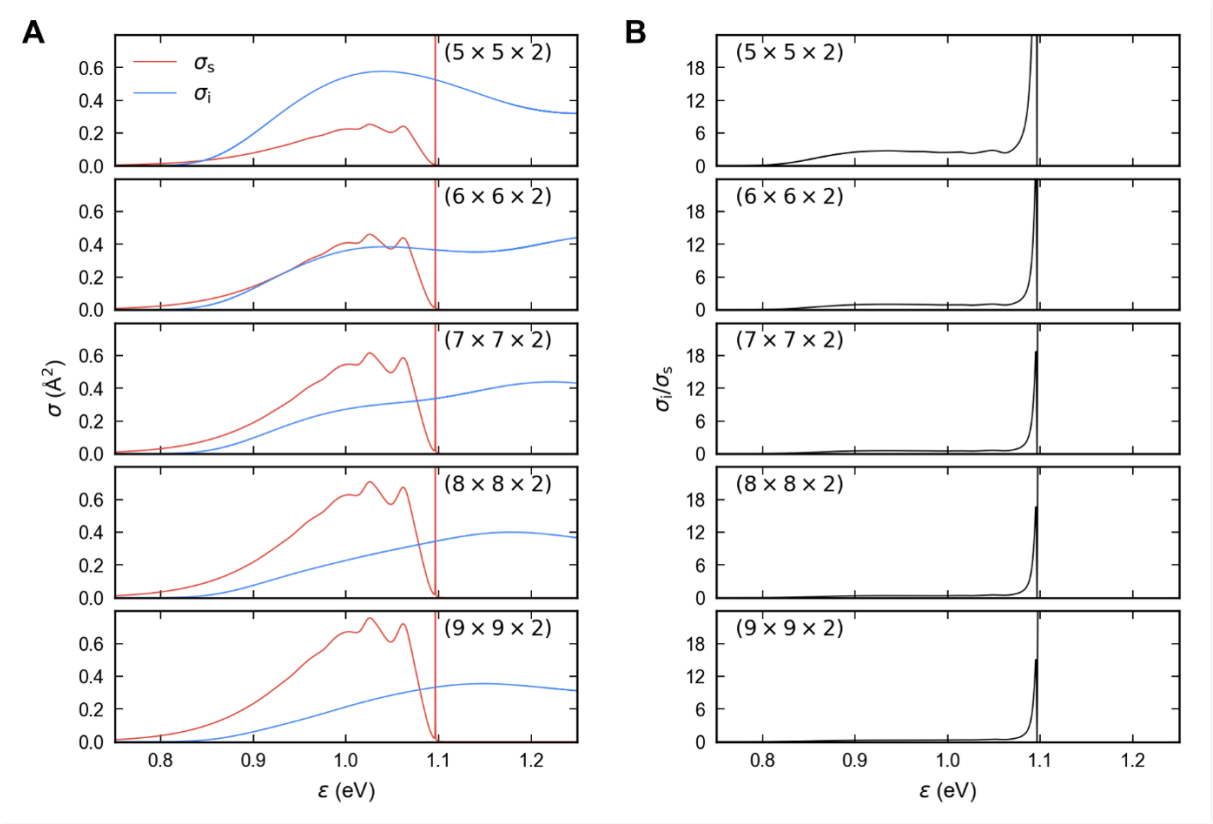

Figure 6.5: Computed stimulated emission (σ_s), ionization (σ_i) cross sections and their ratio as a function of the photon energy for supercells with different sizes. (A) Cross sections (B) and their ratio reach convergence for the $(9 \times 9 \times 2)$ supercell.

6.2 First-principles study of photo-ionization process of the substitutional nitrogen in diamond

This chapter is adapted with permission from J. C. Marcks, M. Onizhuk, Y.-X. Wang, Y. Jin, Y. Zhu, B. S. Soloway, M. Fukami, N. Delegan, F. J. Heremans, A. A. Clerk, G. Galli, and D. D. Awschalom. ArXiv:2312.02894 (2023). https://doi.org/10.48550/arXiv.2312.02894.

6.2.1 Introduction

In this work, we explore the dynamics of nitrogen-vacancy (NV) centers in diamond and their interactions with nearby substitutional nitrogen (N_s) defects, also known as P1 centers,

which are crucial for quantum sensing and understanding charge dynamics within diamond. Employing density functional theory (DFT) calculations, we precisely identify the charge transition levels and ionization cross sections for the N_s center, aligning our theoretical findings with experimental data to enhance our knowledge of its ionization and recapture mechanisms.

6.2.2 Theory and methods

Charge transition level

We computed the charge transition level ($E^{\mathrm{CBM}}_{q+1/q}$) for the $N_s^0 \rightarrow N_s^+ + e^-$ transition using Kohn-Sham density functional theory (DFT):

$$E^{\mathrm{CBM}}_{q+1/q} = \varepsilon(\mathrm{CBM}) - \left(E^{q}_{\mathrm{tot}} - E^{q+1}_{\mathrm{tot}} + \Delta V(q) - \Delta V(q+1)\right), \tag{6.18}$$

where $q = 0$ for N_s^0 and $q+1 = +1$ for N_s^+, E_{tot} is the total energy of the supercell containing the defect, ΔV is a correction term to the total energy as derived by Freysoldt et al., in the case of charged defects [236], and ε(CBM) is the position of conduction band minimum (CBM) of diamond.

We carried out DFT calculations with the Quantum ESPRESSO code [139, 140], and the Perdew-Burke-Ernzerhof (PBE) functional [31] and the dielectric dependent hybrid (DDH) functional [33, 34]. We used a fraction of exact exchange equal to 0.18 in the DDH functional, corresponding to the inverse of the high-frequency dielectric constant of diamond [239]. We used a $(4 \times 4 \times 4)$ supercell containing 512 atoms and sampled the supercell Brillouin zone with the Γ point. We employed SG15 ONCV pseudopotentials [141, 142] and a plane-wave basis with a kinetic energy cut-off of 85 Ry. We computed the Freysoldt correction term with the `sxdefectalign` package [236].

Ionization cross section

We computed the ionization cross section as a convolution [221]:

$$\sigma_{\text{ion}}(\hbar\omega, T) = \hbar\omega \int_{-\infty}^{\infty} \frac{1}{\hbar\omega'} \tilde{\sigma}_{\text{ion}}\left(\hbar\omega'\right) A_{\text{ion}}\left(\hbar\omega - \hbar\omega', T\right) \mathrm{d}\left(\hbar\omega'\right). \tag{6.19}$$

Here, $A_{\text{ion}}\left(\hbar\omega, T\right)$ is the electron-phonon spectral function for ionization, which is computed using the Huang-Rhys theory and the generating function approach [70, 82, 83, 221], with the temperature set to 300 K. The phonons of the $\mathrm{N_s^0}$ defect were used in the calculation of spectral functions, which are computed using the frozen phonon approach and a ($4 \times 4 \times 4$) supercell at the PBE level of theory, with configurations generated with the `PHONOPY` package [45] using a displacement of 0.01 Å from the equilibrium position.

$\tilde{\sigma}_{\text{ion}}(\hbar\omega)$ stands for the ionization cross section in the absence of the lattice relaxation,

$$\tilde{\sigma}_{\text{ion}}(\hbar\omega) = \frac{4\pi^2\alpha}{n}\hbar\omega \sum_j |\mathbf{r}_j|^2 \delta\left(\hbar\omega - E_j\right). \tag{6.20}$$

Here, we used the refractive index $n = 2.4$ of diamond in our calculation of ionization cross sections, and Gaussian functions with a standard deviation of 30 meV to broaden the δ function entering Eq. 6.20. Optical matrix elements, $\mathbf{r}_j$, are computed as the transition dipole moments, i.e., $\mathbf{r}_j = \left\langle a_1 | \mathbf{r} | \varphi_j \right\rangle$, where a_1 is the defect orbital of $\mathrm{N_s^0}$ and φ_j stands for conduction bands of diamond. We computed optical matrix elements between Kohn-Sham orbitals for $\mathrm{N_s^0}$ in its ground state as

$$\left\langle a_1 | \mathbf{r} | \varphi_j \right\rangle = \frac{\left\langle a_1 | [\hat{H}, \mathbf{r}] | \varphi_j \right\rangle}{\varepsilon_{a_1} - \varepsilon_{\varphi_j}} \tag{6.21}$$

Here, $\hat{H}$ is the Kohn-Sham Hamiltonian; ε_{a_1} (ε_{φ_j}) is the energy of the Kohn-Sham orbital with single particle wavefunction a_1 (φ_j), and the contribution of the non-local pseudopotential to the commutator is explicitly taken into account. The calculation of optical matrix

elements was carried out using the WEST code [121, 122] at the PBE level of theory. To check the convergence of the ionization cross section with respect to the supercell size, we calculated optical matrix elements in supercells of different sizes, ranging from a $(4 \times 4 \times 4)$ supercell comprising 512 atoms to a $(9 \times 9 \times 9)$ supercell containing 5832 atoms, with results displayed in Fig. 6.6.

6.2.3 Results

Charge transition level

The computed charge transition level of the $N_s^0 \rightarrow N_s^+ + e^-$ transition relative to the conduction band minimum (CBM) of diamond is reported in Table 6.2. The charge transition level computed using the DDH functional is in good agreement with the theoretical value reported in literature [240].

Table 6.2: Computed charge transition level (eV) of $N_s^0 \rightarrow N_s^+ + e^-$ transition with respect to the conduction band minimum (CBM) of diamond.

PBE (This work)	DDH (This work)	HSE06 [240]
1.48	2.08	1.8

There are a range of values for the charge transition levels reported in experimental literature, from 1.7 eV to 2.3 eV [241–247], with most recent work falling in the range of 2.2 eV to 2.3 eV. Therefore, to be consistent with both our calculation and recent experiments, we report an ionization cross section with a charge transition level ranging from 2.1 eV to 2.3 eV.

Ionization cross section

To investigate the finite-size effects on computed optical matrix elements and the resulting ionization cross sections, we performed calculations using supercells with sizes increasing from $(4 \times 4 \times 4)$ containing 512 atoms to $(9 \times 9 \times 9)$ containing 5832 atoms. We noted that

the ionization cross section first decreased with increasing supercell size, but then converged for larger supercells, as shown in Fig. 6.6.

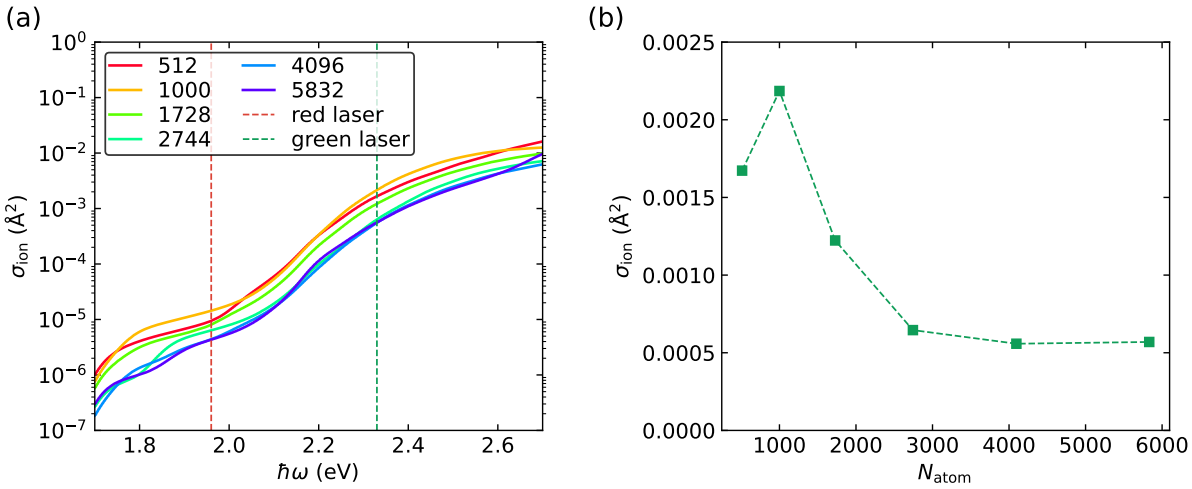

Figure 6.6: (a) Computed ionization cross section σ_{ion} as a function of the photon energy $\hbar\omega$. Calculations are performed using optical matrix elements computed in supercells with sizes increasing from $(4 \times 4 \times 4)$ containing 512 atoms to $(9 \times 9 \times 9)$ containing 5832 atoms. The charge transition level is set to 2.2 eV in the calculation. The energy of the red and green lasers are displayed as red and green dashed vertical lines, respectively. (b) Computed σ_{ion} at the energy of the green laser used in the experiment as a function of the number of atoms N_{atom} in the supercell used in the calculation of optical matrix elements.

We also examined the choice of the charge transition level in the calculation of the ionization cross section, as shown in Fig. 6.7. With a charge transition level in the range of 2.1 eV to 2.3 eV, the ionization cross section falls in the range of 1.3×10^{-3} Å^2 to 1.9×10^{-4} Å^2 ($6^{+7}_{-4} \times 10^{-4}$ Å^2), in reasonable agreement with the value measured experimentally in this work.

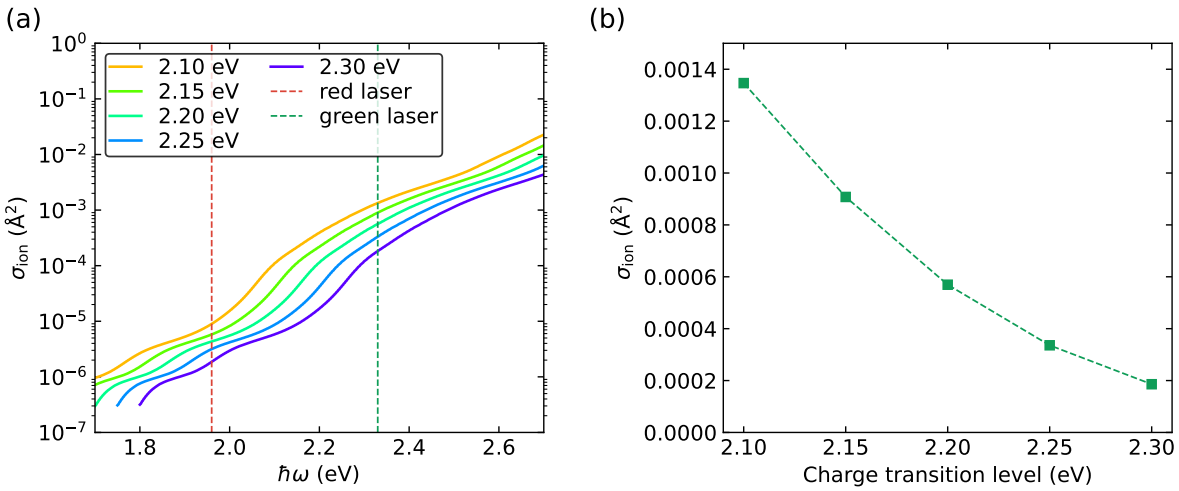

Figure 6.7: (a) Computed ionization cross section σ_{ion} as a function of the photon energy $\hbar\omega$. Calculations are performed using the $(9 \times 9 \times 9)$ supercell containing 5832 atoms. The charge transition level is varied between 2.1 eV and 2.3 eV in the calculation. The energy of the red and green laser are displayed as red and green dashed vertical lines, respectively. (b) Computed σ_{i} at the energy of the green laser as a function of the charge transition level.

CHAPTER 7

SELF-TRAPPED EXCITONS IN METAL-HALIDE PEROVSKITES INVESTIGATED BY TIME-DEPENDENT DENSITY FUNCTIONAL THEORY

We present a theoretical study on the formation of self-trapped excitons (STEs) and the associated broadband emission in metal-halide perovskites Cs_4SnBr_6 and $Cs_2AgInCl_6$, using time-dependent density functional theory (TDDFT) with the dielectric-dependent hybrid (DDH) functional. Our approach allows for an accurate description of the excitonic effect and geometry relaxation in the electronic excited states and yields optical gap, STE emission energy, and emission spectra in reasonable agreement with experiments. We point out the significance of considering geometry relaxations in the electronic excited state by showing that the exciton-phonon coupling computed in the ground-state atomic geometry is insufficient to describe the physical properties of STEs. Overall, we find that TDDFT with the DDH hybrid functional is a suitable approach for the study of the formation of STEs in perovskite and provides insights for designing metal-halide perovskites with tailored emission properties.

7.1 Introduction

In recent years, metal-halide perovskites have attracted considerable attention as efficient light emitters [248–252]. Central to the understanding and design of these luminescent materials is the concept of self-trapped exciton (STE), where an exciton formed upon light absorption becomes trapped into a local potential well caused by a deformation of the crystal lattice induced by the exciton itself. The STE recombination usually results in a broadband light emission with a significant Stokes shift [253–256]. First-principles calculations have played an essential role in clarifying the physical origin of the formation of STEs and the

broadband emission in several metal-halide perovskite materials, through the investigation of their electronic structure and atomic geometries in the electronic ground state (GS) and excited state (ES) [257–260]. However, controversies remain in comparing results obtained at different levels of theory and, in some cases, also in comparing theory with experiments since measurements are often performed on samples that are not completely defect-free.

Theoretical and computational studies of STEs require the ability to model neutral electronic ESs in periodic systems using large supercells containing hundreds of atoms, given the complex geometry of most halide perovskites. The state-of-the-art approach to the problem would, in principle, be Green's function-based GW method combined with the solution of the Bethe-Salpeter equation (GW-BSE) [261]. However, the unfavorable computational scaling with supercell size and, most importantly, the lack of numerically efficient methods to evaluate nuclear gradients with GW-BSE still hinders the applicability of the method to model STEs in metal-halide perovskites [262, 263]. Therefore, many calculations of STEs in these systems use approaches based on Kohn-Sham (KS) density functional theory (DFT), for example, the constrained-occupation DFT, also called ΔSCF, where non-Aufbau occupations of KS orbitals are used [254, 264–272], or the restricted open-shell Kohn–Sham (ROKS) method, which is similar to ΔSCF but uses spin-restricted KS orbitals [257, 273]. With the ΔSCF and the ROKS approaches, one can compute analytical forces acting on nuclei at a computational cost comparable to that of GS DFT calculations. However, these methods are not rigorously derived within a many-body framework and yield results that sometimes need to be further adjusted to compare favorably to experiments [257, 273]. Moreover, the difficulty in setting the occupation for (near-)degenerate KS orbitals and in converging the calculations has prompted the search for alternative methods.

A method widely used in the chemistry community to obtain neutral excitations and to study the photophysics of molecules is time-dependent DFT (TDDFT) [13]. When using hybrid functionals, TDDFT can also capture excitonic effects in solids [107]. However,

its application in periodic calculations for solids has been limited, mainly due to the lack of efficient implementations for evaluating analytical forces acting on nuclei in the ESs. Recently, by combining a series of algorithms, we obtained an efficient implementation of TDDFT and its analytical nuclear forces in periodic boundary conditions, now available in the open-source code WEST [274]. The controlled numerical approximations used in our implementation, together with an efficient parallelization scheme on both CPU and GPU architectures, allowed for the study of the energy and ES geometry relaxation of point defects in semiconductors and insulators with thousands of electrons [98, 150].

In this letter, we reported a hybrid TDDFT study of the electronic structure of two metal-halide perovskites, Cs_4SnBr_6 and $Cs_2AgInCl_6$, chosen as prototypical examples, and we focus on the formation of STEs and the associated broadband emission. We compare our results with those obtained with ΔSCF calculations and with experiments, with the aim of identifying a robust level of theory to describe STEs in these materials and of assessing the effect of several theoretical approximations.

7.2 Results and discussions

In our TDDFT calculations, we used the dielectric-dependent hybrid (DDH) functional [33, 34], where the fraction of the exact exchange is determined by the inverse of the high-frequency dielectric constant ϵ_∞ of the solid, which was computed self-consistently using calculations in finite-field and the Qbox Code [275], resulting in 3.05 for Cs_4SnBr_6 and 3.85 for $Cs_2AgInCl_6$. These values of ϵ_∞ yield a faction of exact exchange of 0.33 and 0.26, respectively. The DDH functional has been shown to improve the description of the electronic structure of a broad range of systems [33, 34, 83, 126–130], over the results obtained with semi-local functionals. Given the inclusion of screening effects in the Coulomb interaction between the electron and the hole in the excited state [107, 131, 132], we expect excitonic effects to be described accurately as well by the DDH functional.

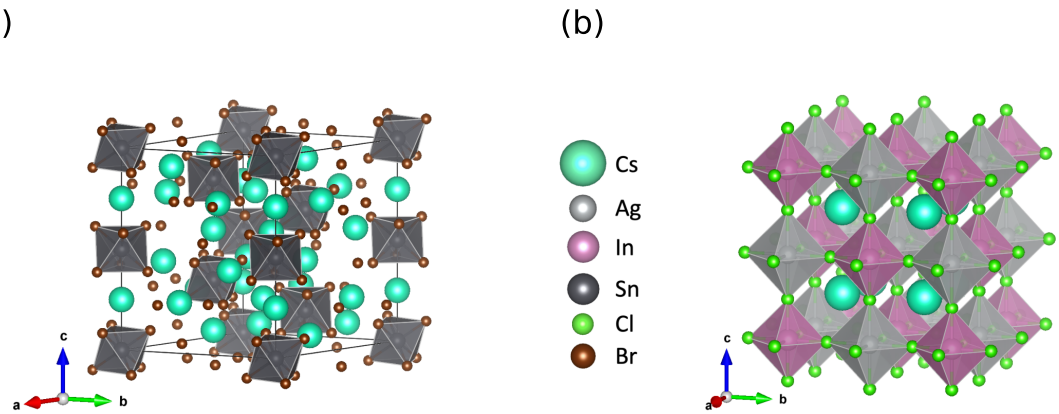

Figure 7.1: Ball-and-stick model of (a) primitive unit cell of Cs_4SnBr_6 and (b) conventional unit cell of $Cs_2InAgCl_6$. The structure of Cs_4SnBr_6 belongs to the $R\bar{3}c$ space group, and the structure of $Cs_2InAgCl_6$ belongs to the $Fm\bar{3}m$ space group.

We first computed the fundamental and the optical gaps of Cs_4SnBr_6 and $Cs_2AgInCl_6$ by carrying out DFT and TDDFT calculations, and the results are summarized in Table 7.1 together with theoretical and experimental results reported in the literature. The DFT calculations were performed using the Quantum ESPRESSO code [139, 140] and the SG15 optimized norm-conserving Vanderbilt (ONCV) pseudopotentials [141, 142] with the following valence electron configurations: Cs [$4s^2 5p^6 6s^1$], Ag [$4s^2 4p^6 5s^1 4d^{10}$], In [$5s^2 4d^{10} 5p^1$], Cl [$3s^2 3p^5$], Sn [$5s^2 4d^{10} 5p^2$], and Br [$4s^2 4p^5$]. A kinetic energy cutoff of 40 Ry was used for the plane-wave basis set, and the Brillouin zone was sampled with the Γ point. The TDDFT calculations were carried out using the WEST code [121, 122, 274] under the Tamm-Dancoff approximation. The analytical forces acting on nuclei were computed using the extended Lagrangian approach by Hutter [17] implemented within a plane-wave approach [274].

The solid Cs_4SnBr_6 is a zero-dimensional (0D) perovskite, where the [$SnBr_6$] octahedra are not directly connected. Both the valence and conduction bands of Cs_4SnBr_6 exhibit a weak dispersion [276]; hence, we performed DFT and TDDFT calculations in the primitive unit cell containing 66 atoms. The fundamental gap computed using the DDH functional is larger than those computed using the PBE0 functional, due to the higher fraction of exact ex-

change (0.33 in DDH, compared to 0.25 in PBE0). The optical gap computed using TDDFT with the DDH functional is also higher than those computed using the ΔSCF approach with the PBE0 functional. The TDDFT (DDH) result overestimates the experimental optical gap reported in literature [277, 278] by 0.4 eV. This discrepancy may have several origins. From a theoretical standpoint, it might stem from the use of a global dielectric constant in the DDH functional, which may underestimate the screening effects on the valence band maximum (VBM) localized on the [$SnBr_6$] octahedra [279]. The use of a hybrid functional that includes the spatial variation of the dielectric screening [145] may improve the description of the screening effects on the VBM and will be considered in future works. Additionally, our calculations have been performed at $T = 0$ while experiments are performed at finite T, and the measured gaps naturally include the dependence on temperature due to exciton-phonon coupling [280], which may well be substantial. It should be noted that the closer alignment of the optical gap calculated using the PBE0 level of theory with experiments is fortuitous as the screening of the PBE0 functional, corresponding to a dielectric constant (ϵ_∞) of 4, does not match the system's dielectric constant of 3.05. Note also that the two different PBE0 calculations reported in the literature yield markedly different exciton binding energies at $T = 0$ (0.6 and 1.25 eV). Our calculations yield 0.86 eV at $T = 0$, and its dependence on T remains to be explored.

In contrast to the previous case, $Cs_2AgInCl_6$ is a three-dimensional perovskite with all [$AgCl_6$] and [$InCl_6$] octahedra connected by vertices, and the valence and conduction bands are more delocalized [257, 273, 281] than those of Cs_4SnBr_6. Therefore, we performed DFT and TDDFT calculations in supercells of different sizes, ranging from 40 to 1080 atoms, and checked the convergence of both the fundamental and optical gaps as a function of size (see Figure 7.2). The fundamental gap is almost constant as a function of the supercell size, resulting in a value of 3.19 eV in the dilute limit, which agrees well with previous GW results [257, 273]. The optical gap has a linear dependence on $1/N_{\text{atom}}^{1/3}$, which arises from

Table 7.1: Electronic and optical properties of inorganic halide perovskites, obtained at different levels of theory (see text) and experiments. E_{gap} and E_{opt} are the fundamental gap and the optical gap, respectively.

		Cs_4SnBr_6	$Cs_2AgInCl_6$
E_{gap} (eV)	DDH	5.15	3.19
	PBE0	4.5[a], 5.01[b]	2.9[f]
	GW		3.27[b]
E_{opt} (eV)	TDDFT (DDH)	4.29	3.00
	ΔSCF (PBE0)	3.90[a], 3.76[b]	
	GW-BSE		3.02[g], 3.22[b]
	Expt.	3.65[d], 3.87[e]	3.3[f]

[a] Ref. 276. [b] The *GW*-BSE calculations were performed on top of PBE ground state calculations, as reported in Ref. 257. [d] Ref. 277. [e] Ref. 278. [f] Ref. 281. [g] The *GW*-BSE calculations were performed on top of PBE ground state calculations, as reported in Ref. 273.

the electron-hole interaction within the exciton. We extrapolated to the dilute limit by considering an exciton radius of 10.4 Å estimated from the Wannier exciton model using the effective electron and hole masses and dielectric screening [282], and we obtained an optical gap of 3.00 eV, in agreement with the experimental value of 3.3 eV [281] and *GW*-BSE results of 3.02 – 3.22 eV [257, 273]. The agreement with the experiment may slightly worsen if we considered temperature effects [283]; however, we note that for this system, the exciton binding energy ($\sim$ 0.2 eV) is much smaller than for the 0D perovskite. Hence, the absolute value of the temperature dependence of the exciton-phonon renormalization is not expected to be substantial.

We note that we also attempted ΔSCF calculations of the optical gap of the 0D and 3D perovskites. However, the difficulty in setting occupation numbers for (near-)degenerate KS orbitals prevented us from obtaining a converged optical gap.

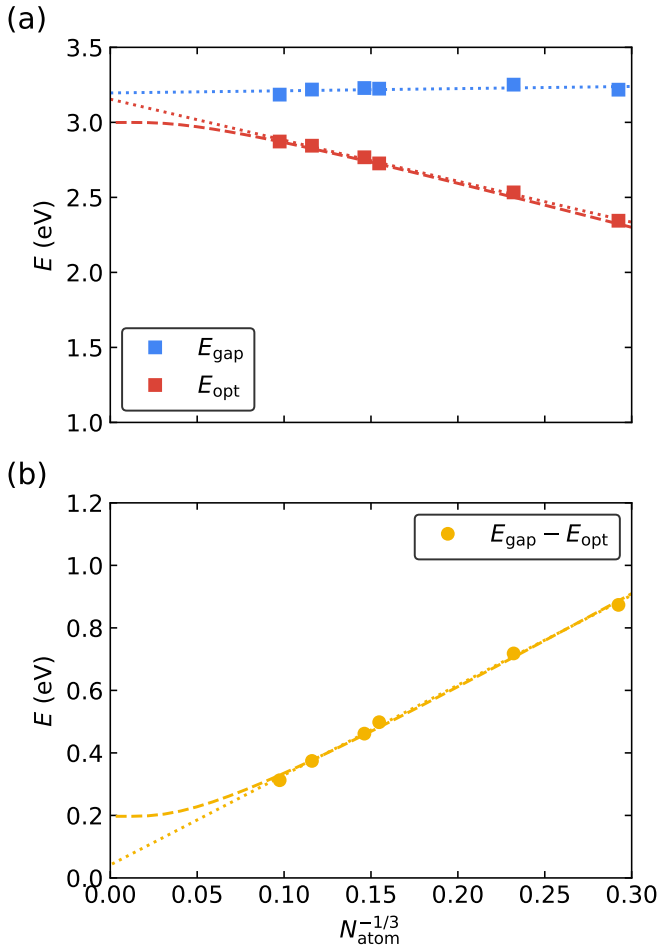

Figure 7.2: (a) Calculated fundamental gap (E_{gap}) and optical gap (E_{opt}), and (b) exciton binding energy ($E_{gap} - E_{opt}$) for $Cs_2AgInCl_6$ plotted against the inverse cube root of the number of atoms ($N_{atoms}^{-1/3}$) in the supercell. The dotted lines represent linear fits of the energies as a function of $N_{atoms}^{-1/3}$. The dashed lines correspond to non-linear fits incorporating a screening length (D) of 38.3 Å, calculated using $D = D_H \frac{\epsilon_\infty}{\mu}$, where $D_H = 1.9$ Å is the hydrogen atom's screening length from DFT calculations [160], $\epsilon_\infty = 3.85$ is the dielectric constant of $Cs_2AgInCl_6$, and $\mu = 0.191$ is the effective mass of the Wannier-Mott exciton [282].

7.2.1 STE and broadband emission of Cs_4SnBr_6

We now turn to the study of the formation of STEs and the associated broadband emission, starting with the Cs_4SnBr_6 perovskite. We optimized the atomic geometry in the electronic singlet and triplet ESs by performing TDDFT calculations using the DDH functional. For

comparison, we also performed ΔSCF calculations for the triplet ES with the same functional. We also attempted ΔSCF calculations for the mixed-spin ES but encountered numerical convergence issues that precluded the completion of the calculation. The resulting STE-related quantities, including the STE emission energy, the self-trapping energy, defined as the energy difference between the free exciton and the STE, and the lattice deformation energy, defined as the energy change in the GS potential energy surface (PES) due to the formation of the STE, are summarized in Table 7.2. We computed the mass-weighted displacements between the atomic geometries of the GS and the STE as

$$\Delta Q = \left[\sum_{\alpha=1}^{N_{\text{atom}}} \sum_{i=x,y,z} M_\alpha \left(R_{\alpha i}^{\text{STE}} - R_{\alpha i}^{\text{GS}} \right)^2 \right]^{1/2}, \tag{7.1}$$

where M_α is the mass of the α-th atom, and $R_{\alpha i}^{\text{GS}}$ ($R_{\alpha i}^{\text{STE}}$) is the atomic coordinate of the α-th atom in the i-th direction of the GS (STE). Our geometry optimization led to an STE geometry with significant Jahn-Teller type distortions at a single [$SnBr_6$] octahedron with two Sn−Br bonds elongated and four Sn−Br bonds contracted, as shown in Figure 7.3(c). Our TDDFT and ΔSCF calculations yield similar geometry distortions. The local geometry distortion leads to the localization of the frontier KS orbitals, at variance with the orbitals at the GS atomic geometry, as shown in Figure 7.3(d).

We then built configuration coordinate diagrams between the atomic geometries of the GS and STE using a linear interpolation method, as shown in Figure 7.3(a). We note that the energy curves of the TDDFT triplet ES and ΔSCF triplet ES are similar, indicating that the ΔSCF approach provides reasonable results for the triplet STE, although we encountered numerical convergence issues in ΔSCF calculations for configurations near the GS atomic geometry. The energy curves of the TDDFT singlet ES and the TDDFT triplet ES have similar shapes but differ by a rigid shift. The singlet STE has an energy of 0.75 eV higher than that of the triplet STE due to the additional exchange interaction between the electron

Table 7.2: Computed properties of self-trapped excitons (STEs) in inorganic halide perovskites. E_{emi}, E_{st}, and E_{d} are the emission energy, self-trapping energy, lattice deformation energy, respectively. ΔQ is the mass-weighted displacements between the atomic geometries of the ground state and the STE. ω_{gs} (ω_{es}) is the effective phonon frequency, and S_{gs} (S_{es}) is the corresponding Huang-Rhys factor for the ground state (excited state). We show results obtained at different levels of theory (see text).

	E_{emi} (eV)	E_{st} (eV)	E_{d} (eV)	ΔQ (amu$^{0.5}$ Å)	$\hbar\Omega_{\mathrm{gs}}$ (meV)	$\hbar\Omega_{\mathrm{es}}$ (meV)	S_{gs}	S_{es}
				Cs_4SnBr_6				
ΔSCF (DDH), triplet	1.96		0.85	11.6	8.06	7.30	130	118
TDDFT (DDH), triplet	1.97	0.76	0.83	11.4	8.11	7.62	125	117
TDDFT (DDH), singlet	2.72	0.77	0.79	12.2	7.62	6.47	137	116
ΔSCF (PBE0), triplet [a]	2.27	0.72	0.77		6.59	6.72	117	107
Expt.	2.30 [b]							
				$Cs_2AgInCl_6$				
ΔSCF (DDH), triplet	1.28		1.15	5.56	19.9	16.4	74	61
TDDFT (DDH), triplet	1.32	0.38	1.04	5.54	18.7	16.4	69	60
TDDFT (DDH), singlet	1.21	0.42	1.13	5.68	19.4	16.3	75	63
ROKS (PBE), singlet [c]	1.82	0.53	0.67		18.3	17.4	37	30
Expt.	2.04 [d]							

[a] Results obtained using the ΔSCF approach with the PBE0 functional as reported in Ref. 257. [b] Ref. 277. [c] Results obtained using the restricted open-shell Kohn-Sham (ROKS) approach with the PBE functional and the scaled Perdew-Zunger self-interaction correction (PZ-SIC) on the unpaired electrons as reported in Ref. 257, 273. The scaling parameter of the Hartree energy was fitted to reproduce the exciton binding energies calculated by the *GW*-BSE approach. The emission energy was adjusted by accounting for the discrepancy between the free-exciton energy derived from the *GW*-BSE calculation and that from the ROKS calculation. [d] Ref. 281

and the hole localized on a single [$SnBr_6$] octahedron. A cusp can be observed in the energy curves of the TDDFT singlet and triplet ESs at the GS atomic geometry. By extrapolating in the negative direction along the configuration coordinate diagram, which corresponds to the contraction of two Sn−Br bonds and the elongation of the other four Sn−Br bonds, we observed a saddle point, as shown in Figure 7.4, which is a signature of Jahn-Teller distortions.

The configuration coordinate diagram allows us to compute the emission line shape for

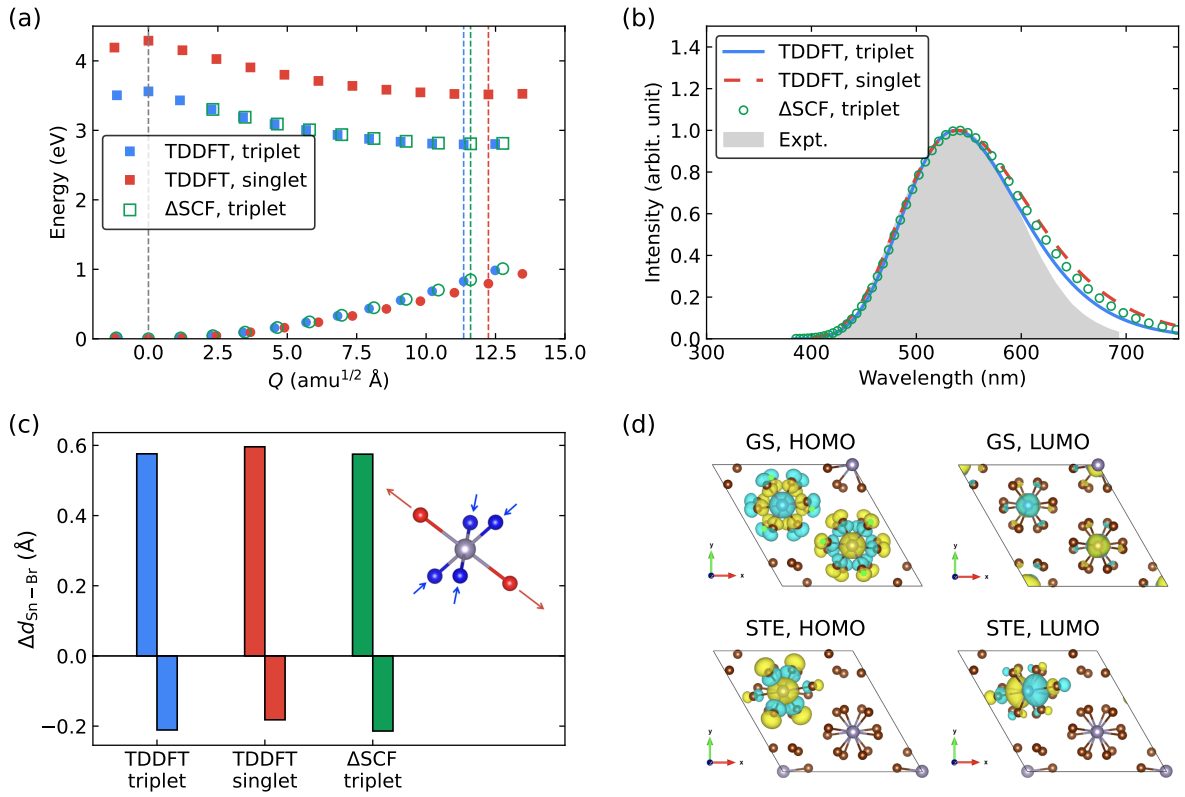

Figure 7.3: Self-trapped exciton (STE) in Cs_4SnBr_6. (a) Configuration coordinate diagrams of the STE calculated using the TDDFT and the ΔSCF approach. The squares represent the excited states (ESs), while the circles denote the ground state (GS). The vertical dashed lines denote the atomic geometry of the GS (gray) and the TDDFT triplet ES (blue), the TDDFT singlet ES (red), and the ΔSCF triplet ES (green). The ΔSCF calculations encountered convergence issues around the GS atomic geometry. (b) Computed emission line shapes at 300 K compared with the experimental spectrum from Ref. 277. The computed emission line shapes were shifted to align the peak position to the experimental one. (c) Change of the Sn−Br bond lengths due to the formation of the STE at a single $[SnBr_6]$ octahedron computed using TDDFT and the ΔSCF approach. Two Sn−Br bonds are elongated while four Sn−Br bonds are contracted in the $[SnBr_6]$ octahedron, as shown in the inset. (d) Kohn-Sham orbital density, $|\varphi(\mathbf{r})|^2$, for the highest occupied molecular orbital (HOMO) and the lowest unoccupied molecular orbital (LUMO) obtained from GS DFT calculations at the atomic geometry of the GS and the STE.

the STE, which corresponds to the transition from the STE ES PES to the GS PES, using Fermi's golden rule and the Franck-Condon principle [83, 257]:

$$L(\hbar\omega, T) \propto (\hbar\omega)^3 \sum_{i,j} P_{ej}(T) \left|\langle \chi_{ej} \mid \chi_{gi} \rangle\right|^2 \delta\left(E_{\mathrm{ZPL}} + j\hbar\Omega_e - i\hbar\Omega_g - \hbar\omega\right), \tag{7.2}$$

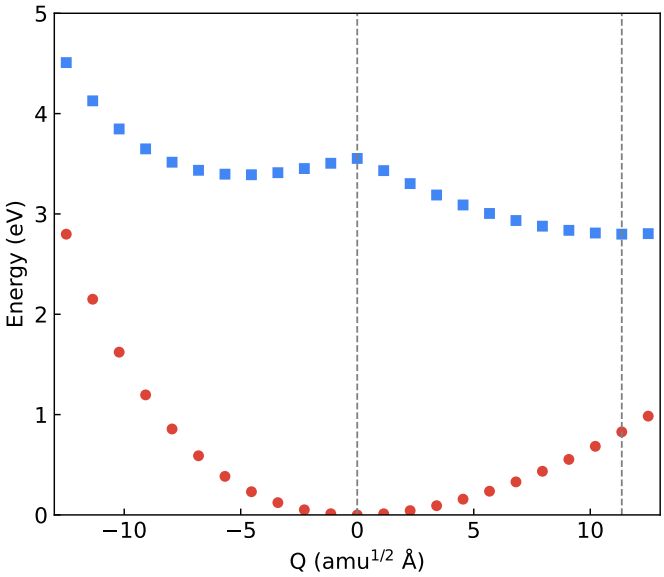

Figure 7.4: Configuration coordinate diagrams of Cs_4SnBr_6 computed using the TDDFT approach for the triplet excited state.

where $\hbar\omega$, T, and E_{ZPL} represent the photon energy, the temperature, and the energy of zero-phonon line emission, respectively. We adopted the one-dimensional effective phonon approximation for the nuclear wave functions, where $|\chi_{gi}\rangle$ ($|\chi_{ej}\rangle$) represents the i-th (j-th) vibrational wave function of the quantum harmonic oscillator with the effective energy of $\hbar\Omega_g$ ($\hbar\Omega_e$). The overlap integrals $\left|\langle\chi_{ej} \mid \chi_{gi}\rangle\right|^2$ can be calculated recursively using $\hbar\Omega_g$, $\hbar\Omega_e$ and ΔQ [284]. The exciton-phonon coupling strength for the formation of STE can be characterized by the Huang-Rhys factor (HRF), computed as [83]

$$S_g = \frac{\Omega_g \Delta Q^2}{2\hbar}, \quad S_e = \frac{\Omega_e \Delta Q^2}{2\hbar}, \tag{7.3}$$

for the GS and the ES, respectively; this quantity can be viewed as the average number of phonons emitted during the optical transition.

The calculated emission line shapes of the STE are shown in Figure 7.3(b), together with the experimental emission line shape. The line shapes computed using parameters from different ES calculations agree well with each other, and they are in reasonable agreement with

experiments, except for a slight overestimate of the peak width. The broadband feature of the emission line shapes can be related to the strong coupling between excitons and phonons in the optical transition, reflected by the large HRFs as shown in Table 7.2. We also examined the temperature dependence of the emission line shape, as shown in Figure 7.5. Interestingly, a similar temperature dependence has been observed experimentally for Cs_4PbBr_6 [285].

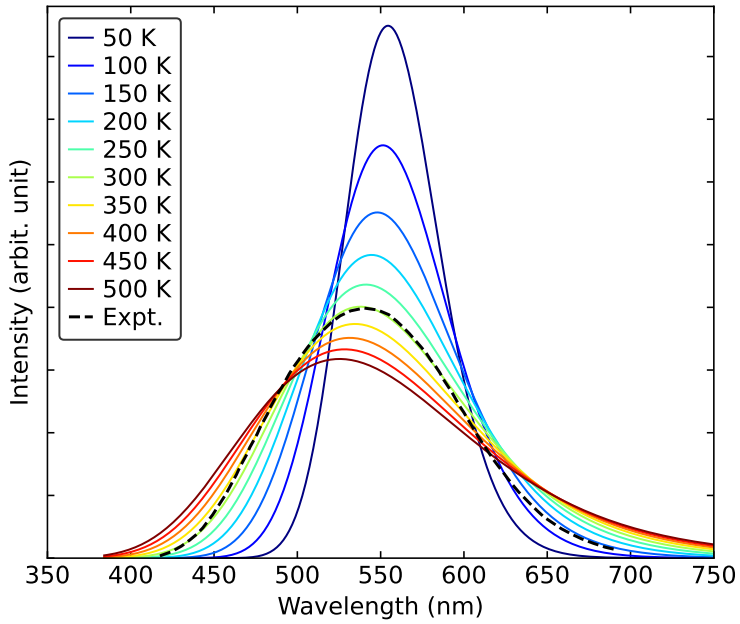

Figure 7.5: Computed temperature dependent emission line shapes for Cs_4SnBr_6 compared with the experimental spectrum at 300 K [277]. The computed emission line shapes were shifted to align the position of the peak to the experimental one.

The computed emission line shapes with TDDFT for the singlet and triplet STEs agree with the experiments. However, the calculated emission energy for the singlet STE is 0.42 eV higher than the experiment, while the computed emission energy for the triplet STE is 0.33 eV lower than the experiment. The STE radiative lifetime of 500 ns obtained by time-resolved photoluminescence measurements suggests that the broadband emission might originate from the triplet STE [277, 278]. We note that the direct calculation of the triplet emission lifetime requires evaluating the spin-orbit coupling strength between singlet and triplet excited states, which is beyond the scope of the current study.

One possible reason for the underestimation of our calculated STE emission energy and the overestimation of the emission peak width compared to the experiment could be from the use of the global dielectric constant in the DDH hybrid functional; such functional is expected to underestimate the screening effect on the distorted [$SnBr_6$] octahedron where the frontier KS orbitals are localized, leading in turn to an overestimated local geometric distortion.

To investigate the exciton-phonon coupling for the STE formation in Cs_4SnBr_6, we examined the partial HRFs for each phonon mode. The partial HRF on the k-th phonon mode, S_k, can be computed as $S_k = \frac{\omega_k \Delta Q_k^2}{2\hbar}$, where ω_k is the vibrational frequency of the k-th phonon mode, and ΔQ_k is the projection of the mass-weighted displacements on the kth phonon mode, which is evaluated using the displacement between the atomic coordinates of the GS and the STE

$$\Delta Q_k^{\mathrm{Dis}} = \sum_{\alpha=1}^{N_{\mathrm{atom}}} \sum_{i=x,y,z} \sqrt{M_\alpha} \left(R_{\alpha i}^{\mathrm{STE}} - R_{\alpha i}^{\mathrm{GS}} \right) e_{k,\alpha i}, \tag{7.4}$$

where $\mathbf{e}_k$ is the eigenvector of the k-th phonon mode. Using the displaced harmonic oscillator approximation, where the GS and the ES PESs are assumed to have the same shape except for a displacement, ΔQ_k can be calculated equivalently using nuclear forces,

$$\Delta Q_k^{\mathrm{Forces}} = \frac{1}{\omega_k^2} \sum_{\alpha=1}^{N_{\mathrm{atom}}} \sum_{i=x,y,z} \frac{F_{\alpha i}^{\mathrm{ES@GS}}}{\sqrt{M_\alpha}} e_{k,\alpha i}, \tag{7.5}$$

where $\mathbf{F}^{\mathrm{ES@GS}}$ represents the atomic forces on the ES PES at the GS atomic geometry. Since $\mathbf{F}^{\mathrm{ES@GS}}$ equals the derivative of the excitation energy with respect to the atomic coordinates at the GS atomic geometry, S_k can be regarded as the exciton-phonon coupling strength of the k-th phonon mode.

We computed the partial HRFs, S_k, using the two approaches, and displayed the spectral

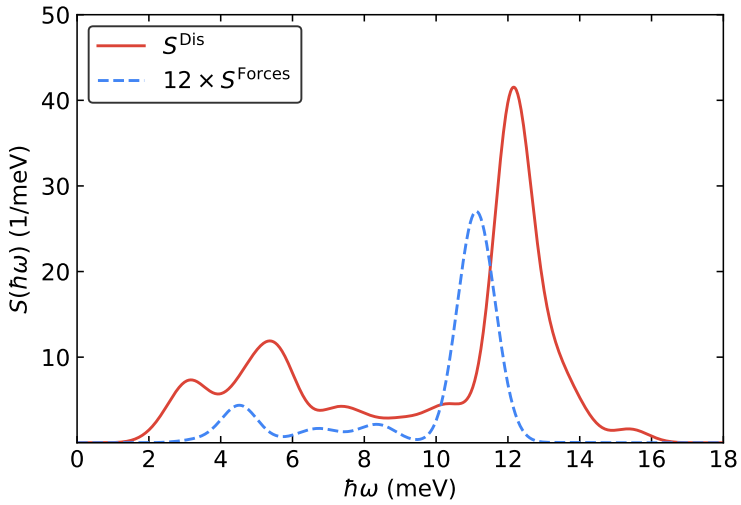

Figure 7.6: Spectral density of the Huang-Rhys factors (HRFs) as a function of the phonon energy for Cs_4SnBr_6. The HRFs are computed either using the displacements between the atomic geometries of the ground state (GS) and the STE, denoted as S^{Dis} (red solid line), or using the excited state forces at the GS atomic geometry, denoted as S^{Forces} (blue dashed line). S^{Forces} was multiplied by 12 times for a better visual comparison with S^{Dis}.

density, $S(\hbar\omega) = \sum_k S_k \delta(\hbar\omega - \hbar\omega_k)$, in Figure 7.6. The spectral density computed using displacements (S^{Dis}) and using forces (S^{Forces}) are different in terms of both the peak position and peak intensity. The peak at 12 meV for S^{Dis} is related to the Jahn-Teller type phonon modes, consistent with the Jahn-Teller type of geometry distortion due to the formation of the STE. The peak at 11 meV for S^{Forces} is related to the bending type phonon modes, and the intensity is more than one magnitude smaller. The drastic difference between S^{Dis} and S^{Forces} indicates that the exciton-phonon coupling at the GS atomic geometry is not appropriate to describe the formation of the STE; direct geometry optimization in ES PES is required instead.

7.2.2 STE and broadband emission of $Cs_2AgInCl_6$

In a similar fashion, we also studied the formation of the STE in $Cs_2AgInCl_6$. A $(2 \times 2 \times 2)$ conventional supercell containing 320 atoms was used to localize the STE. The computed STE emission energy, self-trapping energy, and lattice deformation energy are summarized

in Table 7.2. The configuration coordinate diagram, the optical emission line shape, and the geometry distortion due to the formation of the STE and the localization of frontier KS orbitals are displayed in Figure 7.7.

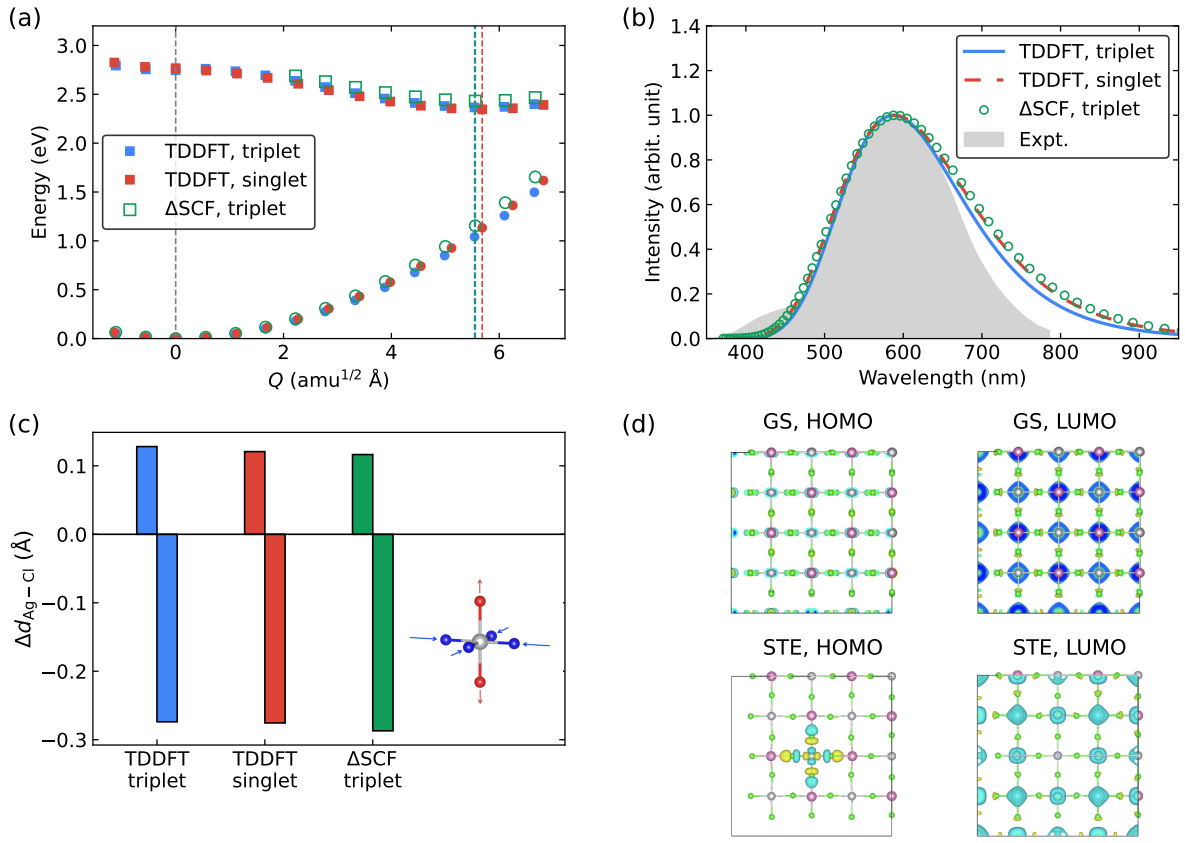

Figure 7.7: Self-trapped exciton (STE) in $Cs_2AgInCl_6$. (a) Configuration coordinate diagrams of the STE calculated using the TDDFT and the ΔSCF approach. The squares represent the excited states (ESs), while the circles denote the ground state (GS). The vertical dashed lines denote the atomic geometry of the GS (gray) and the TDDFT triplet ES (blue), the TDDFT singlet ES (red), and the ΔSCF triplet ES (green). The ΔSCF calculations encountered convergence issues around the GS atomic geometry. (b) Computed emission line shapes at 300 K compared with the experimental spectrum from Ref. 273. The computed emission line shapes were shifted to align the peak position to the experimental one. (c) Change of the Ag−Cl bond lengths due to the formation of the STE at a single $[AgCl_6]$ octahedron computed using TDDFT and ΔSCF approach. Two Ag−Cl bonds are elongated while four Ag−Cl bonds are contracted in the $[AgCl_6]$ octahedron, as shown in the inset. (d) Kohn-Sham orbital density, $|\varphi(\mathbf{r})|^2$, for the highest occupied molecular orbital (HOMO) and the lowest unoccupied molecular orbital (LUMO) obtained from GS DFT calculations at the atomic geometry of the GS and the STE.

The TDDFT geometry optimization in the ES shows a Jahn-Teller type geometry distortion on a single [$AgCl_6$] when the STE is formed, as shown in Figure 7.7(c), which is consistent with the results of previous theoretical studies [257, 273]. At the STE geometry, the highest occupied molecular orbital (HOMO) is localized on a single [$AgCl_6$], while the lowest unoccupied molecular orbital (LUMO) is still delocalized and repelled away from the [$AgCl_6$] octahedron, consistent with the dispersion of the VBM and CBM [281] found in our calculations. These results are consistent with the fact that the TDDFT singlet and triplet ESs have similar emission energies, as a result of minimizing the exchange interaction between the hole at the localized HOMO and the electron at the delocalized LUMO. This is in contrast to the case for Cs_4SnBr_6, where the HOMO and LUMO are localized on the same [$SnBr_6$] octahedron. The STE geometry distortions (Figure 7.7(c)), the configuration coordinate diagrams (Figure 7.7(a)), and the optical emission line shapes (Figure 7.7(b)) for the triplet ES computed using TDDFT and ΔSCF are similar. However, we note that ΔSCF calculations failed to converge near the GS geometry, probably due to the existence of near-degenerate orbitals. In contrast with previous studies that employed the ROKS approach and revealed a significant gradient in the ES PES near the GS geometry [273], the ES PES in the vicinity of the GS geometry computed using TDDFT exhibits a relatively flat profile. The transition from the flat PES to the parabolic PES for the ES suggests a transition from the free exciton to the STE, a process that our TDDFT calculation successfully captures.

The exciton emission energy computed using TDDFT and ΔSCF underestimates the experimental emission energy by 0.7 – 0.8 eV, which is associated with the overestimation of the STE geometry distortion that leads to a broader emission line shape than in experiments, as shown in Figure 7.7(b). The discrepancy between our theoretical results and experiments can be ascribed to several factors. Once more, the use of a global dielectric constant in the DDH functional may be responsible for inaccuracies in the description of the screening effect for the localized HOMO at the STE geometry, thus resulting in a deficient description of the

electronic and geometric properties of the STE. In addition, our TDDFT calculations, despite employing a 320-atom supercell, might still be influenced by finite-size effects, which may be particularly relevant due to the delocalized nature of the LUMO in the STE geometry. Employing a finite-size correction of 0.2 eV, the same as that used for the free exciton in the 320-atom supercell (see our extrapolation in Figure S1), the TDDFT-calculated STE emission energy would become 1.5 eV. Further accounting for a 0.3 eV discrepancy between the calculated and experimental optical gaps, we obtain an STE emission of 1.8 eV. We are not in a position to assess the robustness of these corrections at this time, and we approach the interpretation of the 2.0 eV emission peak to STE with caution. There might be other mechanisms not considered here that come into play, such as the emission from point defects, for example, antisite defects In_{Ag} [286], that should be explored in greater detail.

We also studied the exciton-phonon coupling in $Cs_2AgInCl_6$ by computing the partial HRFs using either the displacement between the GS and STE geometries or the atomic forces on the ES PES at the GS geometry, and the resulting spectral densities are displayed in Figure 7.8. Although S^{Dis} and S^{Forces} share common peaks at 16 meV and 34 meV, with the former corresponding to the Jahn-Teller type phonon modes and the latter related to the stretching modes, their intensity shows a difference of more than twenty times. Therefore, the exciton-phonon coupling computed at the GS geometry is insufficient for the description of the formation of the STE; the direct ES geometry relaxation is critical.

7.3 Conclusions

In summary, we studied the electronic and optical properties of all inorganic halide perovskites Cs_4SnBr_6 and $Cs_2AgInCl_6$, especially the formation of the STE and the associated broadband emission, using TDDFT with the DDH functional. We showed that the approach adopted here allows for an accurate description of the excitonic effects and geometry relaxation in the excited states and yields optical gap, STE emission energy, and optical emission

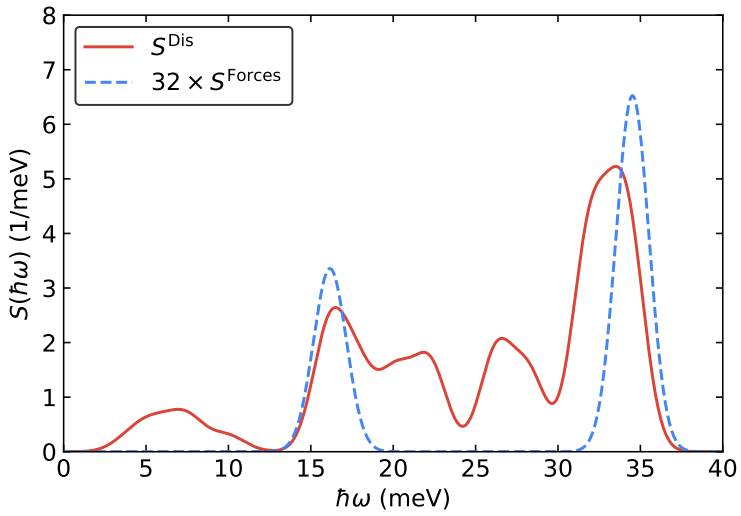

Figure 7.8: Spectral density of the Huang-Rhys factors (HRFs) as a function of the phonon energy for $Cs_2AgInCl_6$. The HRFs are computed either using the displacements between the atomic geometries of the ground state (GS) and the self-trapped exciton (STE), denoted as S^{Dis} (red solid line), or using the excited state forces at the GS atomic geometry, denoted as S^{Forces} (blue dashed line). S^{Forces} was multiplied by 32 times for a better visual comparison with S^{Dis}.

spectra in reasonable agreement with experiments. In addition, TDDFT also allows for the description of the transition from the free exciton to STE. Importantly, we also demonstrated that the exciton-phonon coupling computed at the atomic geometry of the GS is insufficient for the study of STEs and broadband emission; the geometry relaxation in ES PES is required instead. Overall, we found that ΔSCF-based methods, while adequate in some cases, present convergence issues and yield results that are not as accurate as those of TDDFT.

However, some discrepancies between the results obtained here and the experiments remain. In the future, we plan to use hybrid functionals that can describe the spatial variation of the dielectric function [145, 279] in (TD)DFT calculations of perovskite systems and to include spin-orbit coupling, which could further improve the agreement with the experiments. Finally, a careful understanding of the influence of defects on measured emission spectra will need to be explored in detail [287].

CHAPTER 8

CONCLUSIONS AND OUTLOOK

In this dissertation, we presented research projects that fall within two themes: (1) the development of methods and algorithms for first-principles simulations of excited states and optical properties of molecules and materials; and (2) first-principles studies of the electronic structure, excited states, and optical properties of solid-state systems, including point defects in semiconductors and insulators, and metal-halide perovskites.

In terms of method development, we first presented an implementation of linear-response time-dependent density functional theory (TDDFT) and its analytical nuclear forces for both spin-conserving and spin-flip excitations. The combination of a multilevel parallelization scheme, several numerical approximations, and GPU acceleration enabled the study of electronic excited states of different spin multiplicities and the potential energy surfaces for systems with thousands of electrons at the level of hybrid functional DFT, which is necessary for the interpretation of optical absorption and emission mechanisms for heterogeneous systems, including point defects in solids.

We then developed and implemented the generating functional approach for the calculation of temperature-dependent vibrationally resolved optical spectra for molecular and material systems. The method couples the electronic and the vibrational degrees of freedom in the optical processes by using the optimized atomic geometries of the electronic ground and excited states as well as their vibrational modes. We validated the theoretical and numerical approximations used in the calculations against experiments on prototypical point defects in solids. We also demonstrated the importance of the correction for the finite-size effects.

In terms of applications, we presented a number of first-principles predictions for excited states and optical properties of point defects in semiconductors and insulators. In particular, we applied spin-flip TDDFT to study the highly correlated singlet excited states

of the negatively-charged nitrogen-vacancy center in diamond; we studied the multiphonon photoionization process of the neutral divacancy center in silicon carbide and the neutral substitutional nitrogen in diamond. These studies assist in the interpretation of complicated experimental results and provide important insights for the design of operation protocols and the discovery of novel spin defects for quantum technology applications. In addition, we also presented a theoretical study of metal-halide perovskites focusing on the formation of the self-trapped exciton and the associated broadband emission and demonstrated that our approaches can be applied to study a variety of systems.

There are a few directions one would want to explore in this field as the next steps. First, it is beneficial to further improve the efficiency of the TDDFT implementation to enable the study of large and heterogeneous systems. It could be achieved by using additional numerical approximations such as the density fitting techniques [174, 175]. Other interesting future efforts include the implementation of spin-flip TDDFT with the multi-collinear formalism to reduce numerical instabilities [176, 177] and the implementation of mixed-reference spin-flip TDDFT [288, 289] or spin-adapted open-shell TDDFT [290–293] to mitigate spin-contamination issues. One can also leverage the advancement in the machine learning field to assist the study of electronic excited states of large and complex systems [294–298].

Overall, this dissertation highlighted several advancements in first-principles simulations of excited states and optical properties of complex systems. I hope that the presented theories, algorithms, and practical applications will significantly aid the chemistry and materials science fields in large-scale, first-principles simulations of both molecular and condensed systems.

APPENDIX A

LIST OF PUBLICATIONS

1. **Yu Jin**, Marco Govoni, Gary Wolfowicz, Sean E Sullivan, F Joseph Heremans, David D Awschalom, and Giulia Galli. Photoluminescence spectra of point defects in semiconductors: Validation of first-principles calculations. *Phys. Rev. Mater.*, 5(8):084603, 2021.

2. Christopher P. Anderson, Elena O. Glen, Cyrus Zeledon, Alexandre Bourassa, **Yu Jin**, Yizhi Zhu, Christian Vorwerk, Alexander L. Crook, Hiroshi Abe, Jawad Ul-Hassan, Takeshi Ohshima, Nguyen T. Son, Giulia Galli, and David D. Awschalom. Five-second coherence of a single spin with single-shot readout in silicon carbide. *Sci. Adv.*, 8(5):eabm5912, 2022.

3. **Yu Jin**, Marco Govoni, and Giulia Galli. Vibrationally resolved optical excitations of the nitrogen-vacancy center in diamond. *npj Comput. Mater.*, 8(1):238, 2022.

4. Shreya Verma, Abhishek Mitra, **Yu Jin**, Soumi Haldar, Christian Vorwerk, Matthew R Hermes, Giulia Galli, and Laura Gagliardi. Optical properties of neutral F centers in bulk MgO with density matrix embedding. *J. Phys. Chem. Lett.*, 14(34):7703–7710, 2023.

5. Xinghan Guo, Alexander M Stramma, Zixi Li, William G Roth, Benchen Huang, **Yu Jin**, Ryan A Parker, Jesús Arjona Martínez, Noah Shofer, Cathryn P Michaels, et al. Microwave-based quantum control and coherence protection of tin-vacancy spin qubits in a strain-tuned diamond membrane heterostructure. *Phys. Rev. X*, 13(4):041037, 2023.

6. **Yu Jin**, Victor Wen-zhe Yu, Marco Govoni, Andrew C Xu, and Giulia Galli. Excited state properties of point defects in semiconductors and insulators investigated with

time-dependent density functional theory. *J. Chem. Theory Comput.*, 19(23):8689–8705, 2023.

7. Anil Bilgin, Ian Hammock, Jeremy Estes, **Yu Jin**, Hannes Bernien, Alexander High, and Giulia Galli. Donor-Acceptor Pairs in Wide-Bandgap Semiconductors for Quantum Technology Applications. *npj Comput. Mater.*, 10(1):7, 2024.

8. **Yu Jin**, Mariami Rusishvili, Marco Govoni, and Giulia Galli. Time-dependent density functional theory study of self-trapped exciton in metal-halide perovskites. *Submitted*, 2024.

9. **Yu Jin**, Marco Govoni, and Giulia Galli. PyPL, a python package for first-principles calculations of photoluminescence line shapes of point defects in semiconductors. *In preparation*, 2024.

10. Zixi Li, Xinghan Guo, **Yu Jin**, Francesco Andreoli, Anil Bilgin, David D. Awschalom, Nazar Delegan, F. Joseph Heremans, Darrick Chang, Giulia Galli, and Alexander A. High. Atomic optical antennas in solids. *Under revision*, 2024.

11. Jonathan C. Marcks, Mykyta Onizhuk, Yu-Xin Wang, **Yu Jin**, Yizhi Zhu, Benjamin Soloway, Masaya Fukami, Nazar Delegan, F. Joseph Heremans, Aashish A. Clerk, Giulia Galli, and David D. Awschalom. Quantum spin probe of single charge dynamics. *arXiv preprint arXiv:2312.02894*, 2024.

APPENDIX B

SOFTWARE

1. `WEST` code (west-code.org, contributor)
    - TDDFT with hybrid functional
    - Spin-flip TDDFT
    - TDDFT analytical nuclear forces
2. `PyPL` code (To be released, main developer)

REFERENCES

[1] Jeff Greeley, Jens K Nørskov, and Manos Mavrikakis. Electronic structure and catalysis on metal surfaces. *Annu. Rev. Phys. Chem.*, 53(1):319–348, 2002.

[2] Woo Youn Kim, Young Cheol Choi, Seung Kyu Min, Yeonchoo Cho, and Kwang S Kim. Application of quantum chemistry to nanotechnology: electron and spin transport in molecular devices. *Chem. Soc. Rev.*, 38(8):2319–2333, 2009.

[3] Albert Bruix, Johannes T Margraf, Mie Andersen, and Karsten Reuter. First-principles-based multiscale modelling of heterogeneous catalysis. *Nat. Catal.*, 2(8):659–670, 2019.

[4] Benjamin WJ Chen, Lang Xu, and Manos Mavrikakis. Computational methods in heterogeneous catalysis. *Chem. Rev.*, 121(2):1007–1048, 2020.

[5] Steven G Louie, Yang-Hao Chan, Felipe H da Jornada, Zhenglu Li, and Diana Y Qiu. Discovering and understanding materials through computation. *Nat. Mater.*, 20(6):728–735, 2021.

[6] Sharon Hammes-Schiffer and Giulia Galli. Integration of theory and experiment in the modelling of heterogeneous electrocatalysis. *Nat. Energy*, 6(7):700–705, 2021.

[7] Yuan Ping, Dario Rocca, and Giulia Galli. Electronic excitations in light absorbers for photoelectrochemical energy conversion: first principles calculations based on many body perturbation theory. *Chemical Society Reviews*, 42(6):2437–2469, 2013.

[8] Carles Curutchet and Benedetta Mennucci. Quantum chemical studies of light harvesting. *Chem. Rev.*, 117(2):294–343, 2017.

[9] Jörg Grunenberg. *Computational spectroscopy: methods, experiments and applications*. John Wiley & Sons, 2011.

[10] Cristiana Di Valentin, Silvana Botti, and Matteo Cococcioni. *First principles approaches to spectroscopic properties of complex materials*, volume 347. Springer, 2014.

[11] Vincenzo Barone, Silvia Alessandrini, Malgorzata Biczysko, James R Cheeseman, David C Clary, Anne B McCoy, Ryan J DiRisio, Frank Neese, Mattia Melosso, and Cristina Puzzarini. Computational molecular spectroscopy. *Nat. Rev. Methods Primers*, 1(1):38, 2021.

[12] Walter Kohn and Lu Jeu Sham. Self-consistent equations including exchange and correlation effects. *Phys. Rev.*, 140(4A):A1133, 1965.

[13] Erich Runge and Eberhard KU Gross. Density-functional theory for time-dependent systems. *Phys. Rev. Lett.*, 52(12):997, 1984.

[14] E Grossa, J Dobsonb, and M Petersilkaa. Density functional theory of time-dependent phenomena. *Top. Curr. Chem.*, 181:81, 1996.

[15] Mark E. Casida. Time-dependent density functional response theory for molecules. In *Recent Advances in Density Functional Methods*, pages 155–192. WORLD SCIENTIFIC, 1995.

[16] Mark E Casida. Time-dependent density functional response theory of molecular systems: theory, computational methods, and functionals. *Theoretical and Computational Chemistry*, pages 391–439, 1996.

[17] Jürg Hutter. Excited state nuclear forces from the tamm–dancoff approximation to time-dependent density functional theory within the plane wave basis set framework. *J. Chem. Phys.*, 118(9):3928–3934, 2003.

[18] Yihan Shao, Zhengting Gan, Evgeny Epifanovsky, Andrew TB Gilbert, Michael Wormit, Joerg Kussmann, Adrian W Lange, Andrew Behn, Jia Deng, Xintian Feng, et al. Advances in molecular quantum chemistry contained in the Q-Chem 4 program package. *Mol. Phys.*, 113(2):184–215, 2015.

[19] Frank Neese, Frank Wennmohs, Ute Becker, and Christoph Riplinger. The ORCA quantum chemistry program package. *J. Chem. Phys.*, 152(22):224108, 06 2020.

[20] TURBOMOLE V7.2 2017, a development of University of Karlsruhe and Forschungszentrum Karlsruhe GmbH, 1989-2007, TURBOMOLE GmbH, since 2007; available from `http://www.turbomole.com`.

[21] Edoardo Apra, Eric J Bylaska, Wibe A De Jong, Niranjan Govind, Karol Kowalski, Tjerk P Straatsma, Marat Valiev, Hubertus JJ van Dam, Yuri Alexeev, James Anchell, et al. NWChem: Past, present, and future. *J. Chem. Phys.*, 152(18):184102, 2020.

[22] Qiming Sun, Timothy C Berkelbach, Nick S Blunt, George H Booth, Sheng Guo, Zhendong Li, Junzi Liu, James D McClain, Elvira R Sayfutyarova, Sandeep Sharma, et al. PySCF: the Python-based simulations of chemistry framework. *Wiley Interdiscip. Rev. Comput. Mol. Sci.*, 8(1):e1340, 2018.

[23] Qiming Sun, Xing Zhang, Samragni Banerjee, Peng Bao, Marc Barbry, Nick S Blunt, Nikolay A Bogdanov, George H Booth, Jia Chen, Zhi-Hao Cui, et al. Recent developments in the PySCF program package. *J. Chem. Phys*, 153(2):024109, 2020.

[24] Dario Rocca. Time-dependent density functional perturbation theory: new algorithms with applications to molecular spectra, 2007.

[25] Dario Rocca, Ralph Gebauer, Yousef Saad, and Stefano Baroni. Turbo charging time-dependent density-functional theory with Lanczos chains. *The Journal of Chemical Physics*, 128(15):154105, 04 2008.

[26] Tobias Sander, Emanuele Maggio, and Georg Kresse. Beyond the Tamm-Dancoff approximation for extended systems using exact diagonalization. *Phys. Rev. B*, 92:045209, Jul 2015.

[27] Gary Wolfowicz, F Joseph Heremans, Christopher P Anderson, Shun Kanai, Hosung Seo, Adam Gali, Giulia Galli, and David D Awschalom. Quantum guidelines for solid-state spin defects. *Nat. Rev. Mater.*, 6(10):906–925, 2021.

[28] Max Born and Kun Huang. *Dynamical theory of crystal lattices*. Oxford university press, 1996.

[29] Pierre Hohenberg and Walter Kohn. Inhomogeneous electron gas. *Phys. Rev.*, 136(3B):B864, 1964.

[30] John P Perdew and Alex Zunger. Self-interaction correction to density-functional approximations for many-electron systems. *Phys. Rev. B*, 23(10):5048, 1981.

[31] John P. Perdew, Kieron Burke, and Matthias Ernzerhof. Generalized gradient approximation made simple. *Phys. Rev. Lett.*, 77:3865–3868, 1996.

[32] Carlo Adamo and Vincenzo Barone. Toward reliable density functional methods without adjustable parameters: The PBE0 model. *J. Chem. Phys.*, 110(13):6158–6170, 1999.

[33] Jonathan H. Skone, Marco Govoni, and Giulia Galli. Self-consistent hybrid functional for condensed systems. *Phys. Rev. B*, 89:195112, 2014.

[34] Jonathan H. Skone, Marco Govoni, and Giulia Galli. Nonempirical range-separated hybrid functionals for solids and molecules. *Phys. Rev. B*, 93:235106, 2016.

[35] Nicholas P Brawand, Márton Vörös, Marco Govoni, and Giulia Galli. Generalization of dielectric-dependent hybrid functionals to finite systems. *Phys. Rev. X*, 6(4):041002, 2016.

[36] Nicholas P Brawand, Marco Govoni, Márton Vörös, and Giulia Galli. Performance and self-consistency of the generalized dielectric dependent hybrid functional. *J. Chem. Theory Comput.*, 13(7):3318–3325, 2017.

[37] Andreas Görling, Habbo H Heinze, Sergey Ph Ruzankin, Markus Staufer, and Notker Rösch. Density-and density-matrix-based coupled Kohn–Sham methods for dynamic polarizabilities and excitation energies of molecules. *J. Chem. Phys.*, 110(6):2785–2799, 1999.

[38] Filipp Furche. On the density matrix based approach to time-dependent density functional response theory. *J. Chem. Phys.*, 114(14):5982–5992, 2001.

[39] Brent Walker, A Marco Saitta, Ralph Gebauer, and Stefano Baroni. Efficient approach to time-dependent density-functional perturbation theory for optical spectroscopy. *Phys. Rev. Lett.*, 96(11):113001, 2006.

[40] Osman Barış Malcıoğlu, Ralph Gebauer, Dario Rocca, and Stefano Baroni. turboTDDFT–A code for the simulation of molecular spectra using the Liouville–Lanczos approach to time-dependent density-functional perturbation theory. *Comput. Phys. Commun.*, 182(8):1744–1754, 2011.

[41] Xiaochuan Ge, Simon J Binnie, Dario Rocca, Ralph Gebauer, and Stefano Baroni. turboTDDFT 2.0—Hybrid functionals and new algorithms within time-dependent density-functional perturbation theory. *Comput. Phys. Commun.*, 185(7):2080–2089, 2014.

[42] Dario Rocca, Deyu Lu, and Giulia Galli. Ab initio calculations of optical absorption spectra: Solution of the Bethe–Salpeter equation within density matrix perturbation theory. *J. Chem. Phys.*, 133(16):164109, 2010.

[43] Dario Rocca, Yuan Ping, Ralph Gebauer, and Giulia Galli. Solution of the Bethe-Salpeter equation without empty electronic states: Application to the absorption spectra of bulk systems. *Phys. Rev. B*, 85(4):045116, 2012.

[44] Ngoc Linh Nguyen, He Ma, Marco Govoni, François Gygi, and Giulia Galli. Finite-field approach to solving the Bethe-Salpeter equation. *Phys. Rev. Lett.*, 122:237402, 2019.

[45] Atsushi Togo and Isao Tanaka. First principles phonon calculations in materials science. *Scr. Mater.*, 108:1–5, 2015.

[46] Stefano de Gironcoli. Lattice dynamics of metals from density-functional perturbation theory. *Phys. Rev. B*, 51(10):6773, 1995.

[47] Stefano Baroni, Stefano De Gironcoli, Andrea Dal Corso, and Paolo Giannozzi. Phonons and related crystal properties from density-functional perturbation theory. *Rev. Mod. Phys.*, 73(2):515, 2001.

[48] Feliciano Giustino. Electron-phonon interactions from first principles. *Rev. Mod. Phys.*, 89:015003, Feb 2017.

[49] Han Yang, Marco Govoni, Arpan Kundu, and Giulia Galli. Combined first-principles calculations of electron–electron and electron–phonon self-energies in condensed systems. *J. Chem. Theory Comput.*, 17(12):7468–7476, 2021.

[50] Han Yang, Marco Govoni, Arpan Kundu, and Giulia Galli. Computational protocol to evaluate electron–phonon interactions within density matrix perturbation theory. *J. Chem. Theory Comput.*, 18(10):6031–6042, 2022.

[51] John C Burant, Matthew C Strain, Gustavo E Scuseria, and Michael J Frisch. Kohn-Sham analytic energy second derivatives with the Gaussian very fast multipole method (GvFMM). *Chem. Phys. Lett.*, 258(1-2):45–52, 1996.

[52] Peter Deglmann, Filipp Furche, and Reinhart Ahlrichs. An efficient implementation of second analytical derivatives for density functional methods. *Chem. Phys. Lett.*, 362(5-6):511–518, 2002.

[53] Stephen K Wolff. Analytical second derivatives in the Amsterdam density functional package. *Int. J. Quantum Chem.*, 104(5):645–659, 2005.

[54] Dmytro Bykov, Taras Petrenko, Róbert Izsák, Simone Kossmann, Ute Becker, Edward Valeev, and Frank Neese. Efficient implementation of the analytic second derivatives of Hartree–Fock and hybrid DFT energies: a detailed analysis of different approximations. *Mol. Phys.*, 113(13-14):1961–1977, 2015.

[55] Jie Liu and WanZhen Liang. Analytical Hessian of electronic excited states in time-dependent density functional theory with Tamm-Dancoff approximation. *J. Chem. Phys.*, 135(1):014113, 2011.

[56] Jie Liu and WanZhen Liang. Analytical approach for the excited-state Hessian in time-dependent density functional theory: Formalism, implementation, and performance. *J. Chem. Phys.*, 135(18):184111, 2011.

[57] DanPing Chen, Jie Liu, HuiLi Ma, Qiao Zeng, and WanZhen Liang. Analytical derivative techniques for TDDFT excited-state properties: Theory and application. *Sci. China Chem.*, 57:48–57, 2014.

[58] Arthur Marshall Stoneham. *Theory of defects in solids: electronic structure of defects in insulators and semiconductors*. Oxford University Press, 2001.

[59] Audrius Alkauskas, Bob B Buckley, David D Awschalom, and Chris G Van de Walle. First-principles theory of the luminescence lineshape for the triplet transition in diamond NV centres. *New J. Phys.*, 16(7):073026, 2014.

[60] Kun Huang, Avril Rhys, and Nevill Francis Mott. Theory of light absorption and non-radiative transitions in F-centres. *Proc. R. Soc. Lond. Series A*, 204(1078):406–423, 1950.

[61] Lennart Råde and Bertil Westergren. *Mathematics handbook for science and engineering*, volume 4. Springer, 1995.

[62] Marcus W Doherty, Neil B Manson, Paul Delaney, Fedor Jelezko, Jörg Wrachtrup, and Lloyd CL Hollenberg. The nitrogen-vacancy colour centre in diamond. *Phys. Rep.*, 528(1):1–45, 2013.

[63] Ádám Gali. *Ab initio* theory of the nitrogen-vacancy center in diamond. *Nanophotonics*, 8(11):1907–1943, 2019.

[64] Nguyen T. Son, Christopher P. Anderson, Alexandre Bourassa, Kevin C. Miao, Charles Babin, Matthias Widmann, Matthias Niethammer, Jawad Ul Hassan, Naoya Morioka, Ivan G. Ivanov, Florian Kaiser, Joerg Wrachtrup, and David D. Awschalom. Developing silicon carbide for quantum spintronics. *Appl. Phys. Lett.*, 116(19):190501, 2020.

[65] Romana Schirhagl, Kevin Chang, Michael Loretz, and Christian L Degen. Nitrogen-vacancy centers in diamond: nanoscale sensors for physics and biology. *Annu. Rev. Phys. Chem.*, 65:83–105, 2014.

[66] John F Barry, Jennifer M Schloss, Erik Bauch, Matthew J Turner, Connor A Hart, Linh M Pham, and Ronald L Walsworth. Sensitivity optimization for NV-diamond magnetometry. *Rev. Mod. Phys.*, 92(1):015004, 2020.

[67] Lilian Childress and Ronald Hanson. Diamond NV centers for quantum computing and quantum networks. *MRS Bull.*, 38(2):134–138, 2013.

[68] David J. Christle, Paul V. Klimov, Charles F. de las Casas, Krisztián Szász, Viktor Ivády, Valdas Jokubavicius, Jawad Ul Hassan, Mikael Syväjärvi, William F. Koehl, Takeshi Ohshima, Nguyen T. Son, Erik Janzén, Ádám Gali, and David D. Awschalom. Isolated spin qubits in sic with a high-fidelity infrared spin-to-photon interface. *Phys. Rev. X*, 7:021046, 2017.

[69] Gary Wolfowicz, Christopher P Anderson, Andrew L Yeats, Samuel J Whiteley, Jens Niklas, Oleg G Poluektov, F Joseph Heremans, and David D Awschalom. Optical charge state control of spin defects in 4H-SiC. *Nat. Commun.*, 8(1):1876, 2017.

[70] Christopher P. Anderson, Elena O. Glen, Cyrus Zeledon, Alexandre Bourassa, Yu Jin, Yizhi Zhu, Christian Vorwerk, Alexander L. Crook, Hiroshi Abe, Jawad Ul-Hassan, Takeshi Ohshima, Nguyen T. Son, Giulia Galli, and David D. Awschalom. Five-second coherence of a single spin with single-shot readout in silicon carbide. *Sci. Adv.*, 8(5):eabm5912, 2022.

[71] JR Weber, WF Koehl, JB Varley, Anderson Janotti, BB Buckley, CG Van de Walle, and David D Awschalom. Quantum computing with defects. *Proc. Natl. Acad. Sci. U.S.A.*, 107(19):8513–8518, 2010.

[72] G. Waldherr, Y. Wang, S. Zaiser, M. Jamali, T. Schulte-Herbrüggen, H. Abe, T. Ohshima, J. Isoya, J. F. Du, P. Neumann, and J. Wrachtrup. Quantum error correction in a solid-state hybrid spin register. *Nature*, 506(7487):204–207, 2014.

[73] Gergő Thiering and Adam Gali. Theory of the optical spin-polarization loop of the nitrogen-vacancy center in diamond. *Phys. Rev. B*, 98(8):085207, 2018.

[74] NB Manson, JP Harrison, and MJ Sellars. Nitrogen-vacancy center in diamond: Model of the electronic structure and associated dynamics. *Phys. Rev. B*, 74(10):104303, 2006.

[75] Jeronimo R Maze, Adam Gali, Emre Togan, Yiwen Chu, Alexei Trifonov, Efthimios Kaxiras, and Mikhail D Lukin. Properties of nitrogen-vacancy centers in diamond: the group theoretic approach. *New J. Phys.*, 13(2):025025, 2011.

[76] Marcus W Doherty, Neil B Manson, Paul Delaney, and Lloyd CL Hollenberg. The negatively charged nitrogen-vacancy centre in diamond: the electronic solution. *New J. Phys.*, 13(2):025019, 2011.

[77] Christoph Freysoldt, Blazej Grabowski, Tilmann Hickel, Jörg Neugebauer, Georg Kresse, Anderson Janotti, and Chris G Van de Walle. First-principles calculations for point defects in solids. *Rev. Mod. Phys.*, 86(1):253, 2014.

[78] Audrius Alkauskas, Matthew D McCluskey, and Chris G Van de Walle. Tutorial: Defects in semiconductors – combining experiment and theory. *J. Appl. Phys.*, 119(18):181101, 2016.

[79] Cyrus E Dreyer, Audrius Alkauskas, John L Lyons, Anderson Janotti, and Chris G Van de Walle. First-principles calculations of point defects for quantum technologies. *Annu. Rev. Mater. Res.*, 48:1–26, 2018.

[80] Ádám Gali. Recent advances in the *ab initio* theory of solid-state defect qubits. *Nanophotonics*, 12(3):359–397, 2023.

[81] Adam Gali, Erik Janzén, Péter Deák, Georg Kresse, and Efthimios Kaxiras. Theory of spin-conserving excitation of the $N - V^-$ Center in Diamond. *Phys. Rev. Lett.*, 103(18):186404, 2009.

[82] Lukas Razinkovas, Marcus W Doherty, Neil B Manson, Chris G Van de Walle, and Audrius Alkauskas. Vibrational and vibronic structure of isolated point defects: The nitrogen-vacancy center in diamond. *Phys. Rev. B*, 104(4):045303, 2021.

[83] Yu Jin, Marco Govoni, Gary Wolfowicz, Sean E Sullivan, F Joseph Heremans, David D Awschalom, and Giulia Galli. Photoluminescence spectra of point defects in semiconductors: Validation of first-principles calculations. *Phys. Rev. Mater.*, 5(8):084603, 2021.

[84] Qiming Sun and Garnet Kin-Lic Chan. Quantum embedding theories. *Acc. Chem. Res.*, 49(12):2705–2712, 2016.

[85] Christian Vorwerk, Nan Sheng, Marco Govoni, Benchen Huang, and Giulia Galli. Quantum embedding theories to simulate condensed systems on quantum computers. *Nat. Comput. Sci.*, 2(7):424–432, 2022.

[86] He Ma, Marco Govoni, and Giulia Galli. Quantum simulations of materials on near-term quantum computers. *npj Comput. Mater.*, 6(1):85, 2020.

[87] He Ma, Nan Sheng, Marco Govoni, and Giulia Galli. Quantum embedding theory for strongly correlated states in materials. *J. Chem. Theory Comput.*, 17(4):2116–2125, 2021.

[88] Nan Sheng, Christian Vorwerk, Marco Govoni, and Giulia Galli. Green's function formulation of quantum defect embedding theory. *J. Chem. Theory Comput.*, 18(6):3512–3522, 2022.

[89] Gerald Knizia and Garnet Kin-Lic Chan. Density matrix embedding: A simple alternative to dynamical mean-field theory. *Phys. Rev. Lett.*, 109(18):186404, 2012.

[90] Gerald Knizia and Garnet Kin-Lic Chan. Density matrix embedding: A strong-coupling quantum embedding theory. *J. Chem. Theory Comput.*, 9(3):1428–1432, 2013.

[91] Hung Q Pham, Matthew R Hermes, and Laura Gagliardi. Periodic electronic structure calculations with the density matrix embedding theory. *J. Chem. Theory Comput.*, 16(1):130–140, 2019.

[92] He Ma, Nan Sheng, Marco Govoni, and Giulia Galli. First-principles studies of strongly correlated states in defect spin qubits in diamond. *Phys. Chem. Chem. Phys.*, 22(44):25522–25527, 2020.

[93] Abhishek Mitra, Hung Q Pham, Riddhish Pandharkar, Matthew R Hermes, and Laura Gagliardi. Excited states of crystalline point defects with multireference density matrix embedding theory. *J. Phys. Chem. Lett.*, 12(48):11688–11694, 2021.

[94] Jooyong Bhang, He Ma, Donggyu Yim, Giulia Galli, and Hosung Seo. First-principles predictions of out-of-plane group IV and V dimers as high-symmetry, high-spin defects in hexagonal boron nitride. *ACS Appl. Mater. Interfaces*, 13(38):45768–45777, 2021.

[95] Benchen Huang, Marco Govoni, and Giulia Galli. Simulating the electronic structure of spin defects on quantum computers. *PRX Quantum*, 3(1):010339, 2022.

[96] Benchen Huang, Nan Sheng, Marco Govoni, and Giulia Galli. Quantum simulations of fermionic hamiltonians with efficient encoding and ansatz schemes. *J. Chem. Theory Comput.*, 19(5):1487–1498, 2023.

[97] Soumi Haldar, Abhishek Mitra, Matthew R Hermes, and Laura Gagliardi. Local excitations of a charged nitrogen vacancy in diamond with multireference density matrix embedding theory. *J. Phys. Chem. Lett.*, 14(18):4273–4280, 2023.

[98] Shreya Verma, Abhishek Mitra, Yu Jin, Soumi Haldar, Christian Vorwerk, Matthew R Hermes, Giulia Galli, and Laura Gagliardi. Optical properties of neutral F centers in bulk MgO with density matrix embedding. *J. Phys. Chem. Lett.*, 14:7703–7710, 2023.

[99] Yihan Shao, Martin Head-Gordon, and Anna I Krylov. The spin–flip approach within time-dependent density functional theory: Theory and applications to diradicals. *J. Chem. Phys.*, 118(11):4807–4818, 2003.

[100] Fan Wang and Tom Ziegler. Time-dependent density functional theory based on a noncollinear formulation of the exchange-correlation potential. *J. Chem. Phys.*, 121(24):12191–12196, 2004.

[101] Fan Wang and Tom Ziegler. The performance of time-dependent density functional theory based on a noncollinear exchange-correlation potential in the calculations of excitation energies. *J. Chem. Phys.*, 122(7):074109, 2005.

[102] Michael Seth, Grzegorz Mazur, and Tom Ziegler. Time-dependent density functional theory gradients in the Amsterdam density functional package: geometry optimizations of spin-flip excitations. *Theor. Chem. Acc.*, 129:331–342, 2011.

[103] Zhendong Li and Wenjian Liu. Theoretical and numerical assessments of spin-flip time-dependent density functional theory. *J. Chem. Phys.*, 136(2):024107, 2012.

[104] Yves A Bernard, Yihan Shao, and Anna I Krylov. General formulation of spin-flip time-dependent density functional theory using non-collinear kernels: Theory, implementation, and benchmarks. *J. Chem. Phys.*, 136(20):204103, 2012.

[105] David Casanova and Anna I Krylov. Spin-flip methods in quantum chemistry. *Phys. Chem. Chem. Phys.*, 22(8):4326–4342, 2020.

[106] Zeng-Hui Yang, Francesco Sottile, and Carsten A Ullrich. Simple screened exact-exchange approach for excitonic properties in solids. *Phys. Rev. B*, 92(3):035202, 2015.

[107] Jiuyu Sun, Jinlong Yang, and Carsten A Ullrich. Low-cost alternatives to the Bethe-Salpeter equation: Towards simple hybrid functionals for excitonic effects in solids. *Phys. Rev. Res.*, 2(1):013091, 2020.

[108] Marco Caricato, Gary W Trucks, Michael J Frisch, and Kenneth B Wiberg. Oscillator strength: How does TDDFT compare to EOM-CCSD? *J. Chem. Theory Comput.*, 7(2):456–466, 2011.

[109] Toni M Maier, Hilke Bahmann, Alexei V Arbuznikov, and Martin Kaupp. Validation of local hybrid functionals for TDDFT calculations of electronic excitation energies. *J. Chem. Phys.*, 144(7):074106, 2016.

[110] Ádám Gali. Time-dependent density functional study on the excitation spectrum of point defects in semiconductors. *Phys. Status Solidi B*, 248(6):1337–1346, 2011.

[111] Alessio Petrone, Joshua J Goings, and Xiaosong Li. Quantum confinement effects on optical transitions in nanodiamonds containing nitrogen vacancies. *Phys. Rev. B*, 94(16):165402, 2016.

[112] Alessio Petrone, Ryan A Beck, Joseph M Kasper, Xiaosong Li, Yue Huang, Matthew Crane, and Peter Pauzauskie. Electronic structures and spectroscopic signatures of silicon-vacancy containing nanodiamonds. *Phys. Rev. B*, 98(20):205405, 2018.

[113] Jeffrey R Reimers, Jun Shen, Mehran Kianinia, Carlo Bradac, Igor Aharonovich, Michael J Ford, and Piotr Piecuch. Photoluminescence, photophysics, and photochemistry of the $V_B{}^-$ defect in hexagonal boron nitride. *Phys. Rev. B*, 102(14):144105, 2020.

[114] Akib Karim, Igor Lyskov, Salvy P Russo, and Alberto Peruzzo. An ab initio effective solid-state photoluminescence by frequency constraint of cluster calculation. *J. Appl. Phys.*, 128(23):233102, 2020.

[115] Akib Karim, Igor Lyskov, Salvy P Russo, and Alberto Peruzzo. Bright ab initio photoluminescence of NV^+ in diamond. *J. Appl. Phys.*, 130(23):234402, 2021.

[116] Ryan A. Beck, Yue Huang, Alessio Petrone, Joseph W. Abbott, Peter J. Pauzauskie, and Xiaosong Li. Electronic structures and spectroscopic signatures of noble-gas-doped nanodiamonds. *ACS Phys. Chem. Au*, 3(3):299–310, 2023.

[117] Xu Zhang and Gang Lu. Subspace formulation of time-dependent density functional theory for large-scale calculations. *J. Chem. Phys.*, 143(6):064110, 2015.

[118] Mihails Arhangelskis, Dominik B Jochym, Leonardo Bernasconi, Tomislav Friscic, Andrew J Morris, and William Jones. Time-dependent density-functional theory for modeling solid-state fluorescence emission of organic multicomponent crystals. *J. Phys. Chem. A*, 122(37):7514–7521, 2018.

[119] Xu Zhang, Gang Lu, Roi Baer, Eran Rabani, and Daniel Neuhauser. Linear-response time-dependent density functional theory with stochastic range-separated hybrids. *J. Chem. Theory Comput.*, 16(2):1064–1072, 2020.

[120] Jie Liu, Wei Hu, and Jinlong Yang. An efficient implementation of analytical nuclear gradients for linear-response time-dependent density functional theory in the plane wave basis. *Electron. Struct.*, 5(2):024003, 2023.

[121] Marco Govoni and Giulia Galli. Large scale GW calculations. *J. Chem. Theory Comput.*, 11:2680–2696, 2015.

[122] Victor Wen-zhe Yu and Marco Govoni. GPU acceleration of large-scale full-frequency GW calculations. *J. Chem. Theory Comput.*, 18:4690–4707, 2022.

[123] Lin Lin. Adaptively compressed exchange operator. *J. Chem. Theory Comput.*, 12(5):2242–2249, 2016.

[124] Valeria Simoncini and Daniel B. Szyld. Theory of inexact Krylov subspace methods and applications to scientific computing. *SIAM J. Sci. Comput.*, 25(2):454–477, 2003.

[125] Jasper Van Den Eshof and Gerard L. G. Sleijpen. Inexact Krylov subspace methods for linear systems. *SIAM J. Matrix Anal. Appl.*, 26(1):125–153, 2004.

[126] Hosung Seo, He Ma, Marco Govoni, and Giulia Galli. Designing defect-based qubit candidates in wide-gap binary semiconductors for solid-state quantum technologies. *Phys. Rev. Mater.*, 1(7):075002, 2017.

[127] Alex P Gaiduk, Marco Govoni, Robert Seidel, Jonathan H Skone, Bernd Winter, and Giulia Galli. Photoelectron spectra of aqueous solutions from first principles. *J. Am. Chem. Soc.*, 138(22):6912–6915, 2016.

[128] Alex P Gaiduk, Jeffrey Gustafson, Francois Gygi, and Giulia Galli. First-principles simulations of liquid water using a dielectric-dependent hybrid functional. *J. Phys. Chem. Lett.*, 9(11):3068–3073, 2018.

[129] Matteo Gerosa, Francois Gygi, Marco Govoni, and Giulia Galli. The role of defects and excess surface charges at finite temperature for optimizing oxide photoabsorbers. *Nat. Mater.*, 17(12):1122–1127, 2018.

[130] Tuan Anh Pham, Marco Govoni, Robert Seidel, Stephen E Bradforth, Eric Schwegler, and Giulia Galli. Electronic structure of aqueous solutions: Bridging the gap between theory and experiments. *Sci. Adv.*, 3(6):e1603210, 2017.

[131] Alexey Tal, Peitao Liu, Georg Kresse, and Alfredo Pasquarello. Accurate optical spectra through time-dependent density functional theory based on screening-dependent hybrid functionals. *Phys. Rev. Res.*, 2(3):032019, 2020.

[132] Sijia S Dong, Marco Govoni, and Giulia Galli. Machine learning dielectric screening for the simulation of excited state properties of molecules and materials. *Chem. Sci.*, 12(13):4970–4980, 2021.

[133] E. K. U. Gross, J. F. Dobson, and M. Petersilka. Density functional theory of time-dependent phenomena. *Density Functional Theory II: Relativistic and Time Dependent Extensions*, pages 81–172, 2005.

[134] E.K.U. Gross and W. Kohn. Time-dependent density-functional theory. In *Advances in Quantum Chemistry*, pages 255–291. Elsevier, 1990.

[135] So Hirata, Martin Head-Gordon, and Rodney J Bartlett. Configuration interaction singles, time-dependent hartree–fock, and time-dependent density functional theory for the electronic excited states of extended systems. *J. Chem. Phys.*, 111(24):10774–10786, 1999.

[136] Nicholas C Handy and Henry F Schaefer III. On the evaluation of analytic energy derivatives for correlated wave functions. *J. Chem. Phys.*, 81(11):5031–5033, 1984.

[137] François Gygi, Jean-Luc Fattebert, and Eric Schwegler. Computation of maximally localized wannier functions using a simultaneous diagonalization algorithm. *Comput. Phys. Commun.*, 155(1):1–6, 2003.

[138] Ernest R Davidson. The iterative calculation of a few of the lowest eigenvalues and corresponding eigenvectors of large real-symmetric matrices. *J. Chem. Phys.*, 17:87–94, 1975.

[139] Paolo Giannozzi, Oscar Baseggio, Pietro Bonfà, Davide Brunato, Roberto Car, Ivan Carnimeo, Carlo Cavazzoni, Stefano de Gironcoli, Pietro Delugas, Fabrizio Ferrari Ruffino, Andrea Ferretti, Nicola Marzari, Iurii Timrov, Andrea Urru, and Stefano Baroni. Quantum ESPRESSO toward the exascale. *J. Chem. Phys.*, 152:154105, 2020.

[140] Ivan Carnimeo, Fabio Affinito, Stefano Baroni, Oscar Baseggio, Laura Bellentani, Riccardo Bertossa, Pietro Davide Delugas, Fabrizio Ferrari Ruffino, Sergio Orlandini, Filippo Spiga, and Paolo Giannozzi. Quantum ESPRESSO: One further step toward the exascale. *J. Chem. Theory Comput.*, 19(20):6992–7006, 2023.

[141] D R Hamann. Optimized norm-conserving Vanderbilt pseudopotentials. *Phys. Rev. B*, 88:085117, 2013.

[142] Martin Schlipf and François Gygi. Optimization algorithm for the generation of ONCV pseudopotentials. *Comput. Phys. Commun.*, 196:36–44, 2015.

[143] Gordon Davies and MF Hamer. Optical studies of the 1.945 eV vibronic band in diamond. *Proc. Math. Phys. Eng. Sci.*, 348(1653):285–298, 1976.

[144] Qiang Li, Jun-Feng Wang, Fei-Fei Yan, Ji-Yang Zhou, Han-Feng Wang, He Liu, Li-Ping Guo, Xiong Zhou, Adam Gali, Zheng-Hao Liu, Zu-Qing Wang, Kai Sun, Guo-Ping Guo, Jian-Shun Tang, Hao Li, Li-Xing You, Jin-Shi Xu, Chuan-Feng Li, and Guang-Can Guo. Room-temperature coherent manipulation of single-spin qubits in silicon carbide with a high readout contrast. *Natl. Sci. Rev.*, 9(5):nwab122, 2022.

[145] Jiawei Zhan, Marco Govoni, and Giulia Galli. Nonempirical range-separated hybrid functional with spatially dependent screened exchange. *J. Chem. Theory Comput.*, 19(17):5851–5862, 2023.

[146] LJ Rogers, S Armstrong, MJ Sellars, and NB Manson. Infrared emission of the NV centre in diamond: Zeeman and uniaxial stress studies. *New J. Phys.*, 10(10):103024, 2008.

[147] P Kehayias, MW Doherty, D English, R Fischer, Andrey Jarmola, K Jensen, N Leefer, P Hemmer, NB Manson, and Dmitry Budker. Infrared absorption band and vibronic structure of the nitrogen-vacancy center in diamond. *Phys. Rev. B*, 88(16):165202, 2013.

[148] Michael Lurie Goldman, MW Doherty, Alp Sipahigil, Norman Ying Yao, SD Bennett, NB Manson, Alexander Kubanek, and Mikhail D Lukin. State-selective intersystem crossing in nitrogen-vacancy centers. *Phys. Rev. B*, 91(16):165201, 2015.

[149] Michael Lurie Goldman, Alp Sipahigil, MW Doherty, Norman Ying Yao, SD Bennett, M Markham, DJ Twitchen, NB Manson, Alexander Kubanek, and Mikhail D Lukin. Phonon-induced population dynamics and intersystem crossing in nitrogen-vacancy centers. *Phys. Rev. Lett.*, 114(14):145502, 2015.

[150] Yu Jin, Marco Govoni, and Giulia Galli. Vibrationally resolved optical excitations of the nitrogen-vacancy center in diamond. *npj Comput. Mater.*, 8(1):238, 2022.

[151] Lucio Robledo, Hannes Bernien, Toeno Van Der Sar, and Ronald Hanson. Spin dynamics in the optical cycle of single nitrogen-vacancy centres in diamond. *New J. Phys.*, 13(2):025013, 2011.

[152] VM Acosta, A Jarmola, E Bauch, and D Budker. Optical properties of the nitrogen-vacancy singlet levels in diamond. *Phys. Rev. B*, 82(20):201202, 2010.

[153] Joel Davidsson, Viktor Ivády, Rickard Armiento, NT Son, Adam Gali, and Igor A Abrikosov. First principles predictions of magneto-optical data for semiconductor point defect identification: the case of divacancy defects in 4H–SiC. *New J. Phys.*, 20(2):023035, 2018.

[154] Michel Bockstedte, Felix Schütz, Thomas Garratt, Viktor Ivády, and Adam Gali. Ab initio description of highly correlated states in defects for realizing quantum bits. *npj Quantum Mater.*, 3(1):31, 2018.

[155] Brendon C. Rose, Ding Huang, Zi-Huai Zhang, Paul Stevenson, Alexei M. Tyryshkin, Sorawis Sangtawesin, Srikanth Srinivasan, Lorne Loudin, Matthew L. Markham, Andrew M. Edmonds, Daniel J. Twitchen, Stephen A. Lyon, and Nathalie P. de Leon. Observation of an environmentally insensitive solid-state spin defect in diamond. *Science*, 361(6397):60–63, 2018.

[156] BL Green, MW Doherty, Enrik Nako, NB Manson, UFS D'Haenens-Johansson, SD Williams, DJ Twitchen, and Mark E Newton. Electronic structure of the neutral silicon-vacancy center in diamond. *Phys. Rev. B*, 99(16):161112, 2019.

[157] Gergő Thiering and Adam Gali. The $(e_g \otimes e_u) \otimes E_g$ product Jahn–Teller effect in the neutral group-IV vacancy quantum bits in diamond. *npj Comput. Mater.*, 5(1):18, 2019.

[158] Ulrika FS D'Haenens-Johansson, AM Edmonds, BL Green, Mark E Newton, G Davies, PM Martineau, RUA Khan, and DJ Twitchen. Optical properties of the neutral silicon split-vacancy center in diamond. *Phys. Rev. B*, 84(24):245208, 2011.

[159] Elisa Londero, Gergő Thiering, Lukas Razinkovas, Adam Gali, and Audrius Alkauskas. Vibrational modes of negatively charged silicon-vacancy centers in diamond from ab initio calculations. *Phys. Rev. B*, 98(3):035306, 2018.

[160] Zi-Huai Zhang, Paul Stevenson, Gergő Thiering, Brendon C Rose, Ding Huang, Andrew M Edmonds, Matthew L Markham, Stephen A Lyon, Adam Gali, and Nathalie P De Leon. Optically detected magnetic resonance in neutral silicon vacancy centers in diamond via bound exciton states. *Phys. Rev. Lett.*, 125(23):237402, 2020.

[161] Beata Taudul, Elmer Nahuel Monteblanco, Ufuk Halisdemir, Daniel Lacour, Filip Schleicher, François Montaigne, Eric Beaurepaire, Samy Boukari, Michel Hehn, Mébarek Alouani, and Martin Bowen. Tunneling spintronics across MgO driven by double oxygen vacancies. *Adv. Electron. Mater.*, 3(7):1600390, 2017.

[162] F. Schleicher, U. Halisdemir, Daniel Lacour, M. Gallart, S. Boukari, G. Schmerber, V. Davesne, P. Panissod, D. Halley, H. Majjad, Y. Henry, B. Leconte, A. Boulard, D. Spor, N. Beyer, C. Kieber, E. Sternitzky, O. Cregut, M. Ziegler, François Montaigne, E. Beaurepaire, P. Gilliot, Michel Hehn, and M. Bowen. Localized states in advanced dielectrics from the vantage of spin-and symmetry-polarized tunnelling across mgo. *Nat. Commun.*, 5(1):4547, 2014.

[163] Guo-Xing Miao, Young Ju Park, Jagadeesh S Moodera, M Seibt, Gerrit Eilers, and M Münzenberg. Disturbance of tunneling coherence by oxygen vacancy in epitaxial Fe/MgO/Fe magnetic tunnel junctions. *Phys. Rev. Lett.*, 100(24):246803, 2008.

[164] Julian P Velev, Kirill D Belashchenko, Sitaram S Jaswal, and Evgeny Y Tsymbal. Effect of oxygen vacancies on spin-dependent tunneling in Fe/MgO/Fe magnetic tunnel junctions. *Appl. Phys. Lett.*, 90(7):072502, 2007.

[165] Ivan A Popov, Elisa Jimenez-Izal, Anastassia N Alexandrova, and Alexander I Boldyrev. Multicenter bonding effects in oxygen vacancy in the bulk and on the surface of MgO. *J. Phys. Chem. C*, 122(22):11933–11937, 2018.

[166] Maksim Kulichenko, Nikita Fedik, Dmitry Steglenko, Ruslan M Minyaev, Vladimir I Minkin, and Alexander I Boldyrev. Periodic F-defects on the MgO surface as potential single-defect catalysts with non-linear optical properties. *Chem. Phys.*, 532:110680, 2020.

[167] XD Peng, DA Richards, and PC Stair. Surface composition and reactivity of lithium-doped magnesium oxide catalysts for oxidative coupling of methane. *J. Catal.*, 121(1):99–109, 1990.

[168] Yogesh C Sharma, Bhaskar Singh, and John Korstad. Latest developments on application of heterogenous basic catalysts for an efficient and eco friendly synthesis of biodiesel: A review. *Fuel*, 90(4):1309–1324, 2011.

[169] Yoyo Hinuma, Takashi Toyao, Takashi Kamachi, Zen Maeno, Satoru Takakusagi, Shinya Furukawa, Ichigaku Takigawa, and Ken-ichi Shimizu. Density functional theory calculations of oxygen vacancy formation and subsequent molecular adsorption on oxide surfaces. *J. Phys. Chem. C*, 122(51):29435–29444, 2018.

[170] Y Chen, RT Williams, and WA Sibley. Defect cluster centers in MgO. *Phys. Rev.*, 182(3):960, 1969.

[171] Lawrence A Kappers, Roger L Kroes, and Eugene B Hensley. F^+ and F' centers in magnesium oxide. *Phys. Rev. B*, 1(10):4151, 1970.

[172] Christian Vorwerk and Giulia Galli. Disentangling photoexcitation and photoluminescence processes in defective MgO. *Phys. Rev. Mater.*, 7(3):033801, 2023.

[173] Jack Strand, Sergey K Chulkov, Matthew B Watkins, and Alexander L Shluger. First principles calculations of optical properties for oxygen vacancies in binary metal oxides. *J. Chem. Phys.*, 150(4):044702, 2019.

[174] Wei Hu, Jie Liu, Yingzhou Li, Zijing Ding, Chao Yang, and Jinlong Yang. Accelerating excitation energy computation in molecules and solids within linear-response time-dependent density functional theory via interpolative separable density fitting decomposition. *J. Chem. Theory Comput.*, 16(2):964–973, 2020.

[175] Xinming Qin, Wei Hu, and Jinlong Yang. Interpolative separable density fitting for accelerating two-electron integrals: a theoretical perspective. *J. Chem. Theory Comput.*, 19(3):679–693, 2023.

[176] Zhichen Pu, Hao Li, Ning Zhang, Hong Jiang, Yiqin Gao, Yunlong Xiao, Qiming Sun, Yong Zhang, and Sihong Shao. Noncollinear density functional theory. *Phys. Rev. Res.*, 5(1):013036, 2023.

[177] Hao Li, Zhichen Pu, Qiming Sun, Yi Qin Gao, and Yunlong Xiao. Noncollinear and spin-flip TDDFT in multicollinear approach. *J. Chem. Theory Comput.*, 19(8):2270–2281, 2023.

[178] André Schleife and Friedhelm Bechstedt. Ab initio description of quasiparticle band structures and optical near-edge absorption of transparent conducting oxides. *J. Mater. Res.*, 27(17):2180–2189, 2012.

[179] F. Joseph Heremans, Christopher G. Yale, and David D. Awschalom. Control of spin defects in wide-bandgap semiconductors for quantum technologies. *Proc. IEEE*, 104(10):2009–2023, 2016.

[180] David D Awschalom, Ronald Hanson, Jörg Wrachtrup, and Brian B Zhou. Quantum technologies with optically interfaced solid-state spins. *Nat. Photonics*, 12(9):516–527, 2018.

[181] Gang Zhang, Yuan Cheng, Jyh-Pin Chou, and Adam Gali. Material platforms for defect qubits and single-photon emitters. *Appl. Phys. Rev.*, 7(3):031308, 2020.

[182] John Walker. Optical absorption and luminescence in diamond. *Rep. Prog. Phys.*, 42(10):1605, 1979.

[183] Audrius Alkauskas, John L. Lyons, Daniel Steiauf, and Chris G. Van de Walle. First-principles calculations of luminescence spectrum line shapes for defects in semiconductors: The example of GaN and ZnO. *Phys. Rev. Lett.*, 109:267401, 2012.

[184] Michael A Reshchikov. Measurement and analysis of photoluminescence in GaN. *J. Appl. Phys.*, 129(12):121101, 2021.

[185] Ivan A Aleksandrov and Konstantin S Zhuravlev. Luminescence line shapes of band to deep centre and donor–acceptor transitions in AlN. *J. Phys. Condens. Matter*, 32(43):435501, 2020.

[186] Sherif Abdulkader Tawfik, Sajid Ali, Marco Fronzi, Mehran Kianinia, Toan Trong Tran, Catherine Stampfl, Igor Aharonovich, Milos Toth, and Michael J Ford. First-principles investigation of quantum emission from hBN defects. *Nanoscale*, 9(36):13575–13582, 2017.

[187] H. Hamdi, G. Thiering, Z. Bodrog, V. Ivády, and A. Gali. Stone–wales defects in hexagonal boron nitride as ultraviolet emitters. *npj Comput. Mater.*, 6:178, 2020.

[188] Gabriele Grosso, Hyowon Moon, Christopher J. Ciccarino, Johannes Flick, Noah Mendelson, Lukas Mennel, Milos Toth, Igor Aharonovich, Prineha Narang, and Dirk R. Englund. Low-temperature electron–phonon interaction of quantum emitters in hexagonal boron nitride. *ACS Photonics*, 7(6):1410–1417, 2020.

[189] Robin Camphausen, Loris Marini, Sherif Abdulkader Tawfik, Toan Trong Tran, Michael J Ford, and Stefano Palomba. Observation of near-infrared sub-poissonian photon emission in hexagonal boron nitride at room temperature. *APL Photonics*, 5(7):076103, 2020.

[190] Cesar Jara, Tomáš Rauch, Silvana Botti, Miguel A. L. Marques, Ariel Norambuena, Raul Coto, J. E. Castellanos-Águila, Jeronimo R. Maze, and Francisco Munoz. First-principles identification of single photon emitters based on carbon clusters in hexagonal boron nitride. *J. Phys. Chem. A*, 125(6):1325–1335, 2021.

[191] Christopher Linderälv, Witlef Wieczorek, and Paul Erhart. Vibrational signatures for the identification of single-photon emitters in hexagonal boron nitride. *Phys. Rev. B*, 103:115421, 2021.

[192] G. Thiering and A. Gali. Complexes of silicon, vacancy, and hydrogen in diamond: A density functional study. *Phys. Rev. B*, 92:165203, 2015.

[193] Ariel Norambuena, Sebastián A. Reyes, José Mejía-Lopéz, Adam Gali, and Jerónimo R. Maze. Microscopic modeling of the effect of phonons on the optical properties of solid-state emitters. *Phys. Rev. B*, 94:134305, 2016.

[194] G. Thiering and Adam Gali. Ab initio calculation of spin-orbit coupling for an NV center in diamond exhibiting dynamic Jahn-Teller effect. *Phys. Rev. B*, 96:081115, 2017.

[195] Jianhua Zhang, Cai-Zhuang Wang, Zizhong Zhu, Qing Huo Liu, and Kai-Ming Ho. Multimode jahn-teller effect in bulk systems: A case of the NV^0 center in diamond. *Phys. Rev. B*, 97:165204, 2018.

[196] Gerg ő Thiering and Adam Gali. Ab initio magneto-optical spectrum of group-iv vacancy color centers in diamond. *Phys. Rev. X*, 8:021063, 2018.

[197] Isaac Harris, Christopher J. Ciccarino, Johannes Flick, Dirk R. Englund, and Prineha Narang. Group-III quantum defects in diamond are stable spin-1 color centers. *Phys. Rev. B*, 102:195206, 2020.

[198] Marcin Roland Zemła, Kamil Czelej, Paulina Kamińska, Chris G. Van de Walle, and Jacek A. Majewski. Electronic structure and magneto-optical properties of silicon-nitrogen-vacancy complexes in diamond. *Phys. Rev. B*, 102:115102, 2020.

[199] Péter Udvarhelyi, G. Thiering, Naoya Morioka, Charles Babin, Florian Kaiser, Daniil Lukin, Takeshi Ohshima, Jawad Ul-Hassan, Nguyen Tien Son, Jelena Vučković, Jörg Wrachtrup, and Adam Gali. Vibronic states and their effect on the temperature and strain dependence of silicon-vacancy qubits in $4H$-SiC. *Phys. Rev. Applied*, 13:054017, 2020.

[200] Z. Shang, A. Hashemi, Y. Berencén, H.-P. Komsa, P. Erhart, S. Zhou, M. Helm, A. V. Krasheninnikov, and G. V. Astakhov. Local vibrational modes of Si vacancy spin qubits in SiC. *Phys. Rev. B*, 101:144109, 2020.

[201] Q. Hassanzada, I. Abdolhosseini Sarsari, A. Hashemi, A. Ghojavand, A. Gali, and M. Abdi. Theoretical study of quantum emitters in two-dimensional silicon carbide monolayers. *Phys. Rev. B*, 102:134103, 2020.

[202] Arsalan Hashemi, Christopher Linderälv, Arkady V. Krasheninnikov, Tapio Ala-Nissila, Paul Erhart, and Hannu-Pekka Komsa. Photoluminescence line shapes for color centers in silicon carbide from density functional theory calculations. *Phys. Rev. B*, 103:125203, 2021.

[203] Chitraleema Chakraborty, Christopher J Ciccarino, and Prineha Narang. Dynamic modulation of phonon-assisted transitions in quantum defects in monolayer transition-metal dichalcogenide semiconductors. *arXiv preprint arXiv:2007.14399*, 2020.

[204] Zhicheng Su, Zeyang Ren, Yitian Bao, Xiangzhou Lao, Jinfeng Zhang, Jincheng Zhang, Deliang Zhu, Youming Lu, Yue Hao, and Shijie Xu. Luminescence landscapes of nitrogen-vacancy centers in diamond: quasi-localized vibrational resonances and selective coupling. *J. Mater. Chem. C*, 7(26):8086–8091, 2019.

[205] Melvin Lax. The Franck-Condon principle and its application to crystals. *J. Chem. Phys.*, 20(11):1752–1760, 1952.

[206] Ryogo Kubo and Yutaka Toyozawa. Application of the method of generating function to radiative and non-radiative transitions of a trapped electron in a crystal. *Prog. Theor. Phys.*, 13(2):160–182, 1955.

[207] Paolo Giannozzi, Stefano Baroni, Nicola Bonini, Matteo Calandra, Roberto Car, Carlo Cavazzoni, Davide Ceresoli, Guido L Chiarotti, Matteo Cococcioni, Ismaila Dabo, Andrea Dal Corso, Stefano de Gironcoli, Stefano Fabris, Guido Fratesi, Ralph Gebauer, Uwe Gerstmann, Christos Gougoussis, Anton Kokalj, Michele Lazzeri, Layla Martin-Samos, Nicola Marzari, Francesco Mauri, Riccardo Mazzarello, Stefano Paolini, Alfredo Pasquarello, Lorenzo Paulatto, Carlo Sbraccia, Sandro Scandolo, Gabriele Sclauzero, Ari P Seitsonen, Alexander Smogunov, Paolo Umari, and Renata M Wentzcovitch. QUANTUM ESPRESSO: a modular and open-source software project for quantum simulations of materials. *J. Phys.: Condens. Matter*, 21(39):395502, 2009.

[208] P Giannozzi, O Andreussi, T Brumme, O Bunau, M Buongiorno Nardelli, M Calandra, R Car, C Cavazzoni, D Ceresoli, M Cococcioni, N Colonna, I Carnimeo, A Dal Corso, S de Gironcoli, P Delugas, R A DiStasio Jr, A Ferretti, A Floris, G Fratesi, G Fugallo, R Gebauer, U Gerstmann, F Giustino, T Gorni, J Jia, M Kawamura, H-Y Ko, A Kokalj, E Küçükbenli, M Lazzeri, M Marsili, N Marzari, F Mauri, N L Nguyen, H-V Nguyen, A Otero de-la Roza, L Paulatto, S Poncé, D Rocca, R Sabatini, B Santra, M Schlipf, A P Seitsonen, A Smogunov, I Timrov, T Thonhauser, P Umari, N Vast, X Wu, and S Baroni. Advanced capabilities for materials modelling with QUANTUM ESPRESSO. *J. Phys.: Condens. Matter*, 29(46):465901, 2017.

[209] Jochen Heyd, Gustavo E. Scuseria, and Matthias Ernzerhof. Hybrid functionals based on a screened coulomb potential. *J. Chem. Phys.*, 118(18):8207–8215, 2003.

[210] Jochen Heyd, Gustavo E. Scuseria, and Matthias Ernzerhof. Erratum: "Hybrid functionals based on a screened coulomb potential" [J. Chem. Phys. 118, 8207 (2003)]. *J. Chem. Phys.*, 124(21):219906, 2006.

[211] L. Gordon, A. Janotti, and C. G. Van de Walle. Defects as qubits in $3C-$ and $4H-$SiC. *Phys. Rev. B*, 92:045208, 2015.

[212] M. Mackoit-Sinkevičienė, M. Maciaszek, C. G. Van de Walle, and A. Alkauskas. Carbon dimer defect as a source of the 4.1 eV luminescence in hexagonal boron nitride. *Appl. Phys. Lett.*, 115(21):212101, 2019.

[213] Tesfaye A Abtew, YY Sun, Bi-Ching Shih, Pratibha Dev, SB Zhang, and Peihong Zhang. Dynamic Jahn-Teller effect in the NV^- center in diamond. *Phys. Rev. Lett.*, 107(14):146403, 2011.

[214] Z. Shang, Y. Berencén, M. Hollenbach, S. Zhou, H. Kraus, T. Ohshima, and G.V. Astakhov. Microwave-assisted spectroscopy of vacancy-related spin centers in hexagonal SiC. *Phys. Rev. Applied*, 15:034059, 2021.

[215] M. Fukami, C.G. Yale, P. Andrich, X. Liu, F.J. Heremans, P.F. Nealey, and D.D. Awschalom. All-optical cryogenic thermometry based on nitrogen-vacancy centers in nanodiamonds. *Phys. Rev. Applied*, 12:014042, 2019.

[216] Kai-Mei C. Fu, Charles Santori, Paul E. Barclay, Lachlan J. Rogers, Neil B. Manson, and Raymond G. Beausoleil. Observation of the dynamic Jahn-Teller effect in the excited states of nitrogen-vacancy centers in diamond. *Phys. Rev. Lett.*, 103:256404, 2009.

[217] F Duschinsky. The importance of the electron spectrum in multi atomic molecules. Concerning the Franck-Condon principle. *Acta Physicochim. URSS*, 7:551–566, 1937.

[218] Otfried Madelung. *Semiconductors: Group IV Elements and III-V Compounds*. Springer Science & Business Media, 2012.

[219] Charles Kittel, Paul McEuen, and Paul McEuen. *Introduction to Solid State Physics*, volume 8. Wiley New York, 1996.

[220] Michael E Levinshtein, Sergey L Rumyantsev, and Michael S Shur. *Properties of Advanced Semiconductor Materials: GaN, AIN, InN, BN, SiC, SiGe*. John Wiley & Sons, 2001.

[221] Lukas Razinkovas, Marek Maciaszek, Friedemann Reinhard, Marcus W Doherty, and Audrius Alkauskas. Photoionization of negatively charged NV centers in diamond: Theory and ab initio calculations. *Phys. Rev. B*, 104(23):235301, 2021.

[222] Joel Davidsson. Theoretical polarization of zero phonon lines in point defects. *J. Condens. Matter Phys.*, 32(38):385502, 2020.

[223] SangKook Choi, Manish Jain, and Steven G Louie. Mechanism for optical initialization of spin in NV^- center in diamond. *Phys. Rev. B*, 86(4):041202, 2012.

[224] Viktor Ivády, Igor A Abrikosov, and Adam Gali. First principles calculation of spin-related quantities for point defect qubit research. *npj Comput. Mater.*, 4(1):1–13, 2018.

[225] Yuchen Ma, Michael Rohlfing, and Adam Gali. Excited states of the negatively charged nitrogen-vacancy color center in diamond. *Phys. Rev. B*, 81:041204, 2010.

[226] Churna Bhandari, Aleksander L. Wysocki, Sophia E. Economou, Pratibha Dev, and Kyungwha Park. Multiconfigurational study of the negatively charged nitrogen-vacancy center in diamond. *Phys. Rev. B*, 103:014115, 2021.

[227] Y. Dumeige, M. Chipaux, V. Jacques, F. Treussart, J.-F. Roch, T. Debuisschert, V. M. Acosta, A. Jarmola, K. Jensen, P. Kehayias, and D. Budker. Magnetometry with nitrogen-vacancy ensembles in diamond based on infrared absorption in a doubly resonant optical cavity. *Phys. Rev. B*, 87:155202, 2013.

[228] K. Jensen, N. Leefer, A. Jarmola, Y. Dumeige, V. M. Acosta, P. Kehayias, B. Patton, and D. Budker. Cavity-enhanced room-temperature magnetometry using absorption by nitrogen-vacancy centers in diamond. *Phys. Rev. Lett.*, 112:160802, 2014.

[229] Arne Wickenbrock, Huijie Zheng, Lykourgos Bougas, Nathan Leefer, Samer Afach, Andrey Jarmola, Victor M Acosta, and Dmitry Budker. Microwave-free magnetometry with nitrogen-vacancy centers in diamond. *Appl. Phys. Lett.*, 109(5):053505, 2016.

[230] Georgios Chatzidrosos, Arne Wickenbrock, Lykourgos Bougas, Nathan Leefer, Teng Wu, Kasper Jensen, Yannick Dumeige, and Dmitry Budker. Miniature cavity-enhanced diamond magnetometer. *Phys. Rev. Applied*, 8:044019, 2017.

[231] M. L. Goldman, M. W. Doherty, A. Sipahigil, N. Y. Yao, S. D. Bennett, N. B. Manson, A. Kubanek, and M. D. Lukin. Erratum: State-selective intersystem crossing in nitrogen-vacancy centers [Phys. Rev. B 91, 165201 (2015)]. *Phys. Rev. B*, 96:039905, 2017.

[232] Isaac Bersuker. *The Jahn-Teller Effect*. Cambridge University Press, 2006.

[233] Neil Manson, Lachlan Rogers, Marcus Doherty, and Lloyd Hollenberg. Optically induced spin polarisation of the NV-centre in diamond: role of electron-vibration interaction. *Preprint at https://arxiv.org/abs/1011.2840*, 2010.

[234] Lachlan J Rogers, Marcus W Doherty, Michael SJ Barson, Shinobu Onoda, Teraji Ohshima, and Neil B Manson. Singlet levels of the NV^- centre in diamond. *New J. Phys.*, 17(1):013048, 2015.

[235] Chaoyuan Zhu, Kuo Kan Liang, Michitoshi Hayashi, and Sheng Hsien Lin. Theoretical treatment of anharmonic effect on molecular absorption, fluorescence spectra, and electron transfer. *Chem. Phys.*, 358(1):137–146, 2009.

[236] Christoph Freysoldt, Jörg Neugebauer, and Chris G Van de Walle. Fully ab initio finite-size corrections for charged-defect supercell calculations. *Phys. Rev. Lett.*, 102(1):016402, 2009.

[237] Hsiao-Yi Chen, Maurizia Palummo, Davide Sangalli, and Marco Bernardi. Theory and ab initio computation of the anisotropic light emission in monolayer transition metal dichalcogenides. *Nano lett.*, 18(6):3839–3843, 2018.

[238] Björn Magnusson, Nguyen Tien Son, András Csóré, Andreas Gällström, Takeshi Ohshima, Adam Gali, and Ivan G. Ivanov. Excitation properties of the divacancy in 4*H*-SiC. *Phys. Rev. B*, 98:195202, 2018.

[239] PeterY Yu. *Fundamentals of semiconductors*. Springer, 2005.

[240] Peter Deák, Bálint Aradi, Moloud Kaviani, Thomas Frauenheim, and Adam Gali. Formation of NV centers in diamond: A theoretical study based on calculated transitions

and migration of nitrogen and vacancy related defects. *Phys. Rev. B*, 89(7):075203, 2014.

[241] RG Farrer. On the substitutional nitrogen donor in diamond. *Solid State Commun.*, 7(9):685–688, 1969.

[242] Milos Nesládek, LM Stals, Andre Stesmans, K Iakoubovskij, GJ Adriaenssens, J Rosa, and M Vaněček. Dominant defect levels in diamond thin films: A photocurrent and electron paramagnetic resonance study. *Appl. Phys. Lett.*, 72(25):3306–3308, 1998.

[243] Konstantin Iakoubovskii and GJ Adriaenssens. Optical transitions at the substitutional nitrogen centre in diamond. *J. Phys.: Condens. Matter*, 12(6):L77, 2000.

[244] Jan Isberg, Antonella Tajani, and Daniel J Twitchen. Photoionization measurement of deep defects in single-crystalline CVD diamond using the transient-current technique. *Phys. Rev. B*, 73(24):245207, 2006.

[245] FJ Heremans, GD Fuchs, CF Wang, R Hanson, and DD Awschalom. Generation and transport of photoexcited electrons in single-crystal diamond. *Appl. Phys. Lett.*, 94(15):152102, 2009.

[246] R Jones, JP Goss, and PR Briddon. Acceptor level of nitrogen in diamond and the 270-nm absorption band. *Phys. Rev. B*, 80(3):033205, 2009.

[247] Harishankar Jayakumar, Jacob Henshaw, Siddharth Dhomkar, Daniela Pagliero, Abdelghani Laraoui, Neil B Manson, Remus Albu, Marcus W Doherty, and Carlos A Meriles. Optical patterning of trapped charge in nitrogen-doped diamond. *Nat. Commun.*, 7(1):12660, 2016.

[248] Samuel D Stranks and Henry J Snaith. Metal-halide perovskites for photovoltaic and light-emitting devices. *Nat. Nanotechnol.*, 10(5):391–402, 2015.

[249] Qiao Zhang and Yadong Yin. All-inorganic metal halide perovskite nanocrystals: opportunities and challenges. *ACS Cent. Sci.*, 4(6):668–679, 2018.

[250] Ajay Kumar Jena, Ashish Kulkarni, and Tsutomu Miyasaka. Halide perovskite photovoltaics: background, status, and future prospects. *Chem. Rev.*, 119(5):3036–3103, 2019.

[251] Xiao-Ke Liu, Weidong Xu, Sai Bai, Yizheng Jin, Jianpu Wang, Richard H Friend, and Feng Gao. Metal halide perovskites for light-emitting diodes. *Nat. Mater.*, 20(1):10–21, 2021.

[252] Ying Han, Sijia Yue, and Bin-Bin Cui. Low-dimensional metal halide perovskite crystal materials: structure strategies and luminescence applications. *Adv. Sci.*, 8(15):2004805, 2021.

[253] Daniele Cortecchia, Jun Yin, Annamaria Petrozza, and Cesare Soci. White light emission in low-dimensional perovskites. *J. Mater. Chem. C*, 7(17):4956–4969, 2019.

[254] Mao-Hua Du. Microscopic origin of multiple exciton emission in low-dimensional lead halide perovskites. *J. Chem. Phys.*, 151(18):181101, 2019.

[255] Mingze Li and Zhiguo Xia. Recent progress of zero-dimensional luminescent metal halides. *Chem. Soc. Rev.*, 50(4):2626–2662, 2021.

[256] Qingxun Guo, Xue Zhao, Boxiang Song, Jiajun Luo, and Jiang Tang. Light emission of self-trapped excitons in inorganic metal halides for optoelectronic applications. *Adv. Mater.*, 34(52):2201008, 2022.

[257] Xiaoming Wang, Weiwei Meng, Weiqiang Liao, Jianbo Wang, Ren-Gen Xiong, and Yanfa Yan. Atomistic mechanism of broadband emission in metal halide perovskites. *J. Phys. Chem. Lett.*, 10(3):501–506, 2019.

[258] Mao-Hua Du and Fernando A Reboredo. First-principles calculations of quantum transitions at local centers. *Opt. Mater.: X*, 8:100066, 2020.

[259] Xiaoming Wang and Yanfa Yan. Self-trapped excitons and broadband emission in metal halide perovskites. In *HYBRID ORGANIC INORGANIC PEROVSKITES: Physical Properties and Applications: Volume 2-Hybrid Organic Inorganic Perovskites: Optical Properties*, pages 37–63. World Scientific, 2022.

[260] Huai-Yang Sun, Lin Xiong, and Hong Jiang. Toward first-principles approaches for mechanistic study of self-trapped exciton luminescence. *Chem. Phys. Rev.*, 4(3):031302, 2023.

[261] Giovanni Onida, Lucia Reining, and Angel Rubio. Electronic excitations: density-functional versus many-body green's-function approaches. *Rev. Mod. Phys.*, 74(2):601, 2002.

[262] Sohrab Ismail-Beigi and Steven G Louie. Excited-state forces within a first-principles green's function formalism. *Phys. Rev. Lett.*, 90(7):076401, 2003.

[263] J. Villalobos-Castro, Iryna Knysh, Denis Jacquemin, Ivan Duchemin, and Xavier Blase. Lagrangian Z-vector approach to Bethe–Salpeter analytic gradients: Assessing approximations. *J. Chem. Phys.*, 159(2):024116, 07 2023.

[264] Dan Han, Hongliang Shi, Wenmei Ming, Chenkun Zhou, Biwu Ma, Bayrammurad Saparov, Ying-Zhong Ma, Shiyou Chen, and Mao-Hua Du. Unraveling luminescence mechanisms in zero-dimensional halide perovskites. *J. Mater. Chem. C*, 6(24):6398–6405, 2018.

[265] Tianyang Li, Xihan Chen, Xiaoming Wang, Haipeng Lu, Yanfa Yan, Matthew C Beard, and David B Mitzi. Origin of broad-band emission and impact of structural dimensionality in tin-alloyed ruddlesden–popper hybrid lead iodide perovskites. *ACS Energy Lett.*, 5(2):347–352, 2019.

[266] Linyuan Lian, Moyan Zheng, Peng Zhang, Zhi Zheng, Kang Du, Wen Lei, Jianbo Gao, Guangda Niu, Daoli Zhang, Tianyou Zhai, et al. Photophysics in $Cs_3Cu_2X_5$ (X= Cl, Br, or I): highly luminescent self-trapped excitons from local structure symmetrization. *Chem. Mater.*, 32(8):3462–3468, 2020.

[267] Zhengwei Xu, Xingxing Jiang, Hua-peng Cai, Keqiu Chen, Xiaolong Yao, and Yexin Feng. Toward a general understanding of exciton self-trapping in metal halide perovskites. *J. Phys. Chem. Lett.*, 12(43):10472–10478, 2021.

[268] Xingxing Jiang, Zhengwei Xu, Yueshao Zheng, Jiang Zeng, Ke-Qiu Chen, and Yexin Feng. A first-principles study of exciton self-trapping and electric polarization in one-dimensional organic lead halide perovskites. *Phys. Chem. Chem. Phys.*, 24(28):17323–17328, 2022.

[269] Lin Xiong, Huaiyang Sun, Shuoxue Li, and Hong Jiang. First-principles investigation on the stability, electronic structure, and exciton self-trapping mechanism of 0D and 1D $Cs_3Cu_2Cl_5$. *J. Phys. Chem. C*, 127(19):9113–9120, 2023.

[270] Long Zhang, Shuoxue Li, Huaiyang Sun, Qiwen Jiang, Yue Wang, Yuanyuan Fang, Ying Shi, Defang Duan, Kai Wang, Hong Jiang, et al. Revealing the mechanism of pressure-induced emission in layered silver-bismuth double perovskites. *Angew. Chem., Int. Ed.*, 135(14):e202301573, 2023.

[271] Long Zhang, Shuoxue Li, Huaiyang Sun, Yuanyuan Fang, Yonggang Wang, Kai Wang, Hong Jiang, Laizhi Sui, Guorong Wu, Kaijun Yuan, et al. Manipulating lone-pair-driven luminescence in 0D tin halides by pressure-tuned stereochemical activity from static to dynamic. *Angew. Chem., Int. Ed.*, page e202311912, 2023.

[272] Xingyi Liu, Xiaowen Gao, Lin Xiong, Shuoxue Li, Yu Zhang, Qi Li, Hong Jiang, and Dongsheng Xu. A-site coordinating cation engineering in zero-dimensional antimony halide perovskites for strong self-trapped exciton emission. *SmartMat*, page e1224, 2023.

[273] Jiajun Luo, Xiaoming Wang, Shunran Li, Jing Liu, Yueming Guo, Guangda Niu, Li Yao, Yuhao Fu, Liang Gao, Qingshun Dong, Chunyi Zhao, Meiying Leng, Fusheng Ma, Wenxi Liang, Liduo Wang, Shengye Jin, Junbo Han, Lijun Zhang, Joanne Etheridge, Jianbo Wang, Yanfa Yan, Edward H. Sargent, and Jiang Tang. Efficient and stable emission of warm-white light from lead-free halide double perovskites. *Nature*, 563(7732):541–545, 2018.

[274] Yu Jin, Victor Wen-zhe Yu, Marco Govoni, Andrew C. Xu, and Giulia Galli. Excited state properties of point defects in semiconductors and insulators investigated with

time-dependent density functional theory. *J. Chem. Theory Comput.*, 19(23):8689–8705, 2023.

[275] Francois Gygi. Architecture of Qbox: A scalable first-principles molecular dynamics code. *IBM J. Res. Dev.*, 52(1.2):137–144, 2008.

[276] Hongliang Shi, Dan Han, Shiyou Chen, and Mao-Hua Du. Impact of metal ns^2 lone pair on luminescence quantum efficiency in low-dimensional halide perovskites. *Phys. Rev. Mater.*, 3:034604, 2019.

[277] Bogdan M Benin, Dmitry N Dirin, Viktoriia Morad, Michael Wörle, Sergii Yakunin, Gabriele Rainò, Olga Nazarenko, Markus Fischer, Ivan Infante, and Maksym V Kovalenko. Highly emissive self-trapped excitons in fully inorganic zero-dimensional tin halides. *Angew. Chem. Int. Ed.*, 57(35):11329–11333, 2018.

[278] Xiangtong Zhang, Hua Wang, Shixun Wang, Yue Hu, Xuan Liu, Zhifeng Shi, Vicki L Colvin, Shengnian Wang, William W Yu, and Yu Zhang. Room temperature synthesis of all inorganic lead-free zero-dimensional Cs_4SnBr_6 and Cs_3KSnBr_6 perovskites. *Inorg. Chem.*, 59(1):533–538, 2019.

[279] Huihuo Zheng, Marco Govoni, and Giulia Galli. Dielectric-dependent hybrid functionals for heterogeneous materials. *Phys. Rev. Mater.*, 3:073803, 2019.

[280] Antonios M Alvertis, Jonah B Haber, Zhenglu Li, Christopher JN Coveney, Steven G Louie, Marina R Filip, and Jeffrey B Neaton. Phonon screening and dissociation of excitons at finite temperatures from first principles. *arXiv preprint arXiv:2312.03841*, 2023.

[281] George Volonakis, Amir Abbas Haghighirad, Rebecca L Milot, Weng H Sio, Marina R Filip, Bernard Wenger, Michael B Johnston, Laura M Herz, Henry J Snaith, and Feliciano Giustino. $Cs_2InAgCl_6$: a new lead-free halide double perovskite with direct band gap. *J. Phys. Chem. Lett.*, 8(4):772–778, 2017.

[282] Raisa-Ioana Biega, Yinan Chen, Marina R. Filip, and Linn Leppert. Chemical mapping of excitons in halide double perovskites. *Nano Lett.*, 23(17):8155–8161, 2023. PMID: 37656044.

[283] Viet-Anh Ha, George Volonakis, Hyungjun Lee, Marios Zacharias, and Feliciano Giustino. Quasiparticle band structure and phonon-induced band gap renormalization of the lead-free halide double perovskite $Cs_2InAgCl_6$. *J. Phys. Chem. C*, 125(39):21689–21700, 2021.

[284] Peder Thusgaard Ruhoff. Recursion relations for multi-dimensional Franck-Condon overlap integrals. *Chem. Phys.*, 186(2-3):355–374, 1994.

[285] Jun Yin, Yuhai Zhang, Annalisa Bruno, Cesare Soci, Osman M Bakr, Jean-Luc Brédas, and Omar F Mohammed. Intrinsic lead ion emissions in zero-dimensional Cs_4PbBr_6 nanocrystals. *ACS Energy Lett.*, 2(12):2805–2811, 2017.

[286] Viet-Anh Ha, Hyungjun Lee, George Volonakis, and Feliciano Giustino. What is origin of visible photoluminescence in the lead-free double-perovskite $cs_2inagcl_6$? *Bulletin of the American Physical Society*, 66, 2021.

[287] Yang Zhou, Isabella Poli, Daniele Meggiolaro, Filippo De Angelis, and Annamaria Petrozza. Defect activity in metal halide perovskites with wide and narrow bandgap. *Nat. Rev. Mater.*, 6(11):986–1002, 2021.

[288] Seunghoon Lee, Michael Filatov, Sangyoub Lee, and Cheol Ho Choi. Eliminating spin-contamination of spin-flip time dependent density functional theory within linear response formalism by the use of zeroth-order mixed-reference (MR) reduced density matrix. *J. Chem. Phys.*, 149(10):104101, 2018.

[289] Seunghoon Lee, Emma Eunji Kim, Hiroya Nakata, Sangyoub Lee, and Cheol Ho Choi. Efficient implementations of analytic energy gradient for mixed-reference spin-flip time-dependent density functional theory (MRSF-TDDFT). *J. Chem. Phys.*, 150(18):184111, 2019.

[290] Zhendong Li and Wenjian Liu. Spin-adapted open-shell random phase approximation and time-dependent density functional theory. I. Theory. *J. Chem. Phys.*, 133(6):064106, 2010.

[291] Zhendong Li, Wenjian Liu, Yong Zhang, and Bingbing Suo. Spin-adapted open-shell time-dependent density functional theory. II. Theory and pilot application. *J. Chem. Phys.*, 134(13):134101, 2011.

[292] Zhendong Li and Wenjian Liu. Spin-adapted open-shell time-dependent density functional theory. III. An even better and simpler formulation. *J. Chem. Phys.*, 135(19):194106, 2011.

[293] Zikuan Wang, Zhendong Li, Yong Zhang, and Wenjian Liu. Analytic energy gradients of spin-adapted open-shell time-dependent density functional theory. *J. Chem. Phys.*, 153(16):164109, 2020.

[294] He Li, Zun Wang, Nianlong Zou, Meng Ye, Runzhang Xu, Xiaoxun Gong, Wenhui Duan, and Yong Xu. Deep-learning density functional theory hamiltonian for efficient ab initio electronic-structure calculation. *Nat. Comput. Sci.*, 2(6):367–377, 2022.

[295] He Li, Zechen Tang, Xiaoxun Gong, Nianlong Zou, Wenhui Duan, and Yong Xu. Deep-learning electronic-structure calculation of magnetic superstructures. *Nat. Computat. Sci.*, 3(4):321–327, 2023.

[296] Xiaoxun Gong, He Li, Nianlong Zou, Runzhang Xu, Wenhui Duan, and Yong Xu. General framework for E (3)-equivariant neural network representation of density functional theory hamiltonian. *Nat. Commun.*, 14(1):2848, 2023.

[297] Zechen Tang, He Li, Peize Lin, Xiaoxun Gong, Gan Jin, Lixin He, Hong Jiang, Xinguo Ren, Wenhui Duan, and Yong Xu. Efficient hybrid density functional calculation by deep learning. *arXiv preprint arXiv:2302.08221*, 2023.

[298] Edoardo Cignoni, Divya Suman, Jigyasa Nigam, Lorenzo Cupellini, Benedetta Mennucci, and Michele Ceriotti. Electronic excited states from physically-constrained machine learning. *arXiv preprint arXiv:2311.00844*, 2023.